# "SYNTHESIS OF NICKEL TUNGSTATE / REDUCED GRAPHENE OXIDE COMPOSITE ELECTRODE FOR SUPERCAPACITOR APPLICATION"

A THESIS SUBMITTED TO

D. Y. PATIL EDUCATION SOCIETY (DEEMED TO BE UNIVERSITY), KOLHAPUR



# DOCTOR OF PHILOSOPHY IN PHYSICS

UNDER THE FACULTY OF

INTERDISCIPLINARY STUDIES

BY

MR. DILIP JAGANNATH PATIL

M. Sc., B.Ed.

UNDER THE SUPERVISION OF

PROF. CHANDRAKANT D. LOKHANDE M. Sc., Ph. D.

DEAN & RESEARCH DIRECTOR,
CENTRE FOR INTERDISCIPLINARY RESEARCH,
D. Y. PATIL EDUCATION SOCIETY
(DEEMED TO BE UNIVERSITY),
KOLHAPUR- 416 006.

**DECLARATION** 

I hereby declare that the work contained in this thesis entitled,

"Synthesis of nickel tungstate/reduced graphene oxide composite

electrode for supercapacitor application" has not been previously

submitted to meet requirements for an award at this or any other higher

education institute in India or any other country. To the best of my

knowledge and belief, the thesis contains no material previously published

or written by another person except where due reference is made. Further, I

declare that I have not violated any of the provisions under the copyright and

piracy/cyber/IPR act amended from time to time.

Research student

Place: Kolhapur

Date: / / 2024

Dilip Jagannath Patil

Ш

# D. Y. Patil Education Society (Deemed to be University), Kolhapur

Centre for Interdisciplinary Research



# Certificate

This is to certify that, "Synthesis of nickel tungstate / reduced graphene oxide composite electrode for supercapacitor application" the present thesis which is being submitted herewith for the award of Doctor of Philosophy (Ph.D.) in Physics under the faculty of Center for Interdisciplinary Research (CIR) of D. Y. Patil Education Society, Kolhapur, is the result of original research work completed by Mr. Dilip Jagannath Patil under my supervision and guidance and the best of my knowledge and belief, the work embodied in this thesis has not formed earlier the basis for the award of any degree or similar title of this or any other University or examining body.

Research Guide

Place: Kolhapur

Date: / /2024 Prof. C. D. Lokhande

#### *ACKNOWLEDGEMENT*

I would like to express my first profound thanks and respect towards my cherished guide Prof. (Dr.) Chandrakant D. Lokhande (Dean and Research Director, Centre for Interdisciplinary Research, D. Y. Patil Education Society, Kolhapur) for his keen awareness, valuable guidance, strong inspiration, and constant encouragement during my Ph.D. work. This work would not have been possible without his guidance, encouragement, and support. He is not only a helpful advisor but like a family member. I am very much thankful to him for selecting me as a student at this critical stage. I affectionately thank him for his valuable advice and extensive discussions about my work. I gratefully acknowledge his understanding and personal attention, which have provided a virtuous basis for my Ph.D. tenancy. His flexibility in scheduling, mild encouragement, and relaxed character made for a good working relationship and the motivation for me to finish work. His genuine caring, concern, and faith in me enabled me to attend to life while earning my Ph.D.

I would like to express my sincere thanks to Vice-Chancellor Prof. R. K. Mudgal, Pro-Vice Chancellor Dr. Shimpa Sharma, and the Registrar Dr. V. V. Bhosale for the inspiration and support. I thank Dr. U. M. Patil, Dr. J. L. Gunjakar, Dr. Vishwajeet Khot, Dr. Sharad Patil, and Dr. Pravin Pawar who helped me to analyse the results with all their empathy and cooperative mind. I also thank Dr. A. C. Lokhande, Dr. V. C. Lokhande, and Dr. Dhanaji Malavekar for providing me very important sample characterization data during the entire research work.

I would like to sincerely thank my seniors Dhanaji Malavekar, Shital Kale, Satish Jadhav, Sachin Pujari, Shivaji Ubale, Prity Bagwade, Suraj Khalate, Navnath Padalkar, Shrikant Sadavar, Navanath Padalkar, Rohini Shinde, Vikas Mane, Vikas Magdum, Yogesh Chitare, and Shirin

**Kulkarni** for insightful guidance, scientific discussions, and valuable suggestions on the present work.

I would like to acknowledge my colleagues at the Centre for Interdisciplinary Research, Sambhaji Khot, Ranjeet Nikam, Sambhaji Kumbhar, Ajinkya Bagade, Shraddha Bhosale, Satish Phalke, Divya Powar, Joti Thorat, Ketaki Kadam, Sumita Patil, Kuldip Belekar, Rakesh Mohite, Manohar Lad, Prashant Sawant, Shweta Talekar, Shraddha Pawar, Sohel Shaikh, and Sagar Patil for their wonderful collaboration. I want to thank them for their support and valuable suggestions during research work.

I am thankful to Mrs. Namrata, Mr. Ramdas, Mr. Omkar, and Mrs. Sarita Mavshi of the Center for Interdisciplinary Research (CIR) and D. Y. Patil Education Society for co-operation in many ways during my PhD.

On this occasion, I must remember my father Jagannath (Anna), Mother Sushila (Aai), wife Sujata (Suja), Sister Bharti (Akka), Brother Sampat, elder Son Pranav and little Son Prithviraj for their constant support, encouragement and their love affection towards me to cruise through the difficulties to bring me at this position.

I want to express my special profound thanks and respect towards **Dr.** Sanjay D. Patil (Chairman of D. Y. Patil Education Society, Kolhapur) for their financial support, valuable guidance, inspiration, and encouragement during my Ph.D. work.

I would like to acknowledge that even though I tried my best, it is not possible to acknowledge all those known and unknown faces individually for their direct and indirect contribution to the successful completion of my work. I am thankful to all of you for your kind cooperation.

Place- Kolhapur

- Dilip J. Patil

#### LIST OF PATENTS, PUBLICATIONS AND CONFERENCES ATTAINED

#### Patents (02 granted)

- Chemical synthesis of cadmium selenide/reduced graphene oxide composite thin film and photoelectrochemical cell application, Chandrakant D. Lokhande, Ranjit P. Nikam, Sambhaji D. Khot, Prity P. Bagwade, Dilip J. Patil, granted on 28<sup>th</sup> November 2023, Grant number- 473475.
- A method of Synthesizing composite of reduced graphene oxide and nickel tungstate for energy storage, Prof. C. D. Lokhande, Mr. D. J. Patil, Dr. D. B. Malavekar, Mr. S. D. Khot, Mr. R. P. Nikam, granted on 8<sup>th</sup> December 2023, Grant number- 479403.

#### **Research Publications in International Journals (06)**

- 1. D. J. Patil, D. B. Malavekar, V. C, Lokhande, P. P. Bagwade, S. D. Khot, T. Ji, C. D. Lokhande, Binder-free synthesis of mesoporous nickel tungstate for Aqueous Asymmetric Supercapacitor Applications: Effect of film thickness, Energy Technol. (2022), 2200295 (I.F-4.12).
- **2. D. J. Patil**, D. B. Malavekar, J. H. Kim and C.D. Lokhande, Facial synthesis of reduced graphene oxide amorphous nickel tungstate composite for flexible hybrid asymmetric solid state supercapacitor application, Journal of Energy Storage 72 (2023) 108729 (**I.F. 9.5**).
- **3.** D. B. Malavekar, V. C. Lokhande, **D. J. Patil**, S. B. Kale, U. M. Patil, C. D. Lokhande, Amorphous nickel tungstate films prepared by SILAR method for electrocatalytic oxygen evolution reaction, J. Colloid Interface Sci., 609 (2022) 734-745 (**I.F. 8.12**).
- **4.** S.D. Khot, D.B. Malavekar, R.P. Nikam, S.B. Ubale, P.P. Bagwade, **D.J. Patil**, V.C. Lokhande, C.D. Lokhande, SILAR synthesized dysprosium selenide (Dy<sub>2</sub>Se<sub>3</sub>) thin films for hybrid electrochemical capacitors, Synthetic metals, 287, (2022), 117075. (**I.F 3.26**)
- P. P. Bagwade, D. B. Malavekar; V. V. Magdum; S. D. Khot; R. P. Nikam; D. J. Patil;
   U. M. Patil; C. D. Lokhande, Nanocrystalline Cobalt Tungstate Thin Films Prepared
   by SILAR Method for Electrocatalytic Oxygen Evolution Reaction, (2022). (I.F. 7.139)

6. Mr. Satish Jadhav, D. B. Malavekar, D. J. Patil, S. S. Pujari, C. D. Lokhande, P. N. Pawaskar, Dual Functional SILAR Deposited NiWO4 Film Electrodes for Non-enzymatic Glucose Detection and Hydrogen Evolution Reaction., Applied Physics A (2023) 129:524. (I.F. 2.983).

#### Papers presented at national/international conferences (05)

- 1. **D. J. Patil**, D. B. Malavekar, C. D. Lokhande "Preparation and characterization of NiWO4 thin films using SILAR method" the 2nd Asian E-conference on Engineered Science (Theme: Thin Film Materials and Devices) Jointly organized by Prof. C. D. Lokhande Endowment Charitable Trust and Engineered Science Publisher USA held on 5 & 6 Dec.2021.
- **2. D. J. Patil,** C. D. Lokhande, "Effect of film thickness on binder free synthesis of mesoporous nickel tungstate for aqueous asymmetric supercapacitor applications" international conference on Advanced Materials, Synthesis, Characterization, and Applications (AMSCA-2022) from October 18 to 20, 2022 organized by the Department of Physics of Savitribai Phule Pune University.
- 3. **D. J. Patil**, C.D. Lokhande, "Electrochemical Performance of Reduced Graphene Oxide-Nickel Tungstate Electrode Synthesized via Successive Ionic Layer Adsorption and Reaction (SILAR) Method for Asymmetric Solid-State Supercapacitor" Two-Day National Seminar on 'Recent Scenario in Chemical Sciences and Material Sciences' (RSCSMS-2023) on 3rd & 4th March 2023 at Shri Vijaysinha Yadav College, Peth Vadgaon, Dist. Kolhapur.
- **4. D. J. Patil**, C.D. Lokhande "Enhanced Electrochemical Performance of Reduced Graphene Oxide-Nickel Tungstate Thin Films Synthesized via Successive Ionic Layer Adsorption and Reaction (SILAR) Method for Asymmetric Solid-State Supercapacitor" National Conference on Physics of Materials & Material-based Device Fabrication2023 (NCPM-MDF-2023) Organized by Department of Physics Shivaji University, Kolhapur-416004, Maharashtra, India.
- **5. D. J. Patil,** D. B. Malavekar, J. H. Kim and C.D. Lokhande, "Facial synthesis of reduced graphene oxide amorphous nickel tungstate composite for flexible hybrid asymmetric solid state supercapacitor application" International Conference on

Nanotechnology Addressing the Convergence of Materials Science, Biotechnology, and Medical Science, (ICNACMBM-2024) organised by Centre for Interdisciplinary Research, D. Y. Patil Education Society, (Deemed to be University), Kolhapur, Maharashtra, India 416003 on 12th - 14<sup>th</sup> February 2024.

#### **Attended National / International Conference / Seminar (06)**

- **1.** Participated International seminar series on Nanotechnology on Environment and Sustainability, organized by D. Y. Patil Education Society, deemed to be University, Kolhapur held on 12 & 13 Jan. 2021.
- **2.** Actively participated in one day national level webinar on best practices in laboratory safety management, organized by IQAC of Art's, Science and Commerce College, Dist-Amravati held on 26 Dec.2020.
- **3.** Attended National Conference on "Science & Technology for Sustainable Development with Women Empowerment" Sponsored by Indian Science Congress Association, Amravati Chapter held Online on 19 Dec 2020.
- **4.** 2nd Asian E-conference on Engineered Science (Theme: Thin Film Materials and Devices) Jointly organized by Prof. C. D. Lokhande Endowment Charitable Trust and Engineered Science Publisher USA held on 5 & 6 Dec.2021.
- **5.** Attended International Conference on Emerging Trends in Material Science at D. P. Bhosale College, Koregaon, District- Satara, Maharashtra, India on 9th & 10th November 2022.
- **6.** Participated in Recent advances in materials Science and Engineering, AICTE & ISTE approved orientation/Refresher Program organized by SVERI College of Engineering Pandharpur from 18/01/22 to 24/01/22.

#### **Workshop / Training Participation (10)**

1. Attended a 7-day hands-on training workshop on "Challenges and opportunities for innovative research using sophisticated instruments under the scheme STUTI supported by DST, Government of India, organized by SAIF-DST, Shivaji University Kolhapur.

- **2.** Active participation in the 9-day Research Methodology Workshop; Organized by Internal Quality Assurance Cell & Research Guidance Cell at D.Y. Patil Education Society (Deemed to be University), Kolhapur, held on 21 Feb. to 5 Mar 2022.
- **3.** Online participated in a two-day online workshop on writing research articles Using LaTex, Aditya College of Engineering, Andra Pradesh held on 27 &28 Dec.2021.
- **4.** Participated in an online webinar on "Research Opportunities in Electrical Power Engineering" at Prasad V. Potluri Siddhartha Institute of Technology, Andhra Pradesh, India, held from 23 to 27 March 2022.
- **5.** Attended a one-day workshop on ABC and MEME of NEP-2020 at Shivaji University, Kolhapur.
- **6**. Participated in Recent materials Science and Engineering advances, AICTE & ISTE approved orientation/Refresher Program organized by SVERI College of Engineering Pandharpur from 18/01/22 to 24/01/22.
- **7.** Participated in the AICTE Recognized Faculty Development Programme on Soft Skills & Classroom Teaching Conducted by Education and Educational Management Department from 20/03/2023 to 24/03/2023 (One Week) at Dr. D.Y. Patil Pratishtha's College of Engineering, Salokhenagar, Kolhapur organized by NITTR Chandigarh.
- **8.** Participated in National Science Day 2023 (NSD-2023) on 27-28 February, 2023 organized by Department of Engineering Mathematics, Department Physics, Department Chemistry and Department of English, & FED, KL (Deemed-to-be) University, Hyderabad, India.
- **9.** Participated in one weak Faculty development program on research opportunities in Electrical Power Engineering organized by Prasad V. Potluri Siddhartha Institute of Technology, Vijayawada, from 23/03/22 to 27/03/2022.
- **10.** Participated in the AICTE Recognized Faculty Development Programme on Effective Curriculum Implementation Using FOSS from 08/01/2024 to 12/01/2024 (One Week) at Dr. D.Y. Patil Technical Campus, Talsande, Kolhapur organized by NITTR Chandigarh.

# **CONTENTS**

| Candidate' Declaration  | II    |
|---|-------|
| Certificate of Guide  | III   |
| Acknowledgment  | IV    |
| List of patents, Articles in International Journals and   | VI    |
| National/international conferences attended   |       |
| Contents  | X     |
| List of Figures   | XI    |
| List of tables and charts   | XV    |
| List of abbreviations   | XVII  |
| Chapter I: Introduction.  | 1-32  |
| Chapter II: Theoretical background of SILAR method and characterization techniques.               | 35-70 |
| <b>Chapter III:</b> Synthesis and Characterization of nickel tungstate electrode by SILAR method. | 73-94 |
| <b>Chapter IV:</b> Synthesis and Characterization of nickel tungstate @                           | 97-   |
| reduced graphene oxide composite electrode by SILAR method.                                       | 120   |
| Chapter V: Fabrication of asymmetric supercapacitor device and                                    | 123-  |
| performance evaluation.   | 152   |
| Chapter VI: Summary and Conclusions.  | 155-  |
|   | 160   |

# **List of Figures**

|             | Chapter 1   | Page no. |
|-------------|---|----------|
| Figure 1.1  | Performance comparison of capacitor, supercapacitor, and    |          |
|             | battery using Ragone plot.                                  |          |
| Figure 1.2  | Schematic of an electrochemical capacitor.                  | 6        |
| Figure 1.3  | The schematic of FSS-SCs.                                   | 17       |
|             | Chapter 2   | <u> </u> |
| Figure 2.1  | Schematic of four beaker SILAR method.                      | 37       |
| Figure 2.2  | Bragg's diffraction.  | 43       |
| Figure 2.3  | Schematic of X-ray tube.                                    | 44       |
| Figure 2.4  | Figure 2.4: a) Schematic of X-ray instrument, and b)        | 45       |
|             | photograph of RIGAKU MiniFlex600 diffractometer.            |          |
| Figure 2.5  | Basic schematic of FT-IR with Michelson interferometer.     | 46       |
| Figure 2.6  | a) Photograph of ALPHA II compact FT-IR spectrometer,       | 47       |
|             | and b) the basic ray diagram of FT-IR system.               |          |
| Figure 2.7  | Energy level diagram showing the states involved in Raman   | 48       |
|             | spectra.  |          |
| Figure 2.8  | The basic block diagram of Raman spectrometer.              | 49       |
| Figure 2.9  | a) Schematic of FE-SEM, and b) photograph of FE-SEM         | 51       |
|             | instrument.   |          |
| Figure 2.10 | Atomic model of the working principle of XPS.               | 52       |
| Figure 2.11 | Schematic diagram of an XPS instrument                      | 53       |
| Figure 2.12 | a) Image of the Rame-Hart NRL contact angle meter [35],     |          |
|             | and b) measurement of contact angle between a liquid and    | 54       |
|             | a solid sample.   |          |
| Figure 2.13 | Schematic diagram of the dynamic flow method apparatus.     | 56       |
| Figure 2.14 | Schematics of charge-storage mechanisms for a) an EDLC      |          |
|             | [46] and (b-d) different types of pseudocapacitive          | 59       |
|             | electrodes: b) surface redox pseudocapacitors, c)           |          |
|             | intercalation pseudocapacitor, and d) battery-type Faradaic |          |
|             | reaction.   |          |

| Figure 2.15 | The typical cyclic voltammogram for a reversible single                | 61 |
|-------------|--|----|
|             | electron transfer reaction.  |    |
| Figure 2.16 | Charge discharge curves of a SC.                                       | 62 |
| Figure 2.17 | Representative shapes of GCD curves: a) EDLC, b) surface               | 62 |
|             | redox capacitance, c) intercalation capacitance, and d)                |    |
|             | Faradic battery type.  |    |
| Figure 2.18 | Nyquist plot with electrical equivalent circuit consisting             | 63 |
|             | charge Rct in parallel with C  |    |
| Figure 2.19 | Nyquist plots with corresponding electrical equivalent                 | 65 |
|             | circuit a) consisting Rs, Rct and, C, and b) consisting Rs,            |    |
|             | Rct, C, and W.   |    |
|             | Chapter 3  |    |
| Figure 3.1  | a) The crystal structure of NiWO <sub>4</sub> expanded along principal | 75 |
|             | axis a and b plotted using Vesta software, b) unit cell of             |    |
|             | NiWO4 crystal, and c) the schematic of SILAR method                    |    |
|             | employed for NiWO <sub>4</sub> thin film electrode preparation.        |    |
| Figure 3.2  | a) Variation in mass loading with the concentration of                 | 79 |
|             | cationic precursor, b) The XRD patterns, c) the FTIR                   |    |
|             | spectra, and d) Raman spectra of NiWO <sub>4</sub> thin films.         |    |
| Figure. 3.3 | The FE-SEM images of a and b) N1, c and d) N2, e and f)                | 81 |
|             | N3, g and h) N4 at magnifications of 2000X and 50000X                  |    |
|             | respectively.  |    |
| Figure 3.4  | a-c) The TEM images of N3 thin film, d, and e) the HR-                 | 82 |
|             | TEM of N3 at 5, 10, 50, 100, and 200 nm magnifications,                |    |
|             | and f) the SEAD pattern of N3.   |    |
| Figure.3.5  | The XPS spectra of a) NiWO <sub>4</sub> electrode, b) Ni 2p, c) W4f,   | 83 |
|             | and d) O1s.  |    |
| Figure. 3.6 | The BET isotherms of a) N1, b) N2, c) N3, and d) N4, and               | 84 |
|             | e) pore size distribution of N1-N4.                                    |    |
| Figure 3.7  | The contact angle images of a) N1, b) N2, c) N3, and d)                | 85 |
|             | N4.  |    |

| Figure 3.8  | a) Comparative CV curves of N1 to N4, and the CV curves                           | 86  |
|-------------|---|-----|
|             | of b) N1, c) N2, d) N3, and e) N4 for scan rates of 2 to 20                       |     |
|             | $mV s^{-1}$ .   |     |
| Figure. 3.9 | a) The graphs of log $I$ vs. log $v$ , b) graphs of $I/v^{1/2}$ vs. $v^{1/2}$ ,   | 88  |
|             | percentage current contribution of capacitive and diffusion                       |     |
|             | mechanisms for c) N1, d) N2, e) N3, and f) N4.                                    |     |
| Figure 3.10 | a) Comparative GCD plots of N1-N4 at current density of                           | 90  |
|             | 2 A g <sup>-1</sup> NiWO <sub>4</sub> , the GCD plots of b) N1, c) N2, d) N3, and |     |
|             | e) N4 at different current densities, and f) the graph of                         |     |
|             | specific capacitance vs. current density of N1, N2, N3, and                       |     |
|             | N4.   |     |
| Figure 3.11 | a) The Nyquist plots (inset shows electrical equivalent                           | 91  |
|             | circuit) and b) stability curves of NiWO4 electrodes (inset                       |     |
|             | shows a photograph of contact angle after stability)                              |     |
|             | Chapter 4   |     |
| Figure 4.1  | Schematic flow chart of rGO synthesis.  | 100 |
| Figure 4.2  | The photograph of programmable SILAR coating system                               | 100 |
|             | used for preparation of rGO-NiWO <sub>4</sub> thin films.                         |     |
| Figure 4.3  | a) The schematic of the SILAR method employed for                                 | 101 |
|             | rGO/NiWO <sub>4</sub> thin film electrode preparation, b) schematic               |     |
|             | of formation of layered rGO/NiWO4 composite material,                             |     |
|             | and c) photograph of CNW series films deposited at                                |     |
|             | different rGO concentrations.   |     |
| Figure 4.4  | a) Mass loading variation with rGO concentration, b) XRD                          | 104 |
|             | patterns, c) FTIR spectra, and d) Raman spectra of CNW                            |     |
|             | series thin films.  |     |
| Figure 4.5  | The FE-SEM images of a, b) CNW1, c, d) CNW2, e, f)                                | 105 |
|             | CNW3, g, h) CNW4 at magnifications of 10 kX and 100                               |     |
|             | kX.   |     |
| Figure 4.6  | a-c) The TEM images, and d) SEAD pattern of CNW3, The                             | 106 |
|             | EDS elemental mapping of e) CNW2, f) Ni, g) W, h) O, and                          |     |
|             |   |     |

| Figure 4.7  | a) Survey spectrum of rGO-NiWO <sub>4</sub> electrode and wide scan    | 107 |
|-------------|--|-----|
|             | XPS spectra of b) Ni2p, c) W4f, d) C1s, and e) O1s.                    |     |
| Figure 4.8  | The XPS spectra of a) survey spectra of rGO-NiWO <sub>4</sub>          | 108 |
|             | electrodes, and wide scan XPS spectra of b) Ni2p, c) W4f,              |     |
|             | d) C1s, and e) O1s from CNW series.                                    |     |
| Figure 4.9  | The BET isotherms of a) CNW1, b) CNW2, c) CNW3, and                    | 109 |
|             | d) CNW4.   |     |
| Figure 4.10 | Pore size distributions of a) CNW1, b) CNW2, c) CNW3,                  | 110 |
|             | and d) CNW4.   |     |
| Figure 4.11 | a) Comparative CV curves of rGO-NiWO <sub>4</sub> thin films           | 112 |
|             | deposited at different concentrations of rGO at scan rate of           |     |
|             | 100 mV s <sup>-1</sup> , CV scan rates of b) CNW1, c) CNW2, d)         |     |
|             | CNW3, e) CNW4 at scan rates of 2 to 100 mV s <sup>-1</sup> , and f)    |     |
|             | graph of $\log i$ vs $\log v$ .  |     |
|             |  |     |
| Figure 4.12 | GCD plots of a) CNW1, b) CNW2, c) CNW3, d) CNW4 at                     | 113 |
|             | different current densities, e) variation of $C_s$ with scan rate,     |     |
|             | and f) variation of $C_s$ with current densities.                      |     |
| Figure 4.13 | a) The Nyquist plots (inset shows electrical equivalent                | 115 |
|             | circuit) and b) stability curves of rGO/NiWO <sub>4</sub> electrodes,  |     |
|             | and c) comparison of $C_s$ of tungstate materials reported             |     |
|             | earlier with present study.  |     |
| Figure 4.14 | Comparison of electrochemical stability of tungstate                   | 117 |
|             | materials reported earlier with the present study.                     |     |
|             | Chapter 5  |     |
| Figure 5.1  | XRD pattern of Fe <sub>2</sub> O <sub>3</sub> electrode                | 125 |
| Figure 5.2  | SEM images of Fe <sub>2</sub> O <sub>3</sub> material at 10KX and 20KX | 126 |
|             | resolution.  |     |
| Figure 5.3  | a) The CV curves, b) the GCD curves, c) the Nyquist plot,              | 127 |
|             | and d) stability plot for Fe <sub>2</sub> O <sub>3</sub> thin films.   |     |
| Figure 5.4  | a) The CV curves, b) the GCD curves, c) the Nyquist plot,              | 129 |
|             | and d) stability plot for AC thin films.                               |     |

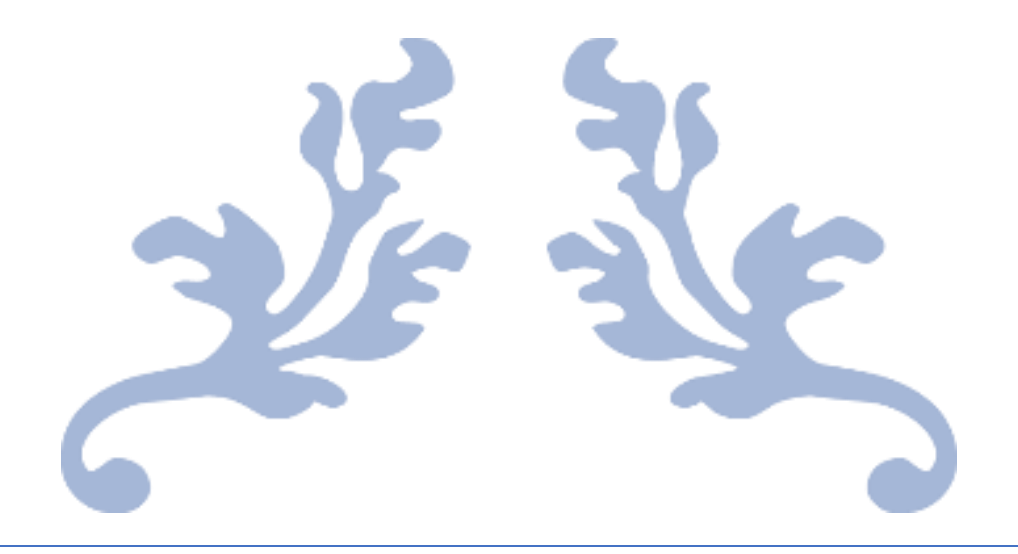
|            |   | 137 |  |  |
|------------|---|-----|--|--|
| Figure 5.5 | a) Combined CV curves of Fe <sub>2</sub> O <sub>3</sub> and N3 electrodes, b) the         |     |  |  |
|            | CV curves, c) the GCD plots, and d) the Ragone plot of                                    |     |  |  |
|            | NiWO <sub>4</sub> /KOH/Fe <sub>2</sub> O <sub>3</sub> ASC device.                         |     |  |  |
| Figure 5.6 | a) The Nyquist plot (inset shows equivalent electrical                                    | 138 |  |  |
|            | circuit) and b) stability plot of NiWO <sub>4</sub> /KOH/Fe <sub>2</sub> O <sub>3</sub> . |     |  |  |
|            |   |     |  |  |
| Figure 5.7 | Variation of specific capacitance of rGO-NiWO <sub>4</sub> //AC ASC                       | 139 |  |  |
|            | with a) scan rate and b) current density.   |     |  |  |
| Figure 5.8 | a) Schematic of ASC device fabrication, b) Picture of ASC                                 | 140 |  |  |
|            | device, c) CV curves, d) GCD plots, e) stability plot, and                                |     |  |  |
|            | f) CV curves at different bending position performed at                                   |     |  |  |
|            | scan rate of 100 mV s <sup>-1</sup> of rGO-NiWO <sub>4</sub> /PVA-KOH/AC.                 |     |  |  |
| Figure 5.9 | a) the Nyquist plot (inset shows equivalent electrical                                    | 144 |  |  |
|            | circuit), and b) Ragone plot of rGO-NiWO <sub>4</sub> /PVA-                               |     |  |  |
|            | KOH/AC device.  |     |  |  |
|            |   |     |  |  |

# **List of Tables and Charts**

| Sr. no.   | Particulars'   | Page no. |  |  |
|-----------|--|----------|--|--|
| Chart 1.1 | Classification of supercapacitors.   | 6        |  |  |
| Chart 1.2 | Classification of supercapacitor electrodes based on charge storage mechanism.   |          |  |  |
| Table 1.1 | The literature survey of electrode materials based on nickel tungstate for energy storage.   | 20       |  |  |
| Chart 2.1 | Categorization of Thin Film Deposition methods.  | 36       |  |  |
| Table 3.1 | Comparison of Cs of N3 with Ni-based electrodes reported for supercapacitor application  | 89       |  |  |
| Table 3.2 | Values of the electrochemical parameters   | 91       |  |  |
| Table 4.1 | Electrochemical impedance spectroscopic data of CNW electrodes.  | 115      |  |  |
| Table 5.1 | Comparison of Cs, SE, and SP of ASC with reported Nibased reported ASC.  | 136      |  |  |
| Image 5.1 | Bending of device images with a) 0, b) 30, c) 60, d) 90, e)120, and f) 150.  | 143      |  |  |
| Table 5.2 | Comparative electrochemical parameters of previously reported supercapacitor devices with proposed rGO-NiWO <sub>4</sub> //AC ASC. | 144      |  |  |
| Image 5.2 | Image 5.2: Charging and discharging demonstration of flexible ASC device   | 146      |  |  |

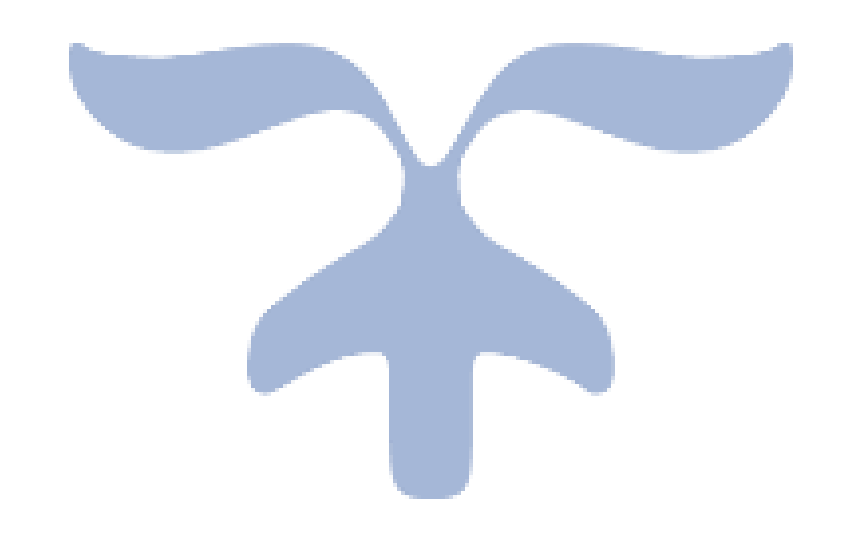
# **List of Abbreviations**

| AC               | Activated carbon                           | PEC         | Photoelectrochemical          |
|------------------|--|-------------|-------------------------------|
| P                | Adsorptive pressure                        | PV          | Photovoltaic                  |
| AR               | Analytical reagent                         | PEO         | poly (ethylene oxide)         |
| $C_a$            | Areal capacitance                          | <b>PMMA</b> | Poly (methyl methacrylate)    |
| ASC              | Asymmetric supercapacitor                  | PVA         | Poly (vinyl alcohol)          |
| BJH              | Barrett-Joyner-Halenda                     | PVF         | Poly (vinylidene fluoride)    |
| BET              | Brunauer-Emmett-Teller                     | PVdF-co-    | Poly (vinylidene fluoride-    |
|                  |  | HFP         | cohexaflluoropropylene)       |
| CF               | Carbon foam                                | PAA         | Polyacrylate                  |
| <b>CNTs</b>      | Carbon nanotubes                           | PAN         | Polyacrylonitrile             |
| $f_{\theta}$     | Characteristics frequency                  | PANI        | Polyaniline                   |
| $R_{ct}$         | Charge transfer resistance                 | PPy         | Polypyrrole                   |
| CCD              | Charge coupled device                      | PTh         | Polythiophene                 |
| CBD              | Chemical bath deposition                   | KOH         | Potassium hydroxide           |
| CVD              | Chemical vapour deposition                 | ΔE          | Potential window              |
| CV               | Cyclic voltammetry                         | PC          | Propylene carbonate           |
| $t_d$            | Discharging time                           | rGO         | Reduced graphene oxide        |
| <b>DDW</b>       | Double distilled water                     | $t_0$       | Relaxation time constant      |
| <b>EDLC</b>      | Electric double-layer capacitors           | SCE         | Saturated calomel electrode   |
| EIS              | Electrochemical impedance                  | $P_s$       | Saturated vapor pressure      |
|                  | spectroscopy                               |             |                               |
| ED               | Electrodeposition                          | Rs          | Series resistance             |
| $\boldsymbol{E}$ | Energy                                     | <b>SP</b>   | Power density                 |
| EDAX             | Energy dispersive X-ray spectroscopy       | $C_s$       | Specific capacitance          |
| <b>EMC</b>       | Ethyl methyl carbonate                     | <b>SE</b>   | Energy density                |
| EC               | Ethylene carbonate                         | SB          | Specific surface area         |
| FE-              | Field emission scanning                    | SS          | Stainless steel               |
| SEM              | electron microscopy                        |             |                               |
| FSS-SCs          | Flexible solid state                       | Q           | Stored charges                |
| FT-IR            | supercapacitors Fourier transform infrared | SILAR       | Successive ionic layer        |
| 1 1-110          | spectroscopy                               | SILITIK     | adsorption and reaction       |
| <b>FWHM</b>      | Full width at half maximum                 | SCs         | Supercapacitors               |
| GCD              | Galvanostatic charge-discharge             | SSC         | Symmetric supercapacitor      |
| GNS              | Graphene nanosheets                        | ST ST       | Total surface area            |
| GO               | Graphene oxide                             | TMCs        | Transition metal chalcogenide |
| HSC              | Hybrid capacitor                           | W           | Warburg impedance             |
| IR               | Internal resistance                        | XRD         | X-ray diffraction             |
| LEDs             | Light emitting diodes                      | XPS         | X-ray photoelectron           |
| LIBs             | Lithium-ion batteries                      |             | spectroscopy                  |
| Hg/HgO           | Mercury/mercury oxide                      |             |                               |
| 115/1150         | William y microury Oxide                   |             |                               |



# **CHAPTER-1**

# INTRODUCTION AND LITERATURE SURVEY



# **CHAPTER-1**

# INTRODUCTION AND LITERATURE SURVEY

| Sr. No. |   | Page No.                                      |    |  |
|---------|---|---|----|--|
| 1.1     | Energy st   | Energy storage systems                        |    |  |
| 1.2     | Supercapa   | acitor  | 3  |  |
|         | 1.2.1   | Supercapacitor background                     | 3  |  |
|         | 1.2.2   | Merits of supercapacitor                      | 4  |  |
|         | 1.2.3   | Working principle of supercapacitor           | 5  |  |
|         | 1.2.4   | Types of supercapacitors                      | 6  |  |
|         | 1.2.4.1   | Symmetric supercapacitors (SSCs)              | 7  |  |
|         | 1.2.4.2   | Asymmetric supercapacitors (ASCs)             | 7  |  |
|         | 1.2.4.3   | Hybrid supercapacitors (HSCs)                 | 8  |  |
|         | 1.2.5   | Types of electrode materials                  | 9  |  |
|         | 1.2.5.1   | Electrochemical double layer capacitor (EDLC) | 9  |  |
|         | 1.2.5.2 Pseudocapacitive material                           |   | 10 |  |
|         | 1.2.5.2A Transition metal chalcogenides (TMCs)              |   | 10 |  |
|         | 1.2.5.2B Conducting polymers                                |   | 11 |  |
|         | 1.2.5.2C  | Other pseudocapacitive material               | 12 |  |
|         | 1.2.6   | Electrolytes                                  | 12 |  |
|         | 1.2.6.1   | Liquid electrolytes                           | 13 |  |
|         | 1.2.6.2   | electrolytes (SSE)                            | 13 |  |
| 1.3     | Flexible s  | Flexible solid state supercapacitors          |    |  |
| 1.4     | Literature survey on the synthesis of nickel tungstate thin |   | 18 |  |
|         | films   |   |    |  |
| 1.5     | Purpose o   | of the research                               | 22 |  |
|         | References  |   |    |  |

#### 1.1 Energy storage systems

Since there is a greater need for energy today, researchers are being pushed to develop cheaper, more reliable energy storage systems. The price of electrical energy storage devices like batteries and supercapacitors (SCs) is affected by the energy crisis and the rising cost of energy storage material [1-3]. In order to satisfy the increasing need for high power, high energy, and affordable energy storage systems, electrical energy storing materials have undergone major research. Due to energy issues and the limited supply of fossil fuels, energy storage is currently the most important need in the globe. Researchers are compelled to develop readily available, inexpensive, maintenance-free, and environmentally friendly energy storing technologies because of environmental degradation, the high cost of fossil fuels, and a lack of supply [4, 5]. Tidal, solar, and wind energies are not always present. It varies from place to place, so to address these issues, scientists have created effective energy storage systems that can be used to store this kind of energy in affordable storage systems [6].

Electrical energy storage systems including fuel cells, batteries, capacitors, and SCs store electrical energy as charges. There is simply electrochemical correspondence in the energy storage mechanism of these devices. When a fuel cell is charging, the liquid electrolyte is crucial for storing electric charge during a chemical process. One of the main drawbacks of fuel cells is the requirement for a constant fuel source. Hydrogen sources are costly and unsafe to supply. In conclusion, fuel cell utilization to fulfil electrical energy storage device needs utilization of fuel cells to fulfil the needs of electrical energy storage devices is restricted. The chemical electrolyte in batteries can be a liquid, but regular dry batteries are more likely to contain a dry powder. Redox reactions, which include charging and discharging, change electrical energy into chemical energy during charging and back again during discharging. There are typically two different kinds of batteries: disposable (primary cells) and rechargeable (secondary cells). The primary cell's dry component slowly releases electrical energy up to and only briefly discharges it totally. Secondary cells performed chemical reactions reversibly with charging and discharging processes, in contrast to primary cells. Automobiles, cell phones, laptops, and other devices all use batteries. Batteries having low power density and shorter cycle life. Ordinary capacitors are prepared using dielectric materials and several types of electrodes. It functions as a battery for storing electrical energy (temporary battery). These capacitors have a charge storage capacity between 10<sup>-6</sup> and 10<sup>-3</sup> F [7]. The electrode of the capacitor is made of conducting materials like metal foil and thin films on a steel substrate. Mica, glass sheets, air, and other dielectric, non-conducting materials are employed as separators. One of the main elements affecting the capacitor's ability to store charge is the distance between two conducting plates. For a variety of electrical devices, it functions as an alternating current (AC) filter by passing direct current (DC) while obstructing AC current according to the capacitor principle [8, 9]. Assuming a capacitor is linked to a DC power source, the capacitance is calculated as by taking into account the potential difference that develops between two plates (V), the charge that builds up at the conducting plates (Q), and the capacitance (C) [10].

$$C = \frac{Q}{V} \tag{1.1}$$

The maximum power (Wmax) of capacitor can be calculated as independent function of the capacity of the capacitor.

$$W_{MAX} = \frac{E}{T} = \frac{V^2}{4R} \tag{1.2}$$

Where 'E' stands for energy, 'T' for time, 'V' for potential difference (voltage), and "R" for the resistance created by the conducting plates and electrolyte material. SCs can store more electrical charge than regular normal capacitors. Researchers are drawn to learn more about SCs because of its great power density (SP) and acceptable energy density (SE). SCs have qualities that make them useful for portable electronic devices, backup power for memory devices, solar devices, hybrid automobiles, and other applications [11–13]. These properties include the capacity to hold more charge, greater SP, flexibility of devices, and smaller size. In contrast, the supercapacitor is a stage in between a battery and a capacitor. The SE of battery is extremely high compared to the capacitor and other devices. A capacitor has a much higher SP than a battery or a supercapacitor, however, the SE of a supercapacitor is more than that of a capacitor [14].

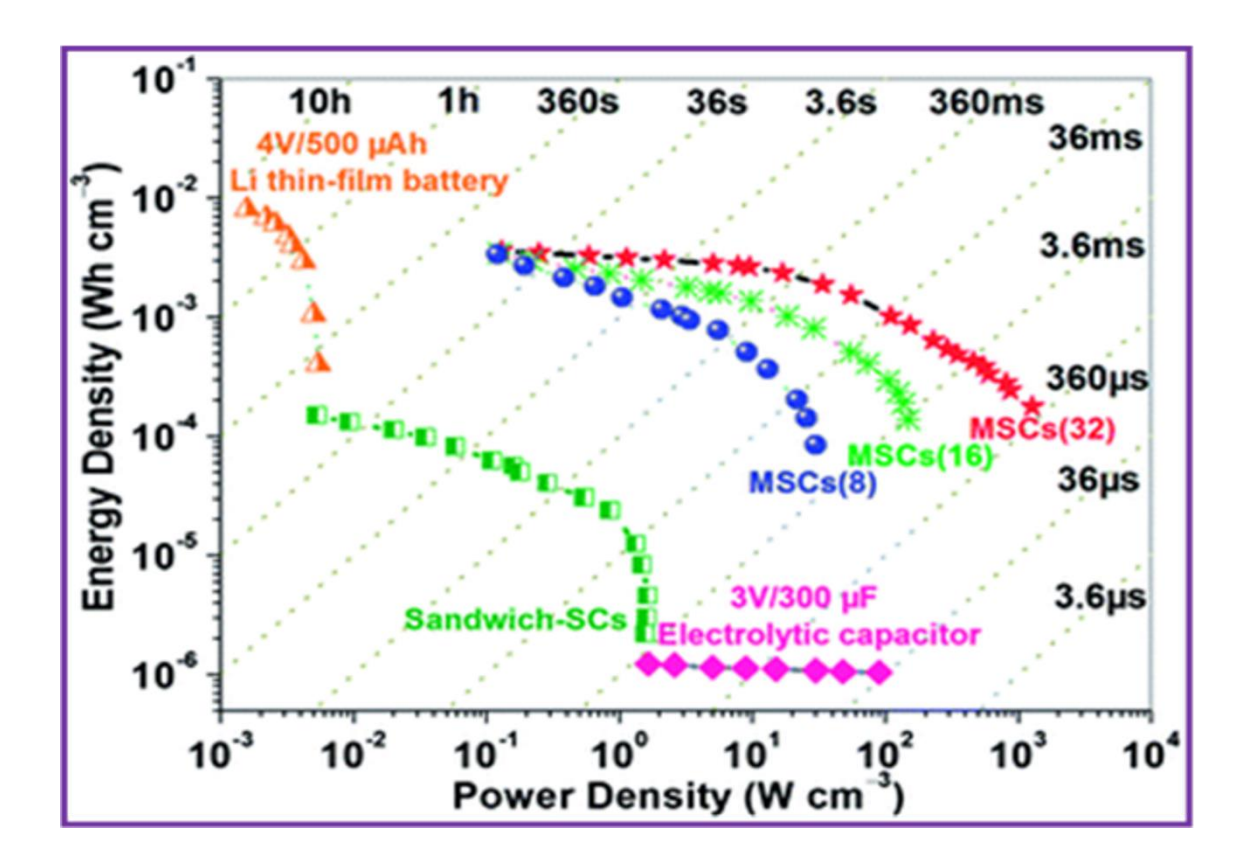


Figure 1.1: Performance comparison of capacitor, supercapacitor, and battery using Ragone plot [15].

The graphical plots of the SE vs SP limits for the capacitor, supercapacitor, and battery are combined in Figure 1.1 (Ragone plot). In comparison to batteries and regular conventional capacitors, SCs provide better specific capacitance (Cs) and electrochemical cycling stability (1,000–10,000 cycles) [16]. These characteristics of the supercapacitor prove its use in upcoming portable electronic gadgets that need for higher SP. SCs give great power during acceleration in hybrid electric vehicles. Fuel cells or batteries are calibrated for high SE and cycle life without a high SP need [17]. Moreover, SCs are necessary for higher SP desired devices such backup power sources for computer memory, lasers, pulse light generators, and camera flash equipment.

#### 1.2 Supercapacitor

#### 1.2.1 Supercapacitor background

H. I. Becker constructed the first electrical double-layered charge storage system in 1957 by using carbon electrodes in a liquid electrolyte [18]. The Standard Oil Company of Ohio (SORIO) corporation developed a high surface area carbon electrode

for non-aqueous electrolytes in 1966 [19]. The unconventional charge storage and pseudocapacitive behavior of some materials were introduced by Convey in 1975. This study completes the novel approach to creating high-capacity SCs. Ruthenium oxide is the primary pseudocapacitive substance examined by Convey (RuO<sub>2</sub>). The licensing of SORIO, the Nippon Electric Corporation (NEC) created the first commercial supercapacitor in 1978. The supercapacitor was commercialized by Panasonic under the name "Goldcap", after that, scientists started working toward using SCs in place of batteries. Supercapacitor devices are currently produced by businesses including Maxwell, ESMA, CAP-XX, NCC, and NessCap for usage in various electronic devices.

#### 1.2.2 Merits of Supercapacitor

Maintaining the ratio of SE and SP in energy storage devices is the key challenge. The SE in a battery is considerable, but the SP is incredibly low. The electric energy is not instantly delivered. The SP and SE of a typical capacitor are higher. Higher SE and SP are required for portable electronic gadgets to reach their desired capacities. SCs have the advantage of being able to deliver a significant amount of energy at high power. The extended electrochemical cycling life, quick chargedischarge rate, simple manufacture, and cheap maintenance of SCs are further benefits [20]. Due to these characteristics, SCs are useful in flexible electronic commercial storage devices. Furthermore, the cost of fabricating a supercapacitor device is a major factor in keeping the device's price stable. As a supercapacitor, it demonstrates these benefits but has a limitation with lower SE [21]. As a result, the primary obligation is to improve supercapacitor SE while maintaining SP. SCs are classified into two types: (a) electrochemical double layer capacitor (EDLC) and (b) pseudocapacitor, with a hybrid capacitor combining the two. In general, carbon-base materials have a high SP that is EDLC type, whereas metal oxides, metal sulfides, and conducting polymers have a high SE that is pseudocapacitive [22-24]. Carbon-base materials with high conductivity have been used as electrode materials for SCs in recent years [25]. The process of preparing carbon materials is expensive, and the Cs of these materials are very low (up to 150 F g<sup>-1</sup>). The requirement for higher Cs in storage devices raises the cost of electrode material preparation. The electrode material, current collector, and electrolyte are critical components in the fabrication of the supercapacitor device. In the future, SCs will be required to combine the best of both batteries and capacitors to store large amounts of electricity. Furthermore, SCs have higher electrochemical cycling stability than batteries, so they benefit device assembly life span [26]. The electrochemical stability and Cs of the supercapacitor device are reduced by the use of an aqueous electrolyte. To address this issue, solid gel electrolyte is the best option for improving supercapacitor performance [27]. As a result, hiring a low-cost pseudocapacitive electrode material with an appropriate solid polymer gel electrolyte is an easy way to achieve the highest SE and SP. The main benefits of SCs are their flexibility, high SP, electrochemical stability, and low fabrication cost [28].

#### 1.2.3 Working Principle of Supercapacitor

In supercapacitors (SCs), electric charges are stored at the interface between the electrodes and the electrolyte, even though electrolyte ions with different charges are organized on the electrolyte side (Figure. 1.2). The basic electric charge storage mechanism in a regular capacitor and a supercapacitor is the same, but the materials used for the dielectric and electrolyte differ. The specific surface area of the electrode plates and the distance between them play a crucial role in determining the capacitance (C<sub>s</sub>) of supercapacitor devices.

The capacitance (C) of an electrochemical capacitor can be calculated using the following equation:

$$C = \frac{\varepsilon A}{d} \tag{1.3}$$

Here, C represents the capacitance of the electrochemical capacitor, d is the distance between the electrolyte ions and the electrode, and A is the specific surface area of the active electrodes.

To determine the specific energy  $(S_E)$  and specific power  $(S_P)$  of an electrochemical capacitor, the following equations can be utilized:

$$S_E = \frac{0.5 \times C_S \times \Delta V^2}{3.6}$$
 (1.4), and

$$S_p = \frac{3600 \times S_E}{dt} \tag{1.5}$$

In equation (1.4),  $C_s$  represents the specific capacitance,  $\Delta V$  is the potential window of the supercapacitor, and dt is the discharging time. Equation (1.5) is used to calculate the specific power ( $S_P$ ) by multiplying the specific energy ( $S_E$ ) by 3600 and dividing it by the discharging time (dt).

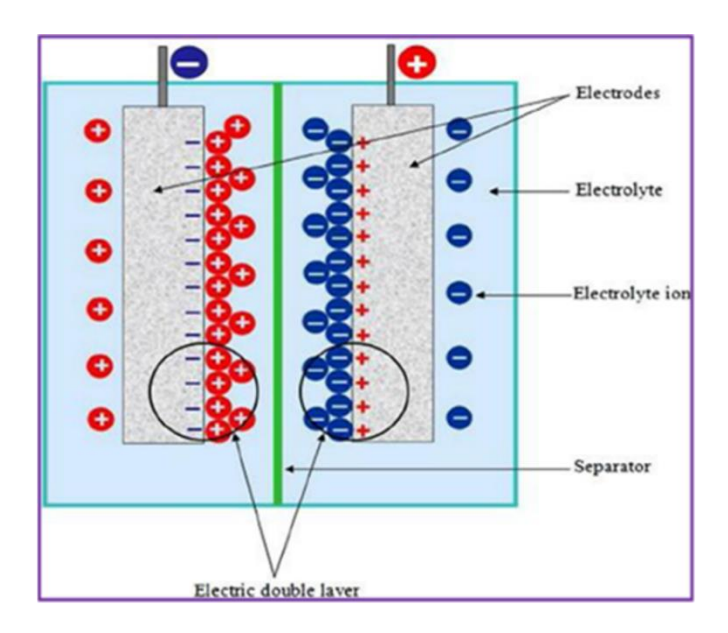
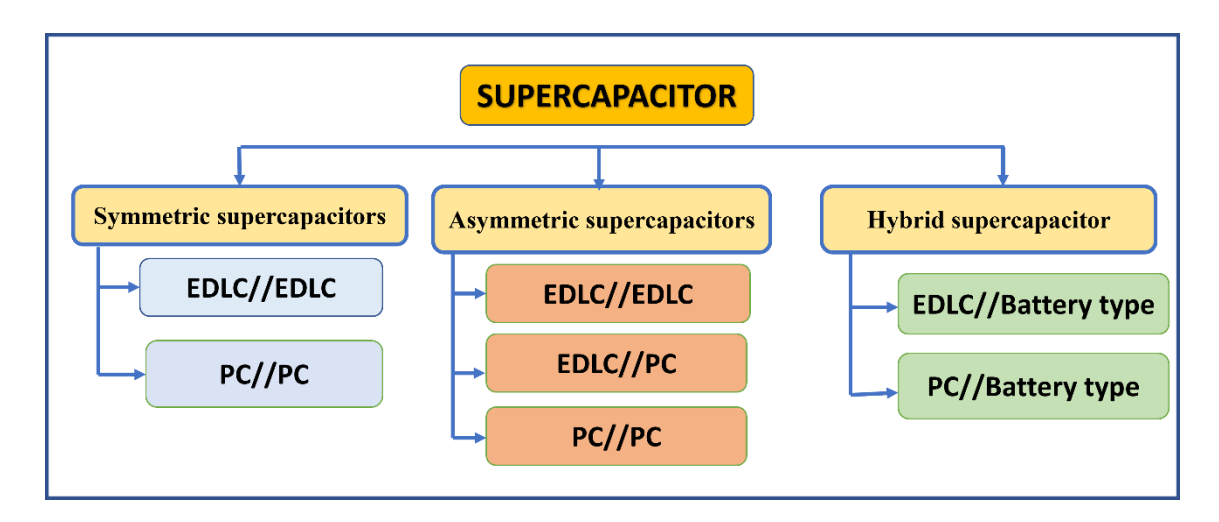


Figure 1.2: Schematic of an electrochemical capacitor [29].

#### 1.2.4 Types of Supercapacitors



**Chart 1.1: Classification of supercapacitors.** 

SCs are classified according to their electric charge storage mechanism as symmetric supercapacitor (SSC), asymmetric supercapacitor (ASC), and hybrid capacitor (HSC) [30]. The same fundamental equations govern SCs as they do

conventional capacitors, but they have a larger specific surface area and use a porous surface electrode and polymer gel electrolyte to achieve higher Cs. Chart 1.1 summarizes the graphical presentation of the various classes of SCs.

#### 1.2.4.1 Symmetric Supercapacitors (SSCs)

The combination of two similar types of electrodes to form SC can be termed as SSC. The  $S_P$  of SSCs could be lower than the ASCs due to the lower potential window. Carbon nanotubes (CNTs)//CNTs and MnO<sub>2</sub>//MnO<sub>2</sub> are representative examples of SSC devices [31]. As both electrodes are from similar materials, the charge balance can be achieved easily in this case.

#### 1.2.4.2 Asymmetric supercapacitors (ASCs)

ASC refers to the SC device configuration that employs two dissimilar electrodes. This type of configuration is expected to be a promising way to assemble a cell with the same S<sub>P</sub> as SCs. Combining electrodes with different charge storage mechanisms, one can improve the electrochemical properties of the new cell. Electrodes based on pseudocapacitive and EDLC charge storage mechanisms were typically assembled. At high current rates, ASCs can operate at high voltage and provide longer electrochemical stability and high energy density. In layman's terms, ASC is used when both EDLC or one EDLC and one pseudocapacitive or both pseudocapacitive electrodes are present in cell assembly. AC/CNTs, AC/MnO<sub>2</sub> [32], and MnO<sub>2</sub>/Fe<sub>2</sub>O<sub>3</sub> [33] are a few examples of ASC devices. The working voltages of the individual electrodes determine the final voltage of ASCs [34]. To achieve the highest working potential and SE, the stored charges (Q) on both constituent electrodes must be balanced, i.e., Q- = Q+ [35]. Typically, the charges stored are associated with the electrode material's electroactive mass (m), potential window (E), and Cs. The best mass ratio of the electrodes was calculated using the following relationship:

$$\frac{m_+}{m_-} = \frac{C_- \times \Delta E_-}{C_+ \times \Delta E_+} \tag{1.6}$$

where the signs + and - indicate the entity for positive and negative electrodes, respectively. The  $C_s$  of the electrode material can be calculated theoretically using following relation [36],

$$C = \frac{nF}{m\Delta E} \tag{1.7}$$

where F, n, and m are the Faraday's constant (96485 C mol<sup>-1</sup>), number of transferred electrons and molecular weight (MW) of active material, respectively.

The selection of electrode materials is critical in determining the final working voltage of an ASC device. The electrolyte use also has an impact on the voltage window of ASC devices. Thermodynamically, the oxidation and reduction reactions in materials are linked to the material's work function. As a result, the electrodes with the greatest work function can provide a higher working voltage. As a result, the following relationship is used to calculate the potential working voltage window of ASCs:

$$E = E_0 + \Delta E_1 + \Delta E_2 = \frac{1}{F(\omega^{\beta} - \omega^{\alpha}) N_A} + \Delta E_1 + \Delta E_2$$
 (1.8)

where  $\omega^{\beta}$  and  $\omega^{\alpha}$  are the work functions for the positive and negative electrodes, respectively and  $N_A$  is the Avogadro's constant (6.02 × 10<sup>23</sup> mol<sup>-1</sup>). For SSCs,

$$\omega^{\beta} = \omega^{\alpha}$$
 and  $\Delta E_1 = -\Delta E_2$ ;

hence, the potential window is limited to their three electrode measurement.

#### 1.2.4.3 Hybrid supercapacitor (HSCs)

Capacitors are high-power devices that store a small amount of electricity, whereas batteries are a type of device with a high SE but a low SP. These two materials can be combined in a single device to boost both SE and SP. HSCs are energy storage devices that combine one capacitive (carbon) and one battery type (NiO) electrode in a single device (HSCs). These SCs deviate from the charge storage mechanism of EDLCs and pseudocapacitors. A high working voltage can be achieved in HSCs to reach the redox potential of pseudocapacitive material, which ultimately improves the SE and SP of the SCs [37]. Despite their high capacity and wide operating voltage, HSCs have a lower rate capacity and cycle life due to one of the battery type electrodes.

These issues are addressee by the development of electrodes made of layered and porous nanostructured materials that allow for easy charge intercalation and deintercalation. There are numerous methods that have been use to prepare porous nanostructured electroactive electrodes. This reduces charge transport length and

increases expose electroactive surface areas, making storage sites more accessible. To overcome the issue of sluggish kinetics in the charge storage process, a systematic composition of pseudocapacitive material with highly conductive carbon allotropes such as graphene, CNTs, activated carbons (AC), and others was proposed [38]. The electrochemical characteristics of the HSCs deviate from the capacitive behaviour due to hybridization.

#### 1.2.5 Types of electrode materials

For effective charge storage, the electrode material should either undergo redox reactions or enable non-faradaic charge transfer. It should possess several key characteristics, including good electrical conductivity, a surface structure with suitable pore size, and a high specific surface area. These features are crucial for achieving exceptional charge storage capacity. Additionally, the electrode material should meet specific requirements such as low synthesis cost, environmental friendliness or reduced hazardousness, good electrical conductivity, thermal and chemical stability within the electrolyte, and a high specific surface area with appropriate pore size. These qualities ensure the availability of numerous electroactive sites for electrochemical redox reactions.

Although it is true that carbon-based materials are thermally and chemically stable and have high conductivity, they are not the first choice for EDLC type SC. Because of their ability to undergo reversible redox reactions and store higher charges than EDLC materials, pseudocapacitive materials such as metal chalcogenides, hydroxides, nitrides, silicates, carbides, and conducting polymers are used as pseudocapacitors [39, 40].

#### 1.2.5.1 Electrochemical double layer capacitor (EDLC)

Carbon-based electrode materials are used in EDLCs. EDLC having greater power capability than batteries, their charge storing and release mechanism is highly reversible, making them extremely promising candidates with long charge/discharge life. Carbon allotropes such as AC, carbon aerogels, graphene, reduced graphene oxide (rGO), graphite paper, and carbon nanotubes (CNTs) have been extensively researched to achieve high electrode performance due to properties such as superior conductivity,

excellent thermal and electrochemical stability in all types of electrolytes. Because of their lower cost and larger specific surface area (up to 3000 m<sup>2</sup> g<sup>-1</sup>), EDLC materials are a first choice for SC applications [41].

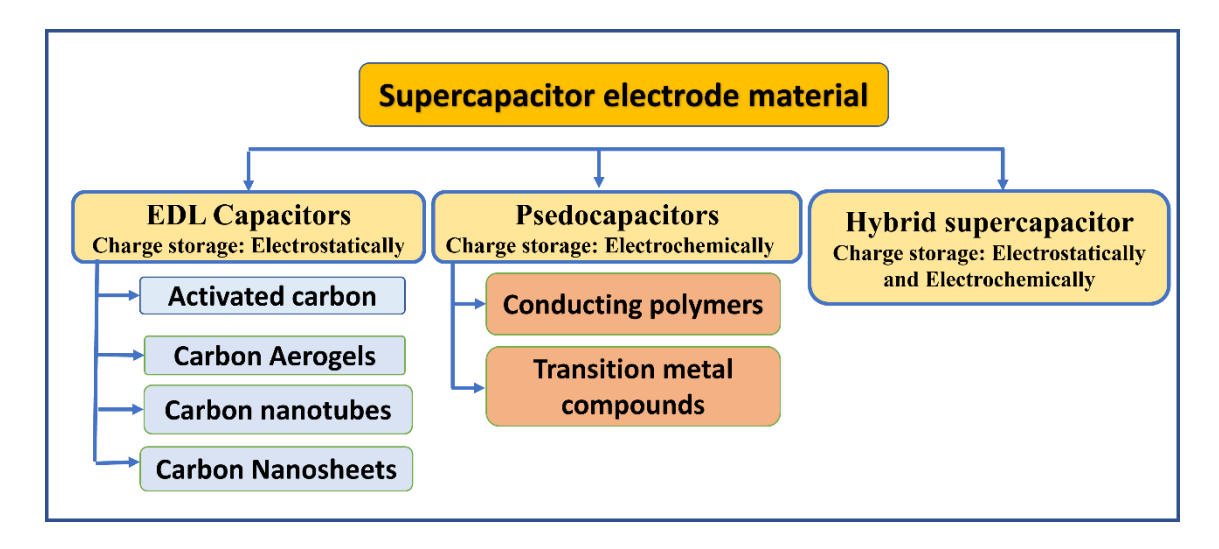


Chart 1.2: Classification of supercapacitor electrodes based on charge storage mechanism.

#### 1.2.5.2 Pseudocapacitive materials

Extensive research is being conducted on transition metal compounds such as chalcogenides, silicates, carbides, nitrides, and polymers such as polyaniline (PANI), polypyrrole (PPy), and polythiophene (PTh), among others. Transition metal chalcogenides (TMCs) have received much attention due to their superior electrical conductivity and thermal stability when compared to other transition metal compounds and polymers, allowing for high capacitance and SE in portable energy storage devices [42, 43].

#### 1.2.5.2A Transition metal chalcogenides (TMCs)

Nanostructured TMCs are currently use as the electroactive material for SC. Different oxidation states of metal constituents affect the electric conductivity of electrode material, which is advantageous for high electrochemical performance [44]. To improve the pseudocapacitive performance, Peng et al. [45] prepared a SC electrode compose of CuS microspheres with a PPy sheet-like structure. Wang et al. [46] use a one-step hydrothermal assisted method to grow a three layer nanostructure of

CuS/rGO/Ni<sub>3</sub>S<sub>2</sub> composite on nickel foam (NF). Zhu et al. [47] use a template engaged chemical conversion route to create arrays of CuS ultrafine nanoneedles supported on a CNT backbone. Bulakhe et al. [48] use successive ionic layer adsorption and reaction (SILAR) to prepare copper sulfide with various morphologies for high performance SCs. Shi et al. [49] reported a double-sided mesh electrode coated with Cu<sub>2</sub>S film and carbon nanoparticles. Hsu et al. [50] demonstrated a CuS nanowire array with a hierarchical nanoarchitecture directly on copper foil using a simple and cost-effective liquid-solid reaction for SC application. Huang et al. [51] synthesized CuS with various morphologies using a simple one-step solvothermal method with or without surfactants. Zhang et al. [52] described the solvothermal method used to create 3D hierarchical covellite CuS microspheres from an ionic liquid precursor. Qian et al. [53] use pseudocapacitance of CuS nanotubes in the electrolyte to achieve a high Cs of 2393 F g<sup>-1</sup> at 10 mV s<sup>-1</sup> for CuS nanotubes in redox active polysulfide electrolyte. Chen et al. [54] reported a one-step hydrothermal synthesis of CuS/MWCNT with a Cs of 2831 F g<sup>-1</sup> obtained from the nanotubes structured surface.

#### 1.2.5.2B Conducting polymers

The polymers employed as the electrode material for SCs include PANI, PPy, and PTh. The improved electric conductivity of polymers improves SC performance. The potential window of these conducting polymers is often stationary. The performance of polymer base electrodes was dramatically diminished during cycling due to polymer breakdown in the electrolyte. For PPy electrodes, Peng et al. [55] obtained a Cs of 480 F g<sup>-1</sup>. Dubal et al. [56] use the electrodeposition approach to create PPy thin films with Cs of 586 F g<sup>-1</sup>. Zhou et al. [57] created a combination of CNTs and conducting polymers for use in pseudocapacitors. Ambade et al. [58] reported the electrochemical production of a PTh electrode with a Cs of 425.4 Fg<sup>-1</sup>.

Recently, polymers were composited with EDLC materials in various compositions and preparation processes to enhance specific surface area, thermal stability, and electrical conductivity.

#### 1.2.5.2C Other pseudocapacitive materials

TMCs have substantially greater capacitance and energy density than carbonbase materials. Unfortunately, the deformation in the microstructure of TMCs cause by the repetitive charge discharge process results in reduced cycle life. Cycling stability is critical for pseudocapacitive materials for practical use and increase energy density. Hence, the synthesis of materials with a high degree of porosity and excellent electrochemical performance is critical for obtaining increase SE and SP. The capacitance of pseudocapacitive materials is widely known to be dependent on a variety of characteristics, including crystallinity, porosity, specific surface area, and electrode mass loading. As a result, the need for sophisticated functional materials is increasing. Several transition metal compounds were produced and investigated for supercapacitive characteristics in order to develop novel materials. Chodankar et al. [59] synthesized MoN nanoparticles as a pseudocapacitive material on a phosphorus-infuse carbon fabric, achieving a Cs of 400 mF cm<sup>-2</sup>. Wang et al. [60] use a hydrothermal technique to manufacture MnSi, CoSi, and NiSi and reported Cs of 517.0, 452.8, and 66.7 F g<sup>-1</sup> at 0.5 A g-1, respectively. Rakhi et al. [61] created nanocrystalline MnO2 whiskers on MXene nanosheet surfaces (MnO<sub>2</sub>/Ti<sub>2</sub>CTx and MnO<sub>2</sub>/Ti<sub>3</sub>C<sub>2</sub>Tx) to create nanocomposite electrodes for aqueous pseudocapacitors, achieving Cs of 212.1 F g<sup>-1</sup> at 1 A g<sup>-1</sup> current density. Marje and co. [62] use chemical bath deposition (CBD) to synthesize nickel phosphate thin films with a Cs of 1031 F g<sup>-1</sup> at a current density of 0.5 mA cm<sup>2</sup>. Lokhande et al. [63] described the hydrothermal production of a cobalt tungstate nanocomposite (CNT-CoWO<sub>4</sub>) as a SC electrode material with a Cs of 1486 F g<sup>-1</sup> at 5 mV s<sup>-1</sup>.

#### 1.2.6 Electrolytes

An electrolyte is an inorganic salt which is dissolved in a perfect ionizing solvent, and the resulting solution is electrically conductive. The conductivity of the electrolyte is determined by the quantity of salt dissolved in the solvent per unit volume. The electrolyte is critical to the electrochemical performance of SC. The kind of electrolyte and solvent use determines the operating potential window of the SC, which has a direct influence on SE and SP. There are two types of electrolytes base on their physical condition: liquid and solid state electrolytes (SSEs). Each of these has

advantages and disadvantages. There are two types of electrolytes base on the nature of the solvent: protic and aprotic electrolytes. Protic electrolytes are electrolytes in which a polar solvent, such as water, is employed to dissolve salt. Nonpolar solvents are employed in aprotic electrolytes to dissolve salts such as ethylene carbonate and propylene carbonate [64, 65].

#### 1.2.6.1 Liquid electrolyte

There are two types of liquid electrolytes base on the solvent use for preparation: aqueous electrolytes and organic electrolytes. Water-base electrolytes are commonly used to produce SCs because of their inexpensive cost, easiness of production, less hazardous nature, and high ionic conductivity (10-3 S cm-1) [66]. Nevertheless, water dissociation at 1.23 V restricts the working potential window and overall performance of SCs. The working potential window of an organic electrolyte may be expanded up to 3.0 V, however, safety considerations like as flammability and the poisonous nature of solvents and solutes are key concerns. The lower Cs in the organic electrolyte is due to the larger size of organic molecules (15-20) and poorer ionic conductivity. Lower Cs values result in lower energy and power density as compared to water-base SCs, although this is offset by the wide working potential window.

Both water-base and organic electrolytes have constraints and disadvantages, such as the high cost of packing material and the need for improved procedures to eliminate electrolyte leakage, as most electrolytes are very poisonous and corrosive. It is difficult to fabricate tiny and flexible SCs using liquid electrolytes. Another restriction of the liquid electrolyte is the reduction in energy efficiency cause by electrolyte evaporation. As a result, it is required to develop innovative electrolyte compositions that are more suitable for flexible and micro SC devices than liquid electrolytes. Too far, however, no optimal electrolyte suited for all types of electrodes has been identified for creating high performance next generation SCs.

#### 1.2.6.2 Solid state electrolyte (SSE)

The use of flammable liquid electrolytes raises concerns about safety and power density. This also limits manufacturing growth. These difficulties will be addressee via the use of SSEs. SSEs substantially improved thermal stability makes them ideal for

next-generation energy storage systems. The inorganic SSE can operate in a broad temperature range (223 K to 473 K or greater). Because of their rigid crystal structure, inorganic SSEs have a high ion conductivity of more than 10<sup>-4</sup> S cm<sup>-1</sup> and a good thermal stability. Nevertheless, the performance of these electrolytes is poor due to inadequate interfacial contact between the electrolyte and the electrode. Another issue is capacity loss cause by mechanical and electrochemical factors. As a result, the development of inorganic SSE suitable with a wide range of electrode materials is urgent [67, 68].

With the growing need for wearable, lightweight, and flexible energy storage systems, polymer gel electrolytes have received substantial scientific attention. Polymer electrolytes use in solid state SCs not only prevent safety risks like as leakage and volatility, but also significantly lower encapsulation costs and enable additional design choices for innovative device configurerations. They are often classified as gel polymer electrolytes (compose of the polymer matrix, plasticizer, and supporting salt) and solid polymer electrolytes (without any solvent). Considering the ultralow room temperature ionic conductivity of solid polymer electrolytes, future use in SCs is limited. Gel polymer electrolytes are preferred and have been thoroughly developed and researched for solid state SC applications.

The study of gel polymer electrolytes includes investigations into the physical and chemical properties of solids with rapid ion mobility inside the bulk, as well as their technical implications. These gel polymer electrolytes are also known as superionic solids or rapid ion conductors. Gel polymer electrolytes have enormous potential for use in the development of solid state mini/micro electrochemical devices such as batteries, fuel cells, SCs, electrochromic displays, sensors, photoelectrochemical (PEC) solar cells, and so on. In SSE, mobile ions are the primary charge carriers. The SSEs have a strong ionic conductivity ranging from  $10^{-2}$  to  $10^{-4}$  S cm<sup>-1</sup>. They have excellent thermal and electrochemical stability.

In this electrolyte, the ion transformation is primarily regulated by thermally produced point defects such as Schottky and Frenkel defects. They have a very low room temperature ionic conductivity on the range of  $10^{-16}$  to  $10^{-12}$  S cm<sup>-1</sup> and are typically regarded as an insulator. Numerous attempts were undertaken, although with little success, to improve the extent of ionic conductivity by aliovalent doping.

Nevertheless, a key advance in materials science occurred in 1973, when the polymer-base solid electrolyte was presented [69]. Polymer electrolytes are polymeric membranes with ion transport properties equivalent to a liquid electrolyte. Polymer electrolytes are distinguished from conventional solid electrolytes by their great mechanical flexibility, ionic conductivity (10<sup>-3</sup> S cm<sup>-1</sup>) at room temperature, and simplicity of manufacture [70]. Polymer electrolytes should have the following characteristics for reliable solid-state electrochemical applications:

- ➤ *High ionic conductivity:* To obtain electrochemical performance equivalent to liquid electrolytes, polymer electrolyte ionic conductivity should be 10<sup>-3</sup> S cm<sup>-1</sup> at ambient temperature.
- Excellent chemical, thermal, and electrochemical stability: The SC is made by sandwiching the polymer electrolyte between two electrodes. Polymer electrolytes must be chemically stable in order to avoid undesirable chemical reactions at the electrode/electrolyte contact. Moreover, in order for SC to have a greater working temperature range, the electrolyte must be thermally stable. In order to have a high working potential window, they need also have strong electrochemical stability.
- ➤ *Mechanical strength:* In order to scale up manufacturing, the polymer electrolyte must have strong mechanical strength.
- > Compatibility: In order to obtain maximum performance without depletion, the polymer electrolyte should be compatible with various electrode materials.
- ➤ *Increase safety:* To increase safety, the polymer electrolyte should be liquid-free and placed in a plastic container rather than a metal container to minimize internal pressure development. This will significantly lower the likelihood of an explosion.
- ➤ Act as a separator: In SC, a polymer electrolyte serves as both a separator and a conducting medium between two electrodes. It eliminates the need for a divider. Several techniques for the manufacture of polymer electrolytes are use base on physiochemical characteristics. Plasticized polymer electrolytes, rubbery electrolytes, and solvent-swollen polymer electrolytes are a few examples [71].

Polymer gel electrolytes have been widely employed to build SCs throughout the last decade because they have both solid-like cohesive qualities and liquid-like diffusive transport capabilities [72, 73]. Polymer gel electrolytes are typically made by entrapping a liquid electrolyte within a polymeric network. Ionic conduction occurs as a result of the movement of liquid electrolytes, whereas polymer offers mechanical integrity. Polymer gel electrolytes are projected to be less reactive than liquid electrolytes due to their gel-like structure and substantially lower liquid concentration [74].

Polymer gel electrolytes have better ionic conductivity (when compared to SSEs), a large potential window (3.0 V), mechanical flexibility, and interfacial stability. Previously, polyacrylate (PAA) [75], poly (ethylene oxide) (PEO) [76], poly (vinyl alcohol) (PVA), polyacrylonitrile (PAN) [77], poly (vinylidene fluoride) (PVDF), poly (vinylidene fluoride-cohexaflluoropropylene) (PVDF-co-HFP) [78] and poly (methyl methacrylate) (PMMA) [79] were use as host polymers for preparing polymer gel electrolytes. Organic solvents such as EC, PC, and ethyl methyl carbonate (EMC) are commonly utilized, however they are typically poisonous, volatile, and costly. As a result, replacing organic solvents with aqueous solvents is an excellent choice. Aqueous gel electrolytes can also significantly cut device costs.

#### 1.3 Flexible solid state supercapacitors (FSS-SCs)

The recent focus on the production of tiny size portable electronic gadgets necessitates the use of a small size flexible electric charge storage mechanism. Li-ion batteries and flexible solid state supercapacitors (FSS-SCs) are now often use in the production of microelectronics. FSS-SCs' features such as extended cycle life, high SP, safety, adaptability, and stability are advantageous for energy storage applications. Figure 1.3 depicts the FSS-SCs design. One electrode is the current collector, which is coated with a thin coating of electroactive material. The two electrodes in a symmetric device are of the same kind. Two electrodes of various sorts are use in the ASCs device. The solid polymer gel electrolyte serves as both an electrolyte and a separator, and the entire assembly is house in a suitable packaging material [80].

Previous publications, present research on common conventional capacitors with aqueous, organic, or ionic liquids as electrolytes. Problems like as leakage and electrochemical cycle stability develop as a result of liquid electrolytes. The problem of leakage necessitates the use of adequate packing. It raises the price of SC devices,

limiting their application in portable electronics. Additionally, due to liquid electrolytes, the size of SCs is reduced to a certain extent, limiting their application in smaller electronic components. Organic electrolytes in liquid form are poisonous and hazardous to humans. Also, at greater temperatures, aqueous electrolytes evaporate. Together with these devices, a new class of energy storage devices known as FSS-SCs gained popularity because to their increase storage and cycling stability. It also provides benefits such as compact size, low weight, convenience, outstanding dependability, a large working potential window, and the ability to tolerate extreme temperatures. Flexible electrodes and solid polymer gel electrolytes that can retain their characteristics even when bent or twisted are required for the production of FSS-SCs devices.

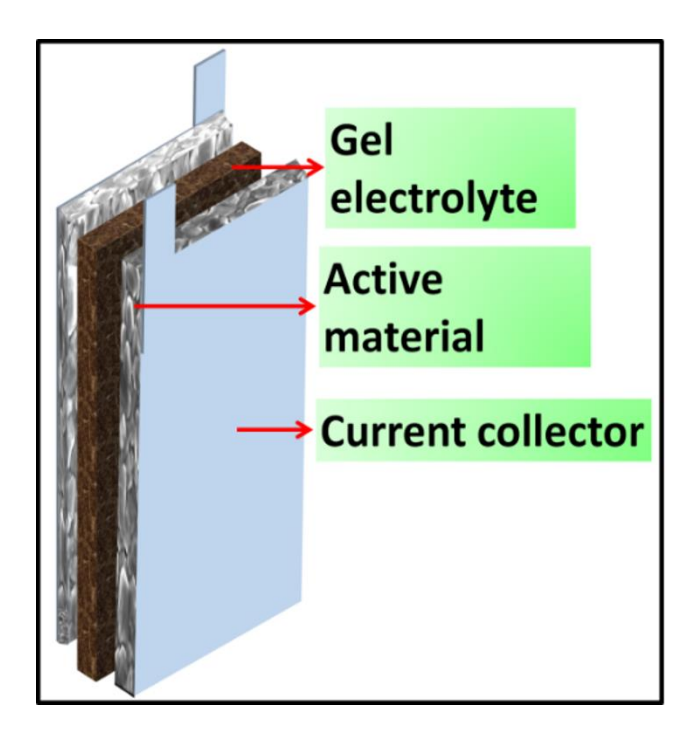


Figure 1.3: The schematic of FSS-SCs.

The FSS-SCs use the identical positive and negative electrodes sandwiched between two layers of polymer gel electrolyte [81, 82]. The total capacitance of a SC device is determined by applying the formula below.

$$1/C = 1/C_p + 1/C_n (1.9)$$

where C is the overall capacitance of the device,  $C_p$  and  $C_n$  are the capacitances of anode and cathode, respectively.

#### 1.4 Literature survey on synthesis of nickel tungstate thin films

The exceptional physical and electrical properties of transition metal tungstates have made them highly attractive for applications in electronic, optical, and optoelectronic devices [83]. In recent years, nanostructured transition metal tungstates have emerged as a new class of energy storage materials. One common characteristic of tungstate's is that their metal constituents can exist in multiple valence states [84]. During the modelling of the anodic oxidation reaction of covellite, it was determined that the equivalent electrical circuit should include a relatively high capacitor.

Metal tungstates have shown significant promise as electrode materials for supercapacitors (SCs) due to their advantageous properties such as high capacitance (Cs), improved cycling stability, and high energy density when compared to conducting polymers. These materials exhibit size and shape-dependent properties, making them well-suited for practical applications. Most metal tungstates belong to the AWO<sub>4</sub> type, where A represents the metal ion, and the majority of these compounds are semiconductors. The specific structure of metal tungstates is determined by the type of metal present. Tungstates containing larger A<sup>2+</sup> cations such as Ba, Ca, Eu, Pb, and Sr exhibit a tetragonal scheelite structure, while those containing smaller A<sup>2+</sup> cations like Ni, Co, Cd, Fe, Mg, and Zn display a monoclinic wolframite structure. The AWO<sub>4</sub>-type metal tungstates have found utility as laser host materials, scintillators, oxide ion conductors, magnetic materials, optoelectronic devices, and even antibacterial agents.

Transition metal oxide and hydroxide electrodes with pseudo-capacitive behaviour are also of great interest in supercapacitors. Transition metal oxides, which exhibit different oxidation states, have been extensively studied as pseudo-capacitive materials. Notable examples include oxides of ruthenium (Ru), nickel (Ni), cobalt (Co), manganese (Mn), and iron (Fe) [85, 86]. Alloys and binary metal oxides offer distinct advantages over single metal oxides owing to their favorable oxidation states and improved current response. Recently, binary metal oxides such as NiCo<sub>2</sub>O<sub>4</sub> [87], FeWO<sub>4</sub> [88], NiMoO<sub>4</sub> [89], ZnWO<sub>4</sub> [90], TbWO<sub>4</sub> [91], and NiWO<sub>4</sub> [92] have been synthesized and have shown excellent pseudo-capacitive performance. However, binary metal oxides do not always exhibit the highest performance in all cases or under all environments. The pseudocapacitive performance of an electrode material depends on various factors, such as electrolyte concentration, type of electrolyte (neutral, alkaline,

or acidic), mass loading, electrical conductivity, crystalline nature, and more. Interestingly, some single-component metal oxides have demonstrated promising electrochemical performance. For instance, cobalt oxide exhibited a capacitance (Cs) of 127.58 F g<sup>-1</sup> in a 1 M KOH electrolyte [93]. Additionally, the pseudo-capacitive nature of tungsten trioxide (WO<sub>3</sub>) has also been reported. Shinde et al. [94] achieved a Cs of 538 F g<sup>-1</sup> for hydrothermally prepared WO<sub>3</sub>. These findings indicate that single metal oxides can also exhibit good electrochemical performance for energy storage. In the case of metal tungstates, their crystalline structure and the presence of binary metals contribute to improved Cs and stability [95]. Previous reports have also suggested that tungstates exhibit better pseudo-capacitive performance than their corresponding oxides [96].

NiWO<sub>4</sub> is a remarkable metal tungstate compound with p-type semiconductor characteristics, demonstrating exceptional catalytic and electrochemical properties [97]. Ikram et al. [98] prepared nickel tungstate using hydrothermal method and achieved specific capacitance 1524 F g<sup>-1</sup> at a current density of 0.5 A g<sup>-1</sup>. Pourmortazavi et al. [99] reported electrochemical method for NiWO<sub>4</sub> preparation and achieved Cs of 468 F g<sup>-1</sup> at the scan rate of 2 mV s<sup>-1</sup>. Electrochemical properties of NiWO<sub>4</sub> synthesized by hydrothermal method were reported by Packiaraj et al. [100]. The solvothermal synthesis of NiWO<sub>4</sub> nanowires for supercapacitor with Cs of 1190 F g<sup>-1</sup> at the current density of 0.5 A g<sup>-1</sup> was reported by Tian et al. [101]. Niu et al. [102] prepared amorphous NiWO<sub>4</sub> using co-precipitation method and achieved Cs of 586.2 F g<sup>-1</sup> at 0.5 A g<sup>-1</sup>. Xu et al. [103] reported preparation of NiWO<sub>4</sub>/reduced graphene oxide (rGO) nanocomposite with specific capacitance (Cs) of 1031.3 F g<sup>-1</sup> for supercapacitor.

Table 1.1 provides a literature survey of electrode materials based on nickel tungstate for energy storage. Various techniques, such as sol-gel, chemical bath deposition (CBD), chemical vapor deposition (CVD), and hydrothermal methods, can be employed to produce nanostructures of NiWO<sub>4</sub> [104-123].

| Table 1.1: The literature survey of electrode materials based on nickel tungstate based supercapacitor. |   |                        |                               |                       |             |   |                         |                        |             |
|---|---|------------------------|-------------------------------|-----------------------|-------------|---|-------------------------|------------------------|-------------|
| Sr.<br>No.  | Material  | Synthesis method       | Substrate                     | Surface<br>morphology | Electrolyte | Specific<br>capacitance<br>(F g <sup>-1</sup> ) | Potential<br>window (V) | Stability (%) (cycles) | Ref.<br>No. |
| 1   | NiWO <sub>4</sub>                                   | Solvothermal           | -                             | Nanowires             | 6М КОН      | 1190  | 0 to 0.5                | -                      | [104]       |
| 2   | NiWO <sub>4</sub>                                   | Co-precipitation       | Nickel foam                   | Nanostructure         | 2M KOH      | 586.2   | 0 to 0.6                | 91.4<br>(5000)         | [105]       |
| 3   | NiWO <sub>4</sub>                                   | Chemical precipitation | -                             | Nanoparticles         | 1М КОН      | 437   | 0 to 0.6                | 54<br>(500)            | [106]       |
| 4   | MnMoO <sub>4</sub> /NiWO <sub>4</sub>               | Hydrothermal           | Nickel foam                   | Microspheres          | 2М КОН      | 598   | 0 to 0.4                | -                      | [107]       |
| 5   | NiWO <sub>3</sub> / NiWO <sub>4</sub>               | Microwave irradiation  | Ni mesh                       | Nanopowder            | 2М КОН      | 171   | 0 to 0.6                | -                      | [108]       |
| 6   | NiWO <sub>4</sub>                                   | Hydrothermal           | Glassy<br>carbon<br>electrode | Chain-like            | 2 M KOH     | 1524  | -1.0 to1.0              | -                      | [109]       |
| 7   | NiWO <sub>4</sub> -CoWO <sub>4</sub>                | Coprecipitation        | GCE                           | Nanoparticles         | 2 M KOH     | 196.7   | 0 to 0.6                | -                      | [110]       |
| 8   | Co <sub>1-x</sub> Ni <sub>x</sub> WO <sub>4</sub>   | Hydrothermal           | Carbon cloth                  | Nanostructure         | 1 M KOH     | 430.3   | -0.1 to +0.3            | 85.4<br>(5000)         | [111]       |
| 9   | Ni <sub>0.5</sub> Co <sub>0.5</sub> WO <sub>4</sub> | Hydrothermal           | Nickel foam                   | Mesoporous            | 3М КОН      | 634.55 Cg <sup>-1</sup>                         | 0 to 0.7                | 92<br>(10000)          | [112]       |

| 10 | NiWO <sub>3</sub> & NiWO <sub>4</sub>               | Microwave irradiation         | -            | Nanoporous              | 2 M KOH | 1.71 @ 0.25           | 0 to 0.4    | -               | [113] |
|----|---|-------------------------------|--------------|-------------------------|---------|-----------------------|-------------|-----------------|-------|
| 11 | CoWO <sub>4</sub> (CWO)–<br>Ni                      | Chemical                      | Nickel foam  | Crystalline             | 6 М КОН | 271 @ 1 A             | -0.1 to 0.5 | 86.4<br>(1500)  | [114] |
| 12 | CoWO <sub>4</sub> /NiCo <sub>2</sub> O <sub>4</sub> | Hydrothermal                  | Nickel foam  | Nanorods                | 6 М КОН | 1076                  | -0.2 to 0.4 | 80<br>(2000)    | [115] |
| 13 | Co1-xNixWO <sub>4</sub>                             | Hydrothermal                  | Carbon cloth | Nanoparticles           | 1 M KOH | 430.30                | -0.1 to 0.3 | 85.4<br>(5000)  | [116] |
| 14 | NiWO <sub>4</sub> /CoWO <sub>4</sub>                | wet chemical                  | Al           | Plate like              | 1 M KOH | 862.26                | 1 to 2.5    | 96.12<br>(2000) | [117] |
| 15 | NiWO <sub>4</sub> and CoWO <sub>4</sub>             | Hydrothermal                  | Nickel foam  | Hill-like<br>hemisphere | 2 М КОН | 797.8 &<br>764.4      | 0 to 0.6    | (3000)          | [118] |
| 16 | NGW (CC)  | Solvothermal                  | -            | Sheet                   | 0.1 PBS | 47.27 @ 1             | 0.1 to 0.7  | -               | [119] |
| 17 | NiWO <sub>4</sub> /Ni/carbon<br>fibre electrode     | Electrospin with spray        | -            | Carbon nanofibers       | 6 М КОН | 151.1 to<br>792.2 @ 5 | 0 to 0.45   | 1500            | [120] |
| 18 | NiWO <sub>4</sub> /Ni<br>CoWO <sub>4</sub> /Ni      | Hydrothermal                  | Nickel Foam  | Semisphere              | -       | 797 @ 1               | 0 to 0.6    | 3000            | [121] |
| 19 | NiWO <sub>4</sub> -CoWO <sub>4</sub>                | Chemical co-<br>precipitation | Nickel foam  | Mesoporous              | 2 М КОН | 196.7 @ 0.5           | 0 to 0.8    | -               | [122] |
| 20 | NiWO <sub>4</sub> /rGO                              | Hydrothermal                  | SS           | Nanoparticle            | 1M KOH  | 440 @ 1               | 0.to 0.7    | -               | [123] |

#### 1.5 Purpose of the research

The purpose of the research based on review and above literature survey could be to investigate the influence of synthesis methods, substrates, and electrolytes on the electrochemical performance of nickel tungstate material and their composites for energy storage applications. This research aims to optimize the fabrication process and enhance the electrochemical performance, stability, and potential window of these materials for applications such as supercapacitors and energy storage devices. Additionally, the research may explore the feasibility of scaling up production for practical applications.

In recent decades, significant efforts have been made to improve the electrochemical performance and design of supercapacitors (SCs) to effectively power portable and flexible electronic devices. One major challenge in achieving higher power densities is the equivalent series resistance (ESR) of SCs, which originates from the electrodes and electrolyte. Various methods have been adopted to reduce ESR, including using rough collector surfaces and directly growing electroactive materials on the current collector. The overall performance of an efficient SC relies on high surface area, fast and reversible redox reactions of active materials, and the need for electrode materials with higher conductivity, greater redox potential of cations, and large porous surface areas. The success of SCs depends on the electrode material and electrolyte being used, with electrode stability and cycling life being influenced by the electrolyte. Therefore, there is considerable potential for developing active materials for SCs and improving the electrolyte.

This work focuses on fabricating flexible and stretchable SC devices using composite nanostructured thin films of NiWO<sub>4</sub> and NiWO<sub>4</sub>@rGO as active electrode materials, along with aqueous and polymer gel electrolyte. The aim of this fabrication is to evaluate the performance of these active electrode materials at the device level and to assess the limitations of using liquid electrolytes. Overall, this research aims to enhance the electrochemical performance of SCs by developing advanced electrode materials and exploring alternative electrolytes, ultimately driving the widespread application of SCs based on their cost-effectiveness and excellent performance.

The SILAR method will be used to prepare nanostructured NiWO<sub>4</sub>@rGO thin films, which exhibit desirable electrochemical properties for supercapacitor (SC) electrodes. This method offers advantages in controlling various preparative parameters such as reactant concentration, deposition cycles, complexing agents, temperature, and time. It enables the production of large-area thin films with different nanostructures on diverse supporting substrates at low reaction temperatures. Additionally, it facilitates the preparation of binderless and additive-free thin films, enhancing the interfacial contact between the active electrode material and supporting substrate. The effects of different preparative parameters will be systematically investigated to obtain well-adherent and uniform thin films.

Characterization plays a crucial role in studying novel materials. Comprehensive characterization involves phase analysis, structural elucidation, compositional analysis, surface analysis, and microstructural analysis, which help define various material properties. Phase identification of the material will be performed using X-ray diffraction (XRD). The surface morphology of the films will be visualized using field emission scanning electron microscopy (FE-SEM). Raman and Fourier transform infrared (FT-IR) spectroscopy will be employed to investigate chemical bonding and confirm phase formation. X-ray photoelectron spectroscopy (XPS) will be used to analyze the oxidation states of constituent elements. Furthermore, Brunauer-Emmett-Teller (BET) measurements will be conducted to examine the specific surface area and pore size distribution of the electrode material.

The electrochemical characteristics of NiWO<sub>4</sub> and NiWO<sub>4</sub>@rGO electrodes will be studied using cyclic voltammetry (CV), galvanostatic charge-discharge (GCD) measurements, and electrochemical impedance spectroscopy (EIS) on an electrochemical workstation. The experimental setup will include NiWO<sub>4</sub> or NiWO<sub>4</sub>@rGO as the working electrode, a reference electrode (Hg/HgO), and a platinum sheet as the counter electrode. The performance of NiWO<sub>4</sub> and NiWO<sub>4</sub>@rGO thin films will be evaluated based on parameters such as specific capacitance (Cs), electrochemical stability, and equivalent series resistance (Rs). Subsequently, asymmetric supercapacitor (ASC) devices will be fabricated, and their electrochemical performance will be assessed in terms of Cs, energy density (SE), power density (SP), electrochemical stability, and Rs. Additionally, the influence of bending on the

electrochemical performance of the solid-state devices will be investigated to assess their suitability for various portable electronic devices. Finally, conclusions will be drawn based on the electrochemical performance of the asymmetric ASC devices in terms of Cs, operating potential window, SE, SP, and electrochemical stability.

#### **References:**

- [1] S. Chen, J. Zhu, X. Wu, Q. Han, X. Wang, ACS Nano, 4, 2010, 2822.
- [2] C. X. Guo and C. M. Li, Energy Environ. Sci., 4, 2011, 4504.
- [3] Y. Tao, X. Xie, W. Lv, D. M. Tang, Z. Huang, H. Nishihara, T. Ishii, B. Li, D. Golberg, F. Kang, T. Kyotani, D. Kong, Q. H. Yang, Sci. Rep., 3, 2013, 2975.
- [4] C. Choi, S. H. Kim, H. J. Sim, J. A. Lee, A. Y. Choi, Y. T. Kim, X. Lepro, G.M. Spinks, R. H. Baughman, S. J. Kim, Sci. Rep., 5, 2015, 1.
- [5] L. Feng, Y. Zhu, H. Ding, C. Ni, J Power Sources, 267, 2014, 430.
- [6] G. S Gund, D. P Dubal, S. S Shinde, C. D Lokhande, ACS Appl Mater Inter., 6, 2014, 3176.
- [7] K. B. Oldham, J. C. Myland, Fundamentals of Electrochemical Science, Academic Press Inc, New York, 1994.
- [8] A. Nishino, J Power Sources, 60, 1996, 137.
- [9] http://electronics.wikia.com/wiki/Capacitor.
- [10] M. S. Halper and J. C. Ellenbogen, MITRE., 2006, 1.
- [11] K. Kotz and M. Carlen, Electrochim. Acta, 45, 2000, 2483.
- [12] E. Frackowiak and E. Beguin, Carbon, 39, 2001, 937.
- [13] Z. Fan, J. Yan, T. Wei, L. Zhi, G. Ning, T. Li, F. Wei, Adv. Funct. Mater. 21, 2011, 2366.
- [14] P. Simon and Y. Gogotsi, Nat. Mater., 7, 2008, 845.
- [15] Z. S. Wu, K. Parvez, X. Feng, K. Mullen, J. Mater. Chem. A, 2, 2014, 8288.
- [16] D. P. Dubal, J. G. Kim, Y. Kim, R. Holze, C. D. Lokhande, W. B. Kim, Energy Technol., 2, 2014, 325.
- [17] http://www.mouser.in/applications/new-supercapacitor applications/
- [18] H. I. Becker, Low voltage electrolytic capacitors. U.S Patent 2800616, 1957.
- [19] R. A. Rightmire, Electrical energy storage apparatus. U.S Patent 3288641, 1966.

- [20] A. M. Patil, V. S. Kumbhar, N. R. Chodankar, A. C. Lokhande, C. D. Lokhande, J Colloid. Interf. Sci. 469, 2016, 257.
- [21] A. Ramadoss, K.Y. Yoon, M. J. Kwak, S. I. Kim, S. T. Ryu, J. H. Jang, J Power Sources, 337, 2017, 159.
- [22] C. D. Lokhande, D. P Dubal, O. Joo, Curr. Appl. Phys., 11, 2011, 255.
- [23] G. Yu, N. Liu, H. Wang, L. Hu, M. Vosgueritchian, Y. Yang, Y. Cui, Z. Bao, Nano Lett., 11, 2011, 4438.
- [24] B. K. Kim, V. Chabot, A. Yu, Electrochim. Acta, 109, 2013, 370.
- [25] L. L. Zhang and X. S. Zhao, Chem. Soc. Rev., 38, 2009, 2520.
- [26] G. S. Gund, D. P. Dubal, B. H. Patil, S. S. Shinde, C. D. Lokhande, Electrochim Acta, 92, 2013, 205.
- [27] http://dx.doi.org/doi:10.1016/j.electacta.2015.02.246.
- [28] X. Lu, M. Yu, G. Wang, Y. Tong, Y. Li, Energy Environ. Sci., 7, 2014, 21.
- [29] S. K. Chang, Z. Zainal, K. B. Tan, N. A. Yusof, W.M.D.W. Yusoff, S.R.S. Prabaharan, Ceram. Int., 41, 2015, 1.
- [30] P. Simon, Y. Gogotsi, B. Dunn, Science, 343, 2014, 1210.
- [31] J. W. Long, D. Bélanger, T. Brousse, W. Sugimoto, M. B. Sassin, O. Crosnier, MRS Bull., 36, 2011, 513.
- [32] F. Chen, H. Wang, S. Ji, V. Linkov, R. Wang Mater. Today Energy, 11, 2019, 211.
- [33] H. Pang, Y. Zhang, W. Y. Lai, Z. Hu, W. Huang, Nano Energy, 15, 2015, 303.
- [34] Y. Wang, Y. Song, Y. Xia, Chem. Soc. Rev., 45, 2016, 5925.
- [35] M. Huang, F. Li, F. Dong, Y. X. Zhang, L. L. Zhang, J. Mater. Chem. A, 3, 2015, 21380.
- [36] U. M. Patil, R. R. Salunkhe, K. V. Gurav, C. D. Lokhande, Appl. Surf. Sci., 255, 2008, 2603.
- [37] G. A. Snook, P. Kao, A. S. Best, J. Power Sources, 196, 2011, 1.
- [38] T. Brousse, D. Bélanger, J. W. Long, J. Electrochem. Soc., 162, 2015, A5185.
- [39] X. Wang, Y. Liu, Y. Wang, L. Jiao, small, 12, 2016, 4865.
- [40] Q. Ke, C. Guan, X. Zhang, M. Zheng, Y. W. Zhang, Y. Cai, H. Zhang, J. Wang, Adv. Mater., 29, 2017, 1604164.

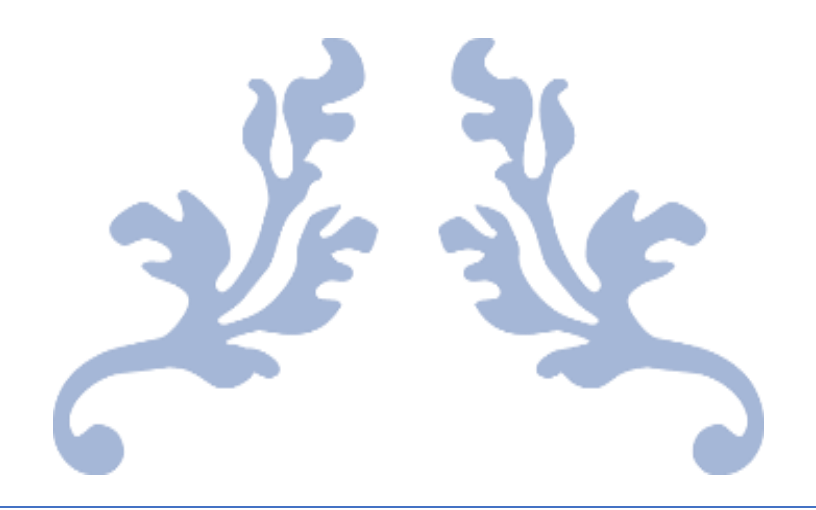
- [41] P. Yu, Z. Zhang, L. Zheng, F. Teng, L. Hu, X. Fang, Adv. Energy Mater., 6, 2016, 1601111.
- [42] J. Wei, Y. Li, D. Dai, F. Zhang, H. Zou, X. Yang, Y. Ji, B. Li, X. Wei, ACS Appl. Mater. Interfaces, 12, 2020, 5786.
- [43] K. S. Kumar, N. Choudhary, Y. Jung, J. Thomas, ACS Energy Lett., 3, 2018, 482.
- [44] A. M. Bryan, L. M. Santino, Y Lu, S. Acharya, J. M. D'Arcy, Chem. Mater., 28, 2016, 5989.
- [45] B. Guan, Y. Li, B. Yin, K. Liu, D. Wang, H. Zhang, Chem. Eng. J, 308, 2017, 1165.
- [46] H. Peng, G. Ma, K. Sun, J. Mu, H. Wang, Z. Lei, J. Mater. Chem. A, 2, 2014, 3303.
- [47] K. Wang, C. Zhao, Z. Zhang, S. Min, X. Qian, RSC Adv., 6, 2016, 16963.
- [48] T. Zhu, B. Xia, L. Zhou. X. W. Lou, J. Mater. Chem., 22, 2012, 785.
- [49] R. N. Bulakhe, S. Sahoo, T. T. Nguyen, C. D. Lokhande, C. Roh, Y. R. Lee, J. J. Shim, RSC Adv., 6, 2016, 14844.
- [50] C. Shi, H. Dong, R. Zhua, H. Lia, Y. Sun, D. Xu, Q. Zhao, D. Yu, Nano Energy, 13, 2015, 670.
- [51] Y. K. Hsu, Y. C. Chen, Y. G. Lin, Electrochim. Acta, 139, 2014, 401.
- [52] K. J. Huang, J. Z. Zhang, Y. Fan, J. Alloys Compd., 625, 2015, 158.
- [53] J. Zhang, H. Feng, J. Yang, Q. Qin, H. Fan, C. Wei, W. Zheng, ACS Appl. Mater. Interfaces, 7, 2015, 21735.
- [54] L. Qian, X. Tian, L. Yang, J. Mao, H. Yuan, D. Xiao, RSC Adv., 3, 2013, 1703.
- [55] H. Chen, J. Li, C. Long, T. Wei, G. Ning, J. Yan, Z. Fan, J. Mar. Sci. Appl., 13, 2014, 462.
- [56] C. Peng, D. Hua, G. Z. Chen, Chem. Commun., 47, 2011, 4105.
- [57] D. P. Dubal, S. H. Lee, J. G. Kim, W. B. Kim, C. D. Lokhande, J. Mater. Chem., 22, 2012, 3044.
- [58] H. Zhou and G. Han, Electrochimi Acta, 192, 2016, 448.
- [59] R. B. Ambade, S. B. Ambade, N. K. Shrestha, Y. Nah, S. H. Han, W. Lee, S. H. Lee, Chem. Commun., 49, 2013, 2308.

- [60] D. P. Dubal, S. Abdel-Azeim, N. R. Chodankar, Y. Han, iScience, 16, 2019, 50.
- [61] Q. Wang, Y. Zhang, H. Jiang, X. Li, Y. Cheng, C. Meng, Chem. Eng. J., 362, 2019, 818.
- [62] R. B. Rakhi, B. Ahmed, D. Anjum, H. N. Alshareef, ACS Appl. Mater. Interfaces, 8, 2016, 18806.
- [63] S. J. Marje, P. K. Katkar, S. S. Pujari, S. A. Khalate, P. R. Deshmukh, U. M. Patil, Mater. Sci. Eng., B, 261, 2020, 114641.
- [64] V. Lokhande, S. J. Lee, A. Lokhande, J. H. Kim, T. Ji, Mater. Chem. Phys., 211, 2018, 214.
- [65] J. Gai, F. Ma, Z. Zhang, D. Sun, Y. Jin, Y. Guo, W. Kim, ACS Sustainable Chem. Eng., 7, 2019, 15896.
- [66] W. Luo, Y. Gong, Y. Zhu, K. K. Fu, J. Dai, S. D. Lacey, C. Wang, B. Liu, X. Han, Y. Mo, E. D. Wachsman, L. Hu, J. Am. Chem. Soc., 138, 2016, 12258.
- [67] C. Zhong, Y. Deng, W. Hu, J. Qiao, L. Zhangd, J. Zhang, Chem. Soc. Rev., 44, 2015, 7484.
- [68] Y. Zheng, Y. Yao, J. Ou, M. Li, D. Luo, H. Dou, Z. Li, K. Amine, A. Yu, Z. Chen, Chem. Soc. Rev., Chem. Soc. Rev., 49, 2020, 8790.
- [69] K. Fu, Y. Gong, B. Liu, Y. Zhu, S. Xu, Y. Yao, W. Luo, C. Wang, S. D. Lacey, J. Dai, Y. Chen, Y. Mo, E. Wachsman, L. Hu, Sci. Adv., 3, 2017, e1601659.
- [70] D. E. Fenton, J. M. Parker, P. V. Wright, Polymer, 14, 1973, 589.
- [71] S. S. Sekhon, Bull. Mater. Sci., 26, 2003, 321.
- [72] C. M. Yang, H. S. Kim, B. K. Na, K. S. Kum, B. W. Cho, J. Power Sources, 156, 2006, 574.
- [73] C. W. Liew, S. Ramesh, A. K. Arof, Int. J. Hydrogen Energ., 39, 2014, 2953.
- [74] R. C. Agrawal and G. P. Pandey, J. Phys. D: Appl. Phys., 41, 2008, 223001.
- [75] G. P. Pandey, A. C. Rastogi, C. R. Westgate, J. Power Sources, 245, 2014, 857.
- [76] P. Sivaraman, A. Thakur, R. K. Kushwaha, D. Ratna, A. B. Samui, Electrochem. Solid State Lett., 9, 2006, A435.
- [77] Y. S. Lee, S. H. Ju, J. H. Kim, S. S. Hwang, J. M. Choi, Y. K. Sun, H. Kim, B. Scrosati, D. W. Kim, Electrochim. Comm., 17, 2012.
- [78] C. Meng, C. Liu, L. Chen, C. Hu, S. Fan, Nano Lett., 10, 2010, 4025.
- [79] S. K. Tripathi, A. Kumar, S. A. Hashmi, Solid State Ionics, 177, 2006, 2979.

- [80] S. Chandra, S. S. Sekhon, N. Arora, lonics, 6, 2000, 112.
- [81] N. R. Chodankar, D. P. Dubal, G. S. Gund, C. D. Lokhande, Energy Technol., 3, 2015, 625.
- [82] N. R. Chodankar, H. D. Pham, A. K. Nanjundan, J. F. S. Fernando, K. Jayaramulu, D. Golberg, Y. Han, D. P. Dubal, small, 16, 2020, 2002806.
- [83] V. Srirapu A. Kumar, P. Srivastava, R. Singh, A. Sinha, Electrochim. Acta, 209, 2016, 75.
- [84] W. Low, P. Khiew, S. Lim, C. Siong, E. Ezeigwe, J. Alloys Compd., 775, 2019, 1324.
- [85] M. Denk, D. Kuhness, M. Wagner, S. Surnev, F. Negreiors, L. Sementa, G. Barcaro, I. Vobornik, A. Fortunelli, F. Netzer, ACS Nano, 8, 2014, 347.
- [86] G. Zhang and X. Lou, Adv. Mater, 25, 2013, 976.
- [87] J. Zhang, F. Lu, J. Chenq, X. Zhang, ACS Appl. Mater. Interface, 7, 2015, 17630.
- [88] G. He, J. Li, W. Li, B. Li, N. Noor, K. Xu, J. Hu, I. Parkin, J. Mater. Chem., A, 3, 2015, 14272.
- [89] N. Bretesche, O. Crosnier, C. Payen, F. Favier, T. Brousse, Electrochem. Commun, 57, 2015, 61.
- [90] D. Cai, D. Wang, B. Liu, Y. Wang, Y. Liu, L. Wang, H. Li, H. Huang, Q. Liu, T. Wang, ACS Appl. Mater. Interfaces, 5, 2013, 12905.
- [91] S. Ede, A. Ramadoss, U. Nithiyanantham, S. Anantharaj, S. Kundu, Inorga. Chem., 54, 2015, 3851.
- [92] A. Sobhani-Nasab, M. Rahimi-Nasrabadi, H. Naderi, V. Pourmohamadian, F. Ahmadi, M. R. Ganjal, H. Ehrlch, Ultrason. Sonochem, 45, 2018, 185.
- [93] X. Xu, L. Pei, Y. Yang, J. Shen, M. Ye, J. Alloys Compd., 654, 2016, 23.
- [94] C. Ling, L. Q. Zhou, H. Jia, RSC Adv., 4, 2014, 24692.
- [95] M. Zhang, H. Fan, N. Zhao, H. Peng, X. Ren, W. Wang, H. Li, G. Chen, Y. Zhu, X.Jiang, P. Wu, Chem. Eng. J., 347, 2018, 291.
- [96] A. Li. Y. Tu, Y. Zhu, D. Li, W. Zhou, X. Zhu, L. Feng, Int. J. Electrochem. Sci., 12, 2017, 5646.
- [97] A. S. Patil, G. M. Lohar, V. J. Fulari, J. Mater. Sci: Mater. Electron., 27, 2016, 9550.

- [98] M. Ikram, Y. Javed, N.A. Shad, M.M. Sajid, M. Irfan, A. Munawar, T. Hussain, M. Imran, D. Hussain, J. Alloys Compd., 878, 2021, 160314.
- [99] S. M. Pourmortazavi, M. Rahimi-Nasrabadi, M. S. Karimi, S. Mirsadeghi, New J. Chem., 42, 2018, 19934.
- [100] R. Packiaraj, P. Devendran, K.S. Venkatesh, N. Nallamuthu, Inorg. Chem. Commun., 126, 2021, 108490.
- [101] J. Tian, Y. Xue, X. Yu, Y. Pei, H. Zhang, J. Wang, RSC advances, 8, 2018, 41740.
- [102] L. Niu, Z. Li, Y. Xu, J. Sun, W. Hong, X. Liu, J, Wang, S. Yang, ACS Appl. Mater. Interfaces., 5, 2013, 8044.
- [103] X. Xu, L. Pei, Y. Yang, J. Shen, M. Ye, J. Alloys Compd., 654, 2016, 23.
- [104] J. Tian, Y. Xue, X. Yu, Y. Pei, H. Zhang, J. Wang, RSC advances, 8, 2018, 41740.
- [105] L. Niu, Z. Li, Y. Xu, J. Sun, W. Hong, X. Liu, J, Wang, S. Yang, ACS Appl. Mater. Interfaces, 5, 2013, 8044.
- [106] Y. Huang, Y. Gao, C. Liu, Z. Cao, Y. Wang, Z. Li, Y. Yan, M. Zhang, G. Cao, J. Phys. Chem. C., 123, 2019, 30067.
- [107] X. Feng, Y. Huang, M. Chen, X. Chen, C. Li, S. Zhou, X. Gao, J. Alloys Compd., 763, 2018, 801.
- [108] R. D. Kumar, Y. Andou, S. Karuppuchamy, J. Alloys Compd., 654, 2016, 349.
- [109] R. Kumar, S. Karuppuchamy, J. Alloys Compd., 674, 2016, 384.
- [110] X. Xing, Y. Gui, G. Zhang, C. Song, Electrochim. Acta, 157, 2015, 15.
- [111] S. Jha, S. Mehta, E. Chen, S. Sankar, S. Kundu, H. Liang, Mater. Adv., 1, 2020, 2124.
- [112] B. Huang, H. Wang, S. Liang, H. Qin, Y. Li, Z. Luo, C. Zhao, L. Xie, L. Chen, Energy Storage Mater. 32, 2020, 105.
- [113] Y. He, L. Wang, D. Jia, Z. Zhao, J. Qiu, Electrochim. Acta., 222, 2016, 446.
- [114] K. Thiagarajan, D. Balaji, J. Madhavan, J. Theerthagiri, S. J. Lee, K-Y Kwon,M. Y. Choi, Nanomaterials, 10, 2020, 2195.
- [115] H. Ma, Z. Shen, Z. Peng, S. Guan, X. Fu, J. Alloys Compd., 845, 2020, 155654.
- [116] S. Prabhu, C. Balaji, M. Navaneethan, M. Selvaraj, N. Anandhan, D.

- Sivaganesh, S. Saravanakumar, P. Sivakumar, R. Ramesh, J. Alloys Compd., 875, 2021, 160066.
- [117] J. Hou, J. Gao, L. Kong, J. Alloys Compd., 878, 2021, 160314.
- [118] V. Lokhande and T.Ji, Adv. Sci. Technol. Lett., 139, 2016, 409.
- [119] Geetanjali, R. Rani, S. Kumar, fuel cells, 19, 2019, 299.
- [120] D. Kumar, Y. Andou, S. Karuppuchamy, J. Alloys Compd., 654, 2016, 349.
- [121] www.rsc.org/materialsA.
- [122] Y. Wang, C. Shen, L. Niu, Z. Sun, F. Ruan, M. Xu, S. Shan, C. Li, X. Liu, Y. Gong, Mater. Chem. Phys., 182, 2016, 394.
- [123] J. Rajkumar, C. Ezhilarasi, P. Saranya, J. Princy Merlin, J. Phys. Chem. Solids, 162, 2022, 110500.



# THEORETICAL BACKGROUND OF SILAR METHOD AND CHARACTERIZATION TECHNIQUES



# THEORETICAL BACKGROUND OF SILAR METHOD AND CHARACTERIZATION TECHNIQUES

| Sr. No | Title   |  |    |  |  |  |  |
|--------|---|--|----|--|--|--|--|
| 2.1    | Introduction  |  |    |  |  |  |  |
| 2.2    | The theoretical background of successive ionic layer adsorption and |  |    |  |  |  |  |
|        | reaction (SILAR) method   |  |    |  |  |  |  |
|        | 2.2.1 Effect of preparative parameters                              |  |    |  |  |  |  |
| 2.3    | Thin film characterization techniques                               |  |    |  |  |  |  |
| 2.3.1  | Physico-chemical characterization techniques                        |  |    |  |  |  |  |
|        | 2.3.1.1   | X-ray diffraction (XRD)                              |    |  |  |  |  |
|        | 2.3.1.2   | Fourier transforms infrared spectroscopy (FT-IR)     | 45 |  |  |  |  |
|        | 2.3.1.3   | Raman spectroscopy                                   | 47 |  |  |  |  |
|        | 2.3.1.4   | Field emission scanning electron microscopy (FE-SEM) | 50 |  |  |  |  |
|        | 2.3.1.5   | X-ray photoelectron spectroscopy (XPS)               | 51 |  |  |  |  |
|        | 2.3.1.6   | Contact angle measurement                            | 53 |  |  |  |  |
|        | 2.3.1.7   | Brunauer-Emmett-Teller (BET) analysis                | 54 |  |  |  |  |
| 2.3.2  | Electrochemical characterization techniques                         |  |    |  |  |  |  |
|        | 2.3.2.1   | Cyclic voltammetry (CV)                              | 60 |  |  |  |  |
|        | 2.3.2.2   | Galvanostatic charge-discharge (GCD)                 | 61 |  |  |  |  |
|        | 2.3.2.3   | Electrochemical impedance spectroscopy (EIS)         | 63 |  |  |  |  |
|        | References  |  |    |  |  |  |  |

#### 2.1 Introduction

In recent years, researchers have been drawn to the significant changes in physical and chemical properties of materials that occur when their dimensions are reduced [1]. This has led to the development of sophisticated instrumentation for material synthesis and structural analysis, as well as computer-based simulations using various computational methods to complement preparation methods [2]. Solid thin films have become widely used in many engineering systems, including photovoltaic, sensors and transducers, energy storage systems, electronics, catalysis systems, and biological applications, due to their ability to improve the physical and chemical characteristics of materials [3]. Control over different preparative parameters and post-deposition treatments allows for modification of specific properties of materials in solid thin film form. Thin films can range in thickness from a few nanometers to several micrometers, although there is no perfect definition of the thickness below which a film becomes thin, as the variation of properties with thickness differs from material to material. The properties of materials in thin film form are changed predominantly from their bulk counterpart due to their nanocrystalline nature, which offers a reduction in density and thermal conductivity, an increase in volume to mass ratio, and changes in electrical conductivity. The method used to prepare thin films greatly affects their properties, including crystal structure, crystallinity, roughness, morphology, and reactivity [4, 5].

Thin film deposition methods are generally classified into physical methods, such as vacuum evaporation and sputtering, and chemical methods, including chemical vapor deposition (CVD), photo CVD, laser CVD, metal organo-chemical vapor deposition (MOCVD) and plasma enhanced CVD, CBD, electrodeposition, SILAR, hydrothermal, anodization, spin coating, spray pyrolysis, liquid phase epitaxy, and sol gel method [6-8]. Chemical deposition methods are generally preferred over physical methods due to their simplicity of instrumentation, inexpensiveness, scalability, lower working temperature, ability to deposit materials on large substrates, and variety of substrate choices. Various kinds of substrates can be employed to deposit thin films due to the lower working temperature, and metallic substrates are protected from oxidation [9].

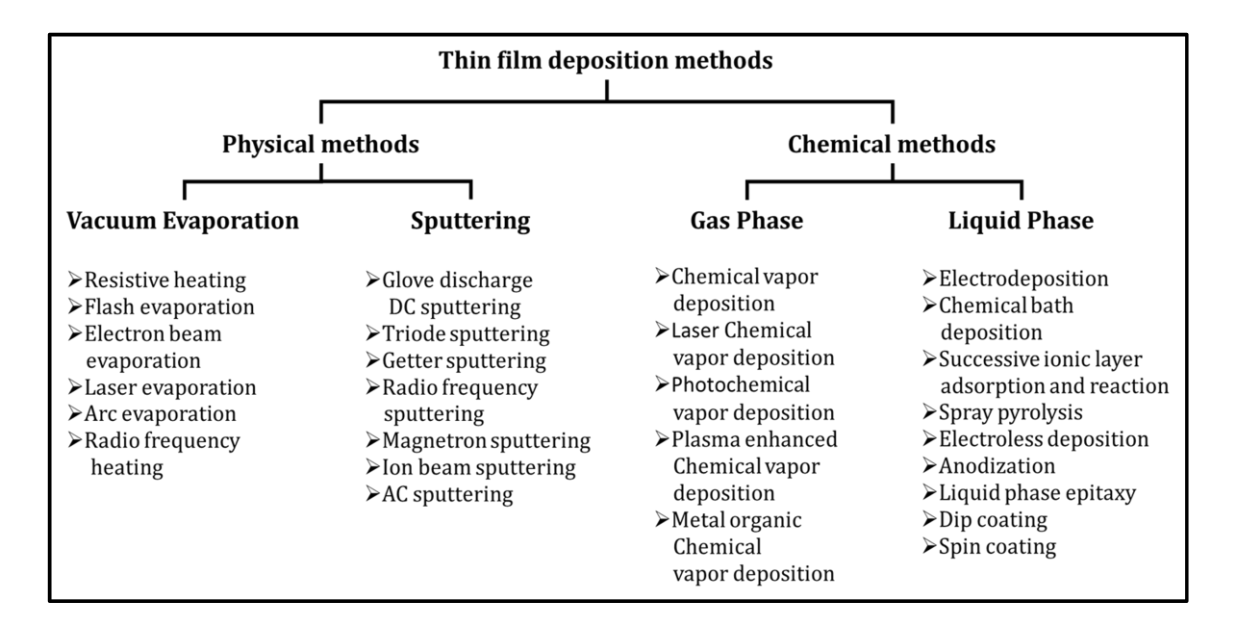


Chart 2.1: Categorization of thin film deposition methods.

To determine the surface properties of thin films, various structural, morphological, and elemental characterization techniques are used, such as XRD, FT-IR, Raman spectroscopy, FE-SEM, EDAX, XPS, and contact angle measurements. The specific surface area of materials and pore size distribution are measured using BET technique and Barrett-Joyner-Halenda (BJH) analysis, respectively. The electrochemical characteristics of films of NiWO<sub>4</sub>, NiWO<sub>4</sub>@rGO, and Fe<sub>2</sub>O<sub>3</sub>, AC are evaluated using various techniques like CV, GCD, and EIS.

# 2.2 Theoretical background of successive ionic layer adsorption and reaction (SILAR) method.

The SILAR (Successive Ionic Layer Adsorption and Reaction) method is a cost-efficient and straightforward technique used for depositing a wide range of materials in thin-film form [10]. One of its advantages is the ability to exert significant control over deposition parameters while the deposition process is ongoing [11]. The mechanism of the SILAR method was initially reported by Ristov *et al.* in 1985, and Nicolau *et al.* named the method SILAR. This technique is useful for depositing various chemical compounds and composite films. The SILAR method is also known as the modified CBD (Chemical Bath Deposition) method.

The SILAR method is based on sequential reactions at the surface of the substrate, followed by rinsing to enable uniform growth of the solid phase. The method is intended for the deposition of thin films of water-insoluble ionic or ion-covalent

compounds of the type KpAa by heterogeneous chemical reactions at the solid-solution interface between adsorbed cations,  $pK_a^+$ , and anions,  $aA_p^-$ . The reaction can be represented by the following relation:

$$(pK_{aq}^{a+} + qX_{aq}^{b-}) + (b'Y_{aq}^{q'+} + aA^{p-}) \to KpAa_s \downarrow + qX_{aq}^{b-} + b'Y_{aq}^{q'+}$$
 (2.1)

where ap = bq = b'q'. Here, K represents cations such as  $Zn^{2+}$ ,  $Fe^{2+}$ ,  $Co^{2+}$ ,  $Fe^{3+}$ ,  $Cu^{2+}$ ,  $Ni^{2+}$ , etc., p represents the number of cations, a represents the numerical value of the charge on the cation, X is an ion in cationic precursors having a negative charge (X =  $SO_4^{2-}$ ,  $Cl^-$ ,  $NO_3^-$ , etc.), q represents the number of X in cationic precursors, and b is the numerical value of the charges on X. Y ion is attached to chalcogen ion, b' is the number of Y in the anionic solution, q' is the numerical value of the charge on Y, and A is the chalcogen ion, and a is the number of anions. In the presence of a complexing agent, the above reaction can be written as:

$$p[(KC)^{a+}]_{aq} + qX_{aq}^{b-} + b'Y^{q'+}_{aq} + aA^{p-} \longrightarrow Kp'Aa'_s \downarrow + C + qX^{b-}_{aq} + b'Y^{q'+}_{aq}$$
 (2.2)

where C is the complexing agent. The basic representation of the four-beaker SILAR method is shown in Figure 2.1. The different processes involved in the SILAR method are elaborated below.

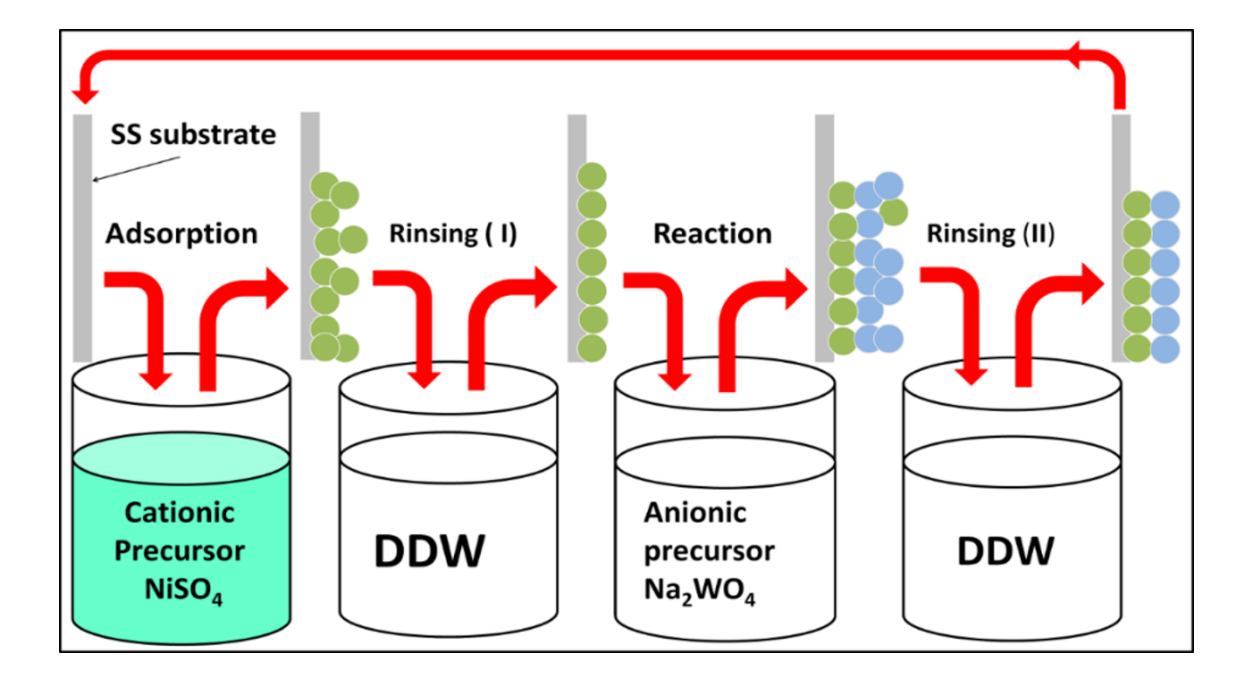


Figure 2.1: Schematic of four beaker SILAR method.

#### (a) Adsorption:

The initial stage of the deposition process involves the adsorption of positive ions onto the substrate's surface, forming the Helmholtz electric double layer. Van der Waals forces contribute to the creation of two layers of ions on the substrate's surface. The inner layer consists of positively charged ions, while the outer layer serves as a counter layer composed of anions.

#### (b) First rinsing:

During this step, the loosely adsorbed cations present on the substrate's surface are eliminated. The rinsing process significantly impacts the morphology, particle size, crystallinity, and thin film adhesion to the substrate. Typically, double-distilled water (DDW) is utilized as the rinsing solution.

#### (c) Reaction:

This is the third step, where the anions from the anionic precursor solution get involved in the reaction process. Due to the high reactivity between cations and anions, a solid substance possessing the chemical composition KpAa forms at the interface. This step involves irreversible chemical reactions between pre-adsorbed cations  $(pK^{a+})$  and anions  $(aA^{p-})$  from the solution.

#### (d) Second Rinsing:

This is last step of SILAR deposition method used to remove unreacted, excess species, and secondary products of the reaction ( $aA^{p-}$ , X, Y) from the diffusion layer. As like in step second, DDW is used as rinsing solution. Thin film growth rate largely depends on various preparative parameters such as temperature of solutions, number of repeated cycles, pH of the solutions, concentration of cationic and anionic precursors, rinsing time, adsorption and reaction time, type and concentration of complexing agent, etc.

#### Advantages of SILAR method

Apart from saving material cost, preparation of thin films using SILAR method has the following advantages:

(i) SILAR is an efficient and cost-effective technique suitable for large-scale deposition.

- (ii) Due to its low temperature nature, SILAR allows for the use of diverse substrates such as metals, semiconductors, insulators, and polymers, minimizing the risk of corrosion or oxidation of metallic substrates.
- (iii) The SILAR method offers excellent feasibility for doping films with precise proportions of various elements.
- (iv) The deposition rate, morphology, and film thickness can be efficiently manipulated by varying the preparative conditions.
- (v) A comparatively uniform film can be deposited on any kind of substrate having a complex configuration.
- (vi) Drawbacks like contamination, interdiffusion, and dopant redistribution, due to high temperature deposition techniques can be avoided in this low temperature deposition method.

Along with the above advantages, SILAR has attractive features that material can be directly deposited from aqueous and nonaqueous baths and used to produce binary metal phosphate materials.

#### 2.2.1 Effect of preparative parameters

The growth kinetics are affected by ion concentration, nucleation, and the growth process on immersing substrates. The composition of the counter ions (namely  $SO_4^{2-}$  and  $Na^+$ ), the nature of the solvent, the presence of impurities causing additional insoluble compounds to be deposited, the added complexing agents, the substrate polishing and etching, and the substrate solubility all have a role. The following shows the effects of various conditions.

#### (i) Concentration of precursors

In almost all chemical deposition processes, the concentration of the precursor solutions influences the rate of film formation. Adsorption and reaction rates are affected by the concentration of the precursor solutions. If the concentration of cations exceeds a particular level, the rate of adsorption rises and the thickness of the film grows, but if the concentration of anionic precursor increases, the reaction rate increases and big particle development occurs. The higher the reaction rate, the less adhesive and nonhomogeneous the film thickness. Greater precursor concentrations result in the production of maximal film thickness and an increased likelihood of the formation of

insoluble contaminants in the film [12]. The optimal concentration of both precursors should be evaluated experimentally.

#### (ii) pH

The pH of solutions is very significant. Extreme pH levels alter the surface state of the substrate as well as the solubility of the target chemical, contaminants, and even the substrate. At certain pH levels, the reaction rate increases, and the ionic product of metal and chalcogenide becomes smaller than the solubility product of metal chalcogenide, and no film is created. A complexing agent can be used to change the pH of a cationic solution.

#### (iii) Temperature

Variations in film thickness are achievable by changing the temperature of the solution bath. The temperature affects the dissociation of the complex and the anion of the chemical. Dissociation is greater at higher temperatures, resulting in a faster rate of deposition. The rate of film production slows down at room temperature or below. The thickness increases linearly as the temperature rises.

#### (iv) Complexing agent

The concentration of metal ions in the solution can be adjusted by adding a complexing agent. Ligands are another name for complexing agents. They have one or more donor atoms which can establish coordination covalent connection with metal ion from the solution. Coordination compound is a compound generated by a metal ion and a complexing agent. Additional complexing agents introduce an additional activated kinetic step of decomplexation, increasing surface relaxation time and promoting regular development. Complexing agent concentration reduces active metal ion concentration. As a result, the pace of reaction and precipitate production slows, resulting in a thicker coating at the terminal. Adsorption is the sole phenomena that occurs when a thin layer is deposited on the surface of a substrate. Thin films are formed by combining released metal ions from complicated metal ion sources and chalcogen sources. The number of binding sites is used to classify complexing agents. Ammonia (NH<sub>3</sub>; monodentate), ethylenediaminetetraacetic acid (C<sub>10</sub>H<sub>16</sub>N<sub>2</sub>O<sub>8</sub>; ethylenediamine hexadentate),  $(C_2H_4(NH_2)_2;$ bidentate), triethanolamine (N(CH<sub>2</sub>CH<sub>2</sub>OH)<sub>3</sub>; monodentate), polyvinyl alcohol (C<sub>2</sub>H<sub>4</sub>O) <sub>x</sub>; monodentate/bidentate), and others are some common complexing agents used in chemical deposition methods.

#### (v) Number of cycles

Each cycle of deposition adds a few layers of material to the substrate, increasing the number of cycles results in a thicker film. A large number of cycles leads to the creation of a particle cluster. As a result, after a certain number of cycles, the thin film begins to peel off.

#### (vi) Rinsing time

The hydrodynamics of washing affect thin film formation because weakly adsorbed ions are eliminated during rinsing. Another source of impurities is the formation of metal hydroxide with various chalcogenides. The optimal washing time after adsorption and reaction should be established experimentally. This helps to avoid particle cluster formation and allows for the deposition of a uniform thin coating.

#### 2.3 Thin film characterization techniques

#### 2.3.1 Physico-chemical characterization techniques

Crystal structure, specific surface area, surface roughness, conductivity, and elemental composition are all highly associated with its electrochemical characteristics. As a result, characterisation of materials using various techniques and detailed analysis of the data to explain the link between different attributes is a significant contribution to the scientific area. This aids in the selection of the appropriate material and its application. These techniques also make it easier to detect material alterations. As a result, the thin film electrodes in this work were examined using several material characterisation techniques. This section provides a full overview of the underlying principles, instrumentation, and operation of various approaches.

The experimental techniques and instruments used in the analysis of the prepared thin films and synthesized material are as follows:

- 1. Crystal Structure and Purity Analysis:
  - Instrument: Rigaku Miniflex-600 X-ray Diffractometer
  - Radiation Source: Cu-Kα radiation with a wavelength (λ) of 1.5418 Å
  - Operating Voltage: 30 kV
- 2. Functional Group Analysis:
  - Instrument: Bruker Tensor 27 FT-IR Spectrometer
- 3. Surface Structure Analysis:
  - Instrument: FE-SEM (Field-Emission Scanning Electron Microscope)

- Model: JEOL JEM 2100
- 4. Elemental Composition Analysis:
  - Instrument: FE-SEM (Field-Emission Scanning Electron Microscope) with Energy Dispersive X-ray Spectroscopy (EDAX) attachment
- 5. Surface Chemical Composition Analysis:
  - Instrument: VG Multilab 2000 X-ray Photoelectron Spectroscope
  - Source: Monochromatic Mg-Kα radiation (1253.6 eV)
- 6. Raman Analysis:
  - Instrument: JASCO NRS-5100 Raman Spectrometer
  - Excitation Wavelength (λ): 514.4 nm
- 7. Contact Angle Measurement:
  - Instrument: Rame-Hart Instrument
- 8. Specific Surface Area and Pore Size Distribution Analysis:
  - Analysis Models: Brunauer, Emmett, and Teller (BET) and Barrett-Joyner-Halenda (BJH)
  - Instrument: Quantachrome Instruments v11.02

These instruments and techniques were utilized to investigate various properties of the thin films, including crystal structure, purity, functional groups, surface structure, elemental composition, surface chemical composition, Raman spectra, contact angle, specific surface area, and pore size distribution.

#### 2.3.1.1 X-ray diffraction (XRD)

The XRD is a very basic, well-established, and commonly utilized strong non-destructive characterization tool in the field of materials science for obtaining information on the atomic scale structure of diverse substances in a range of states [13]. The approach also offers information on the dimensions of unit cells. The XRD technique is the most widely used for determining crystallite size (D), as well as calculating lattice strain, chemical composition, state of order, and phase diagrams.

#### Working principle

The XRD analysis relies heavily on the constructive interference of monochromatic X-rays from a crystalline sample. In materials, the interatomic distance

is measured in Angstroms. This distance is equivalent to the wavelength of X-rays (energy between 3- 8 keV). As a result, constructive and destructive interference patterns are observed when crystalline materials are subjected to X-rays. A diffraction pattern is obtained by measuring the intensity of diffracted X-rays as a function of scattering angle. Bragg's condition (Figure 2.2) states that constructive interference of diffracted X-rays occurs when the path difference (AC+CB) equals the wavelength of X-rays ( $\lambda$ ). The aforementioned condition may be expressed mathematically as [14],

$$d\sin\theta + d\sin\theta = n\lambda \quad \text{or} \quad 2d\sin\theta = n\lambda \tag{2.3}$$

where n is the order of diffraction,  $\theta$  is the glancing angle or Bragg's angle, and d is the interplanar distance.

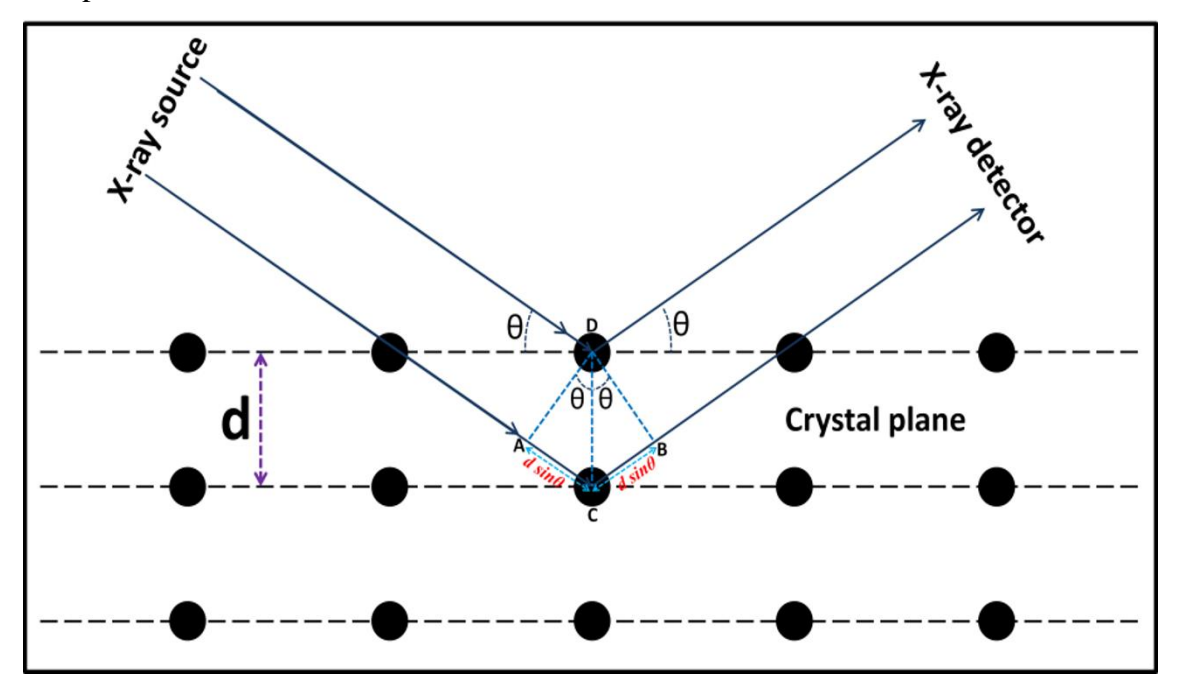


Figure 2.2: Bragg's diffraction.

#### Working of instrument

The X-ray diffractometer is made up of three basic parts: a monochromatic X-ray source, a specimen holder, and an X-ray detector. The X-ray generator is known as a cathode ray tube, and it is composed of a cathode, monochromator, and target material sealed in a glass or ceramic container under vacuum (**Figure 2.3**). To generate electrons, the cathode is heated; typically, it is made of tungsten filament. A voltage was

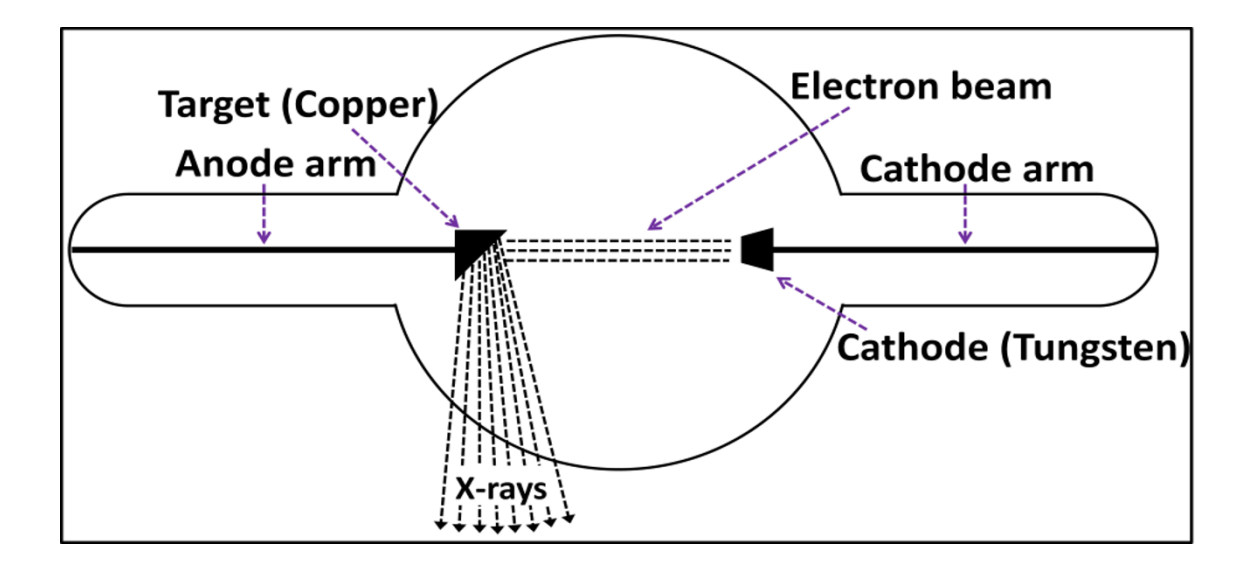


Figure 2.3: Schematic of X-ray tube.

used to accelerate these electrons towards the target material (Cu, Fe, Mo, Cr). If electrons have enough energy to evict inner shell electrons from the target element, the outer electrons from the target element leap into the inner shells, and radiation is released to compensate for the energy difference. This radiation is caused by the properties of the target substance. When copper is used as a target material, radiation consisting of  $K_{\alpha}$  and  $K_{\beta}$  lines is released. This energy is then filtered to generate monochromatic X-rays.  $CuK_{\alpha}=1.5418A^0$  is the wavelength of copper radiation. Now, monochromatic X-rays were collimated and directed toward the material to be studied. When Bragg's condition is met while the specimen and detector are spinning, peaks in the X-ray intensity are recorded. **Figure 2.4a** depicts an X-ray instrument design. The detector captures the signals, transforms them to a count rate, and sends them to the output instrument (computer) for further analysis.

Three methods available to determine crystal structure of sample are Laue method, rotating crystal, and powder method. Powder method is frequently employed to simply analyze crystal structure of material. The Laue method is the earliest method for determining crystal structure, employing a continuous spectrum of X-rays and a constant angle of incidence. This approach produces quicker diffraction than previous methods that employ monochromatic X-rays. As a result, it is utilized to study dynamic processes in crystal structures. The rotating crystal method is used when the angle of incidence is fixed but the wavelength is changeable. A monochromatic beam of hard X-rays is permitted to fall on a sample that is spun at a constant rotational velocity in the

revolving crystal technique. In the case of the powder technique, the wavelength is constant but the angle of incidence is changeable. Figure 2.4b shows the photograph of Bruker D2 phaser X-ray diffractometer. One very important use of XRD when dealing with nanocrystals is to estimate crystal dimensions through the Scherrer relationship [17];

$$D = \frac{0.9\lambda}{\beta\cos\theta} \tag{2.4}$$

where  $\beta$  is full width at half maximum (FWHM) of the diffraction peak,  $\theta$  is peak position in radians.

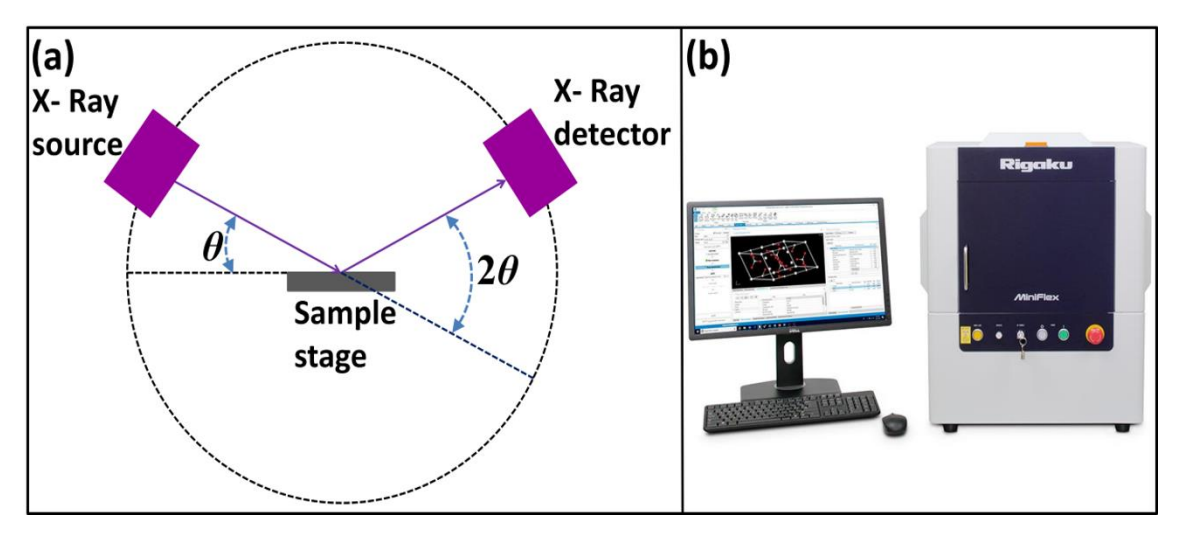


Figure 2.4: a) Schematic of X-ray instrument [15], and b) photograph of RIGAKU MiniFlex600 diffractometer [16].

In the present study, XRD patterns of deposited thin film electrodes are recorded using RIGAKU MiniFlex600 diffractometer with Cu K $\alpha$  characteristic radiations ( $\lambda$ = 1.5406 A $^0$ ) operated at 30 kV in  $\theta/2\theta$  mode.

#### 2.3.1.2 Fourier transforms infra-red spectroscopy (FT-IR)

FT-IR spectroscopy provides qualitative data on chemical bonding in materials. This is a non-destructive examination. This instrument may be used to analyze solids, liquids, and gases. The FT-IR abbreviation stands for Fourier transforms infrared spectroscopy, and the name refers to how data is acquired and transformed from interference pattern to spectrum.

#### Working principle

Depending on the type of bond and the components involved in bonding, molecular bonds vibrate at different frequencies. These frequencies are related to the ground state and numerous excited states in quantum physics. These bonds can escape to the highest potential state of energy when they take in light energy of a specific frequency. The energy of the light must be equal to or greater than the energy difference between the ground state and the first excited state for any given transition between two states. The features of a chemical bond can be seen in the spectrum and are determined by the wavelength that the bond absorbs. The mid-infrared region has a range of 4000 to 200 cm<sup>-1</sup>. Figure 2.5 [18] depicts the schematic of an FT-IR device with a Michelson interferometer.

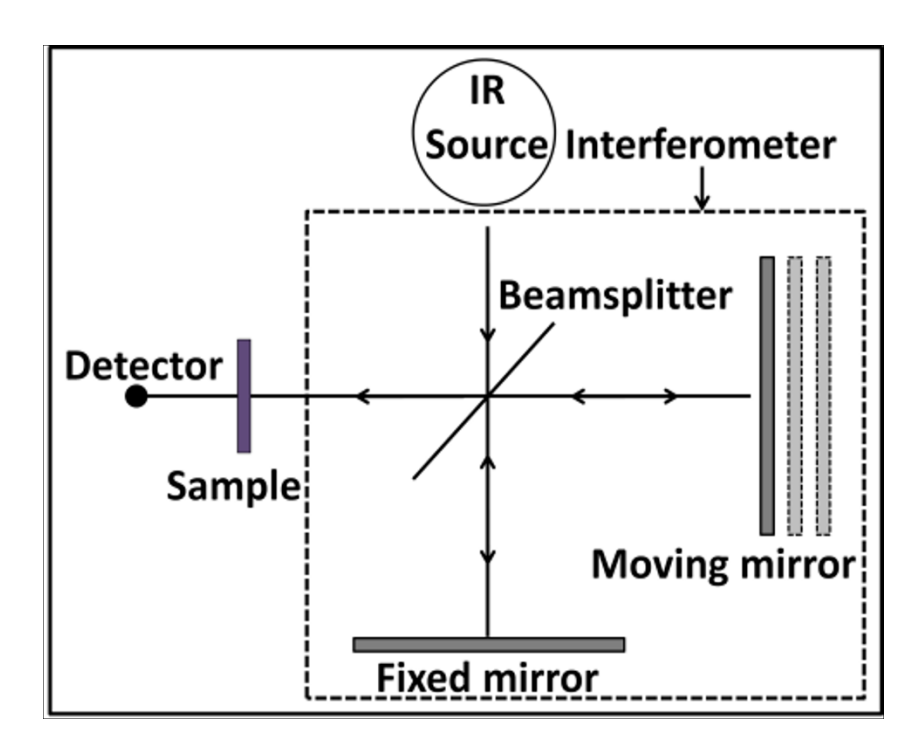


Figure 2.5: Basic schematic of FT-IR with Michelson interferometer.

#### **Working of instrument**

A typical FT-IR spectrometer consists of several essential components: a source of infrared radiation, an interferometer, a sample compartment, a detector, an amplifier, an analog-to-digital (A/D) converter, and a computer. These components work together to facilitate the measurement and analysis of infrared spectra. A picture of the ALPHA II small FT-IR spectrometer is shown in **Figure 2.6a**. **Figure 2.6b** shows the schematic

diagram of the fundamental FT-IR system along with the amplifier and required circuits for data conversion. The infrared spectrum is a graph with the frequency (wavenumber) on the horizontal axis and the substance's ability to absorb infrared light on the vertical axis. The sources of IR radiation include silicon carbide rod, nichrome and kanthanl wire coils, Nernst glowers, and carbon arcs.

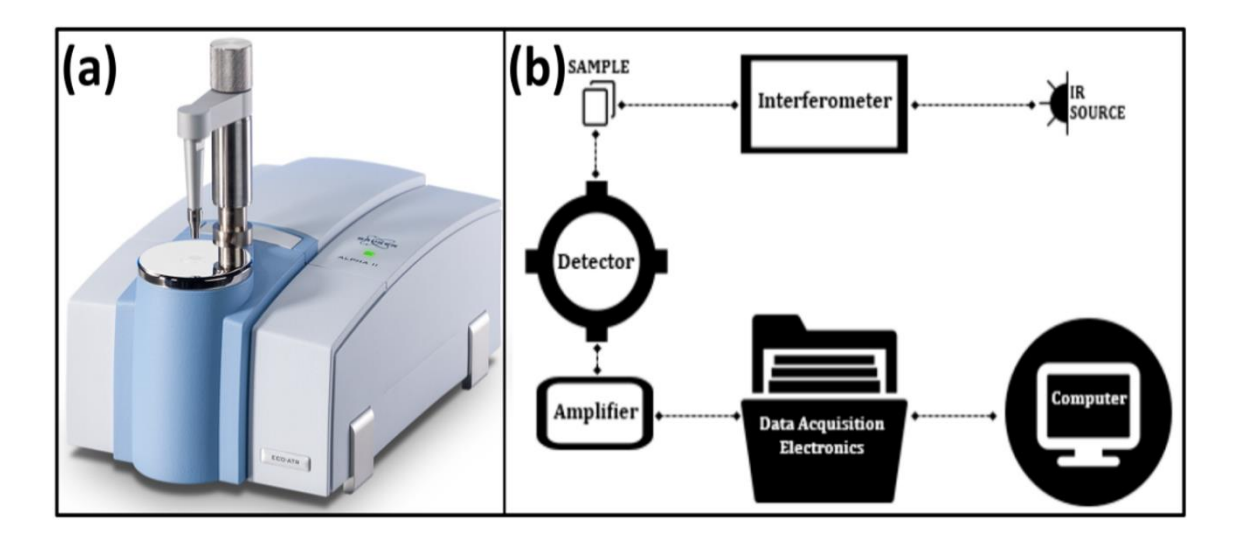


Figure 2.6: a) Photograph of ALPHA II compact FT-IR spectrometer [19], and b) the basic ray diagram of FT-IR system [20].

To allow IR radiation to flow through, the sample for FT-IR must be thin. This is one of the benefits of FT-IR analysis because it just needs a small sample. A portion of the IR radiation that is transmitted through a sample is partially absorbed by the sample. There are two different kinds of detectors: thermal and quantum detectors. Whereas quantum detectors treat received light as light, thermal detectors treat it as heat. Quantum detectors are therefore very sensitive. The acquired data are then transformed using the Fourier method and plotted against wavenumber. The observed data is compared to the available reference patterns for analysis purposes [21].

#### 2.3.1.3 Raman spectroscopy

Raman spectroscopy is powerful analytical technique widely used for nondestructive analysis of organic and inorganic materials [22]. It provides valuable insights into the characteristics of the material and its constituents by measuring various modes of molecules, including rotational, vibrational, and other low-frequency modes [23].

#### Working principle

The working principle of Raman spectroscopy is based on Raman scattering, which is a two-photon process. The electrons possess different vibrational levels, each with specific energy differences. When monochromatic light interacts with a material, an electron within the material absorbs energy from the incoming photon and undergoes a transition to a higher energy state. Subsequently, as the electron returns to its original energy level, it releases energy in the form of a secondary photon. In the case of Rayleigh scattering, the emitted photon retains the same frequency as the incident photon. However, in Raman scattering, the frequency of the emitted photon differs from that of the incident photon because the electron returns to a distinct vibrational level. Raman scattering produces Stokes lines (lower energy than incident radiation) and anti-Stokes lines (higher energy than incident radiation), as shown in Figure 2.7, depending on the final vibrational level of the electron [24]. The Raman shift  $\Delta v$ , positive for Stokes and negative for anti-Stokes, is a characteristic feature of the material undergoing Raman scattering. By analyzing the Raman spectrum, which represents the emitted photons, one can obtain a unique molecular fingerprint for different molecules, enabling qualitative analysis of the sample. Additionally, the intensity of specific Raman lines can be used to determine the concentration of molecules in the sample.

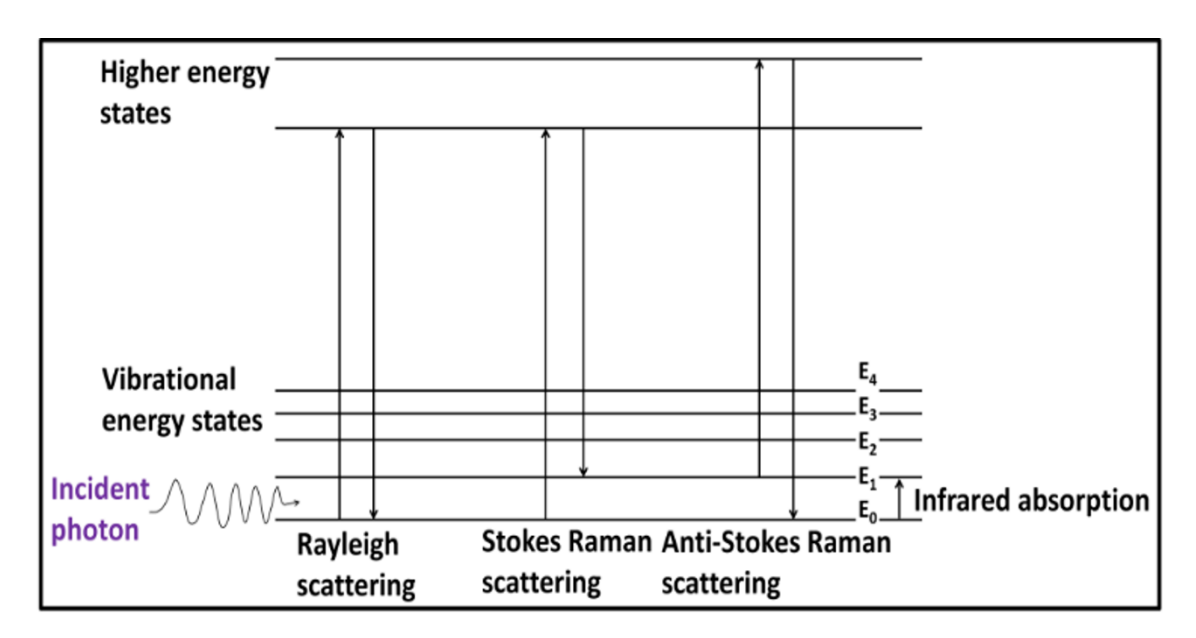


Figure 2.7: Energy level diagram showing the states involved in Raman spectra.

#### **Working of instrument**

A typical Raman spectrometer comprises three primary components, namely an excitation source, a sampling apparatus, and a detector [25 - 27]. The excitation source employed in Raman spectroscopy is often a monochromatic laser with a stable and narrow bandwidth. For organic molecules, a 785 nm diode laser is commonly used to minimize fluorescence, while a 1064 nm laser is preferred for highly colored or strongly fluorescent samples. In the case of inorganic molecules, a 532 nm laser is often chosen to enhance sensitivity.

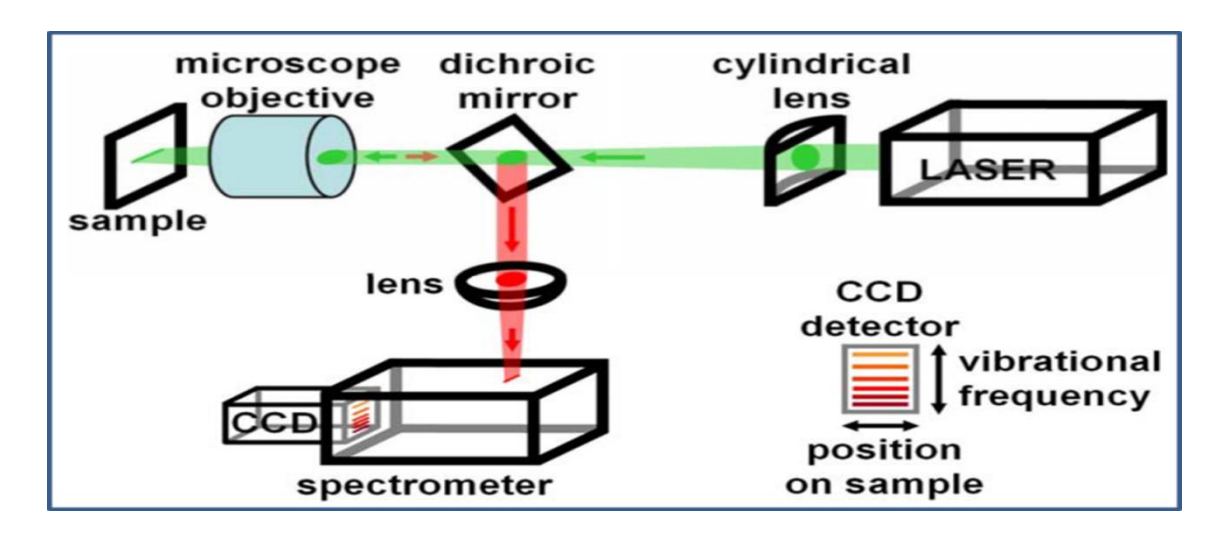


Figure 2.8: The basic block diagram of Raman spectrometer [28].

The sampling apparatus makes use of a fiber optic probe, which serves as a versatile interface. This probe can be brought into contact with solid samples, immersed in liquids or slurries, or connected to microscopes or cuvette holders. It provides flexibility in sample handling and positioning during measurements.

For effective detection of weak Raman scattering, the spectrometer must adhere to specific criteria including a compact design, high resolution capability, low power consumption, and minimal noise. These requirements ensure optimal performance in capturing and analyzing Raman scattering signals. In Raman spectroscopy, charge-coupled devices (CCDs) are commonly employed as detectors. Back-thinned CCDs are particularly advantageous as they offer increased sensitivity, making them suitable for detecting very low concentrations or weak Raman scattering.

#### 2.3.1.4 Field emission scanning electron microscopy (FE-SEM)

The FE-SEM (Field-Emission Scanning Electron Microscope) is a widely used instrument for high-resolution analysis of surface microstructures. Unlike traditional optical microscopes that use photons, the FE-SEM employs electrons for imaging. The microscope works on the principle of raster scanning a high-energy electron beam over the sample surface.

#### Working principle

These electrons are accelerated by an electric field and focused using electromagnetic lenses to form a narrow beam as shown in **Figure 2.9a** Schematic of FE-SEM. The beam is then directed onto the sample surface. When primary electrons interact with atoms within the sample, energy loss occurs, resulting in the production of various types of electrons. This interaction ultimately leads to the emission of secondary electrons from the sample. These secondary electrons carry valuable information about the surface topography and composition of the material.

#### Working of instrument

The detector in the microscope processes the secondary electrons and generates an electric signal. This signal is amplified and transformed into an image. The FE-SEM instrument consists of several main components, including an electron gun, anode (accelerator), magnetic lenses, a sample holder, and a detector. To operate the FE-SEM, the gun head, column, and specimen chamber need to be evacuated. Once the pressure is suitable for operation, the column chamber valve is closed. Nitrogen gas is then introduced into the specimen chamber through a vent valve. Prior to mounting on a special holder, the samples must be made conductive by coating them with a thin layer of electrically conducting metal such as gold, platinum, or silver [29]. This conductive layer prevents charging of the specimen, reduces thermal damage, and increases the signal-to-noise ratio.

The FE-SEM uses high-energy primary electrons, generated by applying a voltage difference between a tungsten filament (cathode) and an anode. The primary electrons are accelerated towards the sample, typically with a voltage ranging from 0.5 to 30 kV. The microscope operates under high vacuum conditions (around 10-6 Pa).

Electromagnetic lenses focus the electron beam to a small spot, and the condenser lens controls the amount of magnification. The objective lens then focuses the electron beam onto the specimen.

When the electron beam strikes the sample surface, it interacts with the atoms and penetrates a few microns into the sample, scattering in various ways depending on factors such as atomic number, atom concentration, and the energy of the primary electrons [30]. The scattered electrons and their interactions are collected by a detector and separated based on their energy values. Backscattered and secondary electrons are utilized to create a sample image by amplifying and transforming the signals.

Moreover, the interaction of primary electrons with inner shell electrons can lead to the emission of characteristic X-rays. Each element in the sample produces its own set of characteristic X-rays, which can be used for elemental composition analysis through energy-dispersive X-ray spectroscopy (EDAX) coupled to the FE-SEM instrument [31].

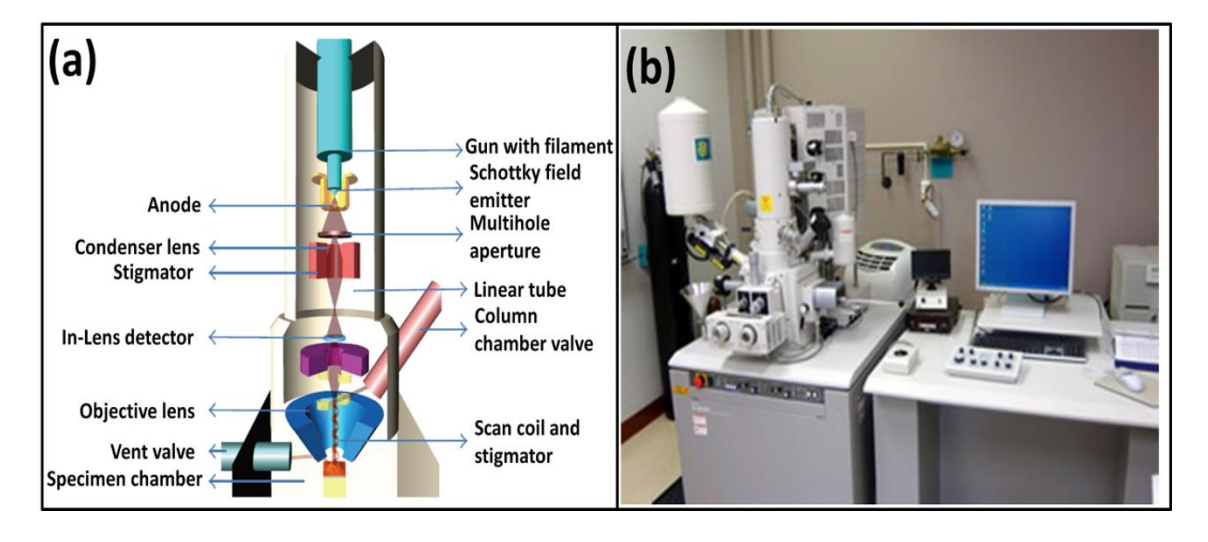


Figure 2.9: a) Schematic of FE-SEM [32], and b) photograph of FE-SEM instrument [33].

#### 2.3.1.5 X-ray photoelectron spectroscopy (XPS)

X-ray Photoelectron Spectroscopy (XPS) is a powerful chemical analysis method primarily employed to analyze the surface composition of materials and determine the oxidation states of the elements within them. XPS allows for the characterization of a shallow depth of the sample, typically ranging from 1 to 10 nanometers. This technique is based on Einstein's photoelectric effect, which states that

when electromagnetic radiation interacts with a material, it causes the emission of electrons, known as photoelectrons.

### Working principle

The absorption of incident X-rays by an atom can lead to the ejection of an inner shell electron through the photoelectric effect, as depicted in Figure 2.10. The resulting kinetic energy of these photoelectrons is measured and used to determine the binding energy of the electron. The binding energy can be calculated using the following formula:

$$E_{binding} = E_{photon} - (E_{kinetic} + \varphi)$$
 (2.5)

Here, the work function  $(\varphi)$  represents the minimum energy required to remove an electron from the atom's inner shell. By analyzing the count of photoelectrons at different binding energies, it becomes possible to deduce the composition of the sample and identify the various oxidation states of the elements present within it.

### **Working of instrument**

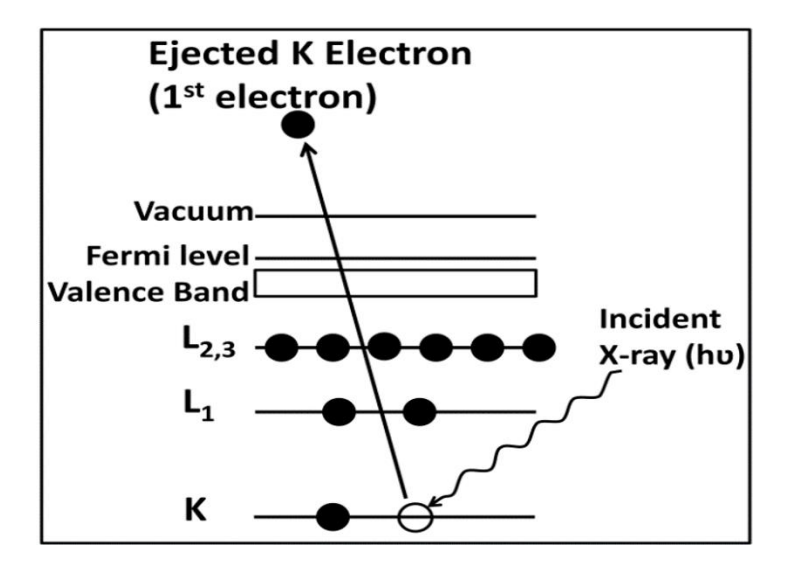


Figure 2.10: Atomic model of the working principle of XPS.

In X-ray Photoelectron Spectroscopy (XPS), a specialized instrument like the Thermo Fisher Scientific K-alpha XPS system is utilized. The process involves the generation of X-rays, typically  $MgK\alpha$  and  $AlK\alpha$ , by an X-ray source. These X-rays are then passed through a monochromator within a high vacuum, which ensures their precise wavelength selection. The monochromatized X-rays are directed towards the

surface of the sample, leading to the excitation of electrons within the atoms present in the sample. These excited electrons are subsequently detected by an electron detector, which not only counts the incoming electrons but also measures their kinetic energy.

The recorded kinetic energy data is then represented in the form of a spectrum, where specific energy values correspond to the presence of particular elements within the sample. By analysing this spectrum, researchers can determine the elemental composition of the sample under investigation. For the present study, the X-ray photoelectron spectroscope chosen is the Thermo Fisher Scientific K-alpha XPS system, based in the United Kingdom.

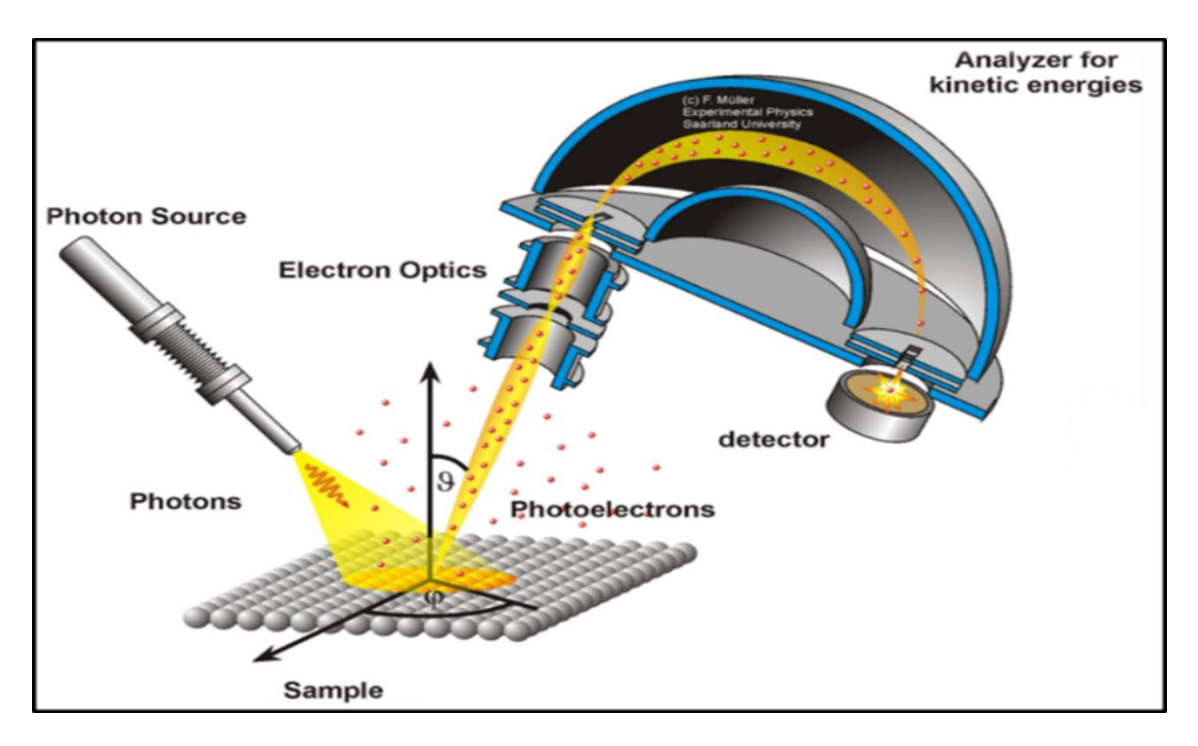


Figure 2.11: Schematic diagram of an XPS instrument [34].

### 2.3.1.6 Contact angle measurement

The contact angle is an important factor in determining the wettability of thin film surfaces and serves as a valuable tool for their characterization. It also enables the calculation of surface free energy. Wettability refers to how well a material can interact with a liquid. Figure 2.12a displays a photograph of the Rame-Hart NRL contact angle meter, while Figure 2.12b presents an image illustrating the contact angle formed by a liquid sample on a solid thin film surface.

The contact angle is a measurement that indicates the angle between the surface of a solid and a tangent drawn to the surface of a liquid. It is commonly used to assess the wetting properties of surface. When contact angle exceeds 90°, surface is considered hydrophobic, meaning it is less prone to wetting. A super hydrophobic surface has contact angle above 170° [36]. Conversely, when contact angle is less than 90°, the surface is hydrophilic and more prone to wetting. A super hydrophilic surface has a contact angle below 5°. Several methods are available to measure the contact angle. The

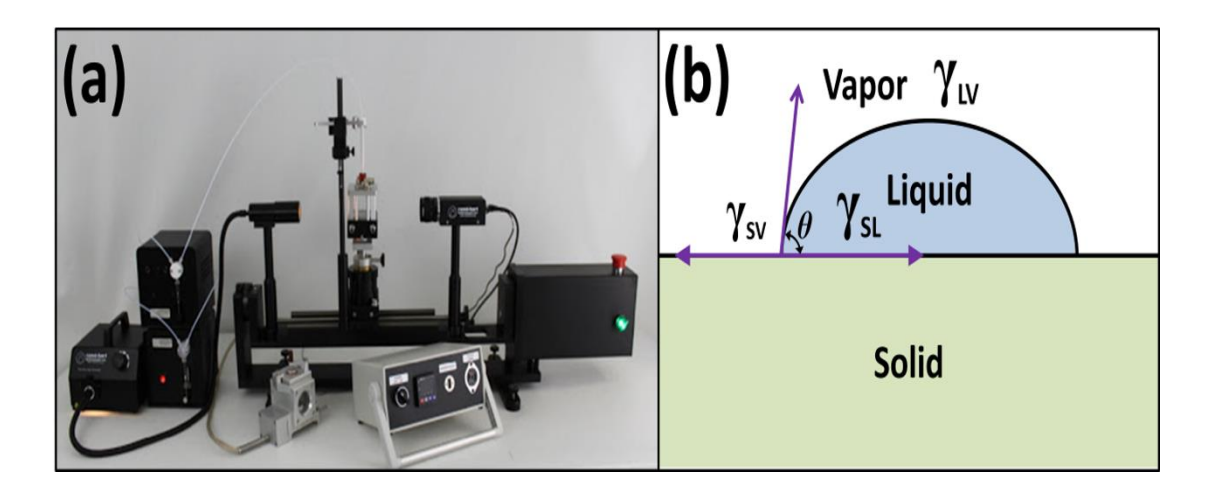


Figure 2.12: a) Image of the Rame-Hart NRL contact angle meter [35], and b) measurement of contact angle between a liquid and a solid sample.

contact angle  $(\theta)$  can be calculated using Young's relation [37] when the three phases (solid, liquid, and vapor) are in equilibrium:

$$\gamma(s,v) = \gamma(s,l) + \gamma(l,v) * \cos\theta$$
 (2.6)

In this equation,  $\gamma_{-}(s,v)$  represents solid-vapor interfacial energy,  $\gamma_{-}(s,l)$  represents solid-liquid interfacial energy, and  $\gamma_{-}(l,v)$  represents liquid-vapor interfacial energy. In the current study, contact angle images of deposited thin film electrodes were captured using a Rame-Hart goniometer (model 260).

### 2.3.1.7 Brunauer-Emmett-Teller (BET) analysis

The specific surface area of a prepared sample can be determined through the physical adsorption of a gas on surface of thin film material and the measurement of the amount of adsorbate gas. The gas not only adsorbs on the surface but also in the pores of the specimen, providing information about the pore size structure.

### Working principle

The BET (Brunauer-Emmett-Teller) method is a popularly employed procedure for determining specific surface area, commonly employing nitrogen gas as the adsorbate [38]. This technique utilizes either gravimetric or volumetric techniques to assess the adsorption isotherm. In both approaches, the adsorbent is kept at a consistent temperature close to the boiling point of the adsorptive. The pressure of the adsorptive is gradually raised and maintained steady for a specific duration, enabling adsorption and temperature reequilibration.

In the volumetric method, the pressure change is measured and compared to the expected pressure change in the absence of adsorbent. On the other hand, the gravimetric method relies on measuring the mass gain, which indicates the amount of adsorbent. The resulting isotherm represents a plot of the amount adsorbed against the adsorptive pressure, typically expressed as the ratio of the adsorptive pressure (P) to the saturated vapor pressure (P0).

While the volumetric method is relatively simple and cost-effective, it may introduce some uncertainty in the results. In contrast, the gravimetric method offers higher accuracy and precision but requires more expensive instrumentation. There are six types of isotherms, and each combination of adsorbent and adsorbate has its own standard curve.

The isotherm types are as follows:

- Type I: This isotherm occurs when chemisorption or physisorption takes place on a material with extremely fine pores.
- Type II: Nonporous and macroporous materials exhibit this isotherm when the energy of adsorption is high.
- Type III: Nonporous and macroporous materials exhibit this isotherm when the energy of adsorption is low.
- Type IV: The described isotherm is typically observed in mesoporous materials that exhibit a high energy of adsorption.
- Type V: This isotherm is observed for mesoporous materials with low energy of adsorption.

 Type VI: The origin of this isotherm can be attributed to several factors, including the adsorbate exhibiting solid-like behavior and forming structured layers at temperatures below the adsorptive triple point, as well as the presence of multiple pore sizes within the material.

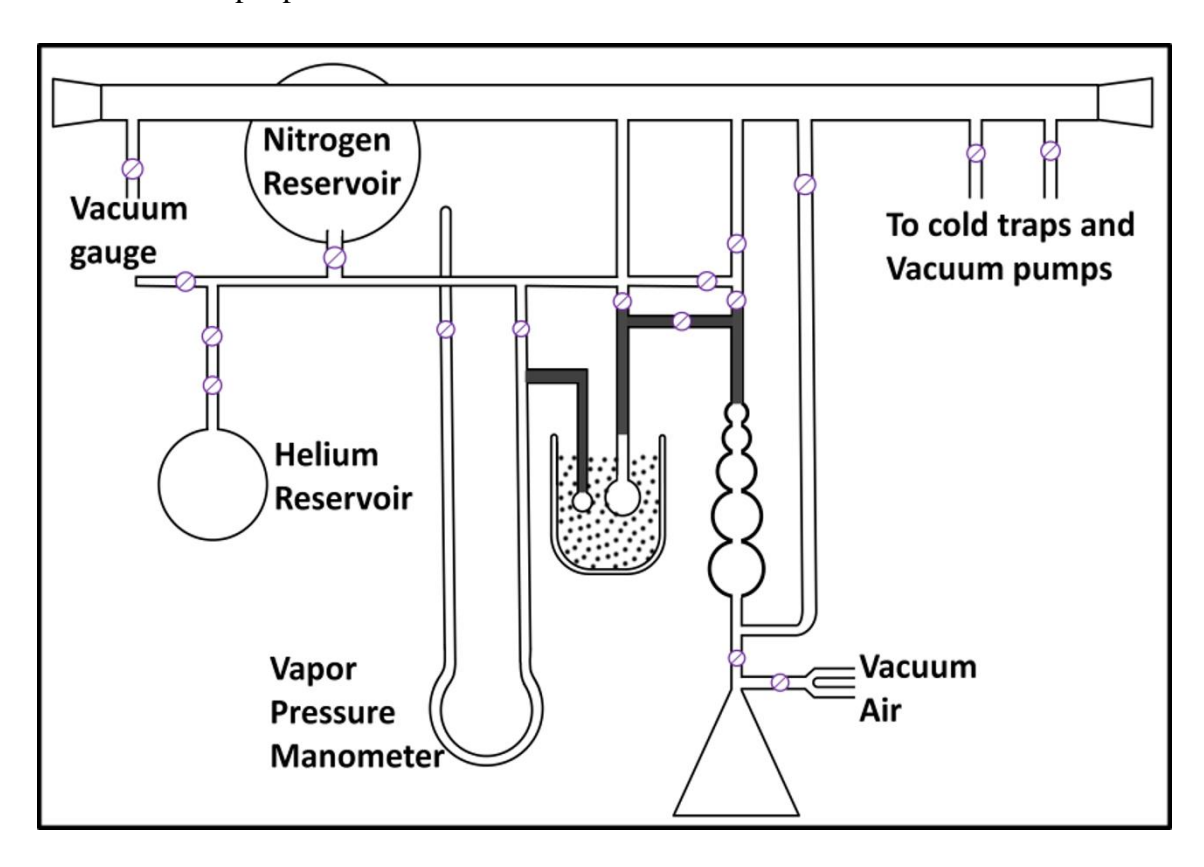


Figure 2.13: Schematic diagram of the dynamic flow method apparatus [39].

Hysteresis is the term used to describe the phenomenon where the desorption isotherm deviates from the adsorption isotherm. The International Union of Pure and Applied Chemistry (IUPAC) has defined four types of hysteresis loops: H1, H2, H3, and H4. It is important to note that hysteresis does not occur at relative pressures (P/P0) below a specific threshold. For nitrogen adsorption, this threshold value is 0.42.

To evaluate the specific surface area (As) using the cross-sectional area of the adsorbate molecule (a) and the number of moles of adsorbate in a monolayer (nm), the following equation is used:

$$A_{s} = n_{m} N_{A}a \tag{2.7}$$

here  $a = (M/\rho)^{2/3} NA^{1/3}$ , M is the molar mass (g mol<sup>-1</sup>),  $\rho$  is the liquid density (gm<sup>-3</sup>), and N<sub>A</sub> is Avogadro's number (6.022×10<sup>23</sup> mol<sup>-1</sup>).

### **Working of instrument**

There are two commonly used methods for determining surface area through physisorption: the volumetric method and the gravimetric method. In both methods, the adsorption process occurs at temperatures and pressures slightly below the boiling point of the gas used. The objective is to measure the amount of gas adsorbed onto the surface as a function of pressure. By analyzing the quantity of adsorbed gas and the corresponding pressure, various properties such as surface area, the strength of adsorption forces, and porosity can be calculated. The volumetric method, as depicted schematically in Figure 2.13 (not to scale), involves sample chambers typically made of Pyrex. The total surface area ( $S_T$ ) and specific surface area ( $S_B$ ) can be determined using the following equations:

$$S_T = \frac{v_m Ns}{V} \tag{2.8}$$

$$S_B = \frac{S_T}{a} \tag{2.9}$$

The equations 2.9 provide a means to calculate the total surface area and specific surface area by considering the properties of the adsorbing gas and the characteristics of the adsorbent material. The equations mentioned allow for accurate determination of the total surface area and specific surface area using the following symbols: S (adsorption cross section of the adsorbing species), N (Avogadro's number), Vm (molar volume of the adsorbate gas), and 'a' (mass of the adsorbent material) [40]. Utilizing these formulas provides an accurate means to calculate the total surface area and specific surface area.

### 2.3.2 Electrochemical characterization techniques

The scientific community has shown increased interest in electrochemical energy storage due to the need for diverse electrical energy storage devices designed for specific purposes, such as wearable and portable electronics, healthcare systems, and more. A Ragone plot (Figure 1.1) depicting the performance of electrochemical energy storage devices indicates that fuel cells have very high specific energy (SE), while capacitors have higher specific power (SP) compared to batteries and supercapacitors (SCs). SCs, along with batteries, bridge the gap between fuel cells and capacitors [41]. SCs, also known as supercapacitors, have garnered global research interest due to their

ability to support various designs according to specific requirements in fields such as aerospace, medical, military, and transportation.

SCs can be classified into different categories based on the mechanism of charge storage, configuration, or the physical state of the electrolyte. Based on charge storage mechanism, SC electrodes are classified as electrochemical double-layer capacitors (EDLCs) with a non-Faradaic mechanism, pseudocapacitors with a Faradaic mechanism, and battery-type capacitors. In terms of configuration, SCs can be symmetric or asymmetric, while based on the physical state of electrolytes, they can be classified as liquid-state or solid-state [42]. A typical configuration of an SC consists of two conducting electrodes separated by a porous membrane immersed in an appropriate electrolyte.

The specific capacitance  $(C_s)$ , specific capacity (C), and areal capacitance  $(C_a)$  of an SC device can be determined using the following relations:

• Specific capacitance 
$$(C_s) = \frac{1}{m \upsilon \Delta V} \int_{V_1}^{V_2} I(V) dV$$
 (CV study) (2.10)

• Areal capacitance 
$$(C_a) = \frac{1}{a_V \Delta V} \int_{V_1}^{V_2} I(V) dV$$
 (CV study) (2.11)

• 
$$C_{\rm S} = \frac{I \times t}{m \times \Delta V}$$
 (GCD study) (2.12)

• 
$$C_a = \frac{I \times t}{a \times \Delta V}$$
 (GCD study) (2.13); and

• Specific capacity (C) = 
$$\frac{C_S \times \Delta V}{3600}$$
 (2.14)

In these equations,  $\int_{V_1}^{V_2} I(V) dV$  represents the area enclosed in a CV curve, m (g) is the deposited mass of the material on both electrodes, v (V s<sup>-1</sup>) is the potential scan rate,  $\Delta$ V (V) is the operational potential window, I (A) is the current response, a (cm<sup>2</sup>) is the area of the SC, and t is the discharge time. Additionally, the SE and SP of an SC can be calculated using Equations (1.4) and (1.5) respectively. To achieve higher values of SE and SP, the working voltage and  $C_s$  of the SC must be large with lower interfacial resistance [43]. However,  $C_s$  and working voltage depend on the combination of electrode and electrolyte materials used in SC fabrication.

EDLC (Electric Double Layer Capacitor) materials typically operate up to 1 V in water-based electrolytes. However, in organic electrolytes, the potential window can

be extended to 2.5 V (sometimes up to 3.0 V). In EDLCs, the electrode material conducts electricity, while the electrolyte facilitates the formation of an electric double layer at the electrode-electrolyte interface. The charge storage in an EDLC-type supercapacitor, as shown in **Figure 2.14a**, can be described by the following equation:

$$Es_1 + Es_2 + K^+ + A^- \leftrightarrow Es_1 - / / K^+ + E_{s2}^+ / / A^-$$
 (2.15)

Here, Es1 and Es2 represent the specific surface areas of the negative and positive electrodes, respectively. The "//" symbol indicates the electric double layer where charges are stored on either side. K<sup>+</sup> and A<sup>-</sup> refer to the cations and anions present in the electrolyte. In EDLCs, the charging and discharging processes are attributed to the adsorption and desorption of ions, and no charge transfer occurs at the electrode-electrolyte interface. The electrodes in EDLCs are chemically inert, hence this process is referred to as non-Faradaic [44]. Pseudocapacitance, on the other hand, arises from fast and reversible redox reactions that occur at the interface between the electrode and electrolyte. It contributes to the charge storage in addition to the double layer capacitance. Figure 2.14b-d illustrates different charge storage mechanisms observed in pseudocapacitive materials. In the Faradaic process, charges are transmitted not only on the electrode material surface but also within the bulk of the electrode material during

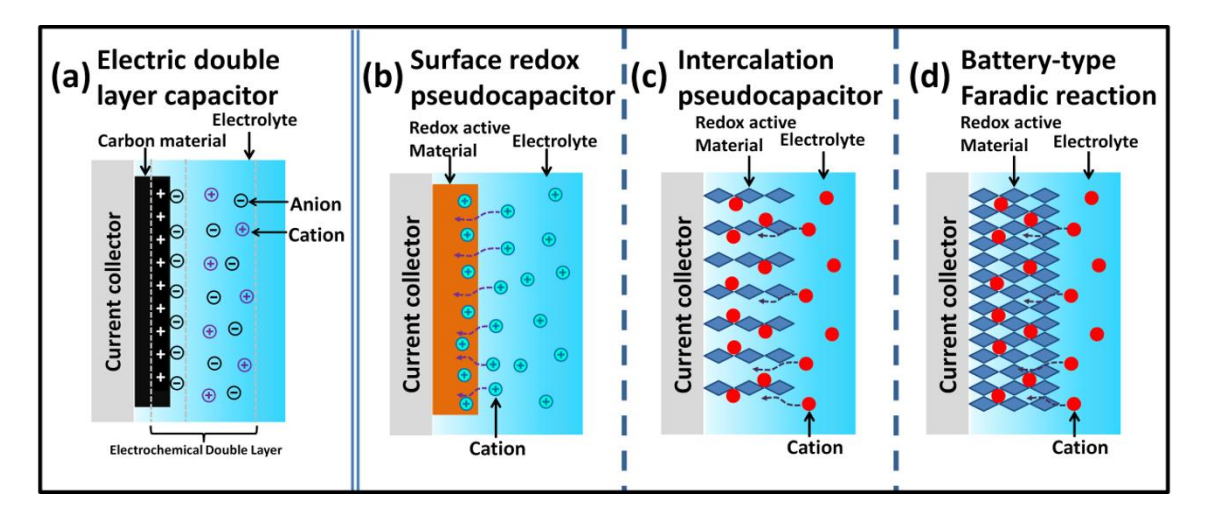


Figure 2.14: Schematics of charge-storage mechanisms for a) an EDLC [46] and (b-d) different types of pseudocapacitive electrodes: b) surface redox pseudocapacitors, c) intercalation pseudocapacitor, and d) battery-type Faradaic reaction [47].

charging and discharging [45]. Pseudocapacitors store charges through a two-step process. First, charges accumulate on the surface of the electrode material, and then a redox reaction occurs both on the electrode surface and within its bulk. These processes are highly dependent on the applied potential, thus pseudocapacitance varies with potential. To better understand the electrochemical properties of electrode materials, measurements such as cyclic voltammetry (CV), galvanostatic charge-discharge (GCD), and electrochemical impedance spectroscopy (EIS) are necessary. These measurements provide valuable information for the application of thin films as active electrodes in supercapacitor devices. Therefore, understanding the electrochemical characteristics of the electrode material is crucial.

### 2.3.2.1 Cyclic voltammetry (CV)

Cyclic voltammetry (CV) is an invaluable experimental technique that offers extensive information and valuable insights into both the thermodynamic and kinetic aspects of numerous chemical systems. It serves as a fundamental characterization method, providing valuable data regarding the electroactivity of electrodes in different electrolyte solutions. CV involves performing a linear scan of the potential while periodically reversing the direction of the scan at specific potentials. This technique is commonly employed to investigate various electrochemical processes. During a CV measurement, a stationary electrode with a surface area of 1 cm<sup>2</sup> is immersed in an electrolyte solution. To minimize the impact of ohmic resistance, a three-electrode system is utilized. The working electrode and the reference electrode are connected by applying a potential, whereas the current is measured by connecting the working electrode to the counter electrode. This setup allows, accurate measurements and reliable analysis of electrochemical reactions.

CV measurement involves sweeping the potential within a specified range. When the voltage reaches the maximum potential limit, the scan direction is reversed, and the voltage is swept back to the minimum range. Figure 2.15 illustrates the CV curve for a reversible single electrode transfer reaction, with a potential limit between V2 and V1. The cathodic and anodic peak currents (I<sub>pc</sub> and I<sub>pa</sub>) represent the maximum current values, while the cathodic and anodic peak voltages (E<sub>pc</sub> and E<sub>pa</sub>) indicate the corresponding potential values of the electrode material. In CV measurement, the choice

of potential limit is crucial because it determines the oxidation and reduction positions on the CV curve. During charging, the electrode material transitions from one state to another, while the reverse direction leads to the electrode material returning to its initial state through a reduction process.

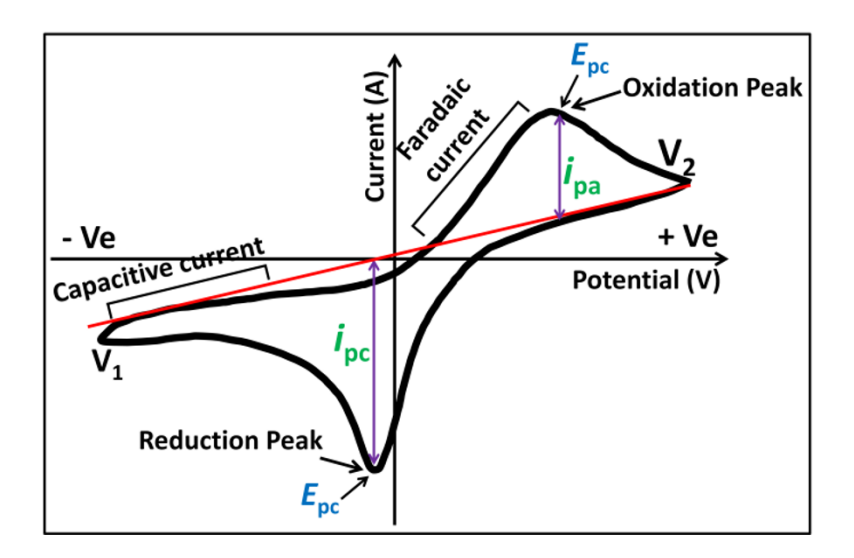


Figure 2.15: The typical cyclic voltammogram for a reversible single electron transfer reaction [48].

The CV technique finds extensive use in various fields. For example, it is employed in studying metal-ligand interactions, where electron pair transfer results in the formation of complex compounds. Additionally, CV is applied in the analysis of solids [49], solutions, polymers [50] (with or without added supporting electrolytes), membranes [51], frozen solutions, emulsions, suspensions [52], liquid-liquid systems [53], and biological systems such as enzymes [54].

### 2.3.2.2 Galvanostatic charge-discharge (GCD)

In the GCD technique, a constant current is supplied to the working electrode, while the potential is recorded over time by the reference electrode. Initially, the potential undergoes a sudden change due to the potential drop, after which it gradually changes over time. This behaviour is depicted in **Figure 2.16**, which shows the charge-discharge curve of a supercapacitor. The gradual change in potential is attributed to the depletion of reactant concentration at the electrode surface **[55, 56]**.

The discharge potential drop resulting from solution and interfacial resistance can be mitigated by applying a constant potential offset. By examining the characteristics of the charge-discharge curve, we can ascertain the type of charge storage mechanism taking place in the sample electrode. If the charge-discharge curve displays a symmetric shape, it suggests that the charge storage is primarily attributed to

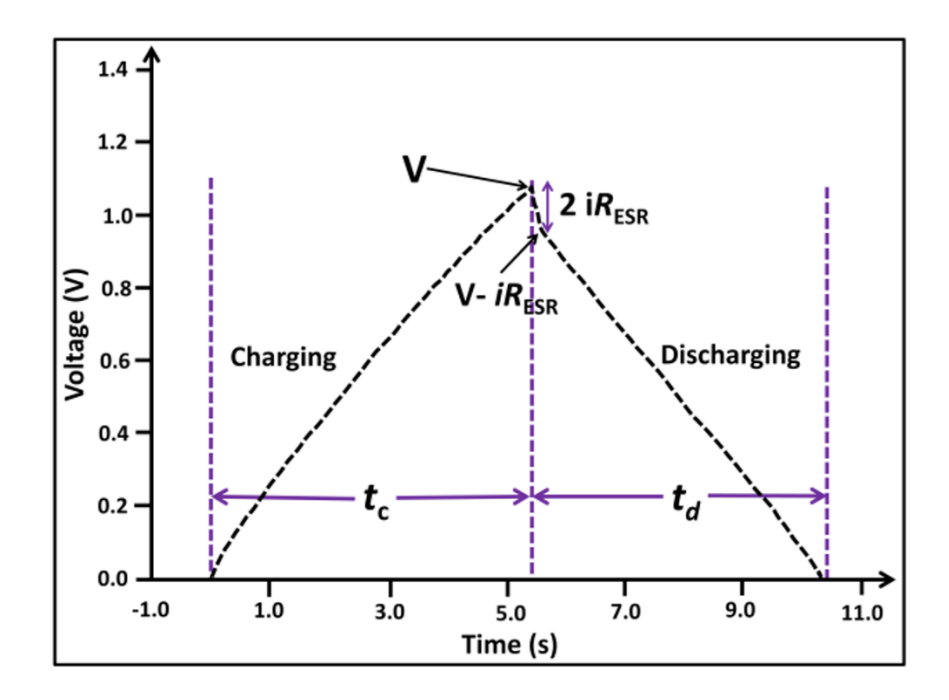


Figure 2.16: Charge discharge curves of a SC [57].

the double-layer mechanism. However, if this is not the case, it indicates that the charge storage is likely due to the pseudocapacitive mechanism [58, 59]. Furthermore, conducting galvanostatic charge-discharge (GCD) analysis is crucial for determining the specific energy (SE) and specific power (SP) of the supercapacitor (SC).

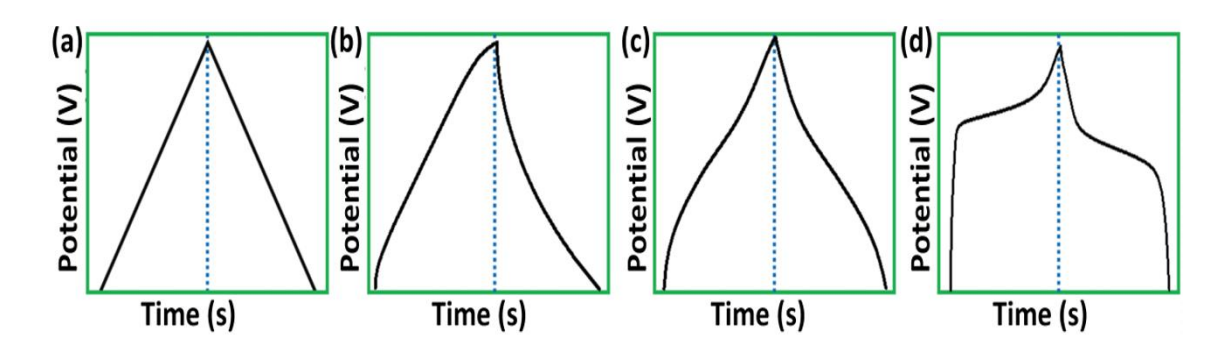


Figure 2.17: Representative shapes of GCD curves: a) EDLC, b) surface redox capacitance, c) intercalation capacitance, and d) Faradic battery-type [60].

### 2.3.2.3 Electrochemical impedance spectroscopy (EIS)

The EIS technique, also known as AC impedance spectroscopy, is used to study the charge storage mechanism at an electrode-electrolyte interface. It involves applying a small AC signal (usually 5 to 10 mV) across a supercapacitor cell at a wide range of frequencies, typically from 1 mHz to 1 MHz. The resulting current response to the applied AC signals is measured.

The Nyquist plot, which is a plot of imaginary impedance against real impedance, is commonly used to analyse the data obtained from EIS measurements [61, 62]. This plot provides valuable information about the resistive parameters of the system, both frequency-independent and frequency-dependent. In the EIS measurement, if a sinusoidal voltage input signal  $V(\omega) = V_0 \sin(\omega t)$  and its corresponding output response is  $I(\omega) = I_0 \sin(\omega t + \phi)$ , then the impedance of the electrode material can be calculated as,

$$Z(\omega) = \frac{V(\omega)}{I(\omega)} = \frac{V_0 \sin(\omega t)}{I_0 \sin(\omega t + \emptyset)} = Z_0 \frac{\sin(\omega t)}{\sin(\omega t + \emptyset)}$$
(2.16).

where  $Z_0$  represents the magnitude of the impedance and  $\varphi$  represents the phase shift.

The Nyquist plot, depicted in Figure 2.18, shows the real and imaginary parts of the impedance. Additionally, the Figure includes an inset diagram illustrating a general equivalent circuit known as the Randles cell, which is associated with the Nyquist plot.

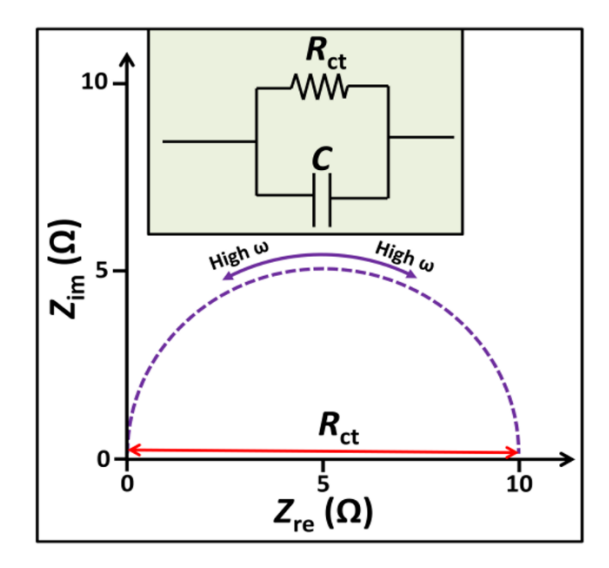


Figure 2.18: Nyquist plot with electrical equivalent circuit consisting charge  $R_{ct}$  in parallel with C [63].

In the Nyquist plot, the charge transfer resistance (R<sub>ct</sub>) represents the resistance to the transfer of charges at the electrode-electrolyte interface [Figure 2.18]. This resistance is dependent on factors such as reaction type, temperature, concentration, and potential of the reaction products. Since the series resistance (R<sub>s</sub>) of the electrochemical cell is usually negligible, the Nyquist plot intercepts at the origin of the Z<sub>re</sub> axis. However, every electrochemical cell has a small internal resistance, causing the first intercept of the Nyquist plot to be on the positive side of the Z<sub>re</sub> axis. This provides the value of the equivalent series resistance (R<sub>s</sub>) [Figure 2.19a]. R<sub>s</sub> is in series with R<sub>ct</sub>. In the lower frequency region, the diffusion of electrolyte ions contributes to an additional component in the equivalent circuit, represented by the Warburg impedance (W). The Warburg impedance reflects the resistance to the diffusion of reactants and is characterized by a straight line in the Nyquist plot [Figure 2.19b]. The value of capacitance can also be determined as a function of frequency using EIS measurements. Overall, EIS is a valuable technique for studying the charge storage mechanism at electrode-electrolyte interfaces, allowing for the determination of various resistive parameters of the system using a wide range of frequencies.

At low frequencies, a supercapacitor behaves primarily as a resistor, while at high frequencies, it behaves primarily as a capacitor. However, in the medium frequency range, the capacitance value of a supercapacitor is influenced by the physical and morphological properties of the electroactive material. In this range, the supercapacitor can be considered as a combination of resistors and capacitors, with the specific properties of the material playing a crucial role.

Experimental data obtained from measurements can be fitted with various interface parameters and algorithms to accurately model the behaviour of the supercapacitor. The fitted parameters and algorithms help in characterizing and understanding the electroactive material's properties, such as its capacitance.

In the context of impedance spectroscopy, the Nyquist plot provides valuable information about the supercapacitor's behaviour. The equivalent circuit corresponding to the Nyquist plot can be represented by an inset circuit, which serves as a graphical representation of the impedance response of the supercapacitor across different frequencies.

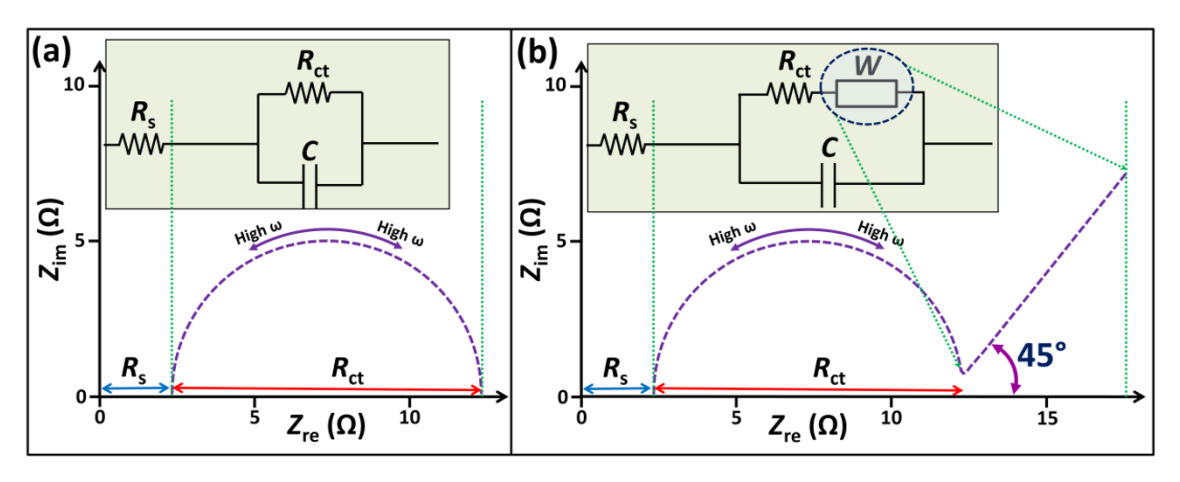


Figure 2.19: Nyquist plots with corresponding electrical equivalent circuit a) consisting  $R_s$ ,  $R_{ct}$  and C, and b) consisting  $R_s$ ,  $R_{ct}$ , C, and W [64].

The sinusoidal voltage and current signals are written as,

$$V(w) = V_0 e^{(iwt)}$$
 (2.17)

$$I(w) = I_0 e^{(iwt - \emptyset)}$$
 (2.18)

The complex quantity is written as,

$$Z(w) = Z_0 e^{i\emptyset} = Z_0 e^{(\cos\emptyset + i\sin\emptyset)}$$
 (2.19)

The expression for  $Z(\omega)$  is composed of a real and an imaginary part.

The ZIVE MP1 electrochemical workstation was used to carry out the electrochemical tests as outlined in section 2.3.2. The data collected from these tests served the purpose of assessing diverse electrochemical characteristics, including Cs (specific capacitance), SE (equivalent series resistance), SP (parallel resistance), Rs (series resistance), and Rct (charge transfer resistance). During the electrochemical impedance spectroscopy (EIS) measurements, an alternating current (AC) amplitude of 5 mV was employed across a frequency range spanning from 0.01 Hz to 0.1 MHz. These measurements were executed at the bias potential corresponding to the open circuit potential.

For the analysis of the EIS data and the subsequent derivation of an equivalent circuit, the "ZSimpWin" editor was utilized. This software tool facilitated the fitting and examination of impedance data, leading to the formulation of an equivalent circuit model that accurately represents the electrical behavior of the supercapacitor or electrochemical system under investigation.

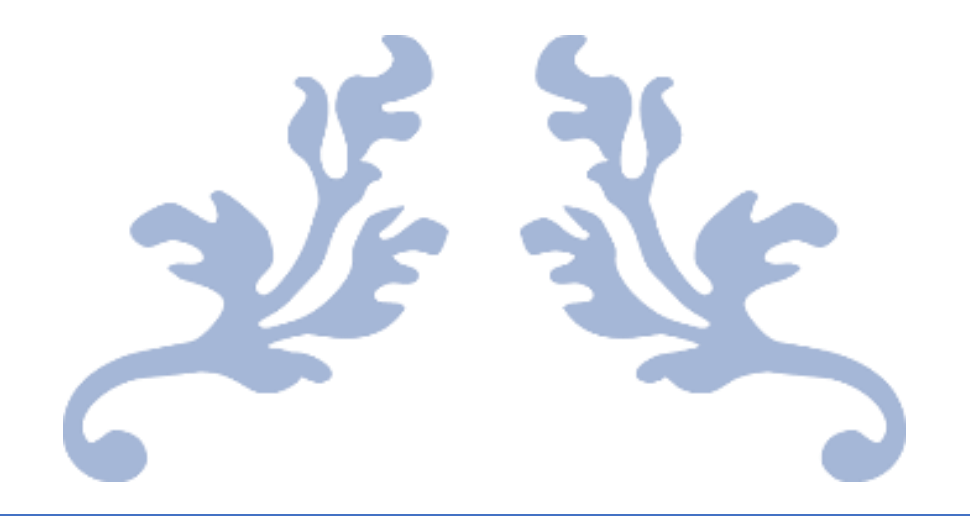
### **References:**

- [1] S. V. Ganachari, N. R. Banapurmath, B. Salimath, J. S. Yaradoddi, A. S. Shettar, A. M. Hunashyal, A. Venkataraman, P. Patil, H. Shoba, Gurusiddesh B. Hiremath, Handbook of ecomaterials, Springer, Cham., 2017,1.
- [2] L. E. Murr, Handbook of materials structures, Properties, Processing and Performance, 2016, 1.
- [3] M. Benelmekkia, A. Erbe, Nanostructured thin films, 14, 2019, 1.
- [4] R. D. Gould, S. Kasap, A. K. Ray, Thin Films, Springer Handbook of Electronic and Photonic Materials, 2017.
- [5] L. B. Freund, S. Suresh, Thin film materials, Cambridge University Press, Cambridge, UK, 2008.
- [6] A. Rockett, The materials science of semiconductors, Springer US, Boston, 2008, 289.
- [7] C. D. Lokhande, Chemical deposition of metal chalcogenide thin films, Mater. Chem. Phys., 28, 1991, 45.
- [8] Z. Cao, Thin Film Growth, Woodhead publishing series in electronic and optical materials, 2011, 185.
- [9] J. L. Robins, Thin film nucleation and growth kinetics, Appl. Surf. Sci., 33/34, 1988, 379.
- [10] M. Ristov, G. J. Sinadinovski, I. Grozdanov, Chemical deposition of Cu<sub>2</sub>O thin films, Thin solid films, 123, 1985, 63.
- [11] Y. F. Nicolau, J. C. Menard, growth mechanism, J. Cryst. Growth, 92, 1988, 128.
- [12] Y. F. Nicolau, Appl. Surf. Sci., 22/23, 1985, 1061.
- [13] M. Birkholz, P. F. Fewster, C. Genzel, Thin film analysis by X-ray scattering, Wiley-VCH, 2006, 1.
- [14] V. Petkov, Nanostructure by high-energy X-ray diffraction, Mater. Today, 11, 2008, 28.
- [15] http://xrd.co/component-parts-x-ray-diffractometer.
- [16] https://www.rigaku.com/products/xrd/miniflex.
- [17] B. D. Cullity, "Elements of X-rays Diffraction", Second ed., Addison-Wesley, London, 1978.
- [18] https://www.findlight.net/blog/2019/03/27/ftir-principles-applications/

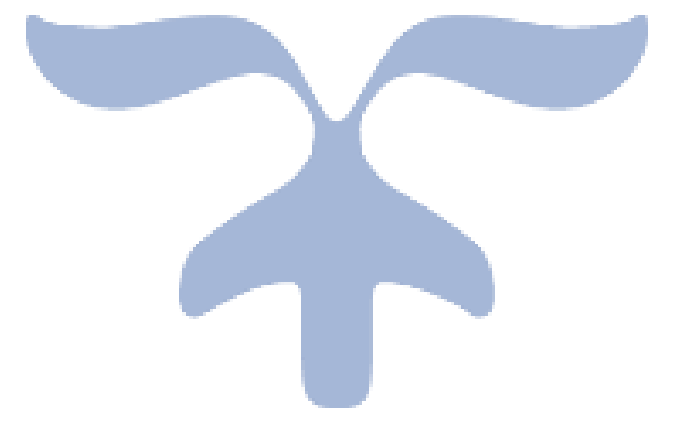
- [19] https://www.sigmaaldrich.com/technical-documents/articles/biology/ir-spectrum-table.html#ir-table-by-compound.
- [20] https://www.bruker.com/products/infrared-near-infrared-and-raman-spectroscopy/ft-ir-routine-spectrometers/compact-ftir-alpha-ii.html.
- [21] A. Munajad, C. Subroto, Suwarno, Fourier transform infrared (FTIR) spectroscopy analysis of transformer paper in mineral oil-paper composite insulation under accelerated thermal aging, Energies, 11, 2018, 364.
- [22] https://en.wikipedia.org/wiki/Raman\_spectroscopy.
- [23] I. J. D. Ebenezar, S. Ramalingam, C. R. Raja, P. C. J. Prabakar, Vibrational spectroscopic [IR and Raman] analysis and computational investigation [NMR, UV-Visible, MEP and Kubo gap] on L-Valinium Picrate, J. Nano. Adv. Mat., 2, 2014, 11.
- [24] J. A. Breier, S. N. White, C. R. German, Mineral-microbe interactions in deep-sea hydrothermal systems: a challenge for Raman spectroscopy, Phil. Trans. R. Soc. A, 368 (2010) 3067.
- [25] A. Downes, A. Elfick, Raman spectroscopy and related techniques in biomedicine, Sensors, 10, 2010, 1871.
- [26] https://bwtek.com/raman-components-of-a-raman-spectrometer/
- [27] https://www.mt.com/in/en/home/applications/L1\_AutoChem\_Applications/Rama n-Spectroscopy.html
- [28] H. Vašková, International journal of mathematical models and methods in applied sciences, 5, 2011, 1205,
- [29] https://www.naun.org/main/NAUN/ijmmas/17-120.pdf.
- [30] <a href="https://www.thermofisher.com/blog/microscopy/sputter-coating-for-sem-how-this-sample-preparation-technique-assists-your-imaging/">https://www.thermofisher.com/blog/microscopy/sputter-coating-for-sem-how-this-sample-preparation-technique-assists-your-imaging/</a>
- [31] A. Mayeen, L. K. Shaji, A. K. Nair, N. Kalarikkal, Advances and key technologies, micro and nano technologies, 2018, 335.
- [32] https://www.hitachi-hightech.com/global/science/products/microscopes/electron-microscope/fe-sem/.
- [33] http://mcff.mtu.edu/acmal/electronmicroscopy/FE\_Form\_Function.html.
- [34] Y. Jusman, S. C. Ng, N. A. A. Osman, Sci. World J., 2014, 1.
- [35] <a href="https://epm.univie.ac.at/fileadmin/user\_upload/p\_epm/xps-machine.png">https://epm.univie.ac.at/fileadmin/user\_upload/p\_epm/xps-machine.png</a>.
- [36] http://www.ramehart.com/790.htm.

- [37] M. M. Vadiyar, S. C. Bhise, S. K. Patil, S. S. Kolekar, A. Shelke, N. Deshpande, J. Chang, K. Ghule, A. V. Ghule, Chem. Commun., 52, 2016, 2557.
- [38] T. T. Chau, W. J. Bruckard, P. T. L. Koh, A. V. Nguyen, Adv. Colloid Interface Sci., 150, 2009, 106.
- [39] P. Sinha, A. Datar, C. Jeong, X. Deng, Y. G. Chung, L. Lin, J. Phys. Chem. C, 123, 2019, 20195.
- [40] http://www.pharmacopeia.cn/v29240/usp29nf24s0\_c846.html.
- [41] D. P. Lapham, J. L. Lapham, Int J Pharm., 568, 2019, 118522.
- [42] A. C. Forse, C. Merlet, J. M. Griffin, C. P. Grey, J. Am. Chem. Soc., 138, 2016, 5731.
- [43] A. Afif, S. M. Rahman, A. T. Azad, J. Zaini, M. A. Islan, A. K. Azad, J. Energy Storage, 25, 2019, 100852.
- [44] Y. Wu, C. Cao, Sci. China Mater., 61, 2018, 1517.
- [45] J. Park, B. Kim, Y. Yoo, H. Chung, W. Kim, ACS Appl. Mater. Interfaces, 6, 2014, 19499.
- [46] S. D. Perera, X. Ding, A. Bhargava, R. Hovden, A. Nelson, L. F. Kourkoutis, R. D. Robinson, Chem. Mater., 27, 2015, 7861.
- [47] Y. Shao, M. F. El-Kady, J. Sun, Y. Li, Q. Zhang, M. Zhu, H. Wang, B. Dunn, R. B. Kaner, Chem. Rev., 118, 2018, 9233.
- [48] V. Augustyn, P. Simon, B. Dunn, Energy Environ. Sci., 7, 2014, 1597.
- [49] V. Climent, J. M. Feliu, Annu. Rev. Anal. Chem., 13, 2020, 201.
- [50] M. V. Portales, A. R. L. Fraga, A. M. D. García, O. García-Zaldívar, A. P. Barranco, M. A. A. Frutis, , J. Solid State Electrochem., 22, 2018, 471.
- [51] A. Wardak, H. T. Tien, Bioelectrochem. Bioenerg., 24, 1990, 1.
- [52] H. Qu, M. Harada, T. Okada, ChemElectroChem, 4, 2017, 35.
- [53] C. Peng, G. A. Snook, D. J. Fray, M. S. P. Shaffer, G. Z. Chen, Chem. Commun., 44, 2006, 4629.
- [54] R. J. Bushby, O. R. Lozman, L. A. Mason, N. Taylor, S. Kumar, Mol. Cryst. Liq. Cryst., 410, 2004, 171.
- [55] D. Qazzazie, O. Yurchenko, S. Urban, J. Kieninger, G. Urban, Nanoscale, 9, 2017, 6436.
- [56] R. R. Salunkhe, Y. V. Kaneti, Y. Yamauchi ACS Nano, 11, 2017, 5293.

- [57] P. Veerakumar, A. Sangili, S. Manavalan, P. Thanasekaran, K. Lin, Ind. Eng. Chem. Res., 59, 2020, 6347.
- [58] B. K. Kim, S. Sy, A. Yu, J. Zhang, Handbook of Clean Energy Systems, 2015, 1.
- [59] K. S. Kumar, N. Choudhary, Y. Jung, J. Thomas, ACS Energy Lett., 3, 2018, 482.
- [60] K. Breitsprecher, C. Holm, S. Kondrat, ACS Nano, 12, 2018, 9733.
- [61] N. R. Chodankar, H. D. Pham, A. K. Nanjundan, J. F. S. Fernando, K. Jayaramulu, D. Golberg, Y. Han, D. P. Dubal, small, 16, 2020, 2002806.
- [62] B. Mei, O. Munteshari, J. Lau, B. Dunn, L. Pilon, J. Phys. Chem. C, 122, 2018, 194.
- [63] D. K. Kampouris, X. Ji, E. P. Randviira, C. E. Banks, RSC Adv., 5, 2015, 12782.
- [64] B. Mei, J. Lau, T. Lin, S. H. Tolbert, B. S. Dunn, L. Pilon, J. Phys. Chem. C, 122, 2018, 24499.



# SYNTHESIS AND CHARACTERIZATION OF NICKEL TUNGSTATE ELECTRODE BY SILAR METHOD



# SYNTHESIS AND CHARACTERIZATION OF NICKEL TUNGSTATE ELECTRODE BY SILAR METHOD

| Sr. No. |          | Title  | Page No. |
|---------|----------|--|----------|
| 3.1     | Introduc | etion  | 73       |
| 3.2     | Experim  | 74   |          |
|         | 3.2.1    | Cleaning of substrate                                | 74       |
|         | 3.2.2    | Chemicals  | 75       |
|         | 3.2.3    | Preparation of NiWO <sub>4</sub> thin film electrode | 75       |
|         | 3.2.4    | Growth mechanism of NiWO <sub>4</sub> thin film      | 76       |
| 3.3     | Materia  | l characterisations                                  | 77       |
|         | 3.3.1    | Physico-chemical characterisations                   | 77       |
|         | 3.3.2    | Electrochemical characterisations                    | 77       |
|         | 3.3.2.1  | CV study   | 77       |
|         | 3.3.2.2  | GCD study  | 78       |
|         | 3.2.2.3  | EIS study  | 78       |
| 3.4     | Results  | and discussion                                       | 78       |
| 3.4A    | Physico  | -chemical characterizations                          | 78       |
|         | 3.4A1    | XRD study  | 78       |
|         | 3.4A2    | FT-IR study  | 79       |
|         | 3.4A3    | Raman study  | 80       |
|         | 3.4A4    | FE- SEM study  | 80       |
|         | 3.4A5    | TEM study  | 82       |
|         | 3.4A6    | XPS study  | 82       |
|         | 3.4A7    | BET study  | 84       |
|         | 3.4A8    | Contact angle measurement                            | 85       |
| 3.4B    | Electroc | chemical characterisations                           | 85       |
|         | 3.4B1    | CV study   | 85       |
|         | 3.4B2    | GCD study  | 88       |
|         | 3.4B3    | EIS study  | 91       |
|         | 3.4B4    | Stability  | 92       |
| 3.5     | Conclus  | 92   |          |
|         | Referen  | 92   |          |

### 3.1 Introduction

In the present era, environmental pollution originating from burning of hydrocarbon fuels is affecting human health along with the surrounding nature. So, the shifting of energy generation and usage habits became the need of an hour. Renewable energy generation/conversion is convincing path for a pollution-free environment. The major challenges faced by these sources are storage of energy because of abruption in the generation. The capacitors, batteries, and supercapacitors (SCs) have been used for electrochemical energy storage from a long time, However, the cost and the energy stored by these devices vary with the design, chemistry, and materials used to fabricate. The specific energy for batteries is comparatively more than the SCs and capacitors [1, 2]. Due to outstanding cycle stability, greater power density, and rapid charge-discharge rate SCs are some of the better optimistic contenders [3, 4]. A significant drawback of SCs is that they are deficient in specific energy to fulfill the growing energy requirements for new-age energy storage equipment [5, 6]. Present-day, more research activities have been concentrated to enhance the specific energy of SCs without losing their specific power and cyclability [7, 8]. The specific energy (E= 0.5 CV<sup>2</sup>) can be raised by improving capacitance (C) and operating potential window (V). Different electroactive materials with rages of capacitance values have been used to fabricate SCs [9]. Hence, the preparation of novel electrode materials possessing high specific capacitance and fabrication of asymmetric supercapacitors (ASCs) to overcome the issue of low cell potential can result in enhanced specific energy.

Metal tungstates have the general formula AWO<sub>4</sub>, where A is a divalent cation (A<sup>2+</sup> = Ni, Fe, Mn, Cu, Co) that acts as a network modifier. The monoclinic crystal structure of metal tungstates (shown in **Figure 3.1a and b**) resembles with the crystal structure of metal sulfates [10]. Normally, metal tungstate materials were tested for SC applications [11], Li-ion battery [12], electrocatalysis [13], gas sensors [14], and photocatalyst [15]. These types of structures may provide facile access of interior sites to the electrolyte ions. Some of the previous reports suggest that nickel tungstate provides excellent performance for electrochemical energy storage. The nanocrystalline materials provide large electrochemical active sites due to chemical homogeneity, and structural flexibility. Due to these properties, nanocrystalline materials possess higher electrochemical stability. Over the past few years, various methods were used to synthesize nanocrystalline

materials such as sol-gel, microwave synthesis, co-precipitation, and electrodeposition [16]. Ikram et al. [17] reported hydrothermal method to prepare nickel tungstate with specific capacitance ( $C_s$ ) of 1524 F g<sup>-1</sup> at 0.5 A g<sup>-1</sup>. Pourmortazavi et al. [18] reported an electrochemical method for NiWO<sub>4</sub> preparation and achieved  $C_s$  of 468 F g<sup>-1</sup> at 2 mV s<sup>-1</sup>. Electrochemical properties of NiWO<sub>4</sub> prepared by hydrothermal method were reported by Packiaraj et al. [19]. The solvothermal synthesized NiWO<sub>4</sub> nanowires showed  $C_s$  of 1190 F g<sup>-1</sup> at 0.5 A g<sup>-1</sup> [20]. Niu et al. [21] synthesized amorphous NiWO<sub>4</sub> using coprecipitation method and achieved  $C_s$  of 586.2 F g<sup>-1</sup>. Xu et al. [22] reported preparation of NiWO<sub>4</sub>/reduced graphene film nanocomposite with  $C_s$  of 1031.3 F g<sup>-1</sup> for supercapacitor. It is found that the morphologies affect the supercapacitor performance. However, no literature is found on preparation of mesoporous and nanocrystalline NiWO<sub>4</sub> using SILAR method on conducting substrate and its application as an electroactive material for SCs so far.

Hence, in the current work, nanocrystalline NiWO<sub>4</sub> thin films with different morphologies were synthesized by changing concentrations of cations at room temperature through a SILAR method. Various characterization methods such as X-ray diffraction (XRD), FTIR, Field-emission scanning electron microscopy (SEM), energy dispersive spectrometry (EDS), X-ray photoelectron spectroscopy (XPS), high-resolution transmission electron microscopy (HR-TEM), and Raman spectroscopy were used for NiWO<sub>4</sub> characterization. Moreover, the electrochemical properties (CV, GCD, and EIS) of NiWO<sub>4</sub> film electrodes with different morphologies were inspected in 2 M KOH solution.

### 3.2. Experimental details

### 3.2.1 Cleaning of Substrate

To prepare high-quality thin films, it is crucial to ensure an extremely clean substrate surface when using chemical methods. Impurities present on the substrate surface can act as nucleation centers and negatively impact the quality of the thin films. The use of a conducting substrate is essential for SCs, and stainless steel (SS) substrates are ideal due to their high conductivity and low cost. The following procedure was employed to clean the SS substrates:

- a) The substrates were polished using zero-grade polishing paper.
- b) Subsequently, the substrates were cleaned with detergent and double distilled water (DDW).
- c) The cleaned substrates were then subjected to ultrasonic cleaning for a duration of 10 minutes.
- d) Finally, the substrates were air dried and deemed ready for the deposition process.

### 3.2.2 Chemicals

The analytical grade chemicals used were NiSO<sub>4</sub>·6H<sub>2</sub>O and Na<sub>2</sub>WO<sub>4</sub>.

### 3.2.3 Preparation of NiWO<sub>4</sub> thin film electrode

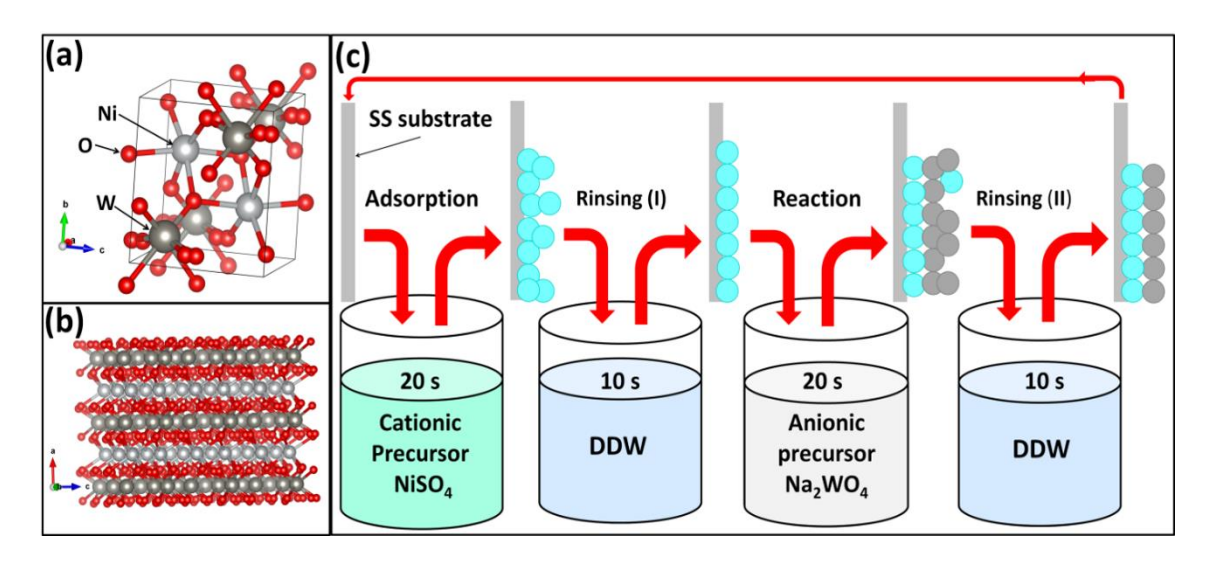


Figure 3.1: a) The crystal structure of NiWO<sub>4</sub> expanded along principal axis a and b plotted using Vesta software, b) unit cell of NiWO<sub>4</sub> crystal, and c) the schematic of SILAR method employed for NiWO<sub>4</sub> thin film electrode preparation.

The SILAR method was employed to deposit NiWO<sub>4</sub> thin films. Aqueous solutions of Na<sub>2</sub>WO<sub>4</sub>.2H<sub>2</sub>O and NiSO<sub>4</sub>.6H<sub>2</sub>O were used as tungstate (WO<sub>4</sub><sup>2-</sup>) and nickel ion (Ni<sup>2+</sup>) sources, respectively. The substrates were dipped in a precursor to adsorb Ni<sup>2+</sup> ion for 20 s followed by rinsing in DDW for 10 s to release feebly Ni<sup>2+</sup> attached ions. Thereafter, the substrate was immersed in an anionic precursor containing tungstate ions (WO<sub>4</sub><sup>2-</sup>) for 20 s, in which the pre-adsorbed Ni<sup>2+</sup> ions react with WO<sub>4</sub><sup>2-</sup> ions from the solution to form an insoluble solid compound NiWO<sub>4</sub> on the surface of SS substrates. Followed by, rinsing of SS substrates in DDW for 10 s to remove loosely attached NiWO<sub>4</sub>

nanoparticles. The schematic of a process employed in the synthesis of NiWO<sub>4</sub> thin films is shown in **Figure 3.1c**. In order to achieve different morphologies, the different thicknesses of films were achieved using different concentrations of Ni<sup>2+</sup> ion (0.05M, 0.1M, 0.15M, and 0.2M) while concentration of WO<sub>4</sub><sup>2-</sup> ion was kept constant at (0.1 M). The films prepared at concentrations of 0.05, 0.1, 0.15, and 0.2 M are denoted as N1, N2, N3, and N4, respectively. After deposition, thin films were calcined at a temperature 723 K in an inert atmosphere for 6 h and used for physical and electrochemical characterizations. The mass loading of nickel tungstate thin films is shown in **Figure 3.2a**. The mass of NiWO<sub>4</sub> thin films varies from 0.00057 g cm<sup>-2</sup> to 0.0061 g cm<sup>-2</sup> with concentration.

### 3.2.4 Growth mechanism of NiWO<sub>4</sub> thin film

The schematic of preparation procedure of NiWO<sub>4</sub> thin films by SILAR method is presented in **Figure 3.1c**. For synthesis, a four-beaker arrangement was used; the first beaker consists of a solution of nickel sulfate (NiSO<sub>4</sub>.6H<sub>2</sub>O). The concentration of NiSO<sub>4</sub>.6H<sub>2</sub>O varied from 0.05 M to 0.2 M with an aim to change rate of adsorption of the Ni<sup>2+</sup>. Then, the adsorbed ions react with tungstate ion (WO<sub>4</sub>)<sup>2-</sup> from anionic precursor (Na<sub>2</sub>WO<sub>4</sub>.2H<sub>2</sub>O) in the third beaker. In between adsorption and reaction, DDW in second and fourth beakers was used for rinsing purpose.

Dissociation reaction of NiSO<sub>4</sub> can be written as,

$$NiSO_4.6H_2O \leftrightarrow Ni^{2+} + (SO_4)^{2-} + 6H_2O$$
 (3.1)

A thin layer of Ni<sup>+2</sup> ions adsorbed on SS substrate after immersion of substrates in a cationic precursor solution. Moreover, Na<sub>2</sub>WO<sub>4</sub>.2H<sub>2</sub>O (anionic precursor) dissociates as per equation 3.2,

$$Na_2WO_4.2H_2O \leftrightarrow 2Na^{2+} + (WO_4)^{2-} + 2H_2O$$
 (3.2)

Furthermore, the reaction occurs after immersion of the substrates in Na<sub>2</sub>WO<sub>4</sub>.2H<sub>2</sub>O solution, where a chemical reaction between (WO<sub>4</sub>)<sup>2-</sup> ions and pre-adsorbed Ni<sup>2+</sup> ions leads to the deposition of nickel tungstate layer on SS substrate,

$$Ni^{2+} + (WO_4)^{2-} \rightarrow NiWO_4$$
 (3.3)

Thus, the thin film of NiWO<sub>4</sub> was grown by the ions-by-ion growth mechanism and nucleation starts by the adsorption of ions at the nucleation centers of the immersed surface of a substrate [23, 24].

### 3.3 Material characterizations

### 3.3.1 Physico-chemical characterizations

An X-ray diffractometer (Rigaku miniflex-600 with CuK $\alpha$  radiation  $\lambda$  = 1.54 Å) was used to study the crystal structure of thin films. The functional group bonding in the synthesized material was studied utilizing the Bruker Tensor 27 Fourier transform infrared (FT-IR) tool. Raman study was performed using JASCO NRS-5100 with  $\lambda$  = 514.4 nm. Topography of the specimens was observed using a field emission scanning electron microscope (FE-SEM) (JEOL JEM 2100). Contact angle images were obtained using the Rame Hart goniometer. The XPS with a monochromatic radiation source of Mg K $\alpha$  (1253.6eV) (VG Multilab 2000, Thermo VG Scientific, U.K.) was used to study chemical composition of the film. The TEM studies were conducted using the JEOL-ARM-200F field emission TEM. Specific surface area and pore size distribution were evaluated through Brunauer-Emmett-Teller (BET) and Barrett-Joyner-Halenda (BJH) analytical models, separately, using Quantachrome Instruments v11.02.2.4.

### 3.3.2 Electrochemical characterizations

To investigate the electrochemical properties of different thin films of NiWO<sub>4</sub>, a three-electrode system was employed. The system consisted of NiWO<sub>4</sub> film as the working electrode, mercury/mercury oxide (Hg/HgO) electrode as a counter, and a platinum sheet as a reference electrode. The measurements were conducted at ambient temperature in 2 M KOH electrolyte solution. The working electrode had an exposed area of 1 cm<sup>2</sup>. The electrochemical properties of the electrodes were evaluated in terms of specific capacitance (Cs), electrochemical stability, solution resistance (Rs), and charge transfer resistance (R<sub>ct</sub>) at the electrode-electrolyte interface. The cyclic voltammetry (CV), galvanostatic charge-discharge (GCD), and electrochemical impedance spectroscopy (EIS) measurements were performed using an electrochemical workstation called ZIVE MP1.

### 3.3.2.1 Cyclic voltammetry (CV) study

Cyclic voltammetry (CV) is a valuable technique for determining redox potentials and investigating electronic transfer in redox reactions. It is commonly employed to calculate the specific capacitance (Cs) of electrode materials. In this study, CV measurements were conducted on NiWO<sub>4</sub> thin film electrodes within a potential range of 0 V to +0.6 V vs. mercury/mercury oxide (Hg/HgO). The Cs values for the electrode materials were determined using Equation 2.10. Additionally, the charge storage mechanism was analyzed using a power law approach.

### 3.3.2.2 Galvanostatic charge discharge (GCD) study

To further investigate the charge storage behavior, galvanostatic charge-discharge (GCD) studies were performed on the same potential window as the CV experiments for NiWO<sub>4</sub> thin film electrodes. The shape of the GCD curves provides insights into the nature of charge storage. The Cs values for the thin film electrodes were calculated using Equation 2.12.

### 3.3.2.3 Electrochemical impedance spectroscopy (EIS)

Electrochemical impedance spectroscopy (EIS) was employed to analyze the resistive parameters of the electrode-electrolyte interface. By utilizing the ZIVE MP1 electrochemical workstation, the EIS measurements allowed for characterization of the interface quality between the electrode and electrolyte. The EIS study involved applying a 5 mV potential amplitude over a frequency range of 0.01 Hz to 0.1 MHz while maintaining an open circuit potential bias.

### 3.4 Results and discussion

### 3.4A Physico-chemical characterizations

### 3.4A1 XRD study

The XRD analysis is performed to evaluate the crystal structure of NiWO<sub>4</sub> thin films. The XRD patterns of NiWO<sub>4</sub> thin films are shown in **Figure 3.2b**. The observed diffraction planes correspond to (100), (011), (111) (021, and (202) crystallographic planes of monoclinic NiWO<sub>4</sub> (JCPDS card No. 96-591-0278). The calculated crystallographic parameters for the structure are a= 4.6000 Å, b=5.6650 Å, c=4.9120 Å and  $\alpha = \gamma = 90^{\circ}$ , and  $\beta = 90.5^{\circ}$ . The diffraction peaks marked by \* are from SS substrate.

The average crystallite size for N series thin films was calculated by Scherrer's relation (equation 2.4). The calculated average crystallite sizes are 2.13, 2.19, 2.25, and 2.32 nm for N1, N2, N3, and N4 films respectively. As cationic concentration increases in N series films, the crystallite size also increases.

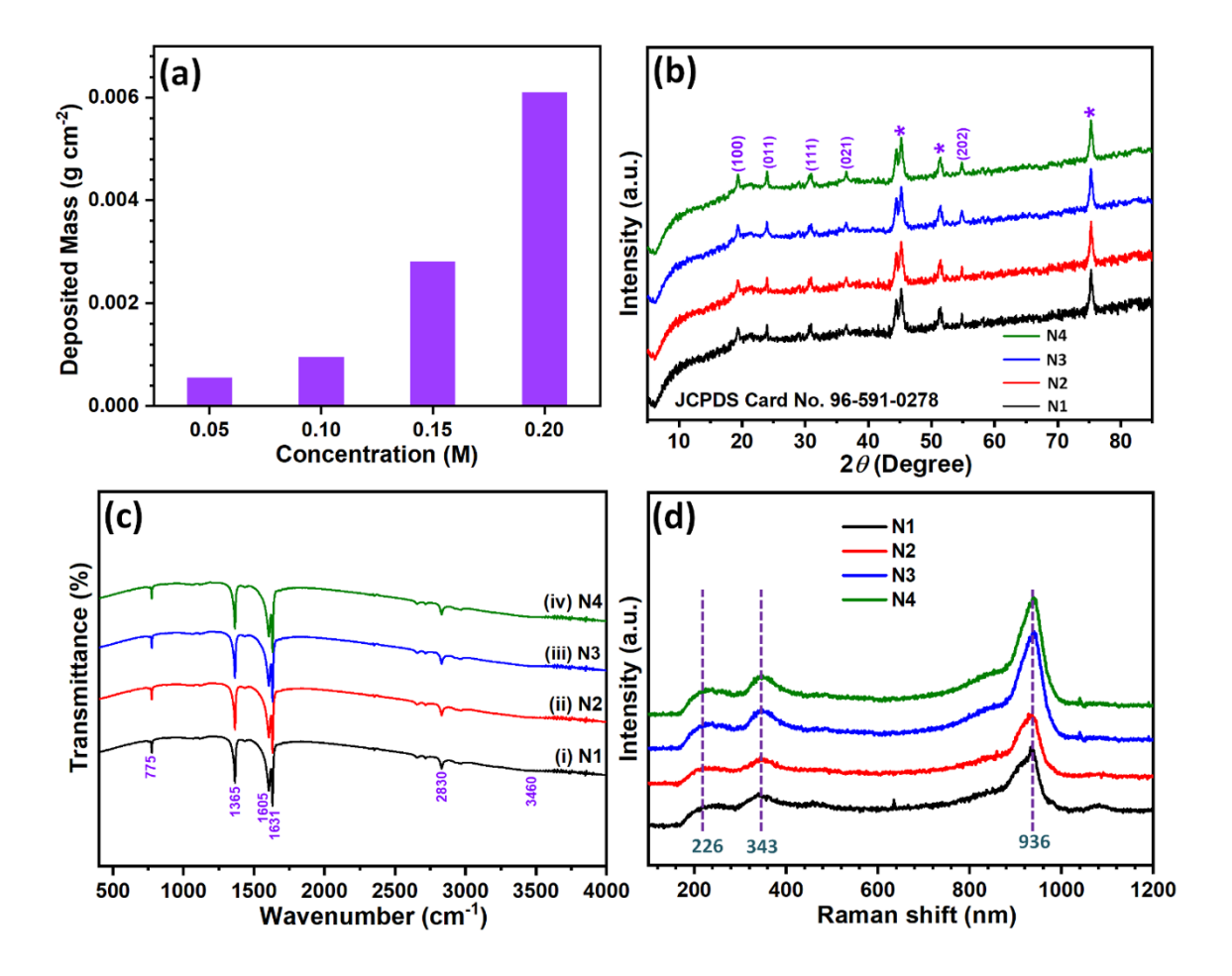


Figure 3.2: a) Variation in mass loading with the concentration of cationic precursor, b) The XRD patterns, c) the FTIR spectra, and d) Raman spectra of NiWO<sub>4</sub> thin films.

### 3.4A2 FT-IR study

The FT-IR spectroscopy is used to investigate the bonding present in NiWO<sub>4</sub>. The FT-IR spectra of N1 to N4 samples are shown in Figure 3.2c. The main absorption bands of wolframite type structure appear in the range of 4000-400 cm<sup>-1</sup> [25]. The wide peak at a wavenumber of 3460 cm<sup>-1</sup> is assigned to stretching vibrations of -OH confirms presence

of adsorbed water in the sample. The absorption peak at 2830 cm<sup>-1</sup> correspond to weak - OH stretching vibrations from the structural hydroxide. The absorption bands at 1605 to 1631 cm<sup>-1</sup> correspond to bending vibrations of the -OH group. The band at 1365 cm<sup>-1</sup> is due to the stretching modes of W=O terminal bond present in each octahedron of WO<sub>3</sub> [26]. The band at 775 cm<sup>-1</sup> arises from vibrations of WO<sub>2</sub> entity present in the W<sub>2</sub>O<sub>8</sub> groups. Karthiga et al. [27] and Eranjaneya et al. [28] reported similar type absorption bands for NiWO<sub>4</sub>. From this analysis, it is concluded that changing cationic concentration does not change bonding in NiWO<sub>4</sub> film material.

### 3.4A3 Raman study

Raman spectra of transition metal tungstate provides a structural analysis. Raman spectra of tungstate-containing molecules is dominated by octahedral tungstate peaks due to the presence of asymmetric bonds. The Raman spectra of N series are shown in Figure 3.2d. Three different peaks are observed in spectra confirming the formation of nanocrystalline NiWO<sub>4</sub> on SS substrate. The peak of 930 cm<sup>-1</sup> corresponds to the symmetric stretching processes of O-W-O bonds. Another peak at 347 cm<sup>-1</sup> is due to the vibrations of the terminal bonds in the WO<sub>6</sub> octahedra. The peak at 221 cm<sup>-1</sup> is due to the vibrations of O-Ni-O bonding [29]. Therefore, the characteristic vibrational modes in the Raman spectra are consistent with the previous reports [30, 31].

### 3.4A4 FE-SEM study

The surface morphology of NiWO<sub>4</sub> thin films was studied using the FE-SEM (Figure 3.3) at magnifications of 2,000X and 50,000X. Spherical nanoparticles combined to form clusters result in different morphologies. The concentration of cationic precursor has affected the nucleation formation rate resulting in different morphologies. The FE-SEM images of N1 (Figure 3.3a, b), depict sheet-like structure while for N2 to N4 thin films, spherical nanoparticles are observed (Figure 3.3c-f). With the increased cationic concentration, overgrowth of nickel tungstate particles is observed. For N3 electrode, cracks were observed (Figure 3.3e). For N4 electrode, overgrowth was more which could cause lower adhesion of active material to the substrate, which could affect electrochemical stability.

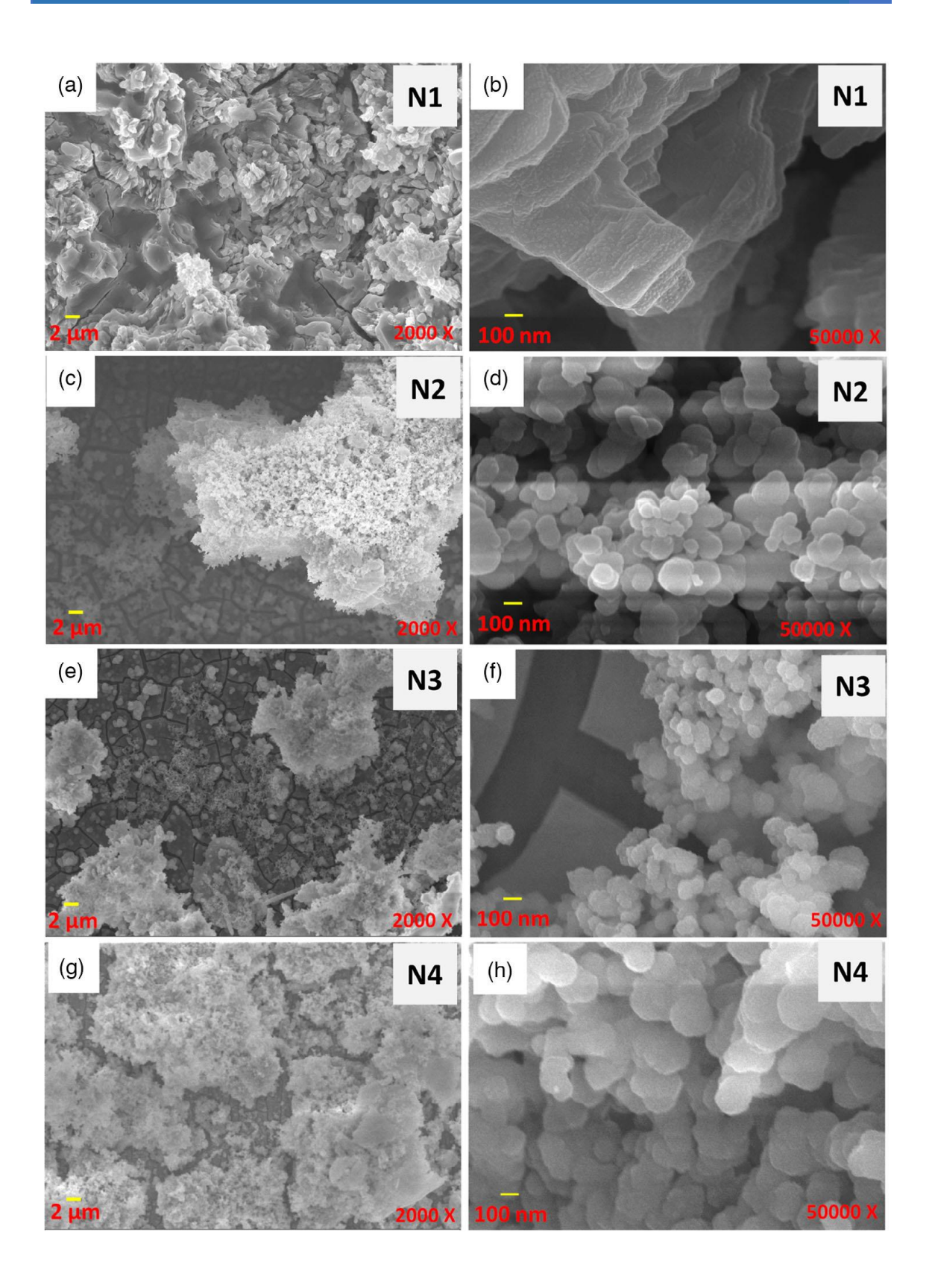


Figure 3.3: The FE-SEM images of a and b) N1, c and d) N2, e and f) N3, g and h) N4 at magnifications of 2000X and 50000X, respectively.

### 3.4A5 TEM study

The transmission electron microscopy images of N3 sample presented in Figures. **3.4a-c**, indicate the spherical nanoparticles similar to as depicted in the FE-SEM. The TEM images with high-resolution are shown in **Figure 3.4d-e**. Interplanar distance of 0.37 nm corresponds to (011) crystallographic plane of NiWO<sub>4</sub>. The selected area electron diffraction (SAED) is shown in **Figure 3.4f**. The interplanar distances of 0.37, 0.29, 0.22, and 0.14 nm correspond to (011), (111), (121), and (132) crystallographic planes, respectively of monoclinic NiWO<sub>4</sub>. The interplanar distance calculated from HR-TEM and SEAD patterns are in consistent with the XRD studies.

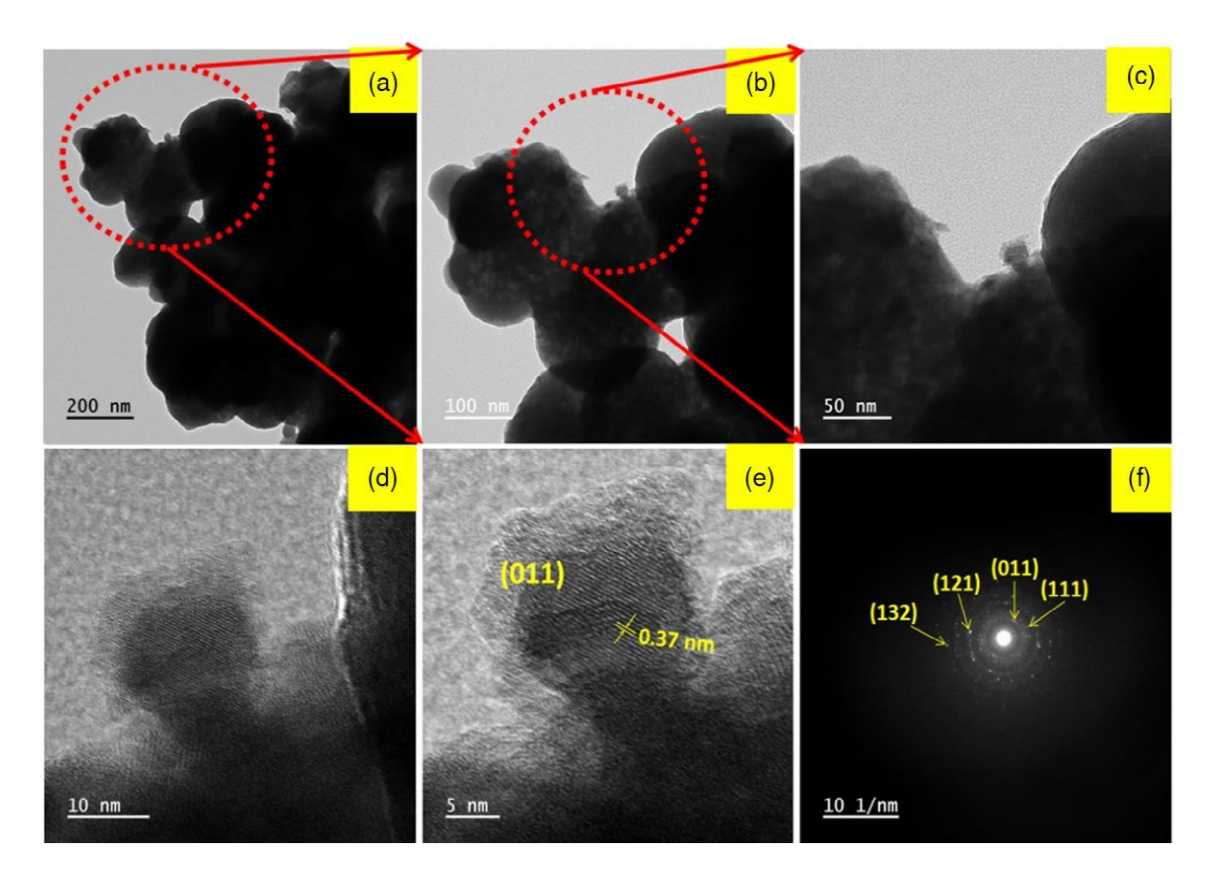


Figure 3.4: a-c) The TEM images of N3 thin film, d, and e) the HR-TEM of N3 at 5, 10, 50, 100, and 200 nm magnifications, and f) the SEAD pattern of N3.

### 3.4A6 XPS study

The elemental composition of surface and oxidation states of constituent elements of NiWO<sub>4</sub> films are investigated from the XPS studies. The XPS survey spectrum of N3 film provided in **Figure 3.5a** confirms the existence of nickel, tungstate, and oxygen in the sample. The Ni2p peak is deconvoluted into the Ni2p<sub>3/2</sub> and Ni2p<sub>1/2</sub> peaks at binding

energies of 855.77 and 873.27 eVs, respectively as shown in **Figure 3.5b**, and denotes the chemical state of element Ni in Ni<sup>+2</sup> state. The separation of energy (17.7 eV) between the two states of Ni2p<sub>3/2</sub> and Ni2p<sub>1/2</sub> is in accordance with the literature **[32]** suggesting formation of Ni<sub>3</sub> on the SS substrate. Also, two satellite peaks at 863.8 and 881.5 eVs binding energies are observed in the XPS spectrum of Ni2p (**Figure 3.5 b**) **[33]**. In **Figure 3.5c**, the XPS spectrum of W4f is made of W4f<sub>5/2</sub> and W4f<sub>7/2</sub> peaks at binding energies of 37.42 and 35.27 eVs, respectively, confirms the chemical state of element W in the W<sup>+6</sup> state. The separation of energy (2.15 eV) between two states is well in accordance with the literature **[34]**. Moreover, the peak of O1s spectrum (**Figure 3.5d**), at 530.73 eV represents metal oxygen bonding **[35]**. The XPS results support XRD, FT-IR, and TEM analyses and confirm that prepared material is NiWO<sub>4</sub>.

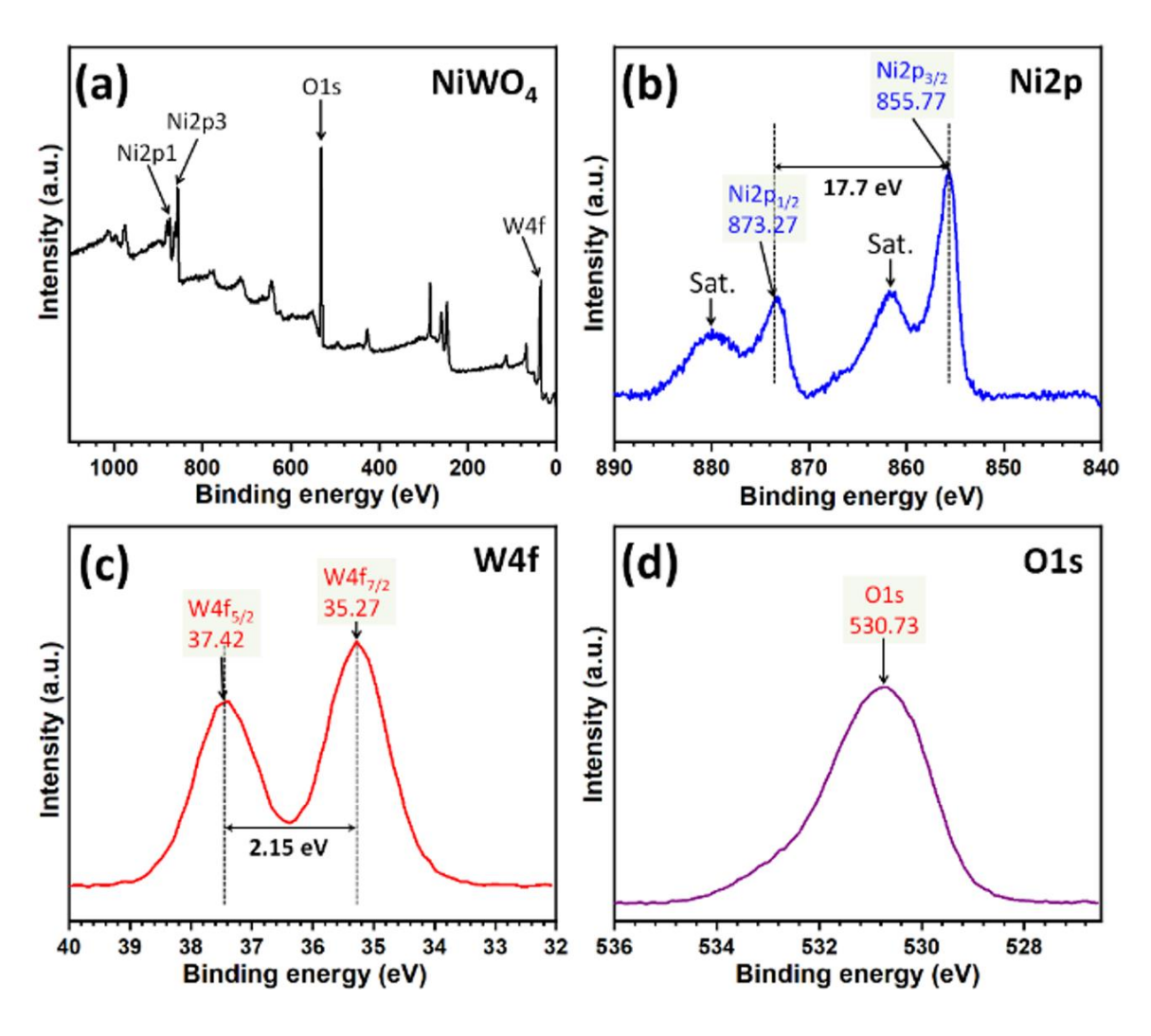


Figure 3.5: The XPS spectra of a) NiWO<sub>4</sub> electrode, b) Ni 2p, c) W4f, and d) O1s.

### 3.4A7 BET study

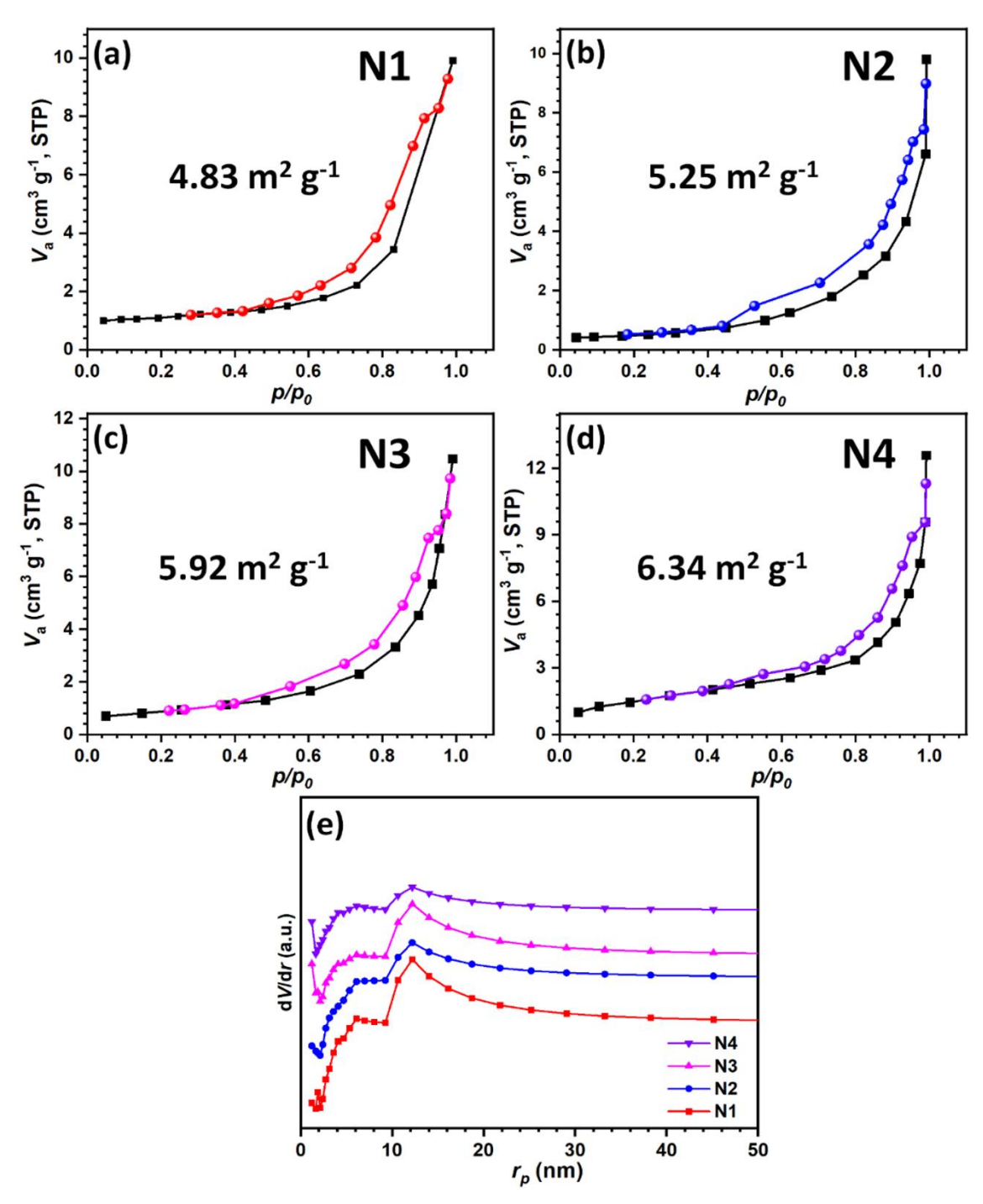


Figure 3.6: The BET isotherms of a) N1, b) N2, c) N3, and d) N4, and e) pore size distribution of N1-N4.

The N<sub>2</sub> adsorption-desorption isotherms of N1, N2, N3, and N4 are shown in **Figure 3.6a-d**. Isotherms of type-III indicate the mesoporous nature of the thin films. The pore size distribution curves shown in **Figure 3.6e** indicate a smaller shift in the average pore

size with the increase in the concentration of the Ni precursor. The values of mean pore size for N1, N2, N3, and N4 samples are 11.5, 11.4, 11.2, and 11.1 nm, respectively. The mesoporous nature of the thin films is beneficial for the supercapacitive application.

### 3.4A8 Contact angle measurement

The electrochemical activity of the electrode is affected by the contact angle with electrolyte. The wettability of electrolytes to the surface of the electrode has been regarded as an important parameter to raise the effective charge storage on the electrode. The contact angle images of N1, N2, N3, and N4 in **Figure 3.7** show the values like 66, 63, 36, and 39°, respectively. Variation in morphologies caused contact angles variations. Lower contact angle value was observed for N3 with mass loading of 0.0032 g cm<sup>-2</sup>.

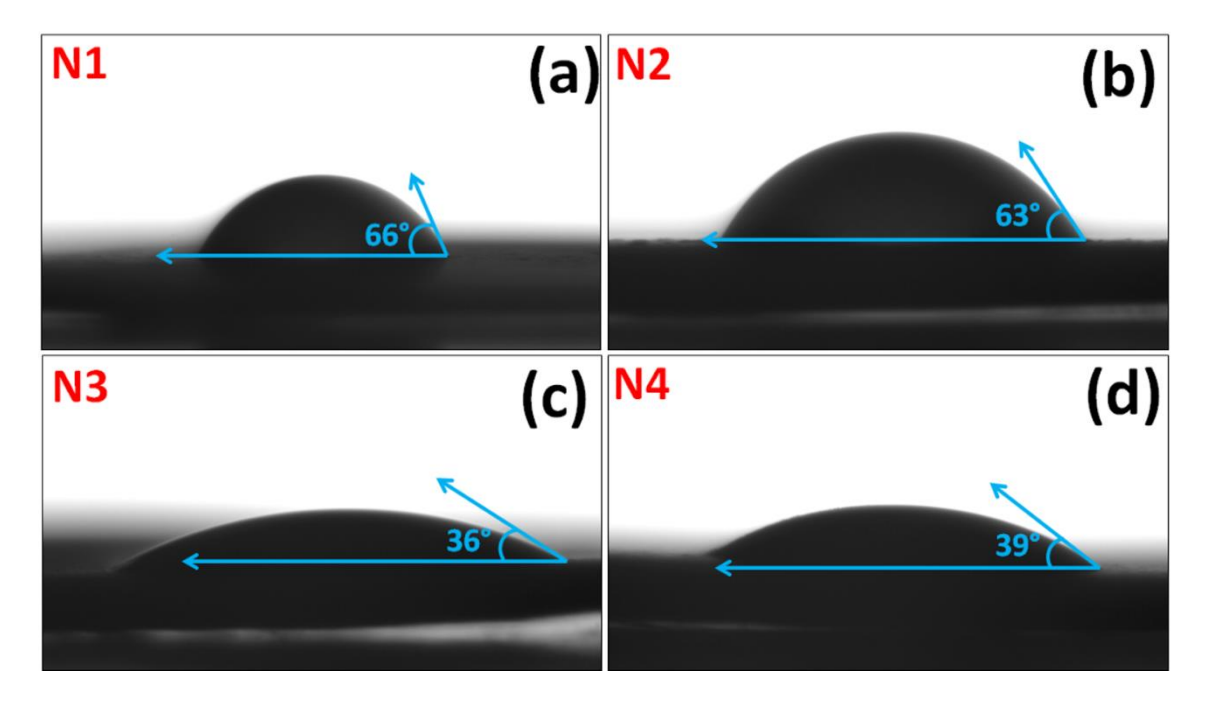


Figure 3.7: The contact angle images of a) N1, b) N2, c) N3, and d) N4.

### 3.4B Electrochemical characterizations

### 3.4B1 CV study

The electrochemical study of NiWO<sub>4</sub> thin films was carried out in 2 M KOH electrolyte in a potential window of 0 to +0.6 vs. (Hg/HgO)/V. Comparative CV curves of N1, N2, N3, and N4 at the potential scan rate of 20 mV s<sup>-1</sup> are shown in **Figure 3.8a**.

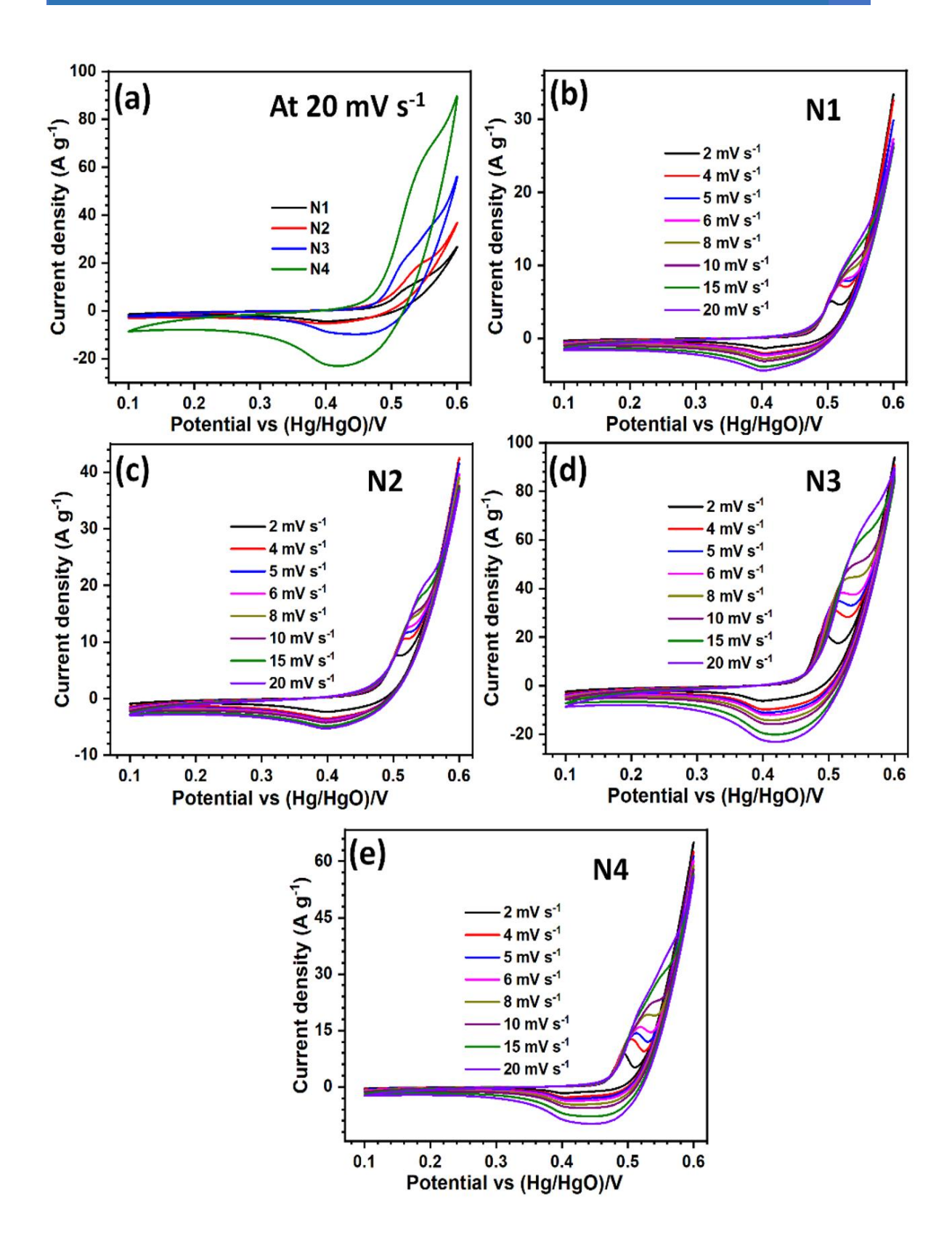


Figure 3.8: a) Comparative CV curves of N1 to N4, and the CV curves of b) N1, c) N2, d) N3, and e) N4 for scan rates of 2 to 20 mV s<sup>-1</sup>.

There is a higher current response for N3 compared to N1, N2, and N4, indicating facile charge transport for N3 electrode which raises the current response capacity of the electrode. The non-rectangular shape of the CV curves with oxidation and reduction peaks confirm the battery-type charge storage mechanism. The CV curves for N1, N2, N3, and N4 electrodes with different scan rates between 2 to 20 mV s<sup>-1</sup> in **Figure 3.8b, c, d, and e,** respectively, show the flexibility of the electrodes with different charging values. Oxidation and reduction peaks shift towards the left and right side, respectively, with increasing scan rate. The reversibility of the electrode material is confirmed from the CV analysis.

$$I_p = a v^b (3.4)$$

The power law (Eq. 3.4) is used to understand the charge storage mechanism [36]. Here, a is the adjustable parameter and b is the slope of a graph of  $\log I$  vs.  $\log v$ .

The slope of graphs shown in **Figure 3.9a** gives values of coefficient b. For N1, N2, N3, and N4 electrodes, these are 0.52, 0.53, 0.64, and 0.56, respectively. These values confirm battery-type charge storage with intercalation of the electrolyte ions in the electrode material. To determine the contribution of the capacitive and diffusion-controlled process in the total current response, additional analysis using modified power law **Eq. (3.5)** is carried out [37].

$$I(v) = k_1 v + k_2 v^{0.5} = I_{surface} + I_{bulk}$$
 (3.5)

where  $k_1v$  and  $k_2v^{0.5}$  are contributions from capacitive and diffusion-controlled processes, respectively. Slope and an intercept of the linear fit of the graph of  $I/v^{0.5}$  versus  $v^{0.5}$  (Figure 3.9b) give the values of  $k_1$  and  $k_2$ , respectively. Percentage contribution of capacitive and diffusion-controlled currents calculated from Eq. (3.5) are shown in Figure 3.9c-f for N series electrodes. It is evident that as the scanning rate decreases, the contribution from the diffusion-controlled process increases and results in a larger value of  $C_s$ . Approximately, 7 and 18% of the charge is stored by a capacitive process in N3 at the scan rates of 2 and 20 mV s<sup>-1</sup>, respectively. The significant contribution from the diffusion-controlled process is due to the nanocrystalline and mesoporous structure that allow easy penetration of the electrolyte itself [38].

#### 3.4B2 GCD study

The GCD studies for N-series electrodes were performed at various current densities between 2 to 4 A g<sup>-1</sup> in the potential window of 0.1 to +0.5 vs. (Hg/HgO)/V.

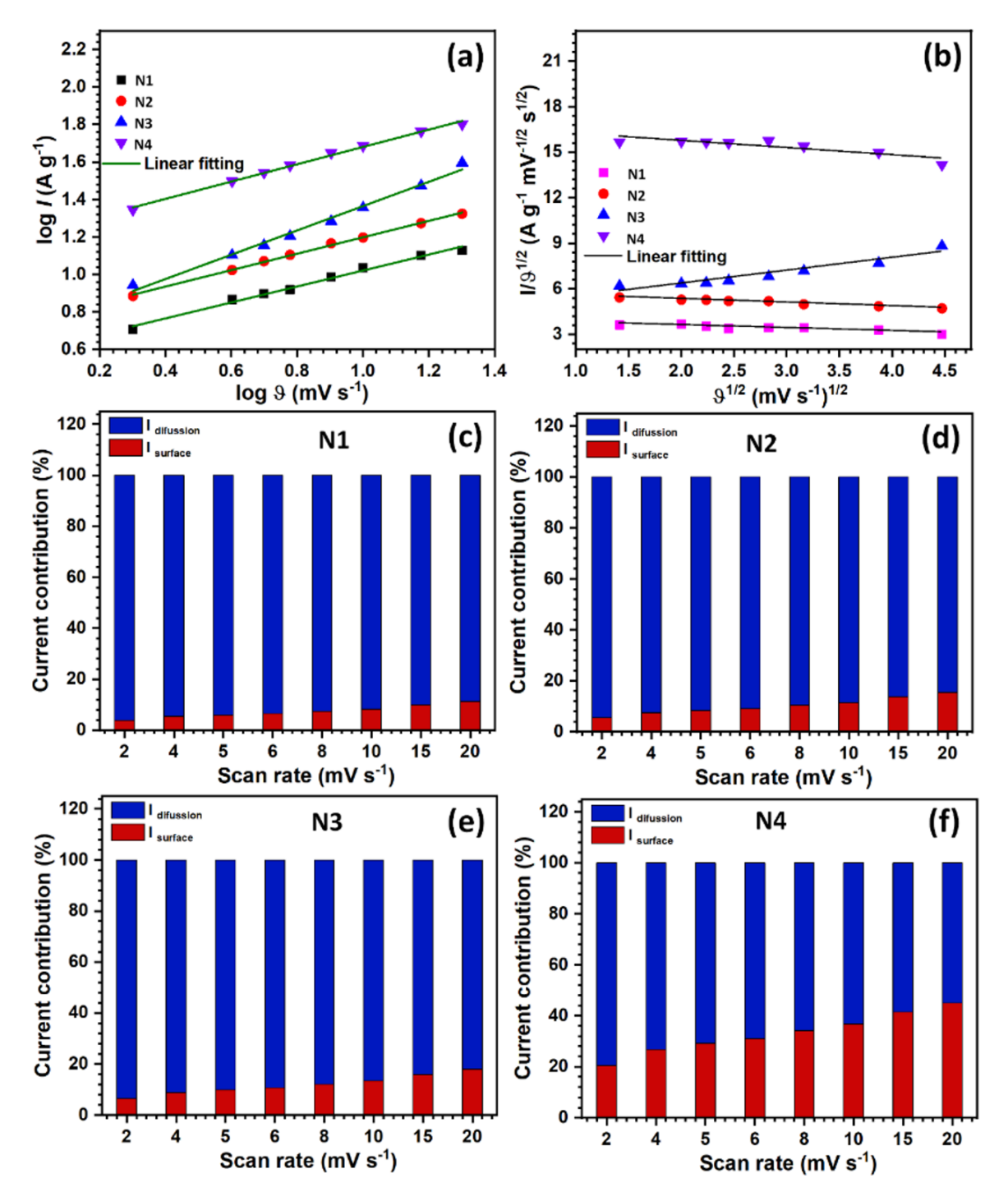


Figure 3.9: a) The graphs of  $\log I$  vs.  $\log v$ , b) graphs of  $I/v^{1/2}$  vs.  $v^{1/2}$ , percentage current contribution of capacitive and diffusion mechanisms for c) N1, d) N2, e) N3, and f) N4.

The comparative GCD curves of N-series electrodes at the different current density of 2 Ag<sup>-1</sup> are shown in Figure 3.10a. At a discharge current density of 2 Ag<sup>-1</sup>, the  $C_s$  values for N1, N2, N3, and N4 electrodes are 320, 696, 1536, and 1056 F g<sup>-1</sup>, respectively. The corresponding specific capacities are 44, 96, 213, and 146 mAh g<sup>-1</sup> for N1, N2, N3, and N4, respectively. The GCD curves of N1, N2, N3, and N4 at different current densities are shown in Figure 3.10b-e. Due to optimum mass loading, N3 electrode has the highest specific capacitance. Comparison of  $C_s$  of N3 with Ni-based electrodes reported for supercapacitor application is shown in Table 3.1 [20, 21, 39-42]. Changes in  $C_s$  with discharging current density are shown in Figure 3.10f. Rate capacity of 50, 38, 27, and 39% of N1, N2, N3, and N4 electrodes at the current density of 4 Ag<sup>-1</sup> confirms a higher rated capacity of the electrodes. The highest specific capacitance is obtained for N3, due to binder free synthesis, which gives huge active sites for charge storage.

Table 3.1: Comparison of  $C_s$  of N3 with Ni-based electrodes reported for supercapacitor application

| Material                                  | Synthesis<br>method           | Morphology                 | Substrate | Electrolyte | C <sub>s</sub> (F g <sup>-1</sup> ) @<br>Current<br>density (A g <sup>-1</sup> ) | Stability (%) (cycles) | Ref.      |
|---|-------------------------------|----------------------------|-----------|-------------|--|------------------------|-----------|
| NiWO <sub>4</sub>                         | SILAR followed by calcination | Spherical nanoparticles    | SS        | 2 M KOH     | 1536@ 2.0  | 87<br>(5000)           | This work |
| NiWO <sub>4</sub>                         | Solvothermal                  | Nanowires                  | -         | 6 М КОН     | 1190.0   | -                      | [20]      |
| NiWO <sub>4</sub>                         | Coprecipitation               | Cauliflower                | NF        | 2 M KOH     | 586.0@0.5  | 90<br>(1000)           | [21]      |
| NiWO <sub>4</sub>                         | Chemical precipitation        | Spherical nanoparticles    | -         | 1 M KOH     | 437.2@0.1  | 44<br>(500)            | [39]      |
| MnMoO <sub>4</sub> /<br>NiWO <sub>4</sub> | Hydrothermal                  | Microspheres               | NF        | 2 M KOH     | 598.0@1.0  | 82<br>(5000)           | [40]      |
| Ni-WO <sub>3</sub>                        | Microwave irradiation         | Agglomerated nanoparticles | NM        | 2 М КОН     | 171.3@0.25   | -                      | [41]      |
| NiWO <sub>4</sub> .<br>CoWO <sub>4</sub>  | Chemical precipitation        | Cauliflower -<br>like      | NF        | 2 М КОН     | 196.7 C g <sup>-1</sup> @<br>0.5   | -                      | [42]      |

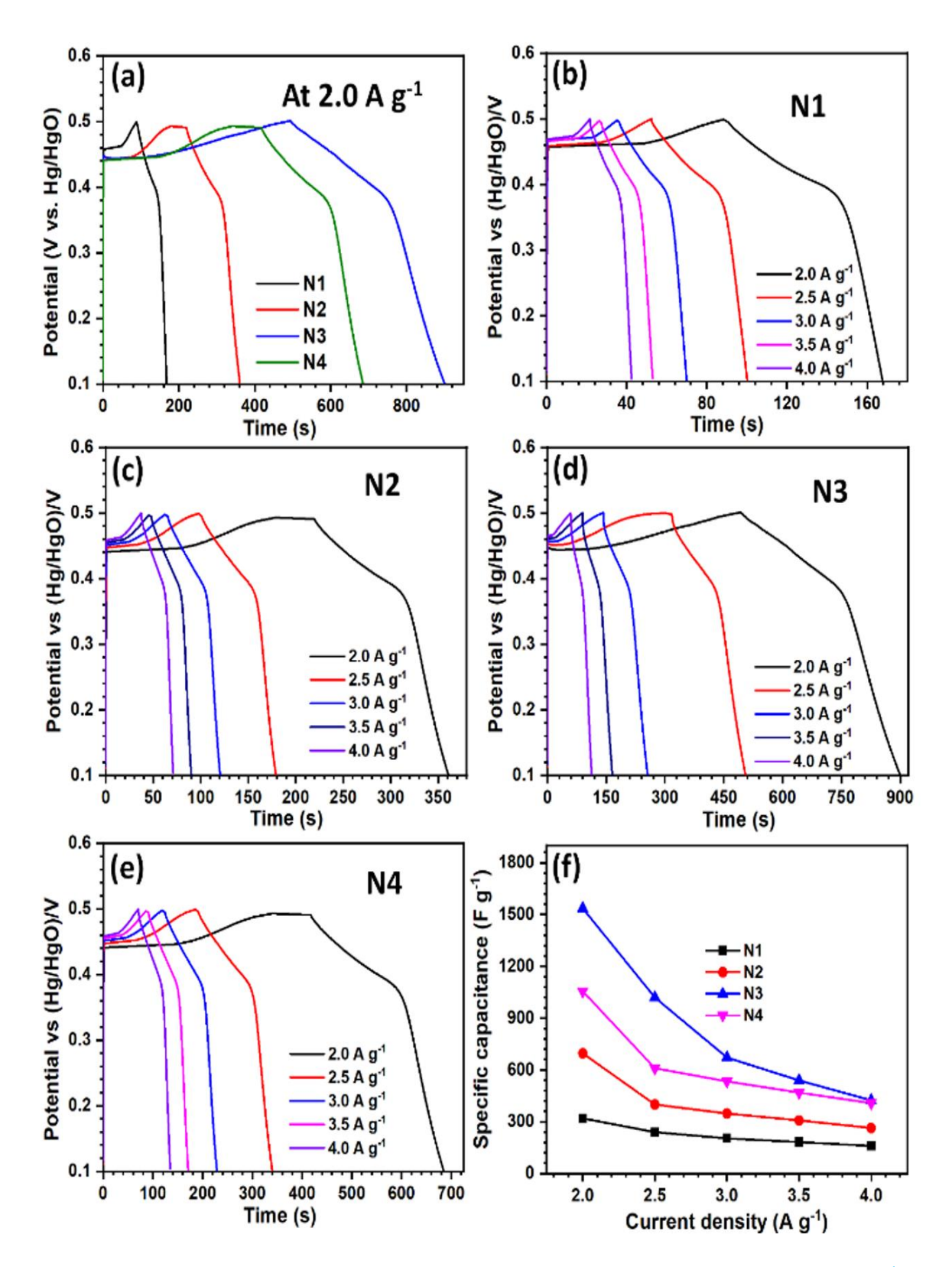


Figure 3.10: a) Comparative GCD plots of N1–N4 at current density of 2 A g<sup>-1</sup> NiWO<sub>4</sub>, the GCD plots of b) N1, c) N2, d) N3, and e) N4 at different current densities, and f) the graph of specific capacitance vs. current density of N1, N2, N3, and N4.

#### 3.4B3 EIS study

The resistive parameters of electrodes play a crucial role in the charge storage process. The Nyquist plots of N-series electrodes are given in **Figure 3.11a**. An equivalent electrical circuit drawn using Zview software is provided as an inset of **Figure 3.11a**. The circuit contains solution resistance ( $R_s$ ), charge transfer resistance ( $R_{ct}$ ), and constant phase element (CPE). Values of the electrochemical parameters are summarized in **Table 3.2**. The  $R_s$  for N series electrodes is ~0.47  $\Omega$  cm<sup>-2</sup> signifying good contact of the electrode with electrolyte. The values of  $R_{ct}$  for N1, N2, N3, and N4 electrodes are 155.5, 179.2, 186.3, 339.2  $\Omega$  cm<sup>-2</sup>, respectively demonstrating facile charge transfer. With an increase in deposition mass, the  $R_{ct}$  is also increased. Values of specific capacitance and  $R_{ct}$  indicate that appropriate mass loading is useful for the highest electrochemical performance.

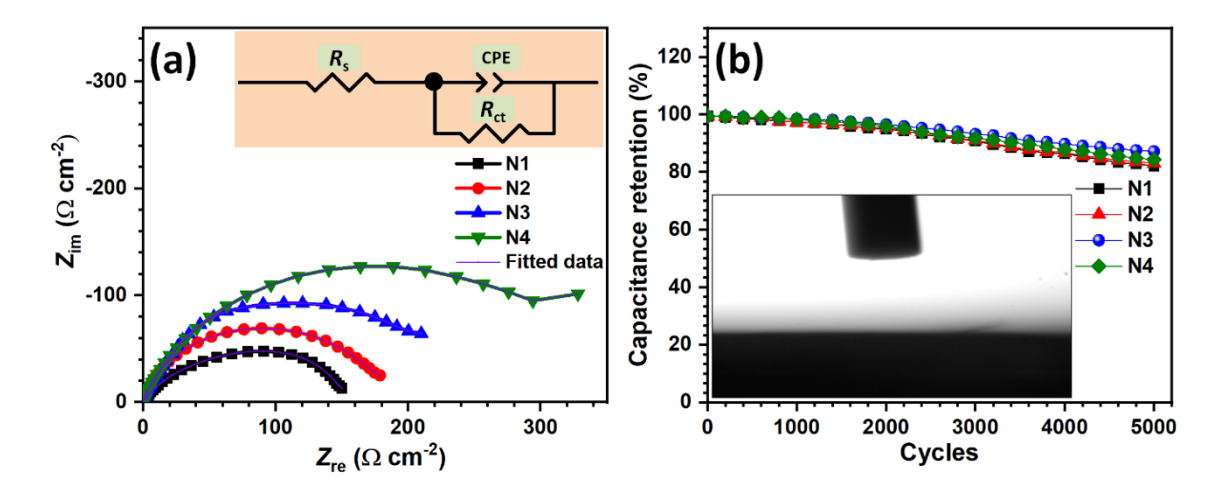


Figure 3.11: a) The Nyquist plots (inset shows electrical equivalent circuit) and b) stability curves of NiWO<sub>4</sub> electrodes (inset shows a photograph of contact angle after stability).

**Table 3.2: Values of the electrochemical parameters** 

| Parameters                            | N1     | N2    | N3    | N4    |
|---------------------------------------|--------|-------|-------|-------|
| R <sub>s</sub> (Ω cm <sup>-2</sup> )  | 0.26   | 0.24  | 0.23  | 0.27  |
| R <sub>ct</sub> (Ω cm <sup>-2</sup> ) | 155.50 | 179.2 | 186.3 | 339.2 |
| CPE (F cm <sup>-2</sup> )             | 0.79   | 0.85  | 0.85  | 0.80  |

#### 3.4B4 Stability study

The retention of NiWO<sub>4</sub> electrodes depends on the adherency of the electrode material to the current collector, and chemical stability in an electrolyte. The retention of  $C_s$  for N series electrodes is evaluated at a current density of 3.0 A g<sup>-1</sup> (Figure 3.11b). Values of 82, 83, 87, and 84% of initial  $C_s$  after 5000 GCD cycles confirm the excellent stability of the electrodes. As thickness increases the stability of the film increases up to N3 and thereafter decreased due to the non-adhesion of the active material to the current collector. After electrochemical stability, the contact angle image of N3 is shown as an inset of Figure 3.11b. The low contact angle ( $\sim 2^{\circ}$ ) is due to alteration in surface topography due to charging-discharging process.

#### 3.5 Conclusions

This study demonstrates synthesis of binder-free NiWO<sub>4</sub> thin films for electrochemical energy storage and opens a new path to improve  $S_E$  for energy storage devices. The effect of the concentration of cationic precursor on the thickness and morphology of the thin film was studied. The concentration of 0.15 M of NiSO<sub>4</sub> is optimum as beyond this concentration leads to nonadherent thin films. NiWO<sub>4</sub> with a specific capacity of 213 mAh g<sup>-1</sup> shows retention of 87% after 5000 cycles. Due to the optimum film thickness and morphology the excellent electrochemical performance of NiWO<sub>4</sub> thin films is achieved.

Highest  $C_s$  of 1536 F g<sup>-1</sup> and stability of 87% with lower impedance values observed for N3 electrode. Therefore, this electrode was selected further for the ASC device fabrication.

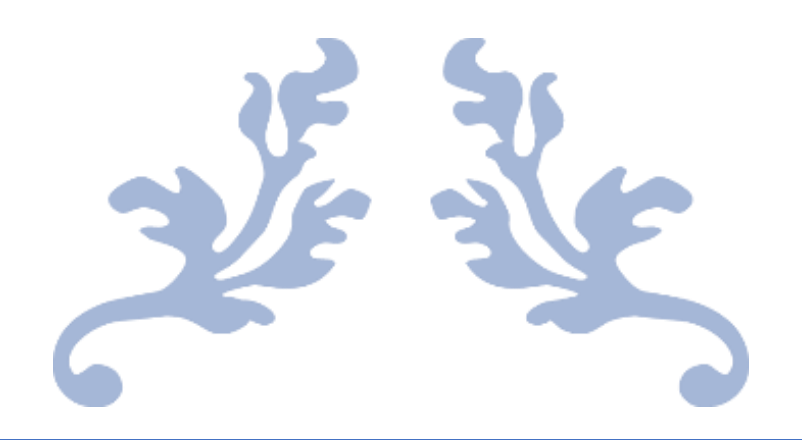
#### **References:**

- [1] C. Geng, A. Liu, J. R. Dahn, Chem. Mater., 32, 2020, 6097.
- [2] B. Zhang, P. Liu, Z. Li, X. Song, Nanomaterials (Basel), 11, 2021, 155.
- [3] K. Fic, A. Platek, J. Piwek, E. Frackowiak, Mater. Today, 21, 2018, 437.
- [4] A. K. Yedluri, H. Kim, Dalton Trans., 47, 2018, 15545.
- [5] M. S. Vidhya, G. Ravi, R. Yuvakkumar, D. Velauthapillai, M. Thambidurai, C. Dang, B. Saravanakumar, RSC Adv., 10, 2020, 19410.

- [6] N. R. Chodankar, H. D. Pham, A. K. Nanjundan, J. F. S. Fernando, K. Jayaramulu, D. Golberg, Y. Han, D. P. Dubal, Small, 16, 2020, 2002806.
- [7] P. A. Shinde, A. C. Lokhande, N. R. Chodankar, A. M. Patil, J. H. Kim, C. D. Lokhande, Electrochim. Acta, 224, 2017, 397.
- [8] S. Shahzad, A. Shah, E. Kowsari, F. J. Iftikhar, A. Nawab, B. Piro, M. S. Akhter, U. A. Rana, Y. Zou, Glob Chall, 3, 2018, 1800023.
- [9] R. K. Tripathy, A. K. Samantara, J. N. Behera, Sustain. Energy Fuels, 5, 2021, 1184.
- [10] A. F. Gouveia, V. E. M. Vieira, J. C. Sczancoski, P. S. Lemos, S. K Rout, N. S. Arul, E. Longo, L. S. Cavalcante J. Inorg. Organomet. Polym Mater., 30, 2020, 2952.
- [11] V. C. Lokhande, S. J. Lee, A. C. Lokhande, J. H. Kim, T. Ji, Mater. Chem. Phys., 211, 2018, 214.
- [12] P. S. Kumar, P. Prakash, A. Srinivasan, C. Karuppiah, J. Power Sources, 482, 2021, 228892.
- [13] A. Tiwari, V. Singh, T. C. Nagaiah, ACS Appl. Mater. Interfaces, 11, 2019, 21465.
- [14] A. Sreedevi, K. P. Priyanka, S. C. Vattappalam, T. Varghese, J. Electron. Mater., 47, 2018, 6328.
- [15] S. M. Alshehri, J. Ahmed, A. M. Alzahrani, T. Ahamad, New J. Chem., 41, 2017, 8178.
- [16] C. R. Lhermitte, B. M. Bartlett, Acc. Chem. Res., 49, 2016, 1121.
- [17] M. Ikram, Y. Javed, N. A. Shad, M. M. Sajid, M. Irfan, A. Munawar, T. Hussain,M. Imran, D. Hussain, J. Alloys Compd., 878, 2021,160314.
- [18] S. M. Pourmortazavi, M. Rahimi-Nasrabadi, M. S. Karimi, S. Mirsadeghi, New J. Chem., 42, 2018, 19934.
- [19] R. Packiaraj, P. Devendran, K. S. Venkatesh, N. Nallamuthu, Inorg. Chem. Commun., 126, 2021, 108490.
- [20] J. Tian, Y. Xue, X. Yu, Y. Pei, H. Zhang, J. Wang, RSC Adv., 8, 2018, 41740.
- [21] L. Niu, Z. Li, Y. Xu, J. Sun, W. Hong, X. Liu, J. Wang, S. Yang ACS Appl. Mater. Interfaces, 5, 2013, 8044.
- [22] X. Xu, L. Pei, Y. Yang, J. Shen, M. Ye, J. Alloys Compd., 654, 2016, 23.

- [23] S. S. Raut, B. R. Sankapal, New J. Chem., 40, 2016, 2619.
- [24] B. Pandit, S. S. Karade, B. R. Sankapal, ACS Appl. Mater. Interfaces, 9, 2017, 44880.
- [25] D. B. Malavekar, R. N. Bulakhe, S. B. Kale, U. M. Patil, I. In, C. D. Lokhande, J. Alloys Compd., 869, 2021, 159198.
- [26] Y. L. Oliveira, M. J. S. Costa, A. C. S. Juca, L. K. R. Silva, E. Longo, N. S. Arul,L. S. Cavalcante, J. Mol. Struct., 1221, 2020, 128774.
- [27] R. Karthiga, B. Kavitha, M. Rajarajan, A. Suganthi, Mater. Sci. Semicond. Process., 40, 2015, 123.
- [28] H. Eranjaneya, P. S. Adarakatti, A. Siddaramanna, C. G. Thimmanna, J. Mater. Sci.: Mater. Electron., 30, 2019, 3574.
- [29] R. L. Andrews, A. M. Heyns, P. M. Woodward, Dalton Trans., 44, 2015, 10700.
- [30] E. S. Babu, B. J. Rani, G. Ravi, R. Yuvakkumar, R. K. Guduru, V. Ganesh, S. Kim, Mater. Lett., 220, 2018, 209.
- [31] P. Sharma, M. Minakshi, J. Whale, A. Jean-Fulcrand, G. Garnweitner Nanomaterials, 11, 2021, 580.
- [32] J. Chang, Q. Lv, G. Li, J. Ge, C. Liu, W. Xing, Appl. Catal. B, 204, 2017, 486.
- [33] W. Bian, Y. Huang, X. Xu, M. Din, G. Xie, X. Wang, ACS Appl. Mater. Interfaces, 10, 2018, 9407.
- [34] T. M. Salama, M. Morsy, R. M. A. Shahba, S. H. Mohamed, M. M. Mohamed. Front. Chem., 7, 2019, 722.
- [35] D. Chen, D. He, J. Lu, L. Zhong, F. Liu, J. Liu, J. Yu, G. Wan, S. He, Y. Luo, Appl. Catal., B, 218, 2017, 249.
- [36] D. B. Malavekar, V. C. Lokhande, V. J. Mane, S. B. Kale, R. N. Bulakhe, U. M. Patil, I. In, C. D. Lokhande. J. Solid State Electrochem., 24, 2020, 2963.
- [37] D. B. Malavekar, V. C. Lokhande, V. J. Mane, S. B. Ubale, U. M. Patil, C. D. Lokhande, J. Phys. Chem. Solids, 141, 2020, 109425.
- [38] A. M. Patil, V. C. Lokhande, T. Ji, C. D. Lokhande, Electrochim. Acta, 307, 2019, 30.
- [39] Y. Huang, Y. Gao, C. Liu, Z. Cao, Y. Wang, Z. Li, Y Yan, M. Zhang, G. Cao, J. Phys. Chem. C, 123, 2019, 30067.

- [40] X. Feng, Y. Huang, M. Chen, X. Chen, C. Li, S. Zhou, X. Gao, J. Alloys Compd., 763, 2018, 801.
- [41] R. D. Kumar, Y. Andou, S. Karuppuchamy, J. Alloys Compd., 654, 2016, 349.
- [42] Y. Wang, C. Shen, L. Niu, Z. Sun, F. Ruan, M. Xu, S. Shan, C. Li, X. Liu, Y. Gong, Mater. Chem. and Phys., 182, 2016, 394.



# SYNTHESIS AND CHARACTERIZATION OF NICKEL TUNGSTATE@REDUCED GRAPHENE OXIDE COMPOSITE ELECTRODE BY SILAR METHOD



# SYNTHESIS AND CHARACTERISATION OF NICKEL TUNGSTATE@REDUCED GRAPHENE OXIDE COMPOSITE BY SILAR METHOD

| Sr. No.   |           | Title  | Page No. |
|---|-----------|--|----------|
| 4.1   | Introduc  | ction  | 97       |
| 4.2   | Depositi  | 98   |          |
|   | 4.2.1     | Chemicals and materials                        | 98       |
|   | 4.2.2     | Synthesis of rGO                               | 98       |
|   | 4.2.3     | Deposition of rGO-NiWO <sub>4</sub> thin films | 100      |
| 4.3   | Material  | characterization                               | 102      |
|   | 4.3.1     | Physico-chemical characterization              | 102      |
|   | 4.3.1A    | XRD studies                                    | 102      |
| 4.3.1B<br>4.3.1C<br>4.3.1D                              |           | FT-IR studies                                  | 103      |
|   |           | Raman studies                                  | 103      |
|   |           | SEM studies                                    | 104      |
| 4.3.1F<br>4.3.1C<br>4.3.2<br>4.3.2F<br>4.3.2F<br>4.3.2C | 4.3.1E    | TEM and HRTEM studies                          | 106      |
|   | 4.3.1F    | XPS studies                                    | 106      |
|   | 4.3.1G    | BET and BJT studies                            | 108      |
|   | 4.3.2     | Electrochemical study of rGO-NiWO <sub>4</sub> | 111      |
|   | 4.3.2A    | CV studies                                     | 111      |
|   | 4.3.2B    | GCD studies                                    | 113      |
|   | 4.3.2C    | EIS studies                                    | 114      |
|   | 4.3.2D    | Stability studies                              | 116      |
| 4.4   | Conclus   | ions   | 117      |
|   | Reference | 118  |          |

#### 4.1. Introduction

Expanding energy storage requirements along with ecological challenges spurred extraordinary research for feasible and elective energy storage assets [1–3]. As aided energy storage device, supercapacitors (SCs) play a significant role because of its high power output, good cycle life, excellent efficiency, and comparative safe nature [4–6]. Therefore, it have been widely utilized in electric vehicles, portable electronics, and different microdevices [7, 8] along with batteries and other electrical energy sources. Moreover, the charge storage mechanism based classification divides SCs into two types: an electrochemical double-layer capacitor (EDLC) and a pseudocapacitor [9]. Generally, pseudocapacitors deliver a higher specific capacitance due to their redox reactions [10, 11], while EDLC are proven materials considering stability. Different pseudocapacitive electrode materials, for example, polymers, metal oxides and hydroxides, sulfides, and phosphides have received tremendous exploration [12, 13]. Binary metal oxides are distinguished among these electrode materials as a promising contender for SCs because of the conjunction of two different cations. For example, CoMoO<sub>4</sub> [14], NiMoO<sub>4</sub> [15], NiCo<sub>2</sub>O<sub>4</sub> [16], NiWO<sub>4</sub> [17], NiMn<sub>2</sub>O<sub>4</sub> [18], and NiFe<sub>2</sub>O<sub>4</sub> [19] have been widely considered and explored materials for supercapacitor applications. Aside from their exceptional electrochemical properties, these binary metal oxides potentially provide stable performance as a supercapacitive material. Composition of an EDLC material with the pseudocapacitive material improves surface area, and modulates crystallinity and therefore enhances electrochemical performance and stability [20]. Considering this, several studies highlighted improvement in the material electrochemical performance [21, 22]. However, fabrication of composite material with optimum ratio of EDLC and pseudocapacitive material remains a challenge [23, 24].

In comparison to single metal oxides, bimetal oxides are able to provide better energy storage due to rearranged d-band electron density causing improvement in electrical conductivity and electrochemical stability. Pourmortazavi et al. [25] reported electrochemical synthesis of NiWO<sub>4</sub> on stainless steel (SS) substrate achieving specific capacitance ( $C_s$ ) of 468 F g<sup>-1</sup>. Packiaraj et al. [26] synthesized nanowire shaped NiWO<sub>4</sub> using hydrothermal method exhibiting  $C_s$  of 1190 F g<sup>-1</sup>. In addition, the surface modification in these bimetal oxides achieved by introduction of carbon allotropes such

as carbon nano tubes (CNTs), activated carbon (AC), graphene and its different variants to improve inpecific surface area. This can also shift average pore size distribution in favor of growing charge storage ability. One such report by Xu et al. [27] suggested improvement in surface area and reduction in average pore size from 371 to 43.5 nm which favor improvement in supercapacitive properties, using solvothermally prepared NiWO<sub>4</sub>/rGO nanocomposites. Despite these, more research needs to be done in order to optimize rGO content in NiWO<sub>4</sub>. Furthermore, amorphous phase of material provides more active sites and sustains under expansion and compression while charge storage when compared to crystalline counterpart [28]. The composition would improve porosity and facilitate 2D conducting channels in the electrode and hence enhance the stability and electrochemical capacitance. Therefore, considering above points, amorphous NiWO<sub>4</sub> composited with 2D rGO films were prepared on stainless steel (SS) substrate using a SILAR method at ambient temperature.

#### 4.2 Deposition of rGO-NiWO<sub>4</sub> electrode

#### 4.2.1 Chemicals and materials

The analytical grade chemicals (NiSO<sub>4</sub>.6H<sub>2</sub>O, Na<sub>2</sub>WO<sub>4</sub>, H<sub>2</sub>SO<sub>4</sub>, NaNO<sub>3</sub>, KMnO<sub>4</sub>, KOH), polyvinylidene fluoride (PVDF), polyvinyl alcohol (PVA) and AC were used with no further purification. For all chemical reactions, double distilled water (DDW) was used as a solvent. Prior to deposition, SS substrate of 304 grade was cleaned with smooth sand paper, ultrasonicated in DDW for 15 minutes and dried in air at room temperature.

#### 4.2.2 Synthesis of rGO

The process described is a common method for the synthesis of reduced graphene oxide (rGO) from graphite flakes. **Figure 4.1** represents a schematic flow chart of rGO synthesis. Here is a step-by-step breakdown of the process:

#### 1. Preparation of GO suspension:

- Take 2 g of graphite flakes with an average diameter of 100  $\mu$ m and place them in a 500 mL conical flask.
- Add 100 mL of concentrated H<sub>2</sub>SO<sub>4</sub> to the flask.

- Put the flask in an ice bath and continuously stir the mixture.
- Add 1 g of NaNO<sub>3</sub> to the mixture.
- Slowly add 8 g of KMnO<sub>4</sub> to the mixture while maintaining the reaction temperature below 293 K.
- Once all the KMnO<sub>4</sub> is added, keep the reaction mixture at room temperature with continuous stirring for 12 hours.
- Add 100 mL of double distilled water (DDW) to the mixture.
- After 1.5 hours, add additional 300 mL of DDW and 8 mL of  $H_2O_2$  (30%). This will result in a yellowish solution.
- Wash the mixture several times with 5% HCl followed by DDW until the pH reaches 6.5.
- 2. Determination of GO concentration and preparation of GO slurry:
  - Use the gravimetric weight difference method to determine the concentration of the GO slurry.
  - Prepare a suspension of GO at a concentration of 0.1 mg mL<sup>-1</sup> by adding the appropriate amount of the GO slurry to a solvent.
  - Sonicate the suspension for 4 hours to ensure uniform dispersion.

#### 3. Reduction of GO to rGO:

- Add 5 mL of hydrazine hydrate to the prepared GO suspension (1000 mL) and mix well.
- Keep the mixture at 368 K for 3 hours to reduce the graphene oxide sheets to reduced graphene oxide.
- Wash the resulting dispersion of rGO with DDW multiple times to remove any remaining traces of hydrazine hydrate.
- 4. Further utilization and characterization:

- The slurry of rGO can now be used for various purposes, such as deposition of thin films or other applications.
- The rGO can be characterized using different techniques to analyze its structural and functional properties.

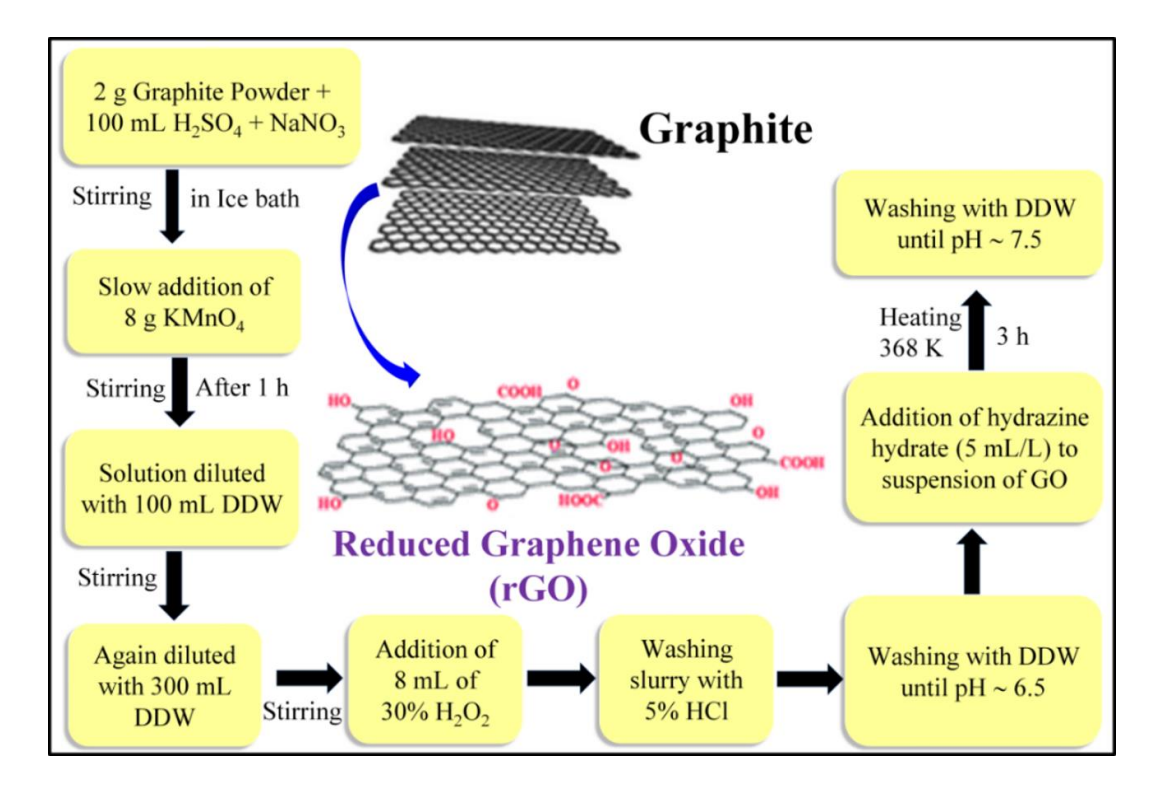


Figure 4.1: Schematic flow chart of rGO synthesis.

#### 4.2.3 Deposition of rGO-NiWO<sub>4</sub> electrode



**Figure 4.2:** The photograph of programmable SILAR coating system used for preparation of rGO-NiWO<sub>4</sub> thin films.

As reported in an earlier article rGO suspension of various concentrations of 8 to 14 mg mL<sup>-1</sup> was prepared [29]. Layered deposition of rGO sheets over a SS substrate was followed by the SILAR deposition of NiWO<sub>4</sub> nanoparticles. The principle of rGO-NiWO<sub>4</sub> thin film deposition process using SILAR method is shown in Figure 4.3. The SS substrate was submerged in rGO solution of specific concentration for 40 s to allow rGO sheets to adhere to it, and then it was dried for 40 s before immersed in the cationic solution for 15 s for the adsorption of Ni<sup>2+</sup> ions. During this adsorption, some of Ni<sup>2+</sup> ions react to charged sites of rGO sheet formed due to oxidation in acidic medium. Thereafter, SS substrate was cleaned in DDW for 5 s to pull out weakly attached Ni<sup>2+</sup> particles, and submerged in the anionic precursor for 15 s to react with WO<sub>4</sub><sup>2-</sup> and then rinsed in DDW for 5 s. Thus, a single rGO-NiWO<sub>4</sub> deposition cycle was completed, and similar 100 cycles were repeated. A HOLMARC-HOTH-03A automated SILAR coating system was used to carry out the deposition process.

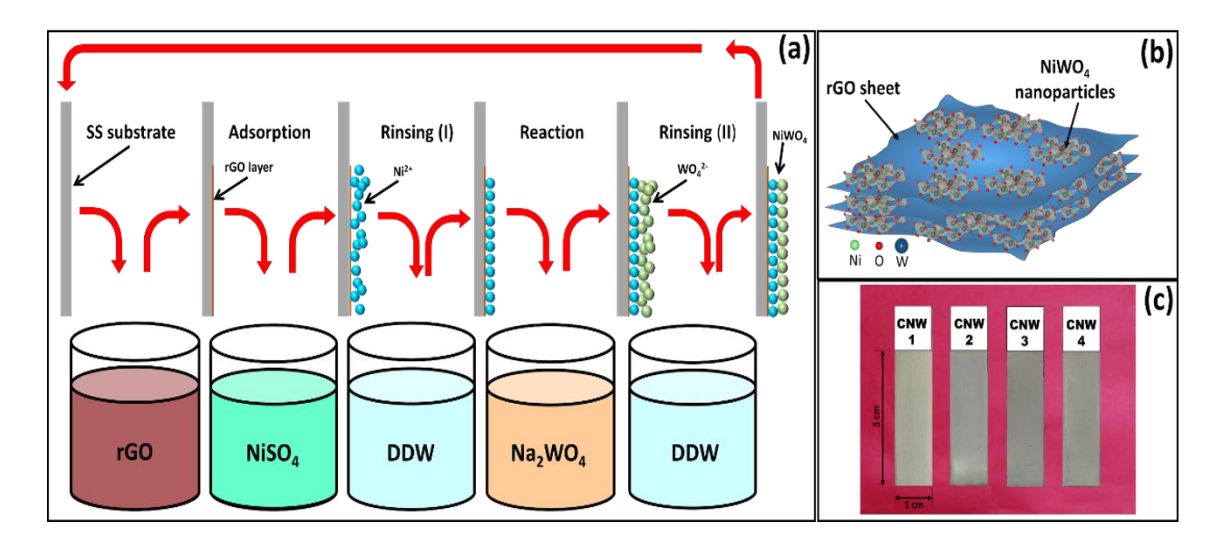


**Figure 4.3:** a) The schematic of the SILAR method employed for rGO/NiWO<sub>4</sub> thin film electrode preparation, b) schematic of formation of layered rGO/NiWO<sub>4</sub> composite material, and c) photograph of CNW series films deposited at different rGO concentrations.

To study effect of rGO variation on electrochemical properties, composite thin films with rGO dispersion concentrations of 8, 10, 12, and 14 mg mL<sup>-1</sup> were prepared and designated as CNW1, CNW2, CNW3, and CNW4, respectively. The mass loading of these films was measured using sensitive micro weight balance. The graphic of thin film development is depicted in **Figure 4.3b**. The formation of composite structure with

one by one layers of NiWO<sub>4</sub> and rGO is expected. The digital photograph of deposited thin films is shown in **Figure 4.3c**. Variation in mass loading is provided in **Figure 4.4a**. It is observed that the mass loading increased with rGO content for CNW1, CNW2, and CNW3, and decreased for CNW<sub>4</sub> due to overgrowth of material. As rGO concentration increases, the amount of rGO deposited per cycle also increases. These rGO sheets electrostatically attract more Ni<sup>2+</sup> ions, causing higher mass loading with increased rGO content.

#### 4.3 Material characterizations

#### 4.3.1 Physico-chemical characterizations

To characterize CNW thin films, Rigaku miniflex-600 X-ray diffractometer was used to examine the crystal structure operating with Cu K $\alpha$  radiation ( $\lambda = 1.54$  Å) operating at 30 kV. The functional group bonding found in the synthesized material was examined using spectroscopic study. Bruker Tensor 27 Fourier transform infrared (FT-IR) spectrometer was used to get IR absorption spectra and JASCO NRS-5100 with a wavelength of 514.4 nm was used for Raman study. With the use of a field emission scanning electron microscope (FE-SEM) (JEOL JEM 2100) attached with energy dispersive spectroscopy (EDS) systems from OXFORD instruments samples' topography and elemental composition were examined. The X-ray photoelectron spectrometer (XPS) (VG Multilab 2000, Thermo VG Scientific, U.K.) with a monochromatic Mg K (1253.6 eV) radiation source was used to examine surface chemical composition. The high resolution morphological and structural studies were performed using JEOL-ARM-200 F field emission transmission electron microscope (TEM). Using Quanta Chrome Instruments' v11.02.2.4 surface analyzer the specific surface area, and pore size distribution were acquired from the Brunauer-Emmett-Teller (BET) and Barrett-Joyner-Halenda (BJH) analytical models, respectively.

#### 4.3.1A XRD studies

The XRD patterns of CNW series thin films are shown in **Figure 4.4b**. It is observed that evident diffraction peaks from NiWO<sub>4</sub> material are absent for CNW1, CNW2, CNW3, and CNW4 thin films. The diffraction peaks marked by '\*' ascribed to the SS substrate. This concludes that the prepared composite films are amorphous in nature. Because the deposition was carried out at ambient temperature, the lowest

energy necessary for particle configurations in a specific direction is only available. As a result, particle mobility is reduced, resulting in a disturbed arrangement of particles forming amorphous thin films [30].

#### 4.3.1B FT-IR studies

The FTIR spectra for CNW series films in the 4000-400 cm<sup>-1</sup> range are shown by Figure 4.4c. The presence of O-H bond from the adsorbed water molecules is indicated by the absorption band at 3390-3428 cm<sup>-1</sup>, while the presence C=C vibrations are indicated by the band at 1605 cm<sup>-1</sup> [31]. The peaks at wavenumbers of 1384 and 1353 cm<sup>-1</sup>, correspond to the stretching frequencies of C-O-H and C=C, respectively, confirming reduction of GO during the chemical reduction process. These bonds can be ascribed to the -OH vibrations from adsorbed water, also. The weak absorption bands at wavenumber of 768 cm<sup>-1</sup> are associated to W-O bond from octahedral WO<sub>6</sub> structure vibrations related to W-O bond stretching vibrations [32]. From this analysis, it is concluded that changing rGO concentration does not change bonding in CNW film material.

#### 4.3.1C Raman studies

For a better understanding of the molecular bonding in CNW series electrodes, Raman spectra were measured (**Figure 4.4d**). The peak associated with C=C ring observed at 1609 cm<sup>-1</sup> (G band), coincides to the E2g phonon of sp2 hybridized carbon atom. The peak ascribed to vibrations from functional groups attached in oxidation process is observed at 1339 cm<sup>-1</sup> (D band). The degree of disorder and oxidation of hexagonal C=C ring is measured using intensity proportion of D band to the G band intensity ( $I_D/I_G$ ) [33]. The  $I_D/I_G$  ratio for all films remains constant, confirming very low possibility of further reduction of rGO during the deposition process. Intensity of D and G bands increases as the concentration of rGO suspension increases, indicating a higher percentage of rGO composition in CNW4 thin film compared to CNW1 thin film. The 2D and 2G bands at the wavenumbers of 2680 and 2931 cm<sup>-1</sup> confirm formation of multilayered rGO sheets. Additionally, the normal vibrational modes of NiWO<sub>4</sub> associated with peaks at 935 (O-W-O), 464, 338 (vibrations form terminal bonds in octahedral WO<sub>6</sub>) and 213 cm<sup>-1</sup> (Ni-O) in Raman spectra of CNW films series electrodes confirm the formation of NiWO<sub>4</sub> on SS substrate.

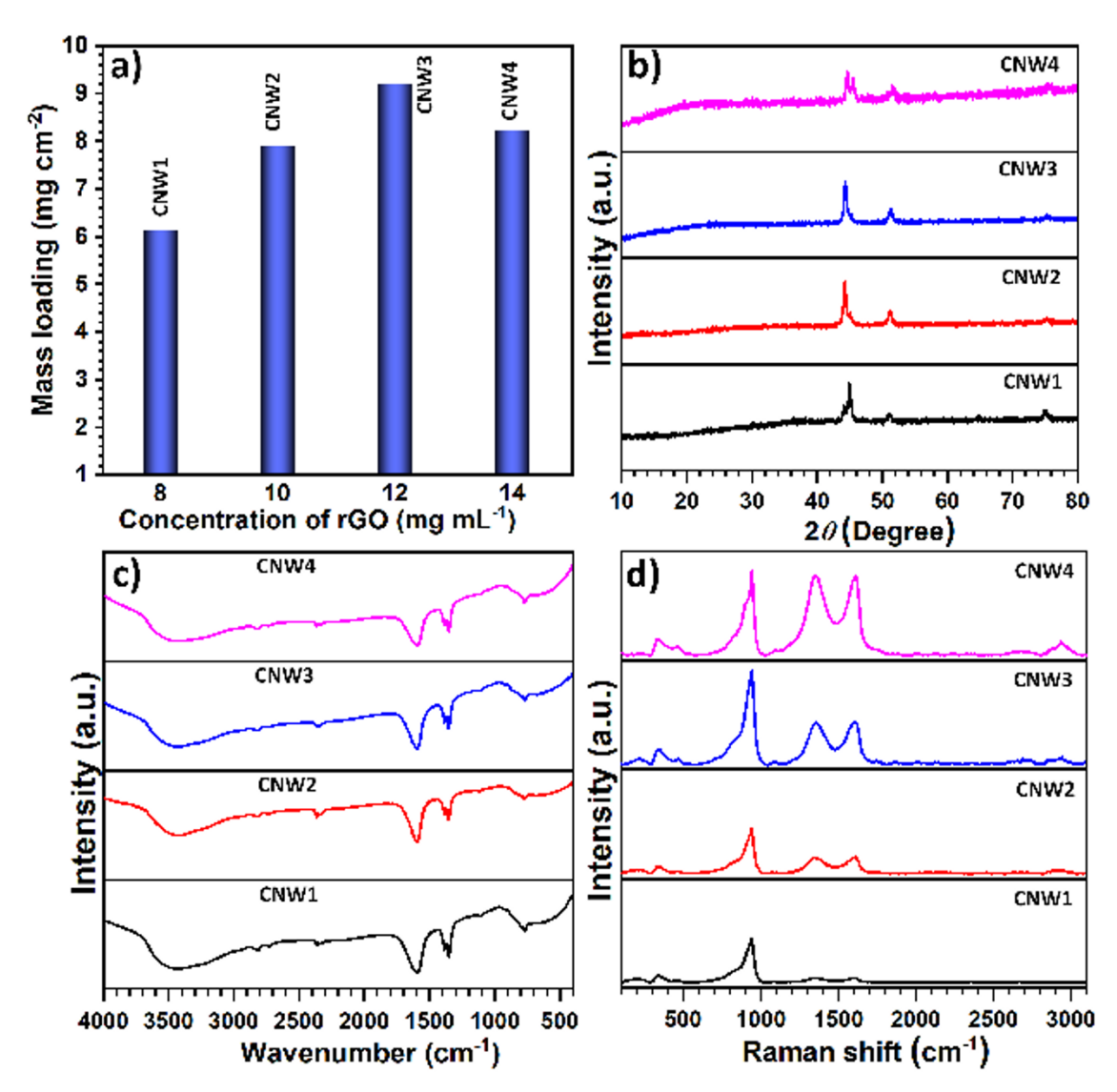


**Figure 4.4: a)** Mass loading variation with rGO concentration, **b)** XRD patterns, **c)** FTIR spectra, and **d)** Raman spectra of CNW series thin films.

#### 4.3.1D SEM studies

The SEM studies was performed to analyze morphology and elemental composition of the films. The SEM images of CNW series composite films at 10 kx and 100 kx are shown in Figure 4.5a-h. Spherical shaped NiWO<sub>4</sub> nanoparticles are uniformly distributed on surface of graphene sheets. These spherical particles may act as spacers to effectively prevent the re-staking of graphene sheets, creating evenly distributed material and porous electrode. A quick path for the movement of electrolyte ions is provided by the overlap of each individual sheet, which can also create a layered structure helpful for electrolyte diffusion and faster redox reactions.

The SEM images illustrate the surface morphology and structure of various CNW composite films at different magnifications. Images (a) and (b) focus on the CNW1 composite film. At 10 kx magnification (image a), the film displays a rough and porous surface. When magnified to 100 kx (image b), the surface reveals densely packed spherical NiWO<sub>4</sub> nanoparticles on the graphene sheets. Similarly, images (c) and (d) depict the CNW2 composite film. At 10 kx magnification (image c), the film shows a textured and porous structure. At 100 kx magnification (image d), the spherical NiWO<sub>4</sub> nanoparticles appear uniformly distributed on the graphene sheets.

The CNW3 composite film is shown in images (e) and (f). At 10 kx magnification (image e), the film's morphology is rough and porous. A closer view at 100 kx magnification (image f) highlights the presence of NiWO4 nanoparticles. Finally, images (g) and (h) present the CNW4 composite film. At 10 kx magnification (image g), the overall surface morphology is consistent with the other samples, showing a porous structure. At 100 kx magnification (image h), the spherical NiWO4 nanoparticles are clearly visible and uniformly distributed on the graphene sheets.

In all the higher magnification images (100 kx), the spherical NiWO<sub>4</sub> nanoparticles are distinctly visible and evenly dispersed. This uniform distribution helps prevent the restacking of graphene sheets, promoting the formation of a porous structure. This porous structure is beneficial for the movement of electrolyte ions, thereby enhancing the electrochemical performance of the material.

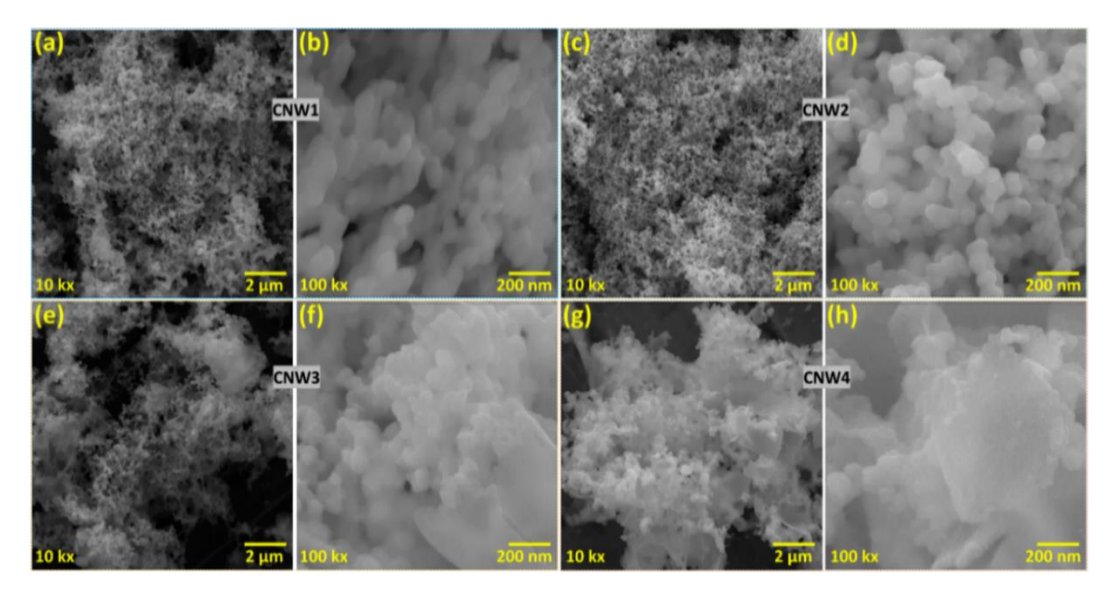


**Figure 4.5:** The FE-SEM images of **a, b)** CNW1, **c, d)** CNW2, **e, f)** CNW3, **g, h)** CNW4 at magnifications of 10 kX and 100 kX.

#### 4.3.1E TEM and HR -TEM study

The TEM images of CNW3 composite (**Figure 4.6a, b**) show spherical microparticles stacked together, consistent with the SEM observation. The material particles do not show any fringe patterns in HR-TEM imaging, as illustrated in **Figure 4.6c**. This strengthens observation from XRD that the formed material is amorphous. However, observation of diffuse circular rings in selected area electron diffraction (SEAD) pattern of TEM (**Figure 4.6d**) suggests amorphous material formation with short range order. In addition, the elemental composition and distribution of CNW2 film were obtained through EDS analysis (**Figure 4.6e-i**). The results confirmed a uniform distribution of constituent elements, namely Ni, W, O, and C. This uniform distribution across the film suggests a homogeneous incorporation of these elements, supporting the integrity and consistency of the composite material.

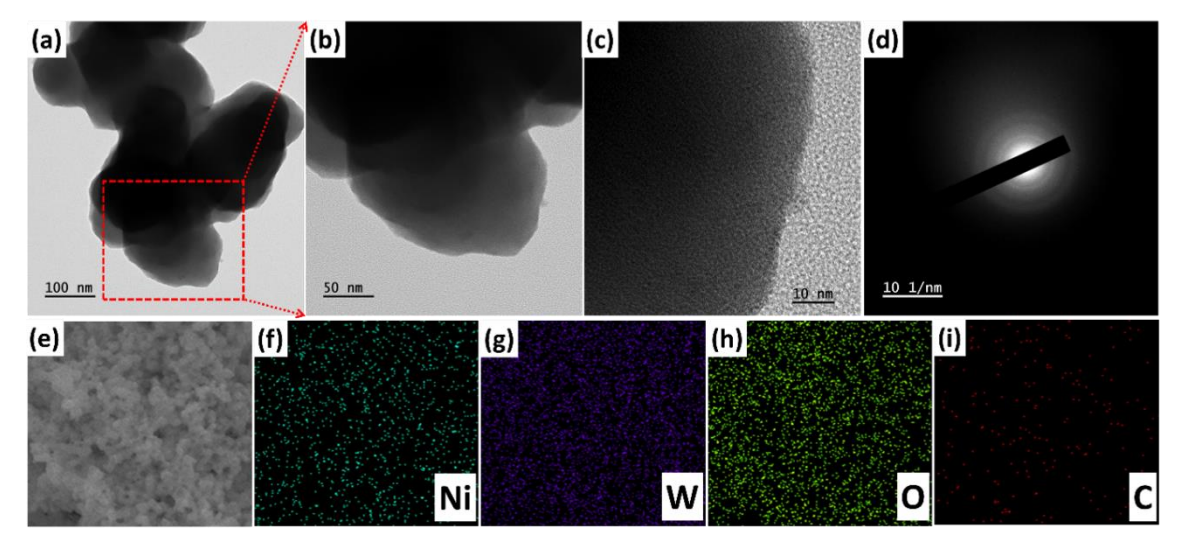


**Figure 4.6: a-c**) The TEM images, and **d**) SEAD pattern of CNW3, The EDS elemental mapping of **e**) CNW2, **f**) Ni, **g**) W, **h**) O, and **i**) C.

#### 4.3.1F XPS study

The XPS analysis was carried out to examine the chemical bonding state and composition of material surface of the deposited films, and the survey spectrum of CNW2 are presented in **Figure 4.7a**. Comparative XPS spectra of all other films are provided in **Figure 4.8**. The spectrum of CNW2 shows peaks corresponding to the signals of Ni2p, C1s, O1s, and W4f, confirming presence of Ni, C, O, and W elements. The spin-orbit doublets typical of Ni2p<sub>3/2</sub> and Ni2p<sub>1/2</sub> are visible in the Ni2p spectra (**Figure 4.7b**) at 856.6 and 874.2 eVs, respectively. Additionally, they have satellite

peaks at 862.6 and 880.6 eVs [34]. Moreover, W4f spectrum (Figure 4.7c) shows two peaks corresponding to W4f<sub>7/2</sub> and W4f<sub>5/2</sub> at binding energies of 35.3 and 37.5 eV, respectively [35, 36]. Three peaks observed in C1s spectrum (Figure 4.7d) of CNW2, each with a binding energy of 284.8 eV (sp2 hybridized carbon in graphene), 286.3 eV (C-OH and C=O functional groups), and 288.2 eV (O-C=O functional group) [37]. Three peaks in O1s spectrum (Figure 4.7e) correspond to conventional metal-oxygen bonds (530.32 and 531.48 eV) and oxygen attached to different hybridized carbon atoms (532.8 eV), respectively. Similar XPS spectra were observed for all prepared films, indicating the composite nature of the films and no large change in the surface composition. Due to even distribution of rGO and NiWO<sub>4</sub> in the film, XPS spectra do not show any large change. The XPS analysis support presence of Ni as Ni<sup>2+</sup> and Ni<sup>3+</sup>, W as W<sup>6+</sup>, and C as C<sup>4+</sup> and O as O<sup>2-</sup> in composite thin film.

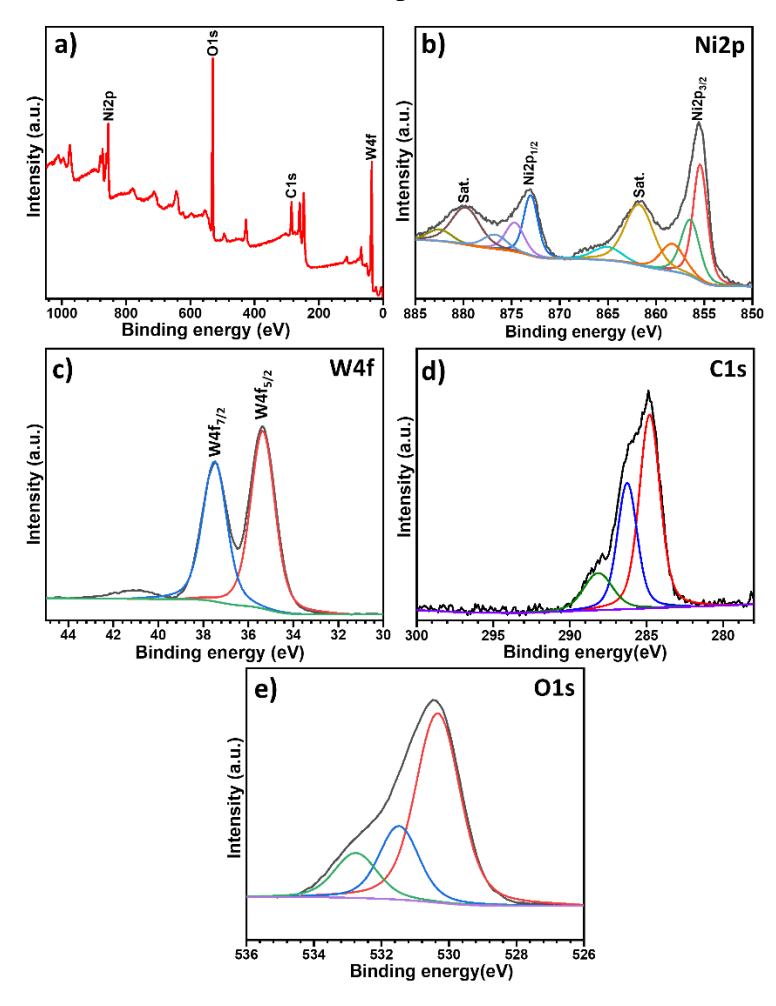


**Figure 4.7: a)** Survey spectrum of rGO-NiWO<sub>4</sub> electrode and wide scan XPS spectra of **b)** Ni2p, **c)** W4f, **d)** C1s, and **e)** O1s.

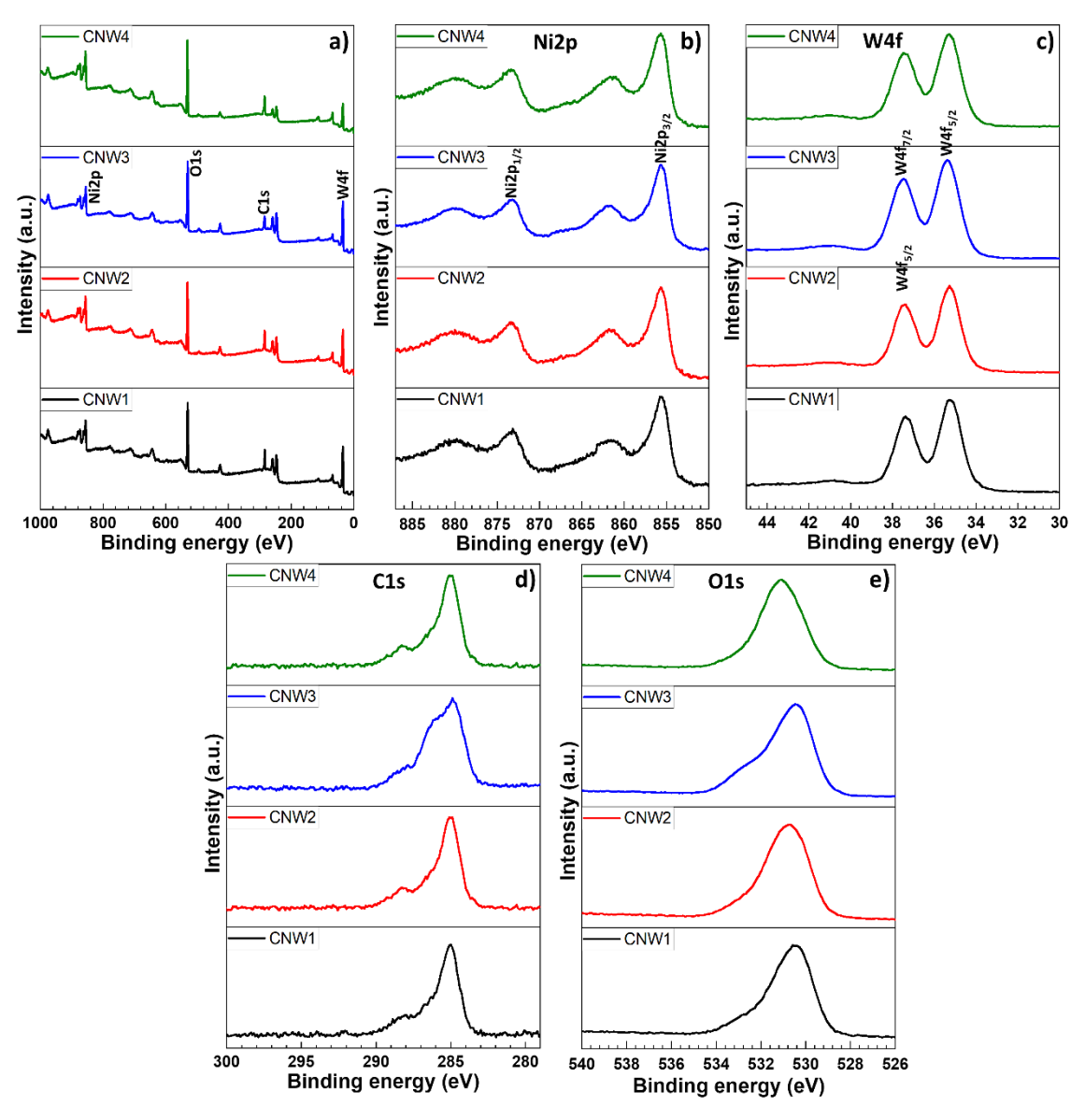


**Figure 4.8:** The XPS spectra of **a**) survey spectra of rGO-NiWO<sub>4</sub> electrodes, and wide scan XPS spectra of **b**) Ni2p, **c**) W4f, **d**) C1s, and **e**) O1s from CNW series.

#### 4.3.1G BET and BJH studies

The specific surface area and pore structure of rGO-NiWO<sub>4</sub> composite were measured using the Brunauer Emmette Teller (BET) technique. The BET surface areas of thin film electrodes CNW1, CNW2, CNW3, and CNW4 are 85, 90, 97, and 107 m<sup>2</sup> g<sup>-1</sup>, respectively (**Figure 4.9a-d**). Presence of increased rGO content leads to improvement in specific surface area from CNW1 to CNW4 thin film electrodes.

However, while the rGO addition improves the specific surface area, it does not have a notable impact on the pore size distribution of the thin films. All the CNW series films maintain a mesoporous structure with average pore sizes ranging between 6.8 and

7.1 nm, as shown in **Figure 4.10**. This consistency in pore size suggests that while rGO enhances the surface area, it does not significantly alter the average pore size or the overall pore structure of the material.

#### Types of B-H curves:

The B-H curves, also known as hysteresis loops, are utilized to analyze the magnetic properties of materials used in supercapacitor electrodes and other components. There are several types of B-H curves relevant to supercapacitors, each offering unique insights into the material suitability for specific applications.

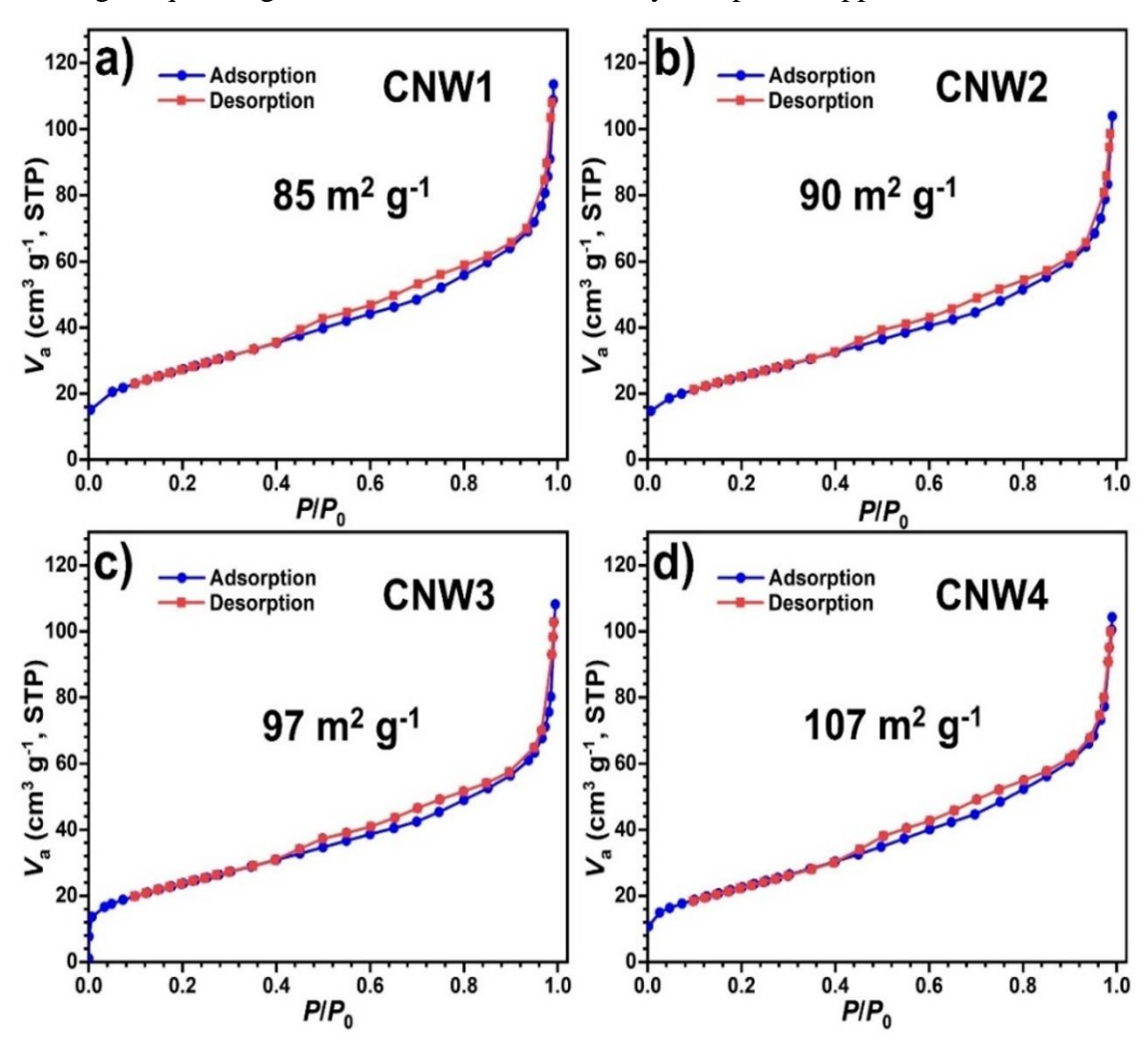


Figure 4.9: The BET isotherms of a) CNW1, b) CNW2, c) CNW3, and d) CNW4.

The linear B-H curve, representing materials with minimal hysteresis like soft magnetic materials, shows a direct and proportional relationship between the magnetic field (H) and magnetic flux density (B). This type of material is often used in supercapacitor applications that demand high efficiency and minimal energy loss.

Nonlinear B-H curves, exhibited by materials that do not have a linear relationship between B and H, reveal a more complex interaction between the magnetic field and flux density, often due to varying magnetic permeability. These materials are suitable for supercapacitor applications that require tailored magnetic responses.

Hysteresis B-H curves are characteristic of ferromagnetic materials with significant hysteresis. These curves form a loop, indicating energy loss due to internal friction and the alignment of magnetic domains. Such materials are used in supercapacitor components that require robust magnetic properties but can tolerate some energy loss. Finally, saturation B-H curves represent materials that reach a point of magnetic saturation. Beyond this point, increases in the magnetic field do not significantly enhance the magnetic flux density. These materials are crucial for applications where supercapacitors are subjected to high magnetic fields, ensuring that the materials can handle extreme conditions without losing performance. Each type of B-H curve is instrumental in determining the efficiency, energy density, and durability of materials used in supercapacitors.

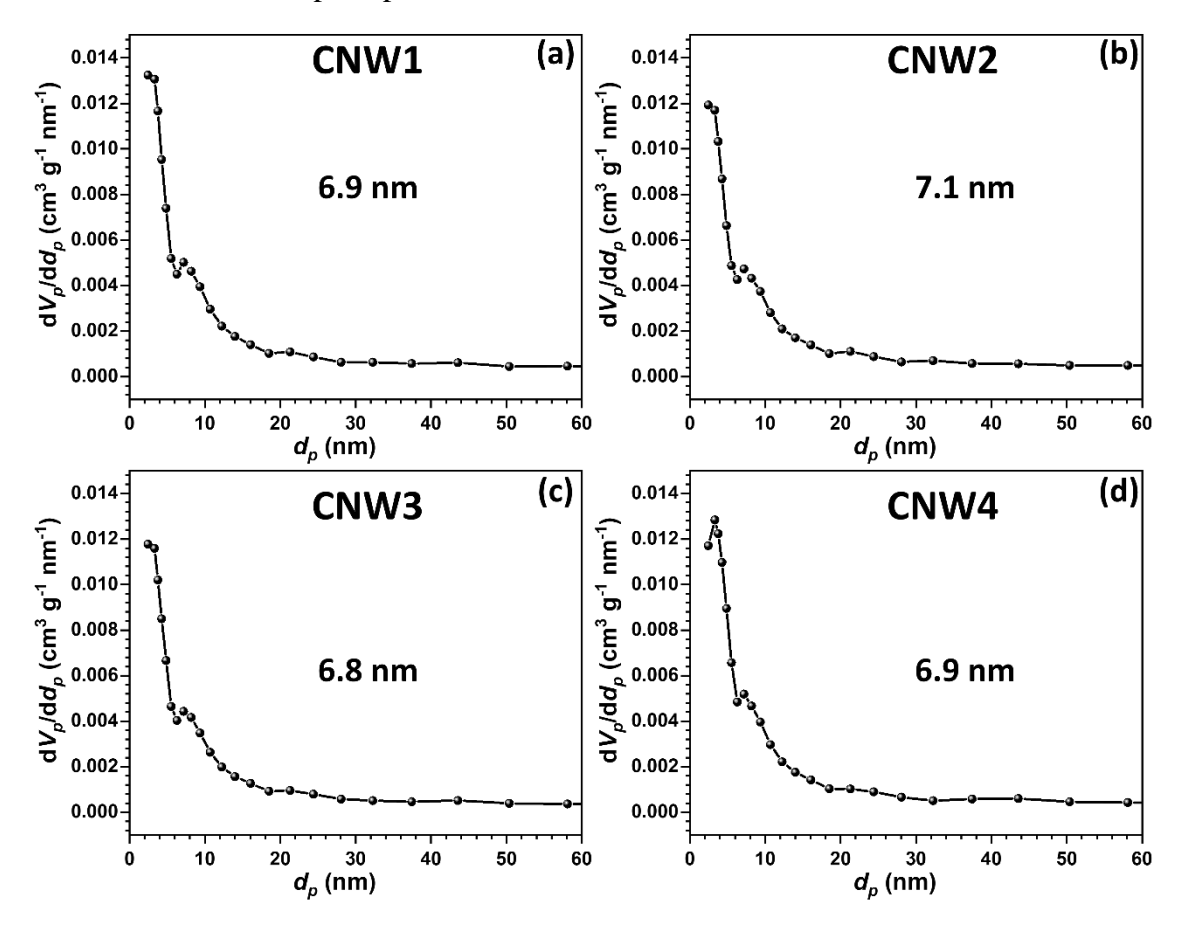


Figure 4.10: Pore size distributions of a) CNW1, b) CNW2, c) CNW3, and d) CNW4.

#### 4.3.2 Electrochemical study of rGO-NiWO<sub>4</sub>

#### 4.3.2A CV studies

The electrochemical measurements of CNW thin films were carried out in the potential window of 0 to +0.6 V vs Hg/HgO. The comparative CV curves presented in Figure 4.11a indicate that CNW3 thin film provides higher current response than other CNW series electrodes, at scan rate of 100 mV s<sup>-1</sup>. As CNW3 has higher mass loading with the highest specific surface area, the highest specific capacitance is identical with the mass loading. The non-rectangular shape of the CV curves shows the existence of pseudocapacitive charge storage mechanism. The CV curves for CNW1, CNW2, CNW3, and CNW4 electrodes at scan rates ranging from 2, 5, 10, 20, 50 and 100 mV s<sup>-1</sup> are shown in Figure 4.11b-e.

The power law in cyclic voltammetry provides valuable information about the kinetics and mechanisms of redox reactions occurring at electrodes. Its importance lies in its ability to elucidate reaction mechanisms, characterize electrodes, and ensure the reliability of electrochemical measurements. Hence, analysis of CV measurements was performed using power law[38], given in Eq. 3.5.

i.e. 
$$i_p = av^b$$

here  $i_p$  is peak current measured at oxidation potential, a and b are variables. The value of b ranges from 0.5 to 1, depending on the dominant charge storage mechanism [39]. If value of b is near 0.5, charge storage is dominantly at the inner side of electrode, causing electrolyte diffusion, and if b=1, surface adsorption and surface redox reactions dominate overall charge storage [40]. The values of b calculated for CNW series electrodes from graph of log i vs log v (Figure 4.11f) are 0.50, 0.51, 0.53 and 0.52 for CNW1, CNW2, CNW3, and CNW4, respectively. Unchanged b-value with rGO content indicates dominant role of NiWO<sub>4</sub> in charge storage. The rGO provided charge transfer channels as well as acts as a spacer that eventually results in smaller particle formations and these smaller particles of NiWO<sub>4</sub> sandwiched between rGO sheets undergo redox reactions rapidly [41, 42]. The comparative CV curves indicate that CNW3 thin film provides higher current response than other CNW series electrodes, at scan rate of 2 to 100 mV s<sup>-1</sup>. As CNW3 has higher mass loading with the highest specific surface area, the highest specific capacitance is identical with the mass loading. Hence CNW3 electrode is selected as anode for ASC.

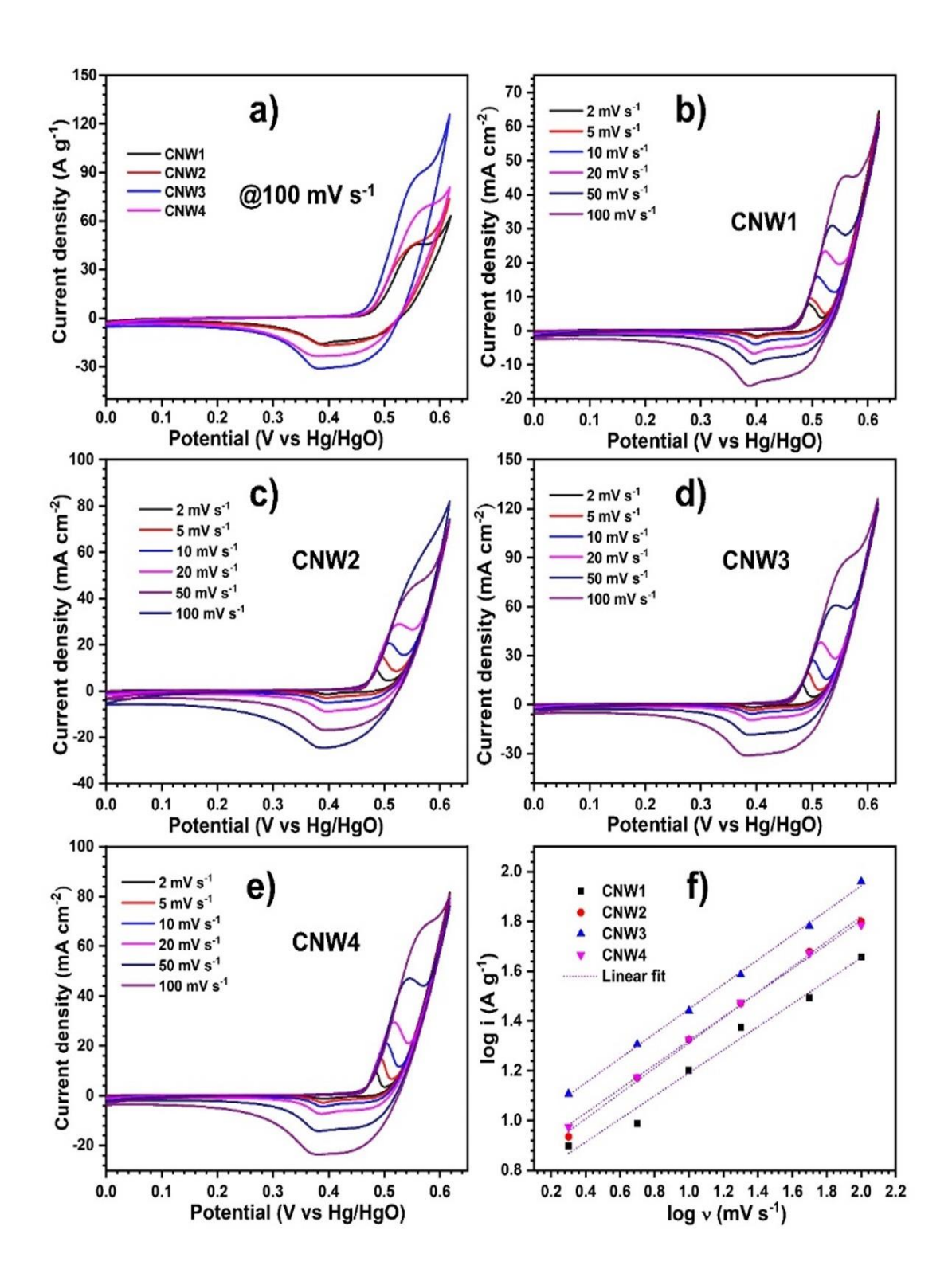


**Figure: 4.11a**) Comparative CV curves of rGO-NiWO<sub>4</sub> thin films deposited at different concentrations of rGO at scan rate of 100 mV s<sup>-1</sup>, CV scan rates of **b**) CNW1, **c**) CNW2, **d**) CNW3, **e**) CNW4 at scan rates of 2 to 100 mV s<sup>-1</sup>, and **f**) graph of log i vs log v.

#### 4.3.2B GCD studies

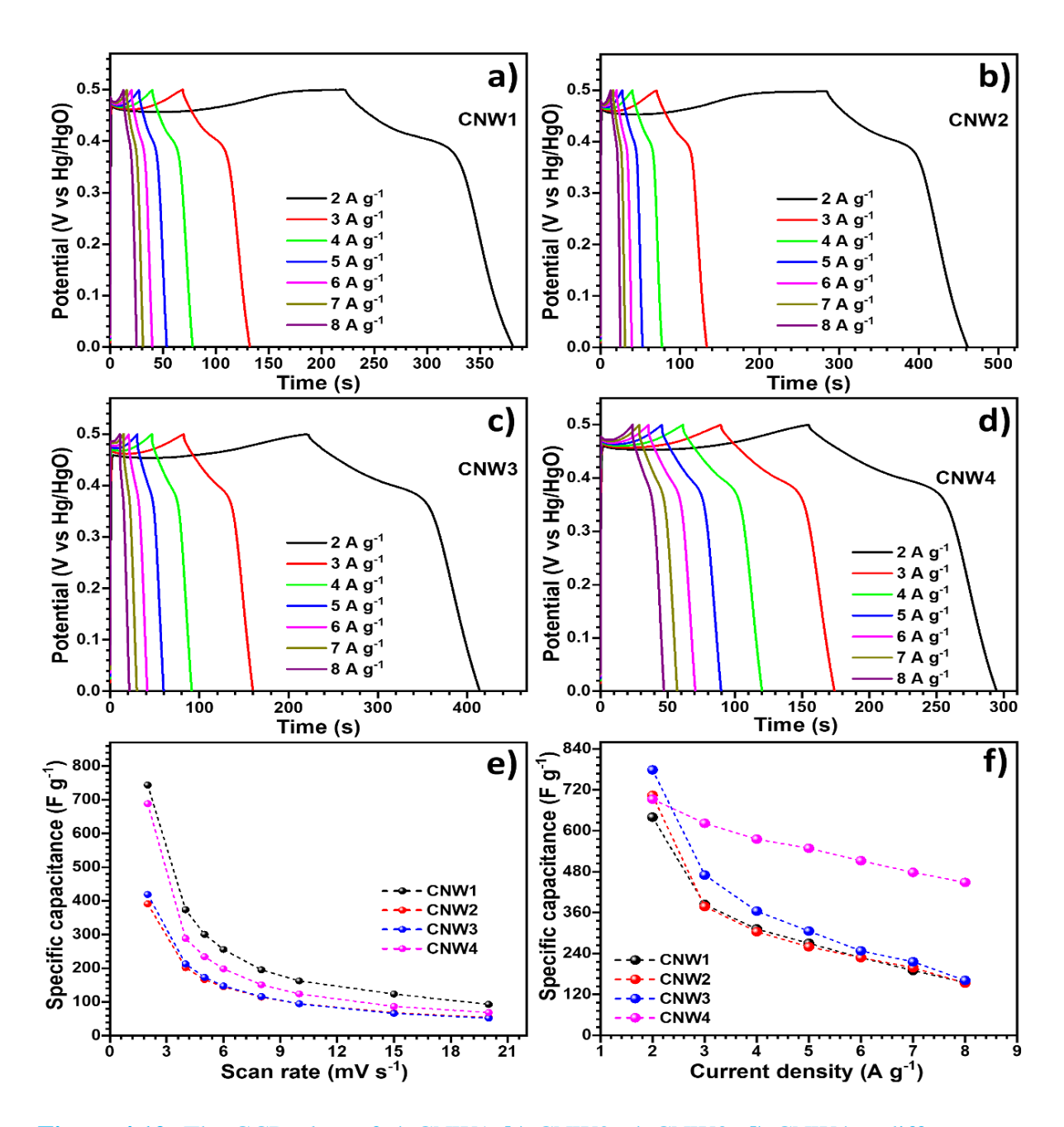


**Figure 4.12:** The GCD plots of **a**) CNW1, **b**) CNW2, **c**) CNW3, **d**) CNW4 at different current densities, **e**) variation of  $C_s$  with scan rate, and **f**) variation of  $C_s$  with current densities.

The GCD plots of CNW1, CNW2, CNW3, and CNW4 at current densities from 2 to 8 A g<sup>-1</sup> are expressed in **Figure 4.12a-d**. The *C*<sub>s</sub> values of CNW1, CNW2, CNW3, and CNW4 calculated from GCD at current density of 2 A g<sup>-1</sup> are 640, 704, 779, and

693 F g<sup>-1</sup>, respectively. The specific capacity of CNW3 electrode is 108.2 mAh g<sup>-1</sup>. The Coulombic efficiencies of CNW1, CNW2, CNW3, and CNW4 thin films are 72, 63, 88, and 91 %, respectively. The improved coulombic efficiencies with rGO content may be related with rGO that facilitates charge transfer channels. As can be in **Figure 4.12e-f**, decrease in Cs with increasing scan rate and current densities for all films. This behaviour was attributed to the limited time available for reversible redox processes at higher scan rates and current densities. The phenomenon was particularly pronounced at faster charging-discharging rates, where the electrode materials exhibited decreased utilization efficiency.

In conclusion, the GCD study provided valuable insights into the electrochemical performance of CNW1, CNW2, CNW3, and CNW4 thin films. The incorporation of rGO was found to positively impact coulombic efficiencies, while the diminishing Cs at higher scan rates underscored the challenges associated with rapid charging-discharging rates in electrode materials.

#### 4.3.2C EIS studies

The supercapacitive nature of rGO-NiWO<sub>4</sub> films, with low solution ( $R_s$ ) and charge transfer ( $R_{ct}$ ) resistances, is confirmed by Nyquist plot given in **Figure 4.13a**. For CNW1, CNW2, CNW3, and CNW4 thin films, values of  $R_s$  are 0.56, 0.53, 0.60, and 0.49 cm<sup>2</sup>, and those of  $R_{ct}$  are 38.9, 42.3, 45.3, and 48.03 cm<sup>2</sup>, respectively. The low solution resistances  $R_s$  indicated efficient electrolyte penetration and ionic conduction within the porous structure of the films, and low  $R_{ct}$  values implied facile electron transfer at the electrode-electrolyte interface, indicating excellent charge transfer kinetics. This was crucial for the rapid redox reactions that occurred during the electrochemical processes. CNW3 is the best electrode among the options provided due to its optimal combination of low solution resistance and low charge transfer resistance, indicating efficient electrolyte penetration and excellent charge transfer kinetics, which are essential for high-performance supercapacitors.

Inclusion of rGO in NiWO<sub>4</sub> optimizes the electrode conductivity, stability, interface characteristics, and electron transport, and collectively enhances its electrochemical performance.

| Table 4.1: Electrochemica | impedance s | pectroscopic data | a of CNW electrodes. |
|---------------------------|-------------|-------------------|----------------------|
|---------------------------|-------------|-------------------|----------------------|

| Electrodes | $R_{\rm s}$ ( $\Omega$ cm <sup>-2</sup> ) | $R_{\rm ct}(\Omega~{\rm cm}^{-2})$ | C <sub>dl</sub> (F) | $W\left( \mathbf{m}\Omega ight)$ |
|------------|---|------------------------------------|---------------------|----------------------------------|
| CNW1       | 0.56                                      | 38.90                              | 0.891               | 1.56                             |
| CNW 2      | 0.53                                      | 42.30                              | 0.932               | 1.89                             |
| CNW 3      | 0.60                                      | 45.30                              | 0.879               | 4.23                             |
| CNW 4      | 0.49                                      | 48.03                              | 0.735               | 6.45                             |

Table 4.1 summarizes  $R_s$ ,  $R_{ct}$ ,  $C_{dl}$ , and W values calculated from the observed values. For CNW1, CNW2, CNW3, and CNW4 thin films, values of  $R_s$  are 0.56, 0.53, 0.60, and 0.49 Ω cm<sup>2</sup>, and those of  $R_{ct}$  are 38.9, 42.3, 45.3, and 48.03 Ω cm<sup>2</sup>, respectively, also Warburg constant (W) are 1.56, 1.89, 4.23 and 6.45 mΩ respectively.

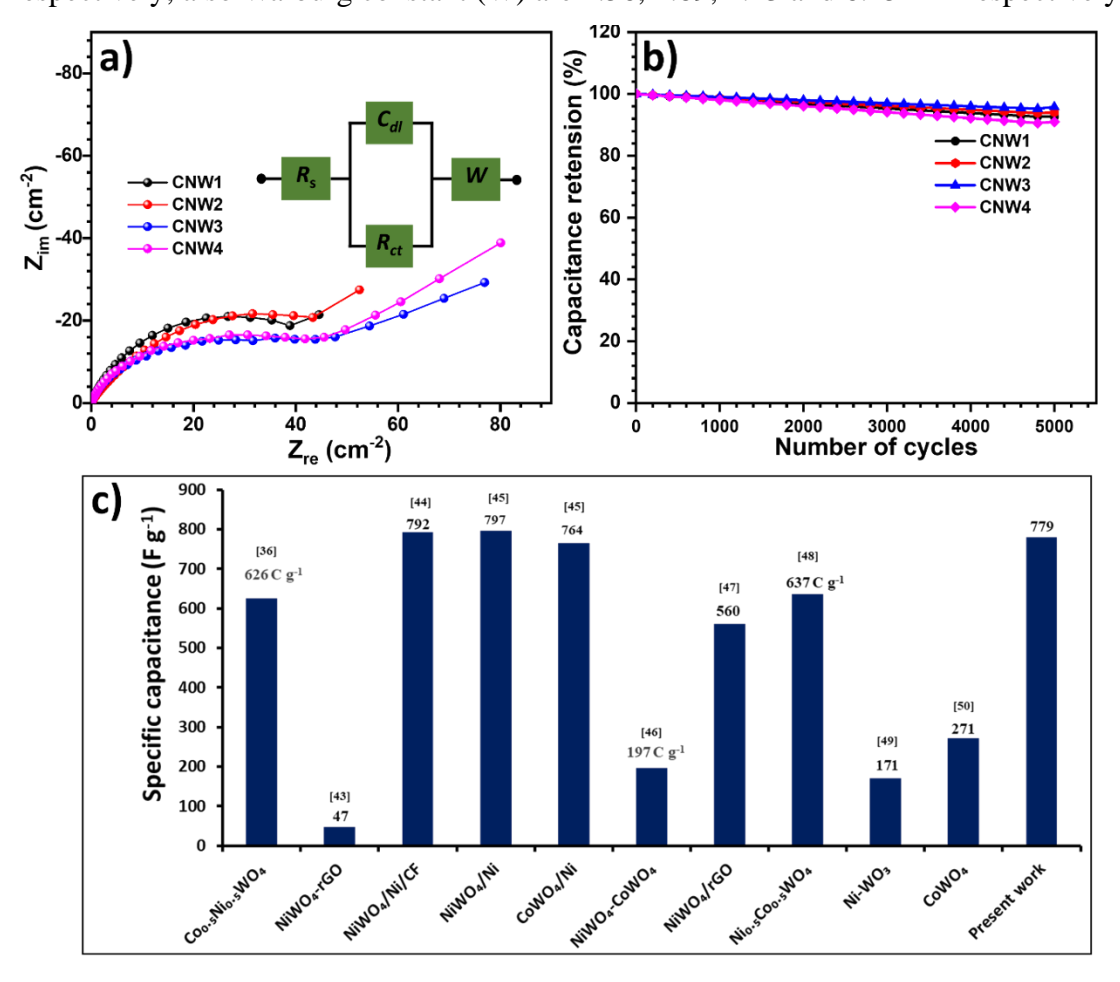


**Figure 4.13: a)** The Nyquist plots (inset shows electrical equivalent circuit), and **b)** stability curves of rGO/NiWO<sub>4</sub> electrodes, and **c)** comparison of  $C_s$  of tungstate materials reported earlier with present study.

#### 4.3.2D Stability studies

To evaluate electrochemical stability, GCD cycles with an applied current density of 4 A g<sup>-1</sup> were repeated for 5000 cycles. Figure 4.13b represents the electrodes capacitance retention for 5000 GCD cycles. Capacitance retentions of 92, 94, 95, and 90% are observed for CNW1, CNW2, CNW3, and CNW4 thin film electrodes, respectively. The differences in capacitance retentions among the CNW thin film electrodes indicate that the choice of CNW type or other factors in the electrode fabrication process can influence stability. The differences in capacitance retentions among the CNW thin film electrodes indicate that the choice of CNW thin film electrode fabrication process can influence stability. CNW3 shows the highest capacitance retention at 95%, suggesting that it may have superior stability compared to the other CNW thin film.

In the electrode CNW, rGO serves vital functions. It enhances electrical conductivity, promoting efficient electron transfer at the electrode-electrolyte interface, thereby reducing impedance and improving electrochemical performance. Additionally, rGO contributes to electrode stability, maintaining structural integrity over charge-discharge cycles for consistent performance. Its presence modifies the electrode-electrolyte interface, influencing charge transfer kinetics and ion diffusion, as observed in electrochemical impedance spectroscopy (EIS) studies. Moreover, rGO acts as a conduit for electron transport within the electrode, facilitating rapid charge transfer between NIWO<sub>4</sub> and the current collector, resulting in improved charge/discharge rates and capacity retention.

The electrochemical stability of thin film electrodes is influenced by a combination of material properties, electrode structure, electrolyte composition, cycling conditions, and surface modifications. The observed capacitance retentions provide valuable insights into the performance of the different electrodes over an extended cycling period.

Specific capacitance and stability of CNW3 electrode (779 F g<sup>-1</sup>/95%) are comparable to recently reported nickel based materials,  $Co_{0.5}Ni_{0.5}WO_4$  (626 C g<sup>-1</sup>/105) [36], NiWO<sub>4</sub>-rGO (47/75%) [43], NiWO<sub>4</sub>/Ni/CF (792/97) [44], NiWO<sub>4</sub>/Ni (797/206) [45], CoWO<sub>4</sub>/Ni (764/281) [45], NiWO<sub>4</sub>-CoWO<sub>4</sub> (197 C g<sup>-1</sup>/-) [46], NiWO<sub>4</sub>/rGO

(560/92) **[47]**, Ni<sub>0.5</sub>Co<sub>0.5</sub>WO<sub>4</sub> (637 C g<sup>-1</sup>/92) **[48]**, Ni-WO<sub>3</sub> (171/-) **[49]**, and CoWO<sub>4</sub> (271/86) **[50]**. Pictorial presentation of this comparison is shown in **Figure 4.13c** and stability of materials is compared in **Figure 4.14**. The moderate stability and highest electrochemical parameters obtained for CNW3 due to optimised rGO and NiWO<sub>4</sub> concentration confirm suitability of preparation method for binder-free composite material deposition.

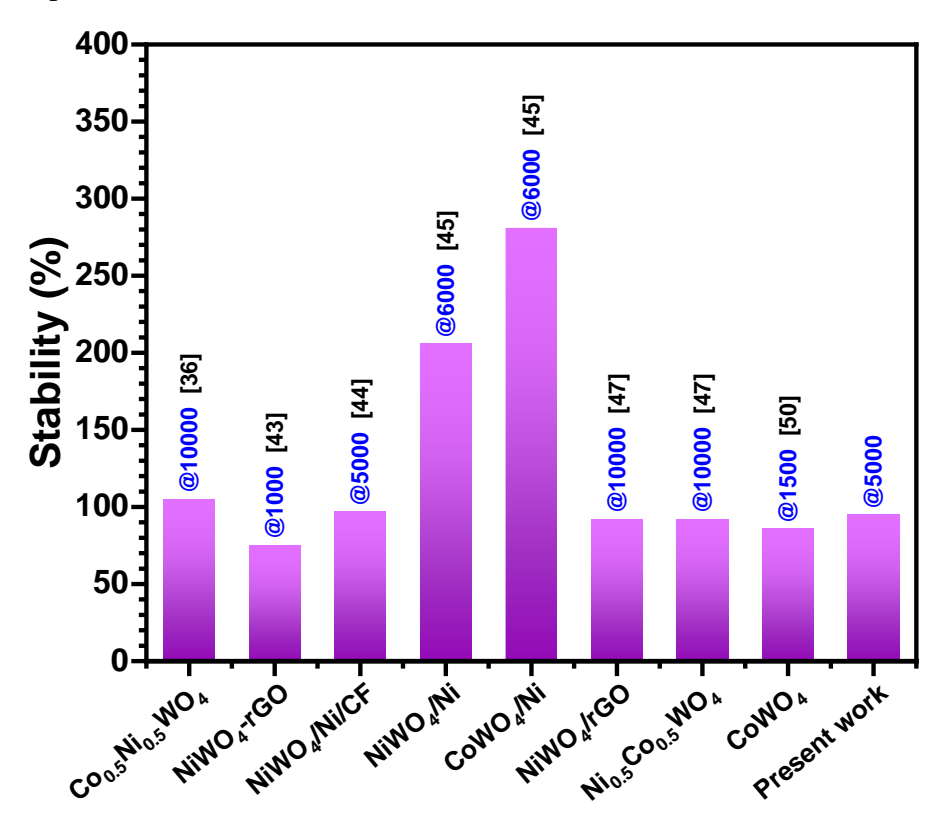


**Figure 4.14:** Comparison of electrochemical stability of tungstate materials reported earlier with the present study.

#### 4.4 Conclusions

The facial SILAR method is utilized for the deposition of thin films of rGO-NiWO<sub>4</sub> composite on SS substrates. Electrodes with a concentration of 12 mg mL<sup>-1</sup> of rGO exhibit spherical morphology of NiWO<sub>4</sub> on rGO sheets and a surface area of 97 m<sup>2</sup>g<sup>-1</sup>. This electrode demonstrates the highest specific capacitance among the tested samples and maintains 95% retention after 5000 cycles.

In comparison, for pristine material, an optimum concentration of 0.15 M of NiSO<sub>4</sub> is determined, as concentrations beyond this led to nonadherent thin films. The

specific capacity of NiWO<sub>4</sub> is found to be 213 mAh g<sup>-1</sup>, with 87% retention after 5000 cycles.

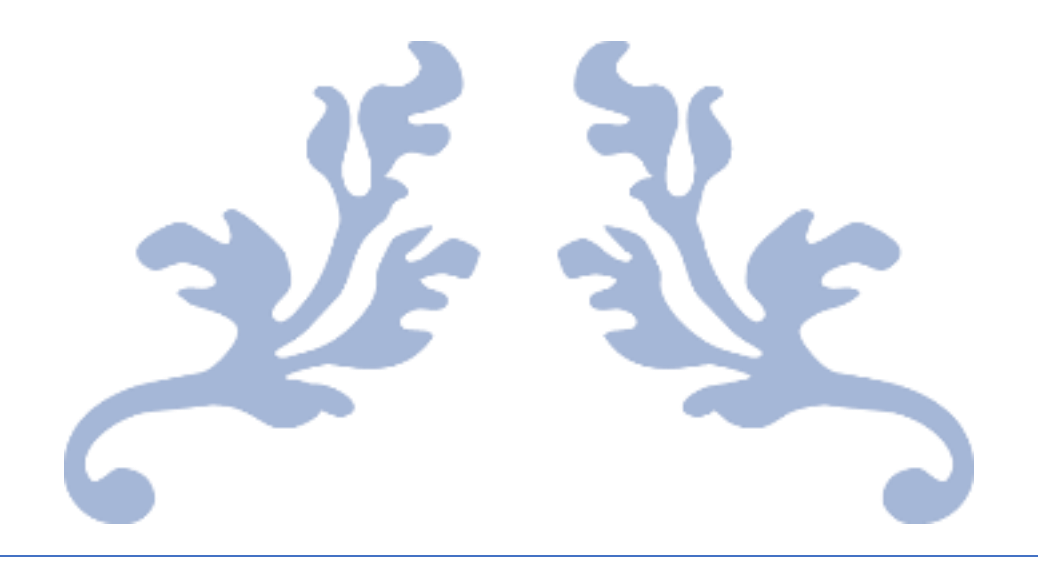
The study highlights the effectiveness of the facial SILAR method in fabricating rGO-NiWO<sub>4</sub> composite electrodes with superior electrochemical performance, showing potential for energy storage applications.

#### **References:**

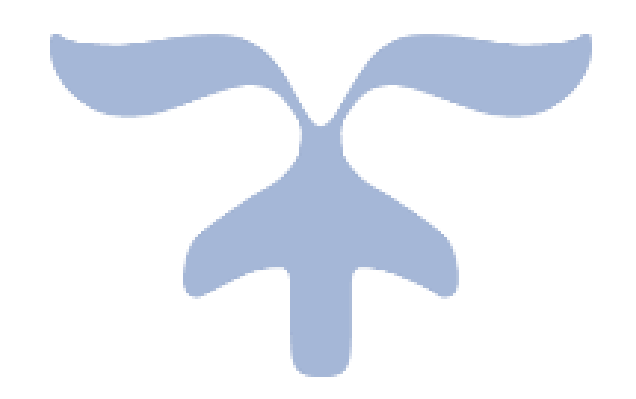
- [1] P. Chen, C. Yang, P. Gao, X. Chen, Y.J. Cheng, J. Liu, K. Guo, Chem. Mater., 34, 2022, 5896.
- [2] M. Pershaana, S. Bashir, S. Ramesh, K. Ramesh, J. Energy Storage., 50, 2022, 104599.
- [3] S. Rawat, R.K. Mishra, T. Bhaskar, Chemosphere, 286, 2022, 131961.
- [4] J. Yan, T. Liu, X. Liu, Y. Yan, Y. Huang Coord. Chem. Rev., 452, 2022, 214300.
- [5] F. Xing, Z. Bi, F. Su, F. Liu, Z.S. Wu, Adv. Energy Mater., 12, 2022, 1.
- [6] T. Xu, Z. Li, D. Wang, M. Zhang, L. Ai, Z. Chen, J. Zhang, X. Zhang, L. Shen, Adv. Funct. Mater., 32, 2022, 2205637.
- [7] S. Shahzad, A. Shah, E. Kowsari, F.J. Iftikhar, A. Nawab, B. Piro, M.S. Akhter, U.A. Rana, Y. Zou, Glob. Challenges., 3, 2019, 1800023.
- [8] A. Beaucamp, M. Muddasar, T. Crawford, M.N. Collins, M. Culebras, Int. J.Biol. Macromol., 221, 2022, 1142.
- [9] P. Sathish Kumar, P. Prakash, A. Srinivasan, C. Karuppiah, J. Power Sources., 482, 2021, 228892.
- [10] A. Tiwari, V. Singh, T.C. Nagaiah, ACS Appl. Mater. Interfaces. 11, 2019, 19 21465.
- [11] M.B. Poudel, H.P. Karki, H.J. Kim, J.Energy Storage., 32, 2020, 101693.
- [12] H. Zhao, Z. Zhang, C. Zhou, H. Zhang, Appl. Surf. Sci., 541, 2021, 148458.
- [13] M. Ikram, Y. Javed, N.A. Shad, M.M. Sajid, M. Irfan, A. Munawar, T. Hussain, M. Imran, D. Hussain, J. Alloys Compd., 878, 2021, 160314.
- [14] Q. Li, Y. Li, J. Zhao, S. Zhao, J. Zhou, C. Chen, K. Tao, R. Liu, L. Han, J. Power Sources., 430, 2019, 51.
- [15] E. Murugan, S. Govindaraju, S. Santhoshkumar, Electrochim. Acta., 392, 2021, 138973.

- [16] S. Wei, C. Wan, L. Zhang, X. Liu, W. Tian, J. Su, W. Cheng, Y. Wu, Chem. Eng. J., 429, 2022, 132242.
- [17] X. Guo, M. Li, Y. Liu, Y. Huang, S. Geng, W. Yang, Y. Yu J. Colloid Interface Sci., 563, 2020, 405.
- [18] A. Ray, A. Roy, M. Ghosh, J. Alberto Ramos-Ramón, S. Saha, U. Pal, S.K. Bhattacharya, Appl. Surf. Sci., 463, 2019, 513.
- [19] P.D. Patil, S.R. Shingte, V.C. Karade, J.H. Kim, T.D. Dongale, S.H. Mujawar, A.M. Patil, P.B. Patil, J. Energy Storage., 40, 2021, 102821.
- [20] Y.A. Kumar, K.D. Kumar, H.J. Kim, Electrochim. Acta., 330, 2020, 135261.
- [21] A. Borenstein, O. Hanna, R. Attias, S. Luski, T. Brousse, D. Aurbach, J. Mater. Chem., A. 5, 2017, 12653.
- [22] M. Cui, X. Meng, Nanoscale Adv., 2, 2020, 5516.
- [23] J. Zhu, Q. Wu, J. Li, ChemistrySelect., 5, 2020, 10407.
- [24] Y. Li, X. Han, T. Yi, Y. He, X. Li, J. Energy Chem., 31, 2019, 54.
- [25] S. M. Pourmortazavi, M. Rahimi-Nasrabadi, M. S. Karimi, S. Mirsadeghi, New J. Chem., 42, 2018, 19934.
- [26] R. Packiaraj, P. Devendran, K.S. Venkatesh, N. Nallamuthu, Inorg. Chem. Commun., 126, 2021, 108490.
- [27] X. Xu, L. Pei, Y. Yang, J. Shen, M. Ye, J. Alloys Compd., 654, 2016, 23.
- [28] O. Li, Y. Xu, S. Zheng, X. Guo, H. Xue, H. Pang, Small., 14, 2018, 1800426.
- [29] D. B. Malavekar, V. C. Lokhande, V. J. Mane, S. B. Kale, R. N. Bulakhe, U. M. Patil, I. In, C. D. Lokhande, J. Solid State Electrochem., 24, 2020, 2963.
- [30] G. C. Zhang, M. Feng, Q. Li, Z. Wang, Z. Fang, Z. Niu, N. Qu, X. Fan, S. Li, J. Gu, J. Wang, D. Wang, ACS Appl. Mater. Interfaces., 14, 2022, 2674.
- [31] K. S. Anuratha, Y. Z. Su, M.K. Huang, C. K. Hsieh, Y. Xiao, J. Y. Lin, J. Alloys Compd., 897, 2022, 163031.
- [32] R. Karthiga, B. Kavitha, M. Rajarajan, A. Suganthi, Mater. Sci. Semicond. Process., 40, 2015, 123.
- [33] J. Ahmed, M. Alam, M.A. Majeed Khan, S.M. Alshehri, J. King Saud Univ. Sci., 33, 2021, 101317.
- [34] Y. Huang, Y. Gao, C. Liu, Z. Cao, Y. Wang, Z. Li, Y. Yan, M. Zhang, G. Cao, J. Phys. Chem., C. 123, 2019, 30067.

- [35] D. B. Malavekar, V. C. Lokhande, D. J. Patil, S. B. Kale, U. M. Patil, T. Ji, C. D. Lokhande, J. Colloid Interface Sci., 609, 2022, 734.
- [36] B. Huang, H. Wang, S. Liang, H. Qin, Y. Li, Z. Luo, C. Zhao, L. Xie, L. Chen, Energy Storage Mater., 32, 2020, 105.
- [37] D. B. Malavekar, R. N. Bulakhe, S. B. Kale, U. M. Patil, I. In, C. D. Lokhande, J. Alloys Compd., 869, 2021, 159198.
- [38] I. Ashraf, Q. Abbas, Y. Huang, N.U. Hassan, M.D. Albaqami, A.M. Tighezza, S.M. Eldin, M.S. Javed, A. Ahmad, R. Luque, J. Energy Storage., 60, 2023, 106601.
- [39] N. Nwaji, H. Kang, M. Goddati, L.T. Tufa, J. Gwak, A. Sharan, N. Singh, J. Lee, J. Mater. Chem., A. 11, 2023, 3640.
- [40] S.R. K. A., K. Pramoda, C. S. Rout, J. Mater. Chem., C. 11, 2023, 2565.
- [41] T. R. Kuo, L. Y. Lin, K. Y. Lin, S. Yougbaré J. Energy Storage., 52, 2022, 104773.
- [42] L. Saleh Ghadimi, N. Arsalani, I. Ahadzadeh, A. Hajalilou, E. Abouzari-Lotf, Appl. Surf. Sci., 494, 2019, 440.
- [43] Geetanjali, R. Rani, S. Kumar, FuelCells., 19, 2019, 299.
- [44] Y. He, L. Wang, D. Jia, Z. Zhao, J. Qiu, Electrochim. Acta., 222, 2016, 446.
- [45] G. He, J. Li, W. Li, B. Li, N. Noor, K. Xu, J. Hu, I.P. Parkin, J. Mater. Chem., A. 3, 2015, 14272.
- [46] Y. Wang, C. Shen, L. Niu, Z. Sun, F. Ruan, M. Xu, S. Shan, C. Li, X. Liu, Y. Gong, Mater. Chem. Phys., 182, 2016, 394.
- [47] X. Xing, J. Wang, J. Mater. Sci. Mater. Electron., 27, 2016, 11613.
- [48] S. Prabhu, C. Balaji, M. Navaneethan, M. Selvaraj, N. Anandhan, D. Sivaganesh, S. Saravanakumar, P. Sivakumar, R. Ramesh, J. Alloys Compd., 875, 2021, 160066.
- [49] R. D. Kumar, Y. Andou, S. Karuppuchamy, J. Alloys Compd., 654, 2016, 349.
- [50] K. Thiagarajan, D. Balaji, J. Madhavan, J. Theerthagiri, S.J. Lee, K. Y. Kwon, M.Y. Choi, Nanomaterials., 10, 2020, 2195.



# FABRICATION OF ASYMMETRIC SUPERCAPACITOR DEVICE AND PERFORMANCE EVALUATION



# FABRICATION OF ASYMMETRIC SUPERCAPACITOR DEVICE AND PERFORMANCE EVALUATION

| Sr. No. |  | Title   |     |  |  |  |  |
|---------|--|---|-----|--|--|--|--|
| 5.1     | Introduc   | oduction  |     |  |  |  |  |
| 5.2     | Experimental details   |   |     |  |  |  |  |
|         | 5.2.1  | Electrode preparation   | 124 |  |  |  |  |
|         | 5.2.1A   | Preparation of Fe <sub>2</sub> O <sub>3</sub> thin film electrode                             | 124 |  |  |  |  |
|         | 5.2.1B   | Physical characterization of Fe <sub>2</sub> O <sub>3</sub> electrode                         | 125 |  |  |  |  |
|         |  | XRD of Fe <sub>2</sub> O <sub>3</sub> electrode   | 125 |  |  |  |  |
|         |  | SEM of Fe <sub>2</sub> O <sub>3</sub> electrode   | 125 |  |  |  |  |
|         | 5.2.2  | Electrochemical analysis of Fe <sub>2</sub> O <sub>3</sub> electrode                          | 126 |  |  |  |  |
|         | 5.2.3A   | Properties of AC (Activated carbon)   | 127 |  |  |  |  |
|         | 5.2.3B   | Electrochemical analysis of AC electrode  | 129 |  |  |  |  |
|         | 5.2.4  | Preparation of polymer gel electrolytes   | 130 |  |  |  |  |
| 5.3     | Fabricat   | tion of devices   | 131 |  |  |  |  |
|         | 5.3.1  | Difference between aqueous and solid state asymmetric supercapacitor (ASC) device             | 131 |  |  |  |  |
|         | 5.3.2  | Fabrication of aqueous asymmetric supercapacitor devices                                      | 133 |  |  |  |  |
|         | 5.3.3  | Fabrication of flexible solid state asymmetric supercapacitor (ASC) device                    | 133 |  |  |  |  |
| 5.4     | Results  | and discussion  | 134 |  |  |  |  |
| 5.4A    | Electro  | chemical analysis of NiWO <sub>4</sub> /KOH/Fe <sub>2</sub> O <sub>3</sub> aqueous ASC device | 134 |  |  |  |  |
|         | 5.4A1  | CV study  | 134 |  |  |  |  |
|         | 5.4A2  | GCD study   | 134 |  |  |  |  |
|         | 5.4A3  | EIS study   | 137 |  |  |  |  |
|         | 5.4A4  | Stability study   | 138 |  |  |  |  |
| 5.4B    | Electrochemical characterization of rGO-NiWO <sub>4</sub> //AC flexible ASC Device                         |   |     |  |  |  |  |
|         | 5.4B1  | CV study  | 139 |  |  |  |  |
|         | 5.4B2  | GCD study   | 139 |  |  |  |  |
|         | 5.4B3  | Stability study   | 141 |  |  |  |  |
|         | 5.4B4  | Flexibility study   | 141 |  |  |  |  |
|         | 5.4B5  | EIS study   | 143 |  |  |  |  |
| 5.5     | Demonstration of rGO-NiWO <sub>4</sub> //AC flexible asymmetric solid state device                         |   |     |  |  |  |  |
| 5.6     | Comparison of NiWO <sub>4</sub> /KOH/Fe <sub>2</sub> O <sub>3</sub> and rGO-NiWO <sub>4</sub> //AC devices |   |     |  |  |  |  |
|         | References   |   |     |  |  |  |  |

#### 5.1 Introduction

Recent advancements in energy storage devices have highlighted the need for portable and small-sized supercapacitors (SCs) [1, 2]. SCs offer mechanical flexibility, lightweight construction, affordability, and environmentally friendly energy storage, making them ideal for applications in portable electronics, wearable devices, and commercial pocket-sized electronics [3, 4]. To improve the energy storage capabilities of these devices, it is crucial to enhance their specific energy ( $S_E$ ) and specific power ( $S_P$ ) by exploring different electrode materials and electrolytes. One effective approach to increase the operating voltage of SCs is through asymmetric design [5]. Asymmetric supercapacitors (ASCs) have been found to exhibit higher  $S_E$  and capacitance (Cs) compared to symmetric supercapacitors (SSCs) [6-9].

Several combinations of anodes and cathodes have been reported in the literature, such as  $MnO_2/Fe_3O_4$  [10],  $CoMoO_4/MnO_2$  [11],  $FeWO_4/MnO_2$  [12],  $NiO//\alpha$ - $Fe_2O_3$  [13], and NiO and  $NiCo_2O_4$  [14]. Solid electrolyte-based SCs offer advantages such as small size, lightweight design, excellent reliability, and a wider range of operating temperatures. Meanwhile, polymer-based gel electrolytes provide mechanical flexibility to SC devices [15, 16].

Transition metal-based electrode, such as nickel tungstate, have shown promising operation within a wide potential window. Combining these electrode materials with polymeric gel electrolytes can contribute to the development of flexible solid-state ASC devices. NiWO<sub>4</sub> is particularly attractive as a positive electrode material due to its higher Cs and operating voltage compared to carbon-based materials. Additionally, the low cost, abundant availability, and high conductivity, make them suitable for fabricating flexible solid-state ASC devices [17-19].

This chapter focused on the fabrication and electrochemical performance evaluation of NiWO<sub>4</sub> thin films as a cathode in aqueous asymmetric supercapacitors (ASC). A NiWO<sub>4</sub>/KOH/Fe<sub>2</sub>O<sub>3</sub> device was developed, with a Fe<sub>2</sub>O<sub>3</sub> thin film serving as the anode and 2M KOH as the electrolyte. Additionally, a flexible solid-state asymmetric supercapacitor (ASC) device was fabricated in the configuration of rGO-NiWO<sub>4</sub>/PVA-KOH/AC, featuring rGO-NiWO<sub>4</sub> film electrodes as the cathode, activated carbon (AC) as the anode, and PVA-KOH gel electrolyte. The chapter aimed to provide

insights into the fabrication process and the electrochemical performance of these aqueous and flexible solid-state ASC devices.

#### **5.2 Experimental details**

The present section describes the electrode preparation (NiWO<sub>4</sub> and Fe<sub>2</sub>O<sub>3</sub>, rGO-NiWO<sub>4</sub>, and AC), polymer gel electrolyte (PVA-KOH) preparation, and fabrication of aqueous NiWO<sub>4</sub>/KOH/Fe<sub>2</sub>O<sub>3</sub> and flexible solid-state rGO-NiWO<sub>4</sub>/PVA-KOH/AC ASC devices.

#### **5.2.1 Electrode preparation**

The SILAR method was employed to prepare NiWO<sub>4</sub>, Fe<sub>2</sub>O<sub>3</sub>, and rGO-NiWO<sub>4</sub>, thin films on flexible SS substrates. The optimized preparative parameters of NiWO<sub>4</sub> and rGO-NiWO<sub>4</sub> thin film electrodes are described in chapters III and IV, respectively. The electrode AC was prepared by reported methods, hence their physical characterizations are not discussed.

#### 5.2.1A Preparation of Fe<sub>2</sub>O<sub>3</sub> thin film electrode

To fabricate an ASC device, Fe<sub>2</sub>O<sub>3</sub> is used as an anode material, because it has a wide potential window and higher specific capacitance. To synthesize Fe<sub>2</sub>O<sub>3</sub> electrode; solutions of 0.2 M KOH (50 mL) and 0.01 M FeCl<sub>3</sub> (50 mL) were utilized as anionic and cationic sources, respectively. The substrate was dipped in cationic precursor for 10s, followed by washing in DDW for 10s. The same substrate was dipped in anionic precursor kept at a temperature of 333K for 10s. In this step, pre-adsorbed Fe<sup>3+</sup> ions reacted with OH<sup>-</sup> in the solution. This was followed by immersion in DDW for 10s to take away loosely attached Fe(OH)<sub>3</sub> particles. Thus a single cycle of SILAR forms a monolayer of Fe(OH)<sub>3</sub>. Moreover, such 120 cycles were repeated to get the appropriate quantity of Fe(OH)<sub>3</sub>. The deposited film was annealed at 573 K in a furnace for 3 h to form Fe<sub>2</sub>O<sub>3</sub> from Fe(OH)<sub>3</sub>. The mass loading of Fe<sub>2</sub>O<sub>3</sub> thin film was 0.3 mg cm<sup>-2</sup> after 120 SILAR cycles.

#### 5.2.1B Physical characterizations of Fe<sub>2</sub>O<sub>3</sub> electrode

#### i) XRD study:

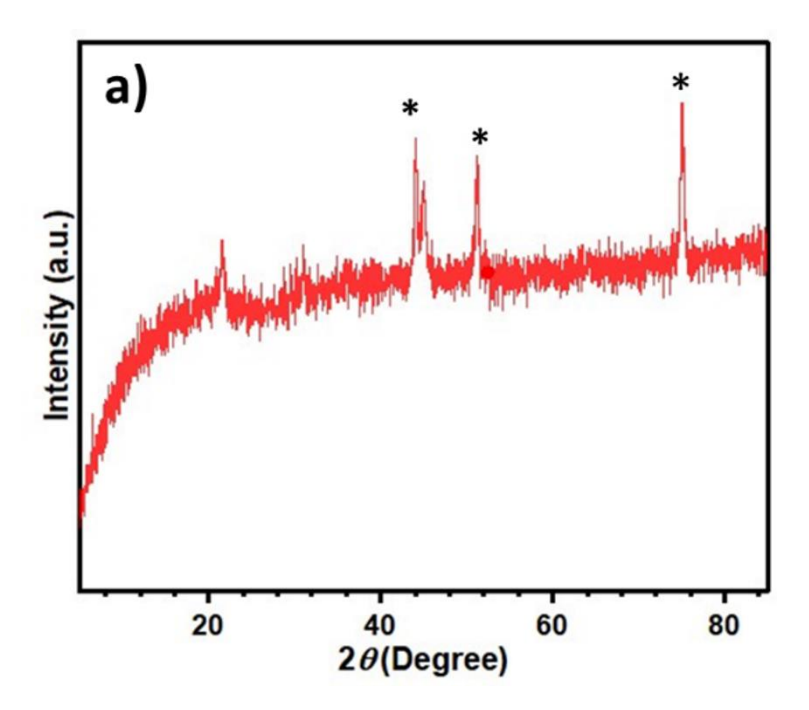


**Figure 5.1:** XRD pattern of Fe<sub>2</sub>O<sub>3</sub> electrode

The X-ray diffraction (XRD) analysis conducted on the Fe<sub>2</sub>O<sub>3</sub> film using a Rigaku Miniflex X-ray diffractometer with CuKα radiation revealed distinctive diffraction peaks at 22°,31°,51° and \* marked are steel peaks as shown in Figure 5.1. These peaks corresponded to the (012), (222), (442) crystallographic planes, respectively, indicating the presence of crystalline structures within the film. Specifically, the identification of these planes suggests the formation of Fe<sub>2</sub>O<sub>3</sub> crystalline phase. The intensity of the peaks provides further insight, offering information about the relative abundance and arrangement of crystalline domains within the film.

The XRD spectra strongly support the characterization of the Fe<sub>2</sub>O<sub>3</sub> film as its crystalline nature and provide valuable details regarding its structural properties.

#### ii) SEM study:

The surface morphology of the Fe<sub>2</sub>O<sub>3</sub> electrode film was investigated using a Zesis scanning electron microscope (SEM), which unveiled intriguing characteristics. The SEM image revealed a coarse grain morphology of the Fe<sub>2</sub>O<sub>3</sub> film as shown in

Figure 5.2. This irregularity in shape, coupled with the granular structure, implies that the film is comprised of small, discrete particles or grains rather than a homogeneous mass. This significant observation suggests a non-uniform distribution of  $Fe_2O_3$  across the electrode surface.

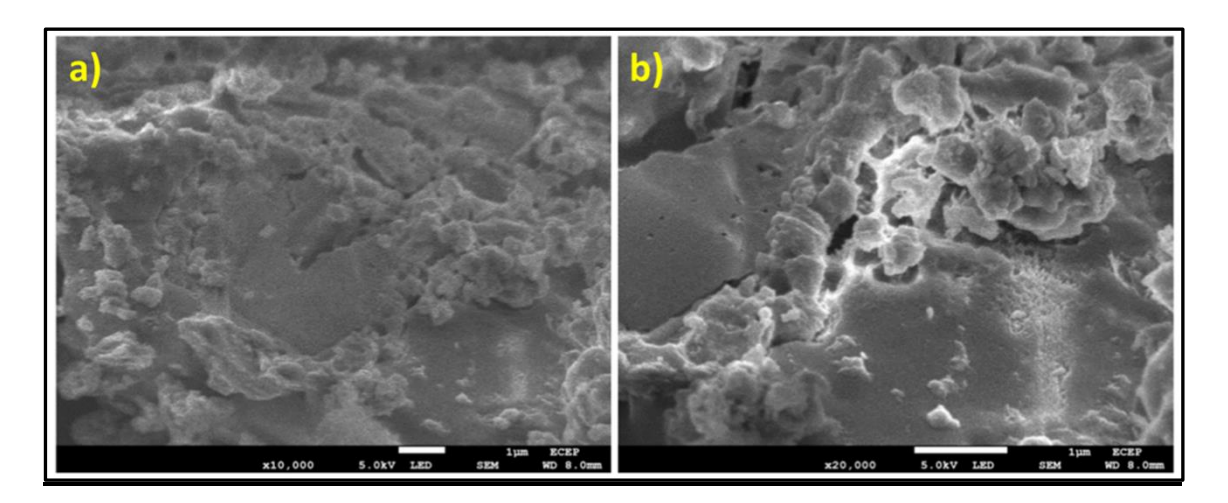


**Figure 5.2**: SEM images of Fe<sub>2</sub>O<sub>3</sub> material at 10KX and 20KX resolution.

The high-resolution imaging capability of SEM enabled the discernment of intricate details, providing valuable insights into the physical structure and texture of the material, by providing a visual representation of the surface morphology. SEM analysis enhances our understanding of the microstructural features, which can be crucial for optimizing the performance of the electrode in various applications, such as catalysis or energy storage.

#### 5.2.2 Electrochemical analysis of Fe<sub>2</sub>O<sub>3</sub> electrode

The electrochemical performance of Fe<sub>2</sub>O<sub>3</sub> electrode was performed using CV, GCD, and EIS techniques. The CV curves at different scan rates shown in Figure 5.3a, suggest charge storage from the redox reactions at the electrode surface, predominantly. As the scan rate rises, the area enclosed by the CV curve also increases proportionally. At a low scan rate, the electrolyte ions from the electrolyte take up more time for interaction hence high charge storage was observed at the lowest scan rates. The GCD curves of the Fe<sub>2</sub>O<sub>3</sub> electrode at current densities varying between 1 to 6 A g<sup>-1</sup> are shown in Figure 5.3b. At a current density of 1 A g<sup>-1</sup> the interactions between electrode and electrolyte ions are higher compared to that of the current density of 6 A g<sup>-1</sup>. Therefore, maximum discharge time is observed at the current density of 1 A g<sup>-1</sup>. The C<sub>s</sub>

of 726 F g<sup>-1</sup> at a current density of 1.0 A g<sup>-1</sup> were obtained for Fe<sub>2</sub>O<sub>3</sub> electrode. An EIS study (**Figure 5.3c**) with  $R_s$  (0.6  $\Omega$  cm<sup>-2</sup>) and  $R_{ct}$  (298.4  $\Omega$  cm<sup>-2</sup>) revealed very good conductivity of Fe<sub>2</sub>O<sub>3</sub> electrode. The capacitive retention of Fe<sub>2</sub>O<sub>3</sub> electrode (**Figure 5.3d**) after 5000 GCD cycles is 86% at current density of 3.0 A g<sup>-1</sup>.

Good specific capacitance, lower resistive parameters, and excellent stability of Fe<sub>2</sub>O<sub>3</sub> electrode make it the best contender for the counter electrode for ASC device fabrication. Hence, this electrode is used as an anode for ASC device fabrication.

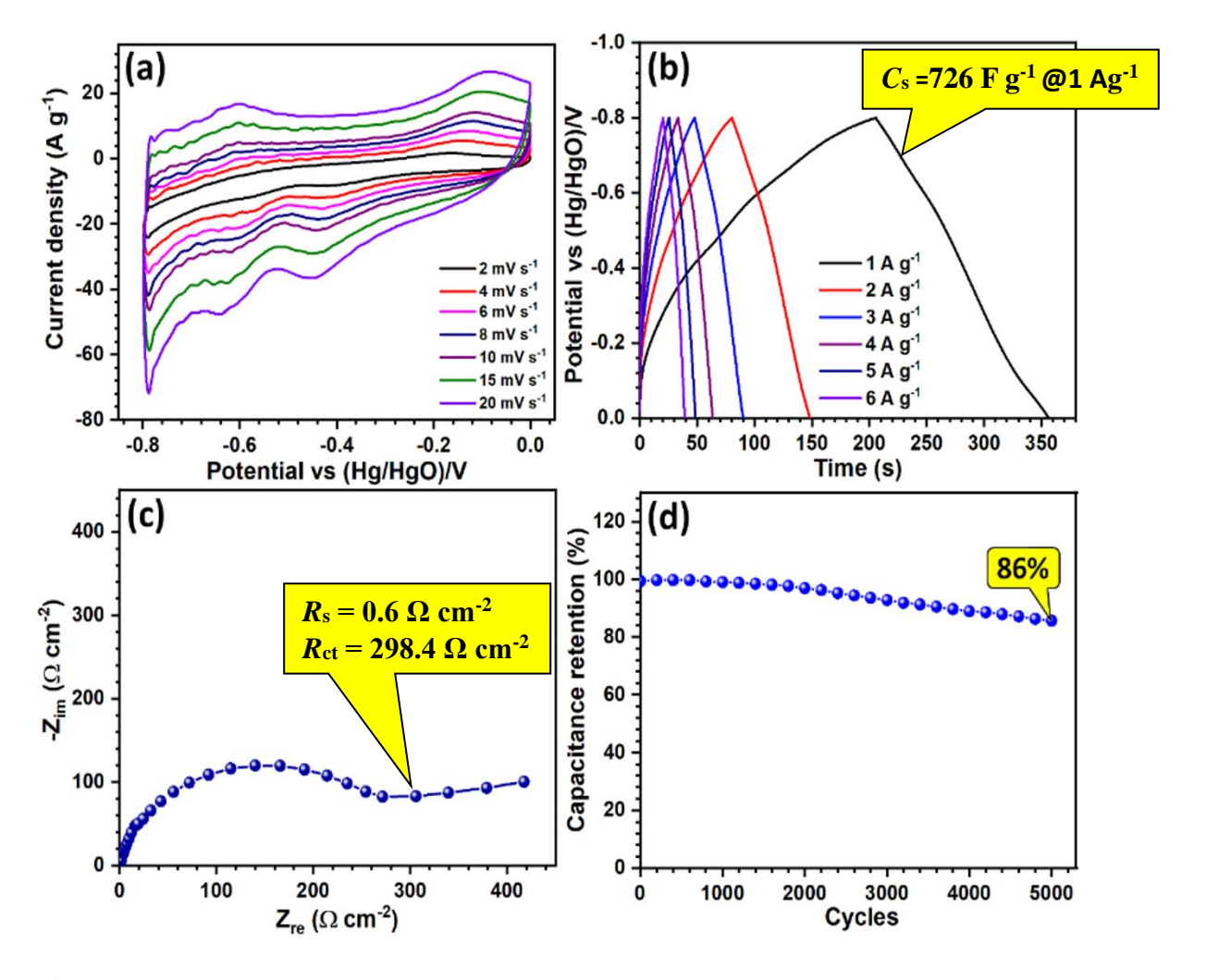


**Figure 5.3:** a) The CV curves, b) the GCD curves, c) the Nyquist plot, and d) stability plot for Fe<sub>2</sub>O<sub>3</sub> thin films.

#### 5.2.3A Properties of AC

Activated carbon is a highly porous form of carbon with a large surface area and high microporosity. Its properties make it an effective adsorbent for a variety of

applications, including water purification, air filtration, and chemical purification. Here are the key properties of activated carbon:

**Surface area:** Activated carbon has an exceptionally high surface area, typically ranging from 500 to 1500 square meters per gram. This extensive surface area provides numerous adsorption sites.

**Porosity:** It is characterized by a high level of porosity, including micropores (< 2 nm), mesopores (2-50 nm), and macropores (> 50 nm). The micropores are primarily responsible for the high adsorption capacity.

**Surface chemistry:** The surface of activated carbon contains various functional groups, such as carboxyls, hydroxyls, and lactones. These functional groups can be modified to enhance specific adsorption properties.

**Adsorption capacity:** Activated carbon is highly effective at adsorbing a wide range of organic and inorganic substances, including gases, vapors, and dissolved solutes. This includes contaminants like chlorine, odors, volatile organic compounds (VOCs), and heavy metals.

**pH stability:** It remains stable across a wide pH range, making it suitable for diverse environments.

**Hardness and abrasion resistance:** It exhibits good mechanical strength and resistance to abrasion, which is crucial for its durability and longevity in filtration systems.

**Density:** The bulk density of activated carbon typically ranges from 0.25 to 0.65 g/cm<sup>3</sup>, depending on the form and source material.

**Thermal stability:** Activated carbon is thermally stable up to high temperatures. However, its adsorption capacity can decrease at very high temperatures due to desorption of adsorbed substances.

**Regenerability:** Activated carbon can be regenerated or reactivated by thermal or chemical processes, restoring its adsorption capacity for repeated use.

**Electrical conductivity:** It has moderate electrical conductivity, which can be useful in specific electrochemical applications.

#### 5.2.3B Electrochemical analysis of AC electrode

The electrochemical characteristics of an AC electrode were evaluated using various techniques, including CV, GCD, and EIS. Figure 5.4a illustrates the voltammograms at different scan rates, indicating that the EDLC-type charge storage. With increasing scan rate, the enclosed area within the CV curve also proportionally increases. Figure 5.4b presents the GCD profiles of AC electrode at different current densities between 1 to 6 A g<sup>-1</sup>. At a current density of 1 A g<sup>-1</sup>, there is enhanced interaction between electrolyte and the electrode compared to a current density of 6 A g<sup>-1</sup>. Consequently, the maximum discharge time was observed at 1 A g<sup>-1</sup> current density. The AC electrode showed a specific capacitance of 231 F g<sup>-1</sup> at a current density of 1 A g<sup>-1</sup>. Furthermore, an EIS study depicted in Figure 5.4c demonstrated excellent conductivity of the AC electrode. The capacitive retention of AC electrode over 5000 GCD cycles, shown in Figure 5.4d, is 80% at a current density of 3.0 A g<sup>-1</sup>, indicating its favourable stability. Considering its excellent specific capacitance, exceptional stability, the AC electrode is used as an anode to fabricate of ASC device.

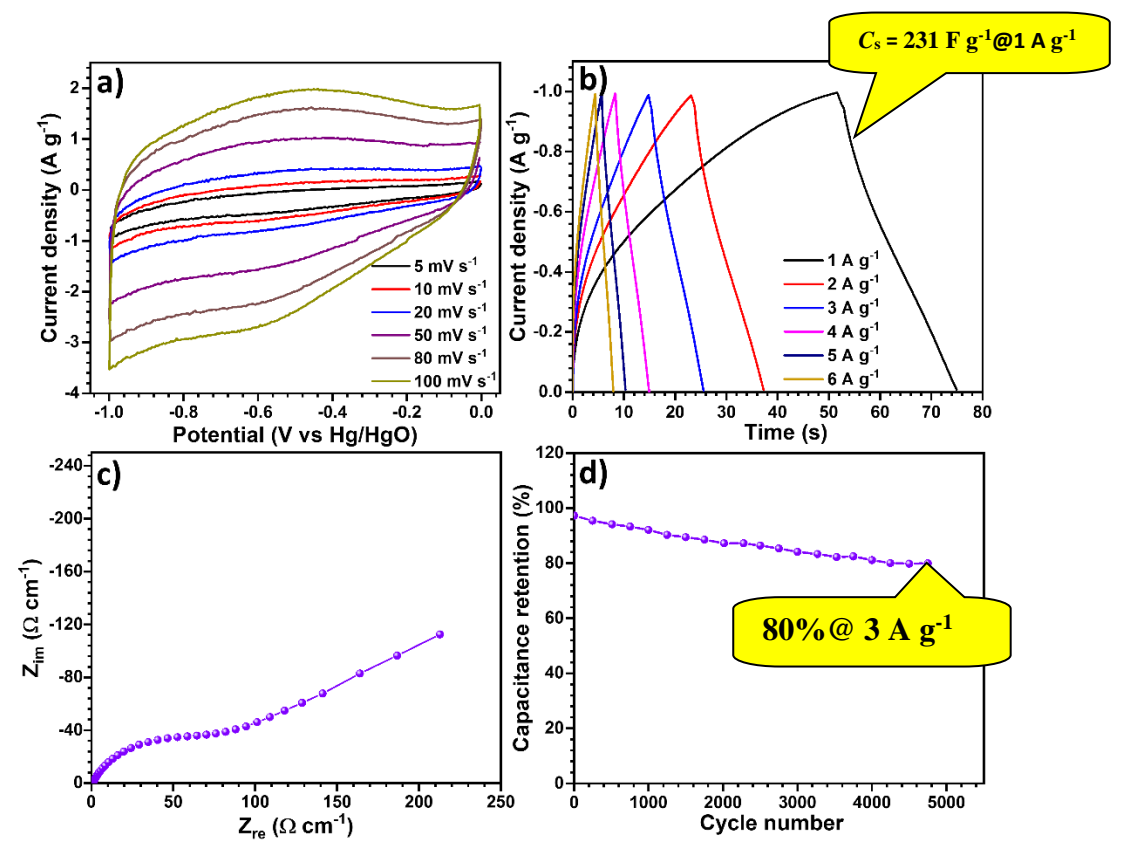


**Figure 5.4:** a) The CV curves, b) the GCD curves, c) the Nyquist plot, and d) stability plot for AC thin films.

#### 5.2.4 Preparation of polymer gel electrolytes

#### Benefits of Gel Electrolyte:

- The gel electrolyte minimized evaporation, which was crucial for maintaining the electrolyte's consistency and preventing the drying out of the supercapacitor.
- Enhanced stability and improved ion conduction contributed to a longer lifespan and better performance of the supercapacitor device.
- The pressurization step further ensured the integrity and performance of the supercapacitor by compacting the components.

The preparation of a gel electrolyte for a supercapacitor device, involved several steps to ensure the proper composition and properties of the electrolyte [20]. The purpose of the gel electrolyte was to minimize evaporation and enhance the performance and lifespan of the supercapacitor device. Here are some points explaining the process:

#### Ingredients and their roles:

- Polyvinyl Alcohol (PVA): 1 gram of PVA was dissolved in 60 mL of double distilled water (DDW) at a temperature of 323 K (50°C). PVA was used as a polymer matrix to create a gel structure, which was necessary for the electrolyte's stability and reduced evaporation.
- Potassium Hydroxide (KOH): After dissolving the PVA, 0.56 grams of KOH
  were added to the solution. KOH served as an electrolyte salt, providing ions for
  charge storage within the supercapacitor. The addition of KOH helped enhance
  the electrolyte's ionic conductivity.
- The PVA was dissolved in DDW for 5 hours at 323 K. This extended duration ensured that the PVA was fully dissolved and properly mixed with the water, forming a homogeneous solution.
- After dissolving the PVA, KOH was added, and the solution was stirred for an additional 4 hours. This allowed for the complete integration of KOH into the PVA solution, forming a consistent gel electrolyte.

#### Gel formation:

 The prolonged mixing and cooling allowed the PVA and KOH to form a gel-like structure. This gel structure was essential as it prevented the evaporation of the electrolyte, ensuring that it remained stable over time. It also provided a stable environment for ion conduction within the supercapacitor.

#### Supercapacitor fabrication:

• After the gel electrolyte was prepared, it was used to assemble the supercapacitor device. The device was subjected to high pressure, specifically 0.5 tons, in an automated hydraulic press for one hour. This step was crucial as it compressed the components of the supercapacitor, including the gel electrolyte, electrodes, and separator. The pressure helped to improve the overall contact between the components, enhancing the performance and reliability of the supercapacitor.

#### **5.3 Fabrication of devices:**

#### 5.3.1 Difference between aqueous and solid-state asymmetric supercapacitor

#### (ASC) device

Supercapacitors serve as energy storage devices that effectively bridge the gap between conventional capacitors and batteries. They are primarily classified based on the type of electrolyte used, resulting in two main categories: aqueous and solid-state supercapacitors. These two types differ significantly in terms of their electrolyte composition, operating voltage, energy and power density, safety, stability, and applications.

Aqueous supercapacitors utilize an aqueous electrolyte, typically composed of water-based solutions containing dissolved salts such as potassium hydroxide (KOH) or sulfuric acid (H<sub>2</sub>SO<sub>4</sub>). This type of electrolyte generally offers higher ionic conductivity, which translates to lower internal resistance and potentially higher power density. However, the operating voltage of aqueous supercapacitors is constrained by the electrolysis potential of water, limiting it to about 1.2 volts per cell. Exceeding this voltage can cause the water to decompose into hydrogen and oxygen, leading to

efficiency losses and potential safety hazards. Consequently, aqueous supercapacitors have a lower energy density due to their limited voltage window but benefit from a higher power density because of their superior ionic conductivity and lower internal resistance.

In contrast, solid-state supercapacitors employ a solid-state electrolyte, which can be a polymer, gel, or solid inorganic material. These electrolytes typically exhibit lower ionic conductivity than their aqueous counterparts, resulting in higher internal resistance and lower power density. However, solid-state supercapacitors can operate at higher voltages, typically between 2.5 to 3 volts per cell or more, since they are not constrained by the electrolysis of water. This capability allows for a higher energy density. Despite their lower power density, solid-state supercapacitors are advantageous in applications requiring higher energy storage.

Regarding safety and stability, aqueous supercapacitors are generally safer in terms of flammability, as their water-based electrolytes are less prone to catching fire compared to the organic solvents used in some other supercapacitors. However, they can be less thermally stable, especially at higher voltages where water electrolysis may occur. On the other hand, solid-state supercapacitors offer enhanced chemical stability and are non-flammable, reducing the risk of thermal runaway. They also exhibit better thermal stability, making them capable of operating at higher temperatures without significant degradation.

The specific applications of aqueous and solid-state supercapacitors further highlight their differences. Aqueous supercapacitors are often used in scenarios that require high power output and quick charge/discharge cycles, such as regenerative braking systems, power backup, and power grid stabilization. Their higher power density makes them ideal for these demanding applications. Conversely, solid-state supercapacitors are well-suited for portable and wearable electronics, energy harvesting, and other applications where compact size, safety, and higher energy density are critical. These attributes make solid-state supercapacitors particularly beneficial in environments where space and safety are paramount.

The choice between aqueous and solid-state supercapacitors depends largely on the specific requirements of the application. Aqueous supercapacitors provide higher power density and better ionic conductivity but are limited by their lower voltage window and energy density. Solid-state supercapacitors, while offering higher energy density and enhanced safety with a higher voltage window, typically exhibit higher internal resistance and lower power density. Each type's unique characteristics make them suitable for different use cases, balancing power and energy needs, safety, size, and operational conditions.

#### 5.3.2 Fabrication of aqueous asymmetric supercapacitor devices

The aqueous asymmetric supercapacitor (ASC), NiWO<sub>4</sub>/KOH/Fe<sub>2</sub>O<sub>3</sub> was fabricated using NiWO<sub>4</sub> thin film as a cathode, Fe<sub>2</sub>O<sub>3</sub> film as an anode, and 2M KOH as an electrolyte. From the potential windows of the two electrodes forming supercapacitor device, the expected operating window of an ASC device can be extended up to 1.2 V [21]. To make an ASC device, the charge balance is well matched using a charge balance relation [22],

$$\frac{m_+}{m_-} = \frac{C_- \times \Delta E_-}{C_+ \times \Delta E_+} \tag{5.1}$$

Here,  $\Delta E$  is a potential window (V), m is the mass of the active material (g), and C represents the specific capacitance (F g<sup>-1</sup>) of the relevant electrode. The + and - sign symbols of the cathode and anode values, respectively. Using this equation,  $m^+/m^-$  is calculated as 1.67. At this quantity of deposited mass, two electrodes provide the same total charge; thus, the charge balance is apparent.

#### 5.3.3 Fabrication of flexible solid-state asymmetric supercapacitor (ASC) device

A flexible solid-state asymmetric supercapacitor (ASC) device for the configuration rGO-NiWO<sub>4</sub>/PVA-KOH/AC was fabricated, with rGO-NiWO<sub>4</sub> film electrodes as cathode, AC as an anode, and PVA-KOH gel electrolyte. To prepare gel electrolyte, 1 g of PVA was dissolved in DDW at temperature of 323 K for 5 h. Afterwards, 0.56 g of KOH was added to the solution, and kept stirring for an additional 4 h. The gel type of electrolyte minimizes evaporation of electrolyte, leading to a longer life span of supercapacitor device. For 1 h, fabricated supercapacitor device was subjected to 0.5 ton pressure in an automated hydraulic press. As both electrodes are made of different materials, the challenge of charge balance must be overcome while

fabricating a device. To achieve same charge storage from both of electrodes, equation given below, is used to adjust mass loading of AC electrode [23]:

$$\frac{M^{+}}{M^{-}} = \frac{C_{S}^{-} \times \Delta V^{-}}{C_{S}^{+} \times \Delta V^{+}}$$
 (5.2)

where M indicates mass loading of electrodes,  $C_s$  stands for specific capacitance in F g<sup>-1</sup> and  $\Delta V$  is the operating potential window of electrode, + and – signs indicate the values for anode and cathode, respectively. The specific energy  $(S_E)$  and specific power  $(S_P)$  of the ASC device were calculated using following relations:

$$S_E = \frac{0.5 \times C_S \times \Delta V^2}{3.6} \tag{5.3}$$

$$S_P = \frac{3600 \times S_E}{dt} \tag{5.4}$$

where  $C_s$  (F g<sup>-1</sup>) gives specific capacitance,  $\Delta V$  (V) represents operating potential window, and dt (s) represents discharge time of ASC device at the respective applied current density.

#### 5.4 Results and discussion

#### 5.4A Electrochemical analysis of NiWO<sub>4</sub>/KOH/Fe<sub>2</sub>O<sub>3</sub> aqueous ASC device

#### 5.4A1 CV Study

To evaluate the electrochemical performance of aqueous ASC with the configuration of NiWO<sub>4</sub>/KOH/Fe<sub>2</sub>O<sub>3</sub>, the CV, GCD, and EIS were used. The CV curves for N3 and Fe<sub>2</sub>O<sub>3</sub> electrode at the scan rate of 20 mV s<sup>-1</sup> are shown in Figure 5.5a. This helps to select the operating potential of ASC. The operating potential window of 1.2 V is chosen for ASC device. The CV curves of the ASC device at various scan rates between 5 and 100 mV s<sup>-1</sup> are shown in Figure 5.5b. The ASC device displayed a good reversible shape of CV curves.

#### 5.4A2 GCD Study

The GCD plots of the ASC device at different current densities between 2 to 8 A  $g^{-1}$  are shown in **Figure 5.5c**. The symmetric nature of the GCD curves at each current density signifies electrochemical charge-discharge reversibility of the ASC device. The highest  $C_s$  of the ASC device is 115 F  $g^{-1}$  at the current density of 2 A  $g^{-1}$ .

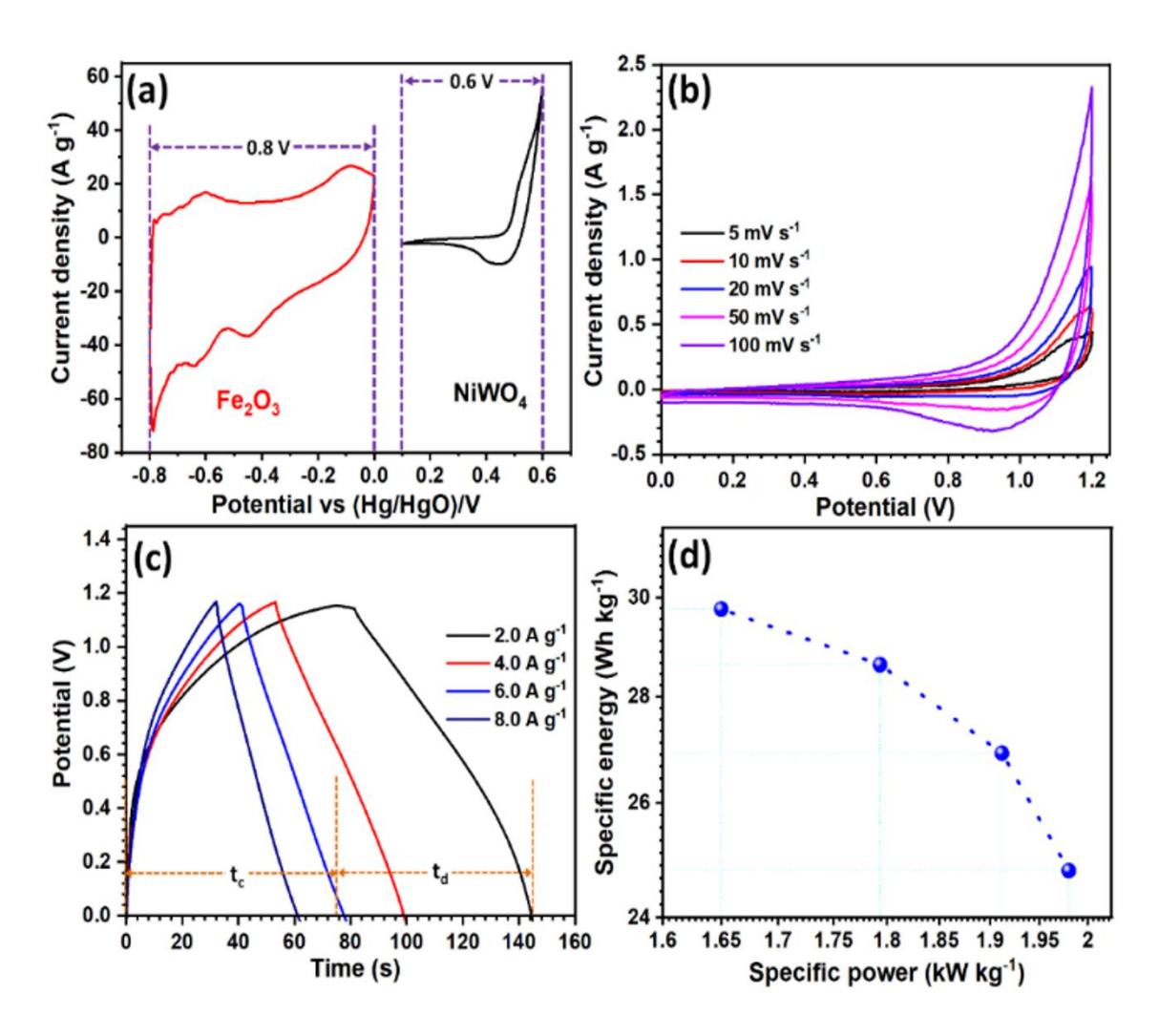


**Figure 5.5:** a) Combined CV curves of Fe<sub>2</sub>O<sub>3</sub> and N3 electrodes, b) the CV curves, c) the GCD plots, and d) the Ragone plot of NiWO<sub>4</sub>/KOH/Fe<sub>2</sub>O<sub>3</sub> ASC device.

The  $C_s$  of the ASC device decreases with increasing current density due to insufficient interaction between the electrode and electrolyte at high current density. The coulombic efficiency of the ASC device is 95% at the current density of 2 A g<sup>-1</sup>. The ASC device delivers a  $S_E$  of 23 Wh kg<sup>-1</sup> at  $S_P$  of 1.2 kW kg<sup>-1</sup>. The variation of  $S_E$  with  $S_P$  is shown in the Ragone plot (Figure 5.5d). Comparison of  $C_s$ ,  $S_E$ , and  $S_P$  of ASC with reported Nibased reported ASC is provided in **Table 5.1 [24-32]**. The ASC device has moderate specific energy and highest specific power among the mentioned devices.

The device is an asymmetric supercapacitor (ASC), which typically combines a high-capacitance material with a material capable of high power delivery. The characteristics described such as high specific capacitance, moderate specific energy, high specific power, and good electrochemical reversibility are consistent with the

performance of an ASC. The high specific power indicates that the device can deliver energy quickly, making it suitable for applications requiring rapid energy delivery and recharge. The moderate specific energy suggests it can store a fair amount of energy, though not as much as batteries.

Table 5.1: Comparison of  $C_s$ ,  $S_E$ , and  $S_P$  of ASC with reported Ni-based reported ASC.

|  |                                    |                                  | Specific               | Specific | Electrochemical | Ref.  |
|--|------------------------------------|----------------------------------|------------------------|----------|-----------------|-------|
| Configuration  | Electrolyte                        | $C_{\rm s}$ (F g <sup>-1</sup> ) | Energy                 | Power    | stability (%)   | No.   |
| Comiguration   |                                    |                                  | (Wh kg <sup>-1</sup> ) | (W kg-1) | (cycles)        | 140.  |
| NiWO4//Fe <sub>2</sub> O <sub>3</sub>                                | 2 M KOH                            | 93                               | 22                     | 1200     | 78 (5000)       | This  |
| 1111104/110203   |                                    |                                  |                        |          |                 | work  |
| NiWO <sub>4</sub> //AC   | 6М КОН                             | 160.0                            | 64.2                   | 425.0    | 92.8 (5000)     | [24]  |
| N'' 170 // A G   | 2) ( ) ( )                         | 71.1                             | 25.2                   | 200.0    | 01.4 (5000)     | F0.77 |
| NiW-70//AC   | 2M KOH                             | 71.1                             | 25.3                   | 200.0    | 91.4 (5000)     | [25]  |
| CoWO <sub>4</sub> @NiWO <sub>4</sub> //AC                            | 1 M KOH                            | 193.7                            | 30                     | 200      | -               | [26]  |
|  |                                    |                                  |                        |          |                 |       |
| AT /I: NEWO //AT/AC  | DVA /II DO                         | 17.01                            | 9.40                   | 500.49   | 84 (2000)       | [27]  |
| AL/lig-NiWO <sub>4</sub> //Al/AC                                     | PVA/H <sub>3</sub> PO <sub>4</sub> | mF cm <sup>-2</sup>              | 8.49                   | 509.48   | 84 (2000)       | [27]  |
| N.C. O GN.MO WYC   | CMKOH                              | 121.7                            | 41.5                   | 7.00     |                 | [20]  |
| NiCo <sub>2</sub> O <sub>4</sub> @NiWO <sub>4</sub> //AC             | 6 M KOH                            | 131.7                            | 41.5                   | 760      | -               | [28]  |
|  |                                    | 862.26                           |                        |          |                 | F7    |
| Lignin/NiCoWO <sub>4</sub> //AC                                      | PVA/H <sub>3</sub> PO <sub>4</sub> | F/cm <sup>-2</sup>               | 5.75                   | 854.76   | 96.12 (2000)    | [29]  |
|  |                                    |                                  |                        |          |                 |       |
| C-FP//Ni <sub>3</sub> (PO <sub>4</sub> ) <sub>2</sub> /GF            | 6 M KOH                            | 48.0                             | 49                     | 500      | 53 (10000)      | [30]  |
| NiO//Fe <sub>2</sub> O <sub>3</sub>                                  | PVA-KOH                            | 57.2                             | 12.4                   | 950      | 85 (10000)      | [31]  |
| N' D O   |                                    |                                  |                        |          |                 |       |
| Ni <sub>3</sub> P <sub>2</sub> O <sub>8</sub> .                      | 6 M KOH                            | 94                               | 33.4                   | 399      | 83 (5000)       | [32]  |
| Co <sub>3</sub> P <sub>2</sub> O <sub>8</sub> .8H <sub>2</sub> O//AC |                                    |                                  |                        |          |                 |       |

#### **5.4A3 EIS Study**

The impedance properties of an ASC (asymmetric supercapacitor) device were investigated using EIS analysis, and the corresponding Nyquist plot was generated to visualize the results. It is a graphical representation of impedance data obtained from EIS measurements. It typically consists of a semicircular portion in the high-frequency region followed by a linear portion in the low-frequency region. Each feature in the plot corresponds to different components of the equivalent circuit used to model the electrochemical system.

In Figure 5.6a, the Nyquist plot for the ASC device is shown, along with an inset displaying the equivalent circuit used to fit the experimental data. The equivalent circuit is a simplified electrical model that represents the various electrochemical processes occurring within the supercapacitor.

The Nyquist plot reveals several important parameters of the ASC device:

- 1. Low values of Rs and Rct: Rs represents the solution resistance, and Rct represents the charge transfer resistance. In this case, both values are observed to be low, with Rs measured at 1.83  $\Omega$  and Rct at 8.82  $\Omega$ . These low values are attributed to the binder-free deposition of the electroactive material, which promotes efficient electron transfer and enhances the overall electrochemical performance of the device.
- 2. Warburg impedance (W): The presence of Warburg impedance indicates the diffusion-controlled processes occurring within the supercapacitor. Warburg impedance is typically represented as a sloping line in the Nyquist plot's low-frequency region. In this case, a Warburg impedance of  $0.8~\text{m}\Omega$  is observed, indicating the diffusion of ions within the electrode material.
- 3. Constant Phase Element (CPE): The presence of a CPE suggests non-ideal behavior in the electrochemical system. CPE is often used to account for doublelayer capacitance and other non-linear effects. In this case, a CPE with a value of 0.023 mF is included in the equivalent circuit.

4. Overall, the Nyquist plot and equivalent circuit analysis provide valuable insights into the impedance properties of the ASC device, highlighting its efficient charge transfer, diffusion-controlled processes, and non-ideal behavior.

In **Figure 5.6b**, the stability of the ASC device is evaluated through galvanostatic charge-discharge (GCD) cycles. The device undergoes 5000 repeated cycles at a constant current density of 8 A g<sup>-1</sup>. This test assesses the device's long-term performance and durability under continuous operation. The excellent pseudocapacitive performance of both electrodes is noted as a key factor contributing to the superior electrochemical performance and stability of the ASC device throughout the extended cycling test.

#### **5.4A4** Stability Study

The impedance properties of the ASC device were investigated through EIS analysis and corresponding Nyquist plot is shown in **Figure 5.6a**. The equivalent circuit for the Nyquist plot is shown as an inset of **Figure 5.6a**. Low values of  $R_s$  (1.83  $\Omega$ ) and  $R_{ct}$  (8.82  $\Omega$ ) are observed due to binder-free deposition of electroactive material. The circuit also contains Warburg impedance (*W*) (0.8 m $\Omega$ ) and CPE (0.023 mF). The excellent pseudocapacitive performance of both electrodes is responsible for better electrochemical performance in the ASC device. The stability of the ASC device was evaluated for 5000 repeated GCD cycles at the current density of 8 A g<sup>-1</sup> (**Figure 5.6b**).

The ASC device showed 78% capacitance retention after 5000 cycles. The stable and high performance of the ASC device promotes further use of the SILAR method to prepare electrode material for the development and re-engineering of electrochemical energy storage materials.

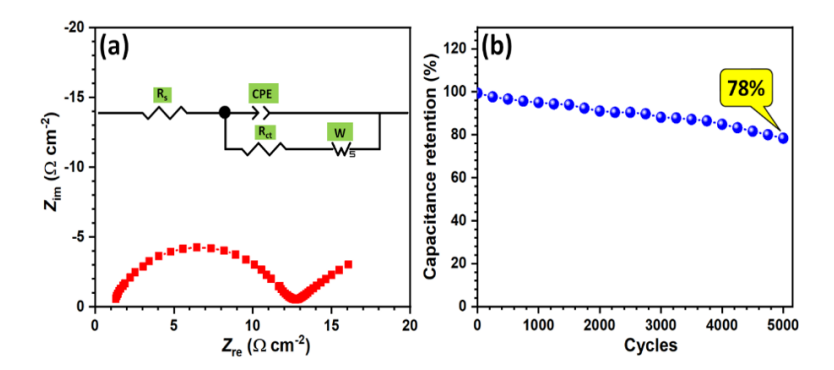


**Figure 5.6:** a) The Nyquist plot (inset shows equivalent electrical circuit) and b) stability plot of NiWO<sub>4</sub>/KOH/Fe<sub>2</sub>O<sub>3</sub>.

#### 5.4B Electrochemical characterization of rGO-NiWO4//AC flexible ASC device

To examine the application of CNW thin films for supercapacitors, the ASC device was built using CNW3 thin film, an AC electrode, and PVA-KOH gel as an electrolyte. **Figure 5.7a** shows the fabrication schematic, and **Figure 5.7b** shows an image of the fabricated device with the configuration NiWO<sub>4</sub>-rGO//AC.

#### 5.4B1 CV study

In order to analyse the charge storage properties, The CV curves of the device were recorded at different scan rates ranging from 5 to 100 mV s<sup>-1</sup> at a potential of 1.6 V (**Figure 5.7c**), and the GCD curves were determined at various current densities ranging from 5 to 9 A g<sup>-1</sup> (**Figure 5.7d**). The maximum specific capacitance of 102.1 F g<sup>-1</sup> is achieved through CV analysis at a scan rate of 5 mV s<sup>-1</sup>. Furthermore, with a current density of 5 A g<sup>-1</sup>, the capacitance value determined from GCD is 94.2 F g<sup>-1</sup>. The  $C_s$  values decreased with the increasing scan rate and current density due to charge storage constraint by limited time at higher scan rates and current densities. Variation of  $C_s$  with scan rate and current density is presented in **Figure 5.6a** and **Figure 5.6b**, respectively.

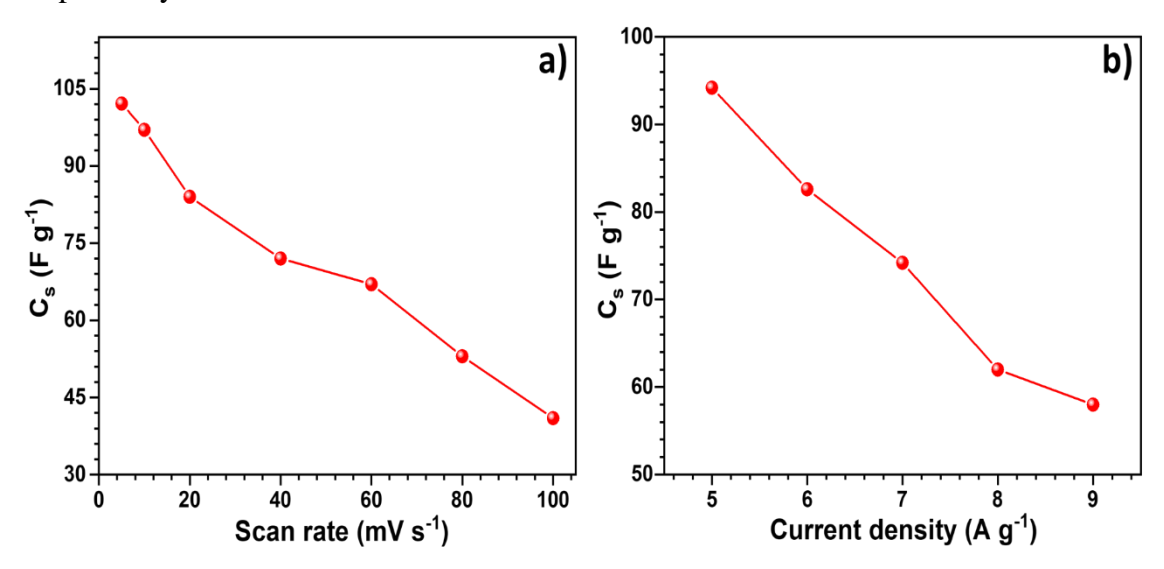
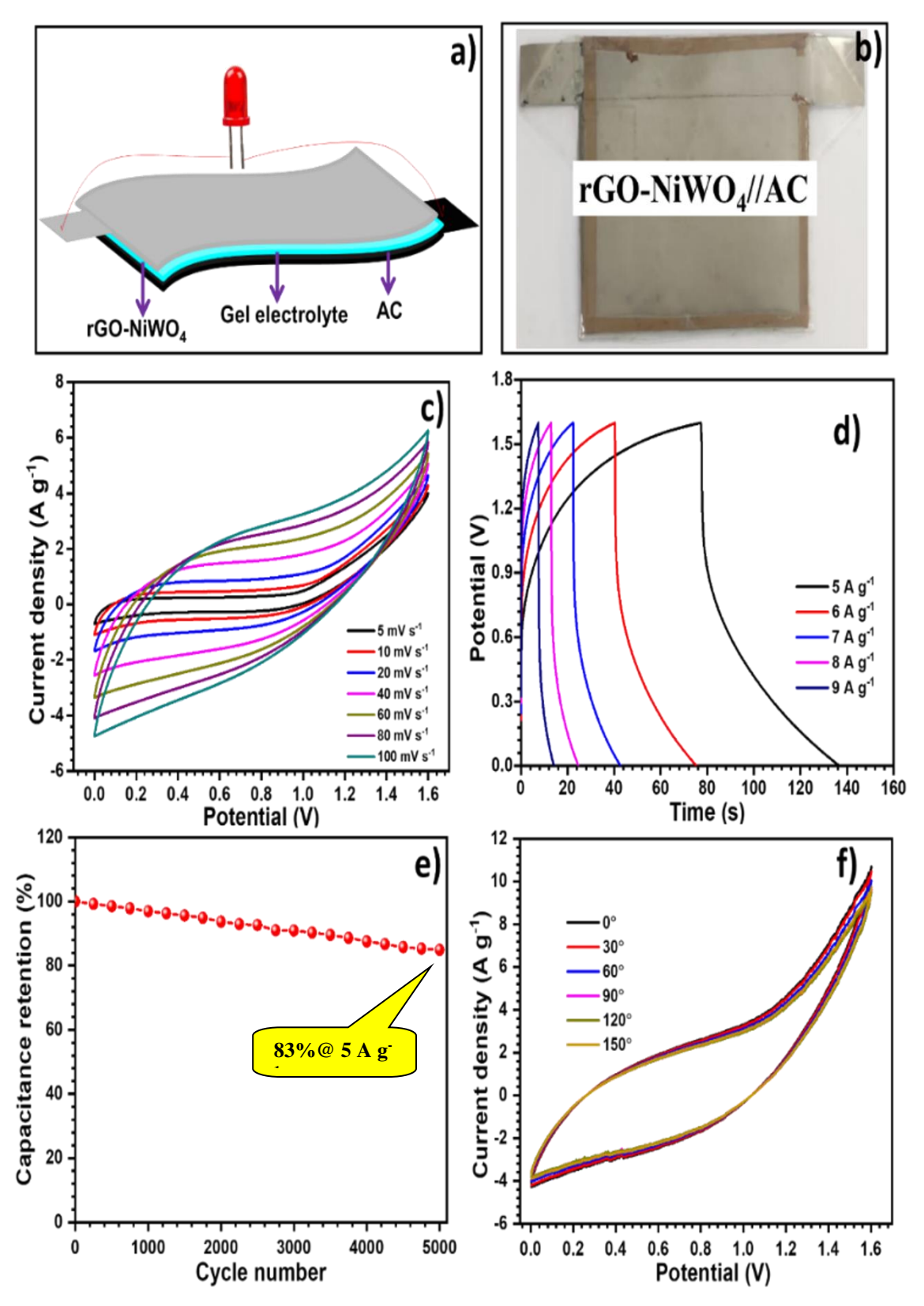


Figure 5.7: Variation of specific capacitance of rGO-NiWO<sub>4</sub>//AC ASC with a) scan rate and b) current density.

#### 5.4B2 GCD study

The similar shape of CV curves at all scan rates and the unchanged GCD profiles indicate good reversibility and ability of device to perform at lower and higher



**Figure 5.8**: a) Schematic of ASC device fabrication, b) Picture of ASC device, c) CV curves, d) GCD plots, e) stability plot, and f) CV curves at different bending position performed at scan rate of 100 mV s-1 of rGO-NiWO<sub>4</sub>/PVA-KOH/AC.

current requirements. At 5 A g<sup>-1</sup>, ASC device has 73% coulombic efficiency. The good coulombic efficiency demonstrated the possible synergic effect of rGO and NiWO<sub>4</sub> structures, in which rGO acts as charge carrier and NiWO<sub>4</sub> provides centers for charge storage. Due to this synergy, the highest value of specific power is 12.37 kW kg<sup>-1</sup> at a specific energy of 33.5 Wh kg<sup>-1</sup>. The lifespan of supercapacitor has been regarded as a key factor in lowering the cost of maintenance for any portable electronic equipment, which results in financially viable appliances.

#### 5.4B3 Stability study

The stability curve of rGO-NiWO<sub>4</sub>//AC ASC device, for 5000 cycles at a current density of 5 A g<sup>-1</sup> is shown in **Figure 5.7e**. At the 5000<sup>th</sup> GCD cycle,  $C_s$  were 83% of their value at the 1<sup>st</sup> GCD cycle. This electrochemical stability can be attributed to the precise composition of pseudocapacitive (NiWO<sub>4</sub>) and non-faradic electroactive materials (rGO), which results in a porous hybrid electrode with the appropriate proportion of pore size.

#### 5.4B4 Flexibility study

The performance evaluation of the device under different bending angles, as illustrated by the CV curves at a scan rate of 100 mV s<sup>-1</sup> in **Figure 5.7f**, indicates minimal variation in electrochemical behavior. This consistency is primarily attributed to several key factors:

- ➤ Flexible substrate: The stainless steel (SS) substrate used in the device is flexible. This flexibility helps maintain structural integrity and consistent contact between the electrode materials and the current collector, even under mechanical deformation.
- Amorphous nature of material: The amorphous nature of the active material allows it to better withstand the mechanical stresses associated with bending. Amorphous materials lack long-range order, which means their atomic structure can more easily accommodate compression and expansion without significant structural damage or phase changes. This adaptability ensures sustained electrochemical performance during the bending process.

- ➤ Short-range ordering: The short-range ordering characteristic of amorphous materials plays a crucial role. During redox reactions, the material can undergo volume changes (expansion and compression) without disrupting the overall structure. This quality ensures that the electrochemical reactions continue efficiently, maintaining performance.
- Adherence and interface quality: The good adherence of the active material to the current collector is essential for maintaining performance. Strong adhesion prevents the delamination or detachment of the active material during bending. Additionally, the high-quality interface between the gel electrolyte and electrode materials ensures efficient ion transport and electrical conductivity, which are critical for maintaining performance under mechanical stress.

#### Analysis of bending images (Image 5.1):

- 0° (a): At this angle, the device is in its unbent state, serving as the reference for evaluating performance changes. The CV curve shows standard electrochemical behavior without any mechanical stress.
- 30° (b): At a slight bend, the CV curve remains largely unchanged, indicating that the device electrochemical properties are not significantly affected by this mild deformation.
- 60° (c): With a moderate bend, there is still no dramatic change in the CV curve, demonstrating the material's flexibility and the robust adherence of the active material.
- 90° (d): At this right-angle bend, the device's performance continues to be stable. The consistency of the CV curve suggests that the amorphous nature and substrate flexibility are effectively mitigating mechanical stress.
- 120° (e): At a sharper bend, the CV curve remains stable, highlighting the durable interface quality and the material's ability to sustain electrochemical performance.
- 150° (f): Even at an extreme bend, the CV curve does not show significant deviation, proving the outstanding flexibility and mechanical resilience of the device.

This performance stability can be attributed to the flexible SS substrate, the amorphous nature of the active material, strong adherence, and excellent interface quality between the gel electrolyte and electrode materials. These factors together enable the device to withstand mechanical deformation without compromising its electrochemical functionality.

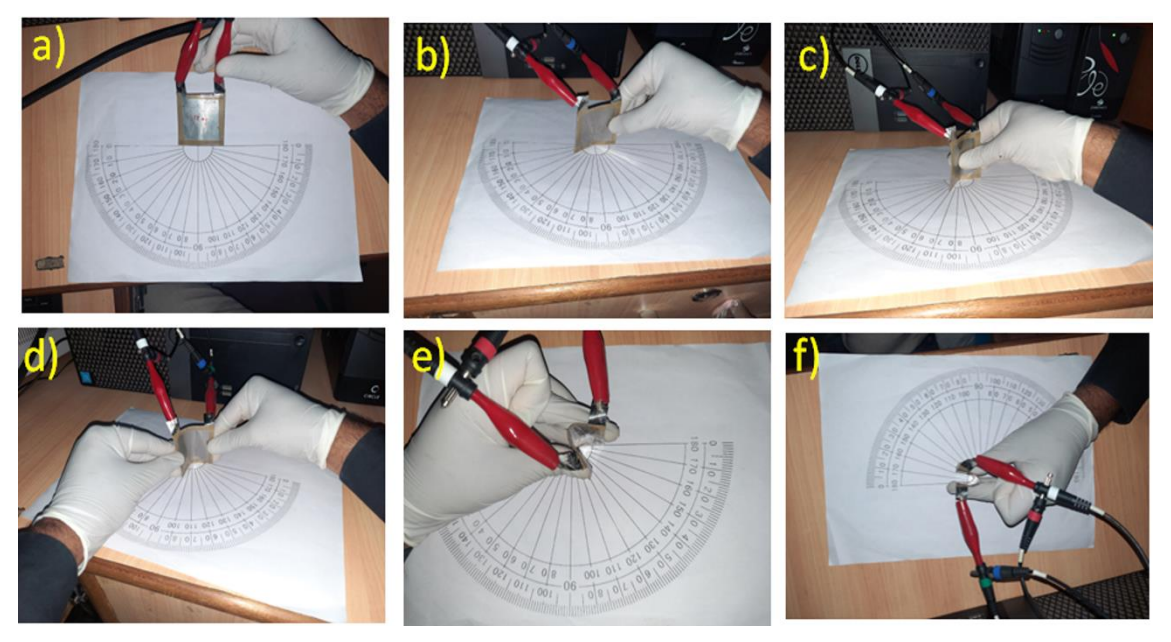


**Image 5.1:** Bending of device images with a) 0°, b) 30°, c) 60°, d) 90°, e)120°, and f) 150°.

#### 5.4B5 EIS study

The EIS measurements were performed to evaluate resistive properties of rGO-NiWO<sub>4</sub>//AC ASC device in frequency of 0.001 Hz to 100 kHz. **Figure 5.8a** displays Nyquist plot of device (the inset image represents an equivalent circuit of the fitted Nyquist plot). The  $R_s$ ,  $R_1$ , and  $R_2$  are 5.94, 16.01 and 51.85  $\Omega$  cm<sup>-2</sup>, respectively.

The values of capacitances  $C_1$  and  $C_2$  are 0.05, and 0.0089 F, respectively. Warburg impedance (W), which has a value of 0.023  $\Omega$ , is represented by an inclined straight line at low frequencies. This Warburg impedance is caused by electrolyte diffusing into electrode. The maximum energy density and power density of rGO-NiWO<sub>4</sub>//AC supercapacitor device assembled in this study (33.5 Wh kg<sup>-1</sup>/12.37 kW kg<sup>-1</sup>) are comparable to those of recently reported ASC devices (Figure 5.8b) such as NiCo<sub>2</sub>O<sub>4</sub>@NiMnO<sub>4</sub>//AC (64/0.75) [33], NiWO<sub>4</sub>-CoWO<sub>4</sub>//AC (30.1/0.2) [34], NiB//rGO (26/2) [35], Ni<sub>2</sub>P<sub>2</sub>O<sub>7</sub>//rGO (26.6/0.87) [36], NiMoO<sub>4</sub>-Ag/rGO//AC (41/0.8)

[37], NiCo<sub>2</sub>O<sub>4</sub>@NiMnO<sub>4</sub>//AC (23/1.2) [38], NiWO<sub>4</sub>//AC (64/0.43) [39], Al/lig-NiWO<sub>4</sub>//Al/AC (2 Wh cm<sup>-2</sup>/100 W cm<sup>-2</sup>) [40], NiCo<sub>2</sub>O<sub>4</sub>@NiWO<sub>4</sub>//AC (41.5/0.76) [41], and Lignin/NiCoWO<sub>4</sub>//AC (6/0.85) [42], Ni-Co-O@rGO//AC (39/7.5) [43], NiCoLDH//Fe<sub>2</sub>O<sub>3</sub> (56.2/0.8) [44], Ni-P//AC (29.2/0.4) [45], and CoNiWO<sub>4</sub>/P-S-GNS//CoNiWO<sub>4</sub>/P-S-GNS (100.8/3.2) [46]. The observed performance of ASC device is associated with the mesoporous material having low *R*<sub>ct</sub> with binder free growth of material.

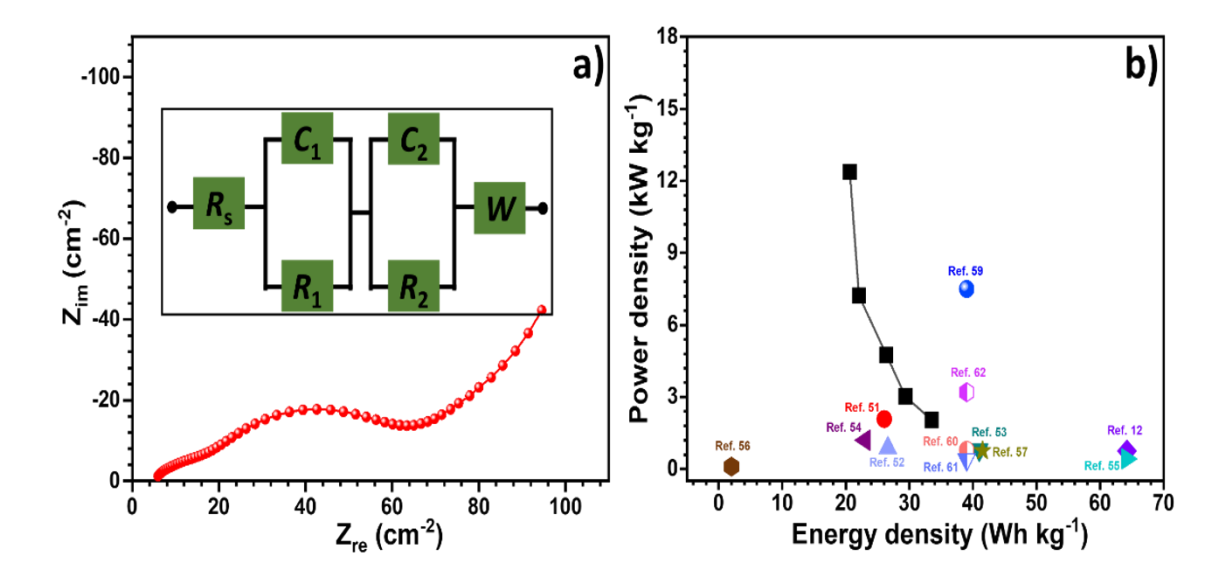


**Figure 5.9:** a) the Nyquist plot (inset shows equivalent electrical circuit), and b) Ragone plot of rGO-NiWO<sub>4</sub>/PVA-KOH/AC device.

Table 5.2: Comparative electrochemical parameters of previously reported supercapacitor devices with proposed rGO-NiWO<sub>4</sub>//AC ASC.

| Configuration   | Electrolyte | C <sub>s</sub> (F g <sup>-1</sup> ) | S <sub>E</sub> (Wh kg <sup>-1</sup> ) | S <sub>P</sub> (kW kg <sup>-1</sup> ) | Capacitance retention (%) (cycles) | Ref. |
|---|-------------|-------------------------------------|---------------------------------------|---------------------------------------|------------------------------------|------|
| NiCo <sub>2</sub> O <sub>4</sub> @NiMnO <sub>4</sub> //AC | 6 M KOH     | 206                                 | 64                                    | 0.75                                  | 87.7(5,000)                        | [33] |
| NiWO <sub>4</sub> -CoWO <sub>4</sub> //AC                 | 2 M KOH     | 136 C g <sup>-1</sup>               | 30.1                                  | 0.2                                   | 100 (5,000)                        | [34] |
| NiB//rGO  | 1 M KOH     | 83.33                               | 26                                    | 2                                     | 96(5,000)                          | [35] |
| Ni <sub>2</sub> P <sub>2</sub> O <sub>7</sub> //rGO       | 1 M KOH     | 74.81                               | 26.6                                  | 0.87                                  | 87.35(5,500)                       | [36] |

| NiMoO <sub>4</sub> -Ag/rGO//AC                                 | 6 M KOH  | 116                         | 41                    | 0.8                    | 73.3(8,000)  | [37]      |
|--|--|-----------------------------|-----------------------|------------------------|--------------|-----------|
| NiWO <sub>4</sub> //Fe <sub>2</sub> O <sub>3</sub>             | 2 M KOH  | 115                         | 23                    | 1.2                    | 78(5,000)    | [38]      |
| NiWO <sub>4</sub> //AC   | 6 M KOH  | 160                         | 64                    | 0.425                  | 93(5,000)    | [39]      |
| Al/lig-NiWO <sub>4</sub> //Al/AC                               | PVA/H <sub>3</sub> PO <sub>4</sub>             | 17 mF<br>cm <sup>-2</sup>   | 2 Wh cm <sup>-2</sup> | 100 W cm <sup>-2</sup> | 84(2,000)    | [40]      |
| NiCo <sub>2</sub> O <sub>4</sub> @NiWO <sub>4</sub> //AC       | 6 M KOH  | 132                         | 41.5                  | 0.76                   | -            | [41]      |
| Lignin/NiCoWO <sub>4</sub> //AC                                | PVA/H <sub>3</sub> PO <sub>4</sub>             | 33.2 mF<br>cm <sup>-2</sup> | 6                     | 855                    | 96.12(2,000) | [42]      |
| Ni-Co-O@rGO//AC  | 1 M KOH/<br>K <sub>3</sub> Fe(CN) <sub>6</sub> | 126                         | 39                    | 7.5                    | 60(3,000)    | [43]      |
| NiCoLDH//Fe <sub>2</sub> O <sub>3</sub>                        | 6 M KOH  | 158                         | 56.2                  | 0.8                    | 75 (10,000)  | [44]      |
| Ni-P//AC   | 2 M KOH  | 105                         | 29.2                  | 0.4                    | 84.5(1,000)  | [45]      |
| CoNiWO <sub>4</sub> /P-S-GNS//<br>CoNiWO <sub>4</sub> /P-S-GNS | 6 М КОН  | -                           | 100.8                 | 3.2                    | 95(7,500)    | [46]      |
| rGO-NiWO4//AC  | 2 M KOH  | 94.2                        | 33.5                  | 12.37                  | 83 (5,000)   | This work |

#### 5.5 Demonstration of rGO-NiWO4//AC Flexible asymmetric solid state device

The experiment involves the fabrication and testing of a supercapacitor device made from reduced graphene oxide (rGO) and nickel tungstate (NiWO<sub>4</sub>) with activated carbon (AC) as the counter electrode. Reduced graphene oxide (rGO) is used due to its high electrical conductivity, large surface area, and excellent mechanical properties. Nickel tungstate (NiWO<sub>4</sub>) is included for its high pseudocapacitance, which enhances the overall capacitance of the device. Activated carbon is commonly used in supercapacitors due to its high surface area and good electrochemical stability. It acts as the counter electrode in this device.

Moreover, two rGO-NiWO<sub>4</sub>//AC devices connected in series and charged for 30 s using a 3.2 V voltage illuminated table lamp of 11 white LED for 35 s. Photos of charging and discharging of ASC device is provided in following Image 5.2. This

demonstrates practical usability of fabricated rGO-NiWO<sub>4</sub>//AC supercapacitor. The observed initial power output of 347 mW indicates good charge-storing capacity of rGO-NiWO<sub>4</sub>//AC. This configuration increases the overall voltage of the system, which is beneficial for applications requiring higher voltage outputs. The devices were charged for 30 seconds using a 3.2 V voltage source. This short charging time indicates a rapid charge-discharge capability, which is crucial for practical applications of supercapacitors. The devices power 11 white LED table lamp for 35 seconds. The ability to power multiple LEDs demonstrates the practical energy storage and delivery capability of the supercapacitor.



**Image 5.2:** a) Charging and b) discharging demonstration of flexible ASC device.

The observed initial power output of 347 mW suggests that the supercapacitor has a significant charge-storing capacity. This high power output is indicative of the effective charge-discharge efficiency of the rGO-NiWO<sub>4</sub>//AC supercapacitor. The experiment demonstrates the practical usability of the fabricated supercapacitor in real-world

applications. Powering a table lamp of 5 Watt with multiple LEDs showcases the potential for using these supercapacitors in low-power electronic devices and possibly in larger-scale energy storage systems. The photos provided in Image 5.2 show the charging and discharging process, visually confirming the performance of the supercapacitor. These images serve as evidence of the successful operation of the device under the experimental conditions.

The rapid charging and effective discharging highlight the efficiency of rGO-NiWO<sub>4</sub>//AC supercapacitor. The high initial power output and practical demonstration suggest a good balance between energy density and power density, which is a critical factor for supercapacitor performance. The ability to power LEDs suggests potential applications in consumer electronics, renewable energy systems, and other fields where efficient energy storage and quick power delivery are essential.

This experiment successfully shows the practical application of rGO-NiWO<sub>4</sub>//AC supercapacitors, highlighting their potential for efficient energy storage and quick power delivery in real-world applications.

#### 5.6 Comparison of NiWO<sub>4</sub>/KOH/Fe<sub>2</sub>O<sub>3</sub> and rGO-NiWO<sub>4</sub>//AC devices

#### 1. Fabrication and material composition:

- The aqueous NiWO<sub>4</sub>/KOH/Fe<sub>2</sub>O<sub>3</sub> device uses pure NiWO<sub>4</sub> thin films, whereas rGO-NiWO<sub>4</sub>//AC flexible asymmetric solid state device incorporates a composite of reduced graphene oxide (rGO) and NiWO<sub>4</sub> using the SILAR method.
- The addition of rGO in the second device enhances the surface area and improves the electrochemical stability and performance.

#### 2. Electrochemical performance:

- The NiWO<sub>4</sub> thin films show a specific capacity of 213 mAh g<sup>-1</sup> with 87% retention after 5000 cycles.
- The rGO-NiWO<sub>4</sub> composite films exhibit a much higher specific capacitance of 779 F g<sup>-1</sup> with a higher retention of 95% after 5000 cycles.

#### 3. Energy storage and power output:

- The NiWO<sub>4</sub>/KOH/Fe<sub>2</sub>O<sub>3</sub> device offers a specific energy of 23 Wh kg<sup>-1</sup> and a specific power of 1.2 kW kg<sup>-1</sup>.
- The rGO-NiWO<sub>4</sub>//AC highest value of specific power is 12.37 kW kg<sup>-1</sup> at a specific energy of 33.5 Wh kg<sup>-1</sup>.
- The rGO-NiWO<sub>4</sub> composite electrode, when used in a solid-state ASC, shows lower specific capacitance (Cs of 94.2 F g<sup>-1</sup>) but maintains good performance under mechanical stress (bending stability).

#### 4. Cycling stability and application potential:

- The NiWO<sub>4</sub> thin film device has good cycling stability with 78% capacitance retention after 5000 GCD cycles at 2 A g<sup>-1</sup>.
- The rGO-NiWO<sub>4</sub> composite device shows excellent stability with 83% cycling performance over 5000 GCD cycles at 2 A g<sup>-1</sup> and impressive mechanical flexibility.
- Practical demonstration of rGO-NiWO<sub>4</sub>//AC device capability to light a
  table lamp of 5 Watt for 35 seconds indicates significant potential for
  various applications, especially where flexibility and stability are
  required.

#### **Conclusions**

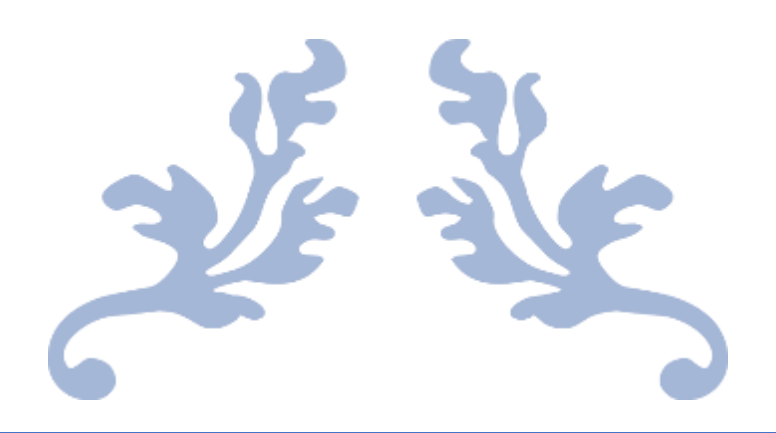
Both devices demonstrate significant advancements in electrochemical energy storage, rGO-NiWO<sub>4</sub> composite thin film device outperforms the pure NiWO<sub>4</sub> thin film device in terms of specific capacitance, cycle retention, and mechanical stability. The incorporation of rGO enhances the overall performance, making it more suitable for applications that require high flexibility and durability. The NiWO<sub>4</sub>/KOH/Fe<sub>2</sub>O<sub>3</sub> device offers a higher specific energy, which might be more advantageous for applications focused on energy density.

#### **References:**

- [1] D. P. Dubal, J. G. Kim, Y. Kim, R. Holze, W. B. Kim, Energy. Technol., 1, 2013, 125.
- [2] S. Shi, C. Xu, C. Yang, J. Li, H. Du, B. Li, F. Kang, Particuology, 11, 2013, 371.
- [3] L. Nyholm, G. Nystrom, A. Mihranyan, M. Stromme, Adv. Mater., 23, 2011, 3751.
- [4] P. Wen, M. Fan, D. Yang, Y. Wang, H. Cheng, J. Wang J. Power Sources, 320, 2016, 28.
- [5] B. G. Choi, S. J. Chang, C. P. Park, H. W. Kang, H. J. Kim, W. H. Hong, S. Lee, Y. S. Huh, Nanoscale, 4, 2012, 4983.
- [6] B. Zheng, T. Huang, L. Kou, X. Zhao, K. Gopalsamy, C. Gao, J. Mater. Chem. A, 2, 2014, 9736.
- [7] M. Jayalakshmi, M. M. Rao, B. M. Choudary, Electrochem. Commun., 6, 2004, 1119.
- [8] K. Krishnamoorthy, G. K. Veerasubramani, P. Pazhamalai, S. J. Kim, Electrochim. Acta, 190, 2016, 305.
- [9] Y. Munaiah, B. G. S. Raj, T. P. Kumar, P. Ragupathy, J. Mater. Chem. A, 1, 2013, 4300.
- [10] T. Brousse and D. Belanger, Electrochem. Solid-State Lett., 6, 2003, A244.
- [11] J. Wang, S. Liu, X. Zhang, X. Liu, X. Liu, N. Li, J. Zhao, Y. Li, Electrochim. Acta, 213, 2016, 663.
- [12] N. G. Bretesche, O. Crosnier, G. Buvat, F. Favier, T. Brousse J. Power Sources, 326, 2016, 695.
- [13] S. Zhang, B. Yin, Z. Wang, F. Peter, Chem. Eng. J., 306, 2016, 193.
- [14] L. Zhang, W. Zheng, H. Jiu, C. Ni, J. Chang, G. Qi, Electrochim. Acta, 215, 2016, 212.
- [15] E. Guneri, and A. Kariper, J. Alloys Compd., 516, 2012, 20.

- [16] S. Bernardini, F. Bellatreccia, A. C. Municchia, G. D. Ventura, A. SodoJ. Raman Spectrosc., 50, 2019, 873.
- [17] A. Phuruangrat, T. Thongtem, S. Thongtem Chalcogenide Lett., 8, 2011, 291.
- [18] P. R. Deshmukh, S. N. Pusawale, V. S. Jamadade, U. M. Patil, C. D. Lokhande, J. Alloys Compd., 509, 2011, 5064.
- [19] K. J. Huang, J. Z. Zhang, K. Xing, Electrochim. Acta, 149, 2014, 28.
- [20] Y. A. Kumar, K. D. Kumar, H. J. Kim, Electrochim. Acta. 330, 2020, 135261.
- [21] P. S. Kumar, P. Prakash, A. Srinivasan, C. Karuppiah, J. Power Sources, 482, 2021, 228892.
- [22] P. P. Bagwade, D. B. Malavekar, T. T. Ghogare, S. B. Ubale, V. J. Mane, R. N. Bulakhe, I. In, C. D. Lokhande, J. Alloys and Compd., 859, 2021, 157829.
- [23] J. Tian, Y. Xue, X. Yu, Y. Pei, H. Zhang, J. Wang, RSC Adv., 8, 2018, 41740.
- [24] L. Niu, Z. Li, Y. Xu, J. Sun, W. Hong, X. Liu, J. Wang, S. Yang, ACS Appl. Mater. Interfaces, 5, 2013, 8044.
- [25] Y. Wang, C. Shen, L. Niu, Z. Sun, F. Ruan, M. Xu, S. Shan, C. Li, X. Liu, Y. Gong, Mater. Chem. and Phys., 182, 2016, 394.
- [26] S. Jha, S. Mehta, Y. Chen, P. Renner, S. S. Sankar, D. Parkinson, S. Kundu, H. Liang, J. Mater. Chem. C, 8, 2020, 3418.
- [27] S. Chen, G. Yang, Y. Jia, H. Zheng, J. Mater. Chem. A, 5, 2017, 1028.
- [28] S. Jha, S. Mehta, E. Chen, S. S. Sankar, S. Kundu, H. Liang, Mater. Adv., 1, 2020, 2124.
- [29] A. Mirghni, M. Madito, K. Oyedotun, T. Masikhwa, N. Ndiaye, S. Ray, N. Manyala, RSC Adv, 8, 2018, 11608.
- [30] S. Zhang, B. Yin, Z. Wang, F. Peter, Chem. Eng. J; 306, 2016, 193.
- [31] M. Liu, J. Li, Y. Hu, Q. Yang, L. Kang, Electrochim. Acta, 201, 2016, 142.

- [32] H. Zhao, Z. Zhang, C. Zhou, H. Zhang, Appl. Surf. Sci., 541, 2021, 148458.
- [33] Y. Wang, C. Shen, L. Niu, Z. Sun, F. Ruan, M. Xu, S. Shan, C. Li, X. Liu, Y. Gong, Mater. Chem. Phys., 182, 2016, 394.
- [34] R. D. Kumar, Y. Andou, S. Karuppuchamy, J. Alloys Compd., 654, 2016, 349.
- [35] R. K. Tripathy, A. K. Samantara, J. N. Behera, Sustain. Energy Fuels., 5, 2021, 1184.
- [36] S. J. Marje, P. K. Katkar, S. S. Pujari, S. A. Khalate, A. C. Lokhande, U. M. Patil, Synth. Met., 259, 2020, 116224.
- [37] B. Huang, D. Yao, J. Yuan, Y. Tao, Y. Yin, G. He, H. Chen, J. Colloid Interface Sci., 606, 2022, 1652.
- [38] D. J. Patil, D. B. Malavekar, V. C. Lokhande, P. P. Bagwade, S. D. Khot, T. Ji, C. D. Lokhande, Energy Technol., 10, 2022, 2200295.
- [39] J. Tian, Y. Xue, X. Yu, Y. Pei, H. Zhang, J. Wang, RSC Adv., 8, 2018, 41740.
- [40] S. Jha, S. Mehta, Y. Chen, P. Renner, S.S. Sankar, D. Parkinson, S. Kundu, H. Liang, J. Mater. Chem. C. 8, 2020, 3418.
- [41] S. Chen, G. Yang, Y. Jia, H. Zheng, J. Mater. Chem. A. 5, 2017, 1028.
- [42] S. Jha, S. Mehta, E. Chen, S. S. Sankar, S. Kundu, H. Liang, Mater. Adv., 1, 2020, 2124.
- [43] C. Lamiel, Y.R. Lee, M.H. Cho, D. Tuma, J.-J. Shim, J. Colloid Interface Sci., 507, 2017, 300.
- [44] H. Liang, H. Jia, T. Lin, Z. Wang, C. Li, S. Chen, J. Qi, J. Cao, W. Fei, J. Feng, J. Colloid Interface Sci., 554, 2019, 59.
- [45] D. Wang, L. B. Kong, M. C. Liu, W. B. Zhang, Y. C. Luo, L. Kang, J. Power Sources., 274, 2015, 1107.
- [46] A. S. Rajpurohit, N. S. Punde, C. R. Rawool, A. K. Srivastava, Chem. Eng. J., 371, 2019, 679.



## 80-RECOMMONDATIONS SUMMARY AND FUTURE FINDINGS



## 80-RECOMMONDATIONS SUMMARY AND FUTURE FINDINGS

| Sr. No. | Title           |  |     |  |  |  |
|---------|-----------------|--|-----|--|--|--|
|         |                 |  |     |  |  |  |
| 6.1     | Recommendations |  |     |  |  |  |
| 6.2     | Conclusions     |  |     |  |  |  |
| 0.2     | Conclusions     |  |     |  |  |  |
| 6.3     | Summa           | 156  |     |  |  |  |
|         |                 |  |     |  |  |  |
| 6.4     | Future          | findings   | 158 |  |  |  |
|         | 6.4A            | Large area device study                            | 158 |  |  |  |
|         | 6.4B            | Reasons for stability decay and its investigations | 159 |  |  |  |

#### 80-Recommendations

#### **6.1 Recommendations:**

In this research, thin films of nickel tungstate and a composite of nickel tungstate reduced graphene oxide (rGO) were prepared using the successive ionic layer adsorption and reaction (SILAR) method. The enhancement of charge storage capacity in these thin film electrodes was achieved by improving the specific surface area. The primary goal of preparing the composite electrode was to enhance the specific capacitance and stability compared to the pristine nickel tungstate material. The aqueous and solid-state supercapacitor devices, fabricated using pristine and composite thin film electrodes, exhibited specific energy of 23 Wh kg<sup>-1</sup> at specific power of 1.2 kW kg<sup>-1</sup>, and specific energy of 33.5 Wh kg<sup>-1</sup> at specific power is 12.37 kW kg<sup>-1</sup>, respectively.

Ultimately, the research recommends that NiWO<sub>4</sub> thin film demonstrates optimal electrochemical performance at 1.5 M cationic concentration, while for rGO-NiWO<sub>4</sub>, it is at 12 mg mL<sup>-1</sup> rGO concentration. The optimized concentration of rGO for the best electrochemical performance is found to be 12 mg mL<sup>-1</sup>. The simplicity and scalability of the deposition method suggest its potential translation to an industrial level with minimal modifications.

#### **6.2 Conclusions:**

- 1. NiWO<sub>4</sub> thin films were deposited on stainless steel (SS) using the SILAR method, with thickness controlled by Ni<sup>2+</sup> ion concentration. The Crystallite size increases with an increase in thickness.
- 2. The electrode N3 achieved a high specific capacitance of 1536 F g<sup>-1</sup> and demonstrated 87% stability with lower impedance values, making it suitable for further use in ASC device fabrication.
- 3. The aqueous NiWO<sub>4</sub>/KOH/Fe<sub>2</sub>O<sub>3</sub> device offers a specific energy of 23 Wh  $kg^{-1}$  and a specific power of 1.2 kW  $kg^{-1}$ .
- 4. The composite of rGO with nickel tungstate improves the specific surface area, leading to an increase in electrochemically active sites and improved charge storage through a capacitive-assisted mechanism. Considering the low specific capacitance of pristine NiWO<sub>4</sub>, the optimization of the composition of each

- material is necessary. A concentration of 12 mg mL<sup>-1</sup> of rGO suspension for nickel tungstate provides a better effect on electrochemical properties.
- 5. A flexible asymmetric solid-state supercapacitor device fabricated using rGO-NiWO<sub>4</sub> and activated carbon delivers an energy density of 33.5 Wh kg<sup>-1</sup> at a power density of 12.37 W kg<sup>-1</sup>.
- 6. Both devices demonstrate significant advancements in electrochemical energy storage, the rGO-NiWO<sub>4</sub> composite thin film device outperforms the pure NiWO<sub>4</sub> thin film device in terms of specific capacitance, cycle retention, and mechanical stability. The incorporation of rGO enhances the overall performance of pristine NiWO<sub>4</sub>, making it more suitable for applications that require high flexibility and durability. The aqueous NiWO<sub>4</sub>/KOH/Fe<sub>2</sub>O<sub>3</sub> device, however, offers a higher specific energy, which might be more advantageous for applications focused on energy density.

#### **6.3 Summary**

This study focuses on the synthesis of nickel tungstate and a composite of reduced graphene oxide with nickel tungstate thin films using a simple, cost-effective, and binder-free chemical approach. Several preparative parameters were fine-tuned to achieve a porous surface morphology with an increased specific surface area, enhancing the electrochemical properties of NiWO<sub>4</sub> and rGO-NiWO<sub>4</sub> thin films. The composite thin films exhibited superior supercapacitive (SC) performance compared to pristine NiWO<sub>4</sub> and rGO-NiWO<sub>4</sub> thin film electrodes. Consequently, these composite thin film electrodes, characterized by excellent electrochemical features, were utilized as one electrode in the fabrication of ASC device. In addition, Fe<sub>2</sub>O<sub>3</sub> and activated carbon (AC) were chosen as positive electrodes due to their wide potential window.

This study demonstrates a synthesis of binder-free NiWO<sub>4</sub> thin films for electrochemical energy storage and opens a new path to improve specific energy (S<sub>E</sub>)

for energy storage devices. The effect of the concentration of cationic precursor on the thickness and morphology of the thin film was studied. The concentration of 0.15 M of NiSO<sub>4</sub> is optimum as beyond this concentration leads to nonadherent thin films. NiWO<sub>4</sub> with a specific capacity of 213 mAh g<sup>-1</sup> shows retention of 87% after 5000 cycles. Due to the optimum thin film thickness and morphology the excellent electrochemical performance of NiWO<sub>4</sub> thin films is achieved. Highest C<sub>8</sub> of 1536 F g<sup>-1</sup> and excellent stability of 87% with lower impedance values observed for N3 electrode. Therefore, this electrode was selected for the ASC device fabrication.

A facial SILAR method is used to deposit thin films of rGO-NiWO<sub>4</sub> composite on SS substrates. Electrodes deposited with 12 mg mL<sup>-1</sup> of rGO concentration showed spherical morphology of NiWO<sub>4</sub> on rGO sheets and 97 m<sup>2</sup> g<sup>-1</sup> surface area. This electrode exhibited highest C<sub>s</sub> of 779 F g<sup>-1</sup> with retention of 95% after 5000 cycles. The composite structure improved electrochemical stability. The charge stored through capacitive process increased for CNW1, CNW2, and CNW3 with the rGO content and decreased for CNW4.

The composite CNW3 electrode based solid-state ASC with a PVA-KOH gel electrolyte showed C<sub>s</sub> of 94.2 F g<sup>-1</sup> with retention of 85% at a 150° bending angle and 83% cycling performance over 5000 GCD cycles. More significantly, the series pairing of two rGO-NiWO<sub>4</sub>//AC devices illuminates table lamps for 35 s demonstrating the significant potential of the rGO-NiWO<sub>4</sub>//AC device in various applications.

#### **6.4 Future findings**

This study involved the synthesis of nickel tungstate thin films and their composites with rGO using the automated SILAR method. The incorporation of rGO

led to enhancements in electrical conductivity, specific surface area, and the overall electrochemical performance of the pristine NiWO<sub>4</sub> material. Alternatively, various carbon allotropes such as fullerene, carbon nanotubes (CNTs), carbon aerogel, and carbon foam can replace with rGO in the composite composition. Additionally, introducing other transition metals tungstates (Mn, Fe, Cu, Co) to form bimetallic compounds is suggested to further improve the electrochemical energy storage properties of the electrode material. To comprehend the energy storage process in transition metal oxide-based compounds, it is essential to conduct physical characterizations of these materials, examining changes in crystal structure, surface morphology, and chemical composition using techniques like X-ray diffraction (XRD), scanning electron microscopy (SEM), transmission electron microscopy (TEM), and X-ray photoelectron spectroscopy (XPS). Furthermore, gaining insights into the actual processes involved in charge storage can be achieved through in situ characterizations of ASC devices using TEM.

#### 6.4A Large area device study

In the pursuit of scalable energy storage solutions, future research on NiWO<sub>4</sub> and rGO-NiWO<sub>4</sub> supercapacitors is likely to emphasize the development and characterization of large-area devices. Investigations will focus on:

Reproducibility in electrochemical performance: Ensuring that the
electrochemical properties are consistent across larger surface areas, addressing
issues like potential gradient formation and current distribution.

- Manufacturing techniques: Refining deposition methods such as spray coating, spin coating, or printing methods to produce uniform and defect-free films over large areas.
- Interfacial engineering: Optimizing the interfaces between NiWO<sub>4</sub>, rGO, and current collectors to minimize resistance and enhance charge transfer across extensive areas.
- Mechanical flexibility and stability: To Study the mechanical properties of these materials when applied to flexible substrates, which is crucial for wearable electronics and flexible energy storage systems.

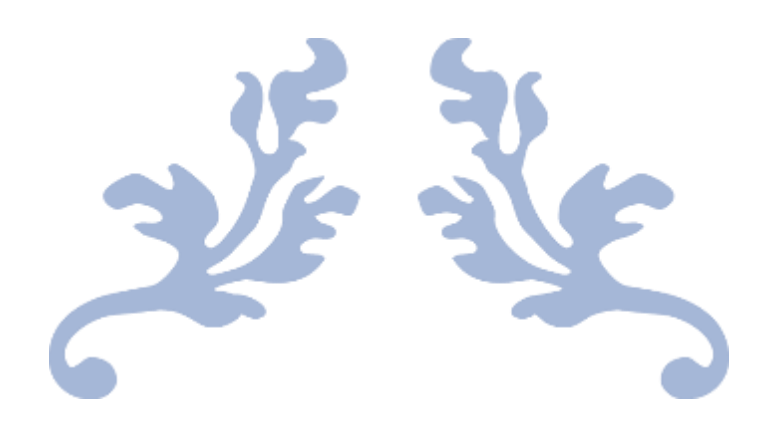
#### 6.4B Reasons for stability decay and its investigations:

Stability is a critical aspect of SC device performance. Future studies will delve deeper into the reasons behind the stability decay in NiWO<sub>4</sub> and rGO-NiWO<sub>4</sub> SCs devices:

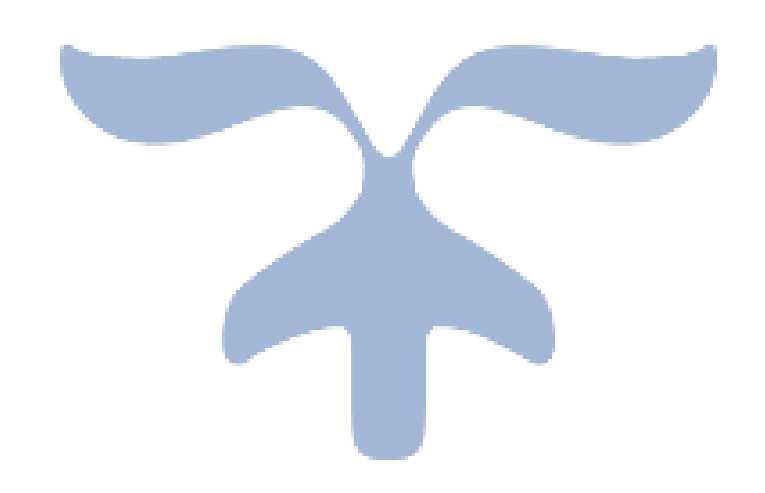
- **Electrochemical degradation**: Analyzing the changes in the electrochemical properties over long cycling periods to identify degradation mechanisms such as electrode dissolution, ion intercalation issues, and electrolyte decomposition.
- **Structural and morphological changes**: Utilizing advanced characterization techniques like in-situ TEM, XRD, and Raman spectroscopy to monitor the structural integrity of the materials during cycling and understand how structural changes affect performance.

- **Surface chemistry**: Investigating the surface reactions and chemical changes using techniques such as XPS and FTIR to determine how interactions with the electrolyte contribute to performance decay.
- Heat management: Studying the thermal effects on stability, as excessive heat generation during rapid charge/discharge cycles can accelerate degradation processes.
- Performance metrics for commercial application: Defining clear performance benchmarks for energy density, power density, cycle life, and operational stability that align with commercial application requirements.
- Reliability testing: Implementing rigorous reliability testing protocols to
  evaluate the long-term performance and durability of SCs under various
  operational conditions, including different temperatures, humidity levels, and
  mechanical stresses.

In short, future research on NiWO<sub>4</sub> and rGO-NiWO<sub>4</sub> supercapacitors will likely focus on addressing the challenges related to scaling up production, understanding and mitigating stability issues, and ensuring reproducibility and repeatability. These efforts will be crucial for the development of high-performance, durable, and commercially viable supercapacitors.



## **PUBLICATIONS**



Check for updates

www.entechnol.de

### Binder-Free Synthesis of Mesoporous Nickel Tungstate for Aqueous Asymmetric Supercapacitor Applications: Effect of Film Thickness

Dilip J. Patil, Dhanaji B. Malavekar, Vaibhav C. Lokhande, Prity P. Bagwade, Sambhaji D. Khot, Taeksoo Ji, and Chandrakant D. Lokhande\*

Nickel tungstate thin films of different thicknesses are synthesized using the binder-free successive ionic layer adsorption and reaction (SILAR) method at ambient temperature and subsequent calcination at a temperature of 727 K. The physicochemical characterizations of NiWO4 thin films are carried out using different techniques. The electrochemical performances of NiWO4 films are evaluated in 2 M KOH electrolyte using a standard three electrode system. The specific capacitance of 1536 F  $g^{-1}$  at the current density of 2 A  $g^{-1}$  is obtained for the NiWO<sub>4</sub> film. The film exhibits excellent electrochemical stability of 87% after 5000 galvanostatic charge-discharge (GCD) cycles at the current density of 3 A g<sup>-1</sup>. This study highlights use of SILAR-deposited NiWO<sub>4</sub> thin films as a cathode in aqueous asymmetric supercapacitors (ASCs). The ASC device NiWO<sub>4</sub>/  $KOH/Fe_2O_3$  exhibits a specific capacitance of 115 F g<sup>-1</sup> at 2 A g<sup>-1</sup> and specific energy of 23Wh kg<sup>-1</sup> at specific power of 1.2 kW kg<sup>-1</sup>. The device shows remarkable electrochemical cycling stability (78% capacitance retention after 5000 GCD cycles). The SILAR-deposited NiWO<sub>4</sub> thin films are expected to emerge as a potential candidate for supercapacitors.

1. Introduction

In the present era, environmental pollution originating from burning of hydrocarbon fuels is affecting human health along with the surrounding nature. So, the shifting of energy generation and usage habits became the need of an hour. Renewable energy generation/conversion is convincing path for the pollution-free environment. The major challenge faced by these sources is storage of energy because of abruption in the generation. The capacitors, batteries, and supercapacitors (SCs) have been used for electrochemical energy storage from a long time.

D. J. Patil, D. B. Malavekar, P. P. Bagwade, S. D. Khot, C. D. Lokhande Centre for Interdisciplinary Research

D. Y. Patil Education Society Kolhapur 416006, India

E-mail: I\_chandrakant@yahoo.com

V. C. Lokhande, T. Ji Department of Electronics and Computer Engineering Chonnam National University Gwangju 61186, South Korea

The ORCID identification number(s) for the author(s) of this article can be found under https://doi.org/10.1002/ente.202200295.

DOI: 10.1002/ente.202200295

However, the cost and the energy stored by these devices vary with the design, chemistry, and materials used to fabricate. The specific energy for batteries is comparatively more than the SCs and capacitors. [1,2] Due to outstanding cycle stability, greater power density, and rapid charge-discharge rate, SCs are some of the better optimistic contenders.[3,4] A significant drawback of SCs is that they are deficient in specific energy to fulfill the growing energy requirements for new-age energy storage equipment.<sup>[5,6]</sup> Nowadays, more research activities have been concentrated to enhance the specific energy of SCs without losing their specific power and cyclability. The specific energy ( $E = 0.5 CV^2$ ) can be raised by improving capacitance (C) and operating potential window (V). Different electroactive materials with rages of capacitance values have been used to fabricate SCs. [9–11] Hence, the preparation of

novel electrode materials possessing high specific capacitance and fabrication of asymmetric supercapacitors (ASCs) to overcome the issue of low cell potential can result in enhanced specific energy.[12,13]

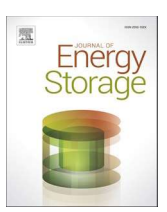
Metal tungstates have the general formula  $AWO_4$ , where A is a divalent cation ( $A^{2+}$  = Ni, Fe, Mn, Cu, Co) that acts as a network modifier. The monoclinic crystal structure of metal tungstates (shown in Figure 1a,b) resembles with the crystal structure of metal sulfates. [14] Crystal structure formed by tungstate ion with bivalent metal ion forms tetrahedral coordination. However, due to the smaller radius of bivalent cations like nickel having ionic radius of less than 0.77 Å will perform well for the supercapacitors. In addition to this, the bimetallic nature of the metal tungstates helps to improve the energy storage capacity of materials compared to a single metal compound like NiO and WO3. Compared to nickel oxide and hydroxide, NiWO4 have higher molecular mass, leading to lower theoretical capacitance. Higher cost of preparation due to addition of W in synthesis process can be considered a disadvantage. Metal oxides, including tungsten oxide and metal tungstates, show several advantages over other materials, such as low toxicity, low synthetic cost, high resistance against photocorrosion, and compatibility with up-scale. Normally, metal tungstate materials were tested for SC applications, [15] Li-ion battery, [16] electrocatalysis, [17] gas

ELSEVIER

Contents lists available at ScienceDirect

#### Journal of Energy Storage

journal homepage: www.elsevier.com/locate/est



#### Research papers



# Facial synthesis of reduced graphene oxide – Amorphous nickel tungstate composite for flexible hybrid asymmetric solid state supercapacitor application

D.J. Patil<sup>a,1</sup>, D.B. Malavekar<sup>b,1</sup>, J.H. Kim<sup>b</sup>, C.D. Lokhande<sup>a,\*</sup>

- <sup>a</sup> Centre for Interdisciplinary Research, D. Y. Patil Education Society (Deemed to Be University), Kolhapur 416 006, India
- <sup>b</sup> Department of Materials Science and Engineering, Chonnam National University, Gwangju 61186, South Korea

#### ARTICLE INFO

# Keywords: Asymmetric electrochemical supercapacitor Composite material Energy storage Nickel tungstate Reduced graphene oxide Successive ionic layer adsorption and reaction

#### ABSTRACT

Supercapacitors are crucial as an additional type of energy storage device assisting various types of energy storage systems for high power requirement. Herein, using successive ionic layer adsorption and reaction (SILAR) method, thin films of reduced graphene oxide (rGO) composited with nickel tungstate (NiWO<sub>4</sub>) were synthesized with different rGO content. The synthesized material showed spherical morphology with rGO sheets and a specific surface area in the range of 85 to 107 m<sup>2</sup> g<sup>-1</sup>. The three-electrode method was used, and the electrochemical performance of rGO-NiWO<sub>4</sub> films was assessed in 2 M KOH electrolyte. A composite film deposited at 12 mg mL<sup>-1</sup> concentration of rGO (CNW3) film exhibited a specific capacitance of 779 F g<sup>-1</sup> at a current density of 2 A g<sup>-1</sup>. At a current density of 4 A g<sup>-1</sup>, CNW3 film showed outstanding electrochemical stability with 95 % capacitance retention after 5000 galvanostatic charge-discharge (GCD) cycles. This study emphasizes the usage of rGO-NiWO<sub>4</sub> (CNW3) thin films deposited using SILAR method as a cathode in solid-state asymmetric supercapacitors (ASC). The rGO-NiWO<sub>4</sub>/PVA-KOH/AC ASC device exhibited a specific capacitance of 94.2 F g<sup>-1</sup> at 5 A g<sup>-1</sup>, a specific energy of 33.5 Wh kg<sup>-1</sup> and a specific power of 12.37 kW kg<sup>-1</sup> with 83 % capacitance retention after 5000 GCD cycles. This suggests that rGO-NiWO<sub>4</sub> thin film produced using SILAR method is a suitable candidate for supercapacitors.

#### 1. Introduction

Expanding energy storage requirements along with ecological challenges spurred extraordinary research for feasible and elective energy storage assets [1–3]. As aided energy storage device, supercapacitors (SCs) play a significant role because of its high power output, good cycle life, excellent efficiency, and comparative safe nature [4–6]. Therefore, it has been widely utilized in electric vehicles, portable electronics, and different microdevices [7,8] along with batteries and other electrical energy source. Moreover, the charge storage mechanism based classification divides SCs into two types: an electrochemical double-layer capacitor (EDLC) and a pseudocapacitor [9]. Generally, pseudocapacitors deliver a higher specific capacitance due to their redox reactions [10,11], while EDLC are proven materials considering stability. Different pseudocapacitive electrode materials, for example, polymers, metal oxides and hydroxides, sulfides, and phosphides, have received

tremendous exploration [12,13]. Binary metal oxides are distinguished among these electrode materials as a promising contender for SCs because of the conjunction of two different cations [20]. For example, CoMoO<sub>4</sub> [14], NiMoO<sub>4</sub> [15], NiCo<sub>2</sub>O<sub>4</sub> [16], NiWO<sub>4</sub> [17], NiMn<sub>2</sub>O<sub>4</sub> [18], and NiFe<sub>2</sub>O<sub>4</sub> [19] have been widely considered and explored materials for supercapacitor applications. Aside from their exceptional electrochemical properties, these binary metal oxides potentially provide stable performance as a supercapacitive material. Composition of an EDLC material with the pseudocapacitive material improves surface area, and modulates crystallinity and therefore enhances electrochemical performance and stability [20]. Considering this, several studies highlighted improvement in the material electrochemical performance [21,22]. However, fabrication of composite material with optimum ratio of EDLC and pseudocapacitive material remains a challenge [23,24].

In comparison to single metal oxides, bimetal oxides are able to provide better energy storage due to rearranged d-band electron density

E-mail address: <a href="mailto:lchandrakant@yahoo.com">lchandrakant@yahoo.com</a> (C.D. Lokhande).

<sup>\*</sup> Corresponding author.

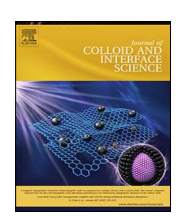
<sup>&</sup>lt;sup>1</sup> Authors contributed equally.

ELSEVIER

Contents lists available at ScienceDirect

#### Journal of Colloid and Interface Science

journal homepage: www.elsevier.com/locate/jcis



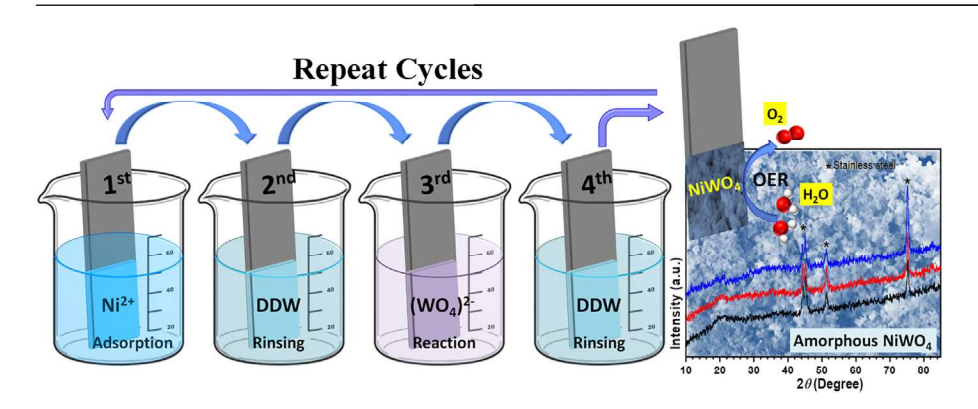
## Amorphous nickel tungstate films prepared by SILAR method for electrocatalytic oxygen evolution reaction



D.B. Malavekar <sup>a</sup>, V.C. Lokhande <sup>b</sup>, D.J. Patil <sup>c</sup>, S.B. Kale <sup>a</sup>, U.M. Patil <sup>a</sup>, T. Ji <sup>b</sup>, C.D. Lokhande <sup>a,\*</sup>

- <sup>a</sup> Centre for Interdisciplinary Research, D. Y. Patil Education Society, Kolhapur 416 006, India
- <sup>b</sup> Department of Electronics and Computer Engineering, Chonnam National University, Gwangju 61186, South Korea
- <sup>c</sup> Department of General Engineering, D. Y. Patil Technical Campus, Talsande 416 112, India

#### G R A P H I C A L A B S T R A C T



#### ARTICLE INFO

Article history: Received 18 August 2021 Revised 11 November 2021 Accepted 14 November 2021 Available online 17 November 2021

Keywords:
Amorphous electrocatalyst
Nickel tungstate
Successive ionic layer adsorption and
reaction (SILAR)
Thin film, Water electrocatalysis

#### ABSTRACT

Development of electrocatalyst using facile way from non-noble metal compounds with high efficiency for effective water electrolysis is highly demanding for production of hydrogen energy. Nickel based electrocatalysts were currently developed for electrochemical water oxidation in alkaline pH. Herein, amorphous nickel tungstate (NiWO<sub>4</sub>) was synthesized using the facile successive ionic layer adsorption and reaction method. The films were characterized by X-ray diffraction, Raman spectroscopy, Fourier transfer infrared spectroscopy, scanning electron microscopy, X-ray photoelectron spectroscopy, and transmission electron microscopy techniques. The electrochemical analysis showed 315 mV of overpotential at 100 mA cm<sup>-2</sup> with lowest Tafel slope of 32 mV dec<sup>-1</sup> for oxygen evolution reaction (OER) making films of NiWO<sub>4</sub> compatible towards electrocatalysis of water in alkaline media. The chronopotentiometry measurements at 100 mA cm<sup>-2</sup> over 24 h showed 97% retention of OER activity. The electrochemical active surface area (ECSA) of NW120 film was 25.5 cm<sup>-2</sup>.

© 2021 Elsevier Inc. All rights reserved.

#### 1. Introduction

The serious environmental issues associated with the fossil fuels have speeded up the adoption of alternate energy sources mainly wind turbine, solar photovoltaic and hydrogen [1,2]. Hydrogen is considered as a most promising green fuel for future.

<sup>\*</sup> Corresponding author.

E-mail address: l\_chandrakant@yahoo.com (C.D. Lokhande).

#### ARTICLE IN PRESS

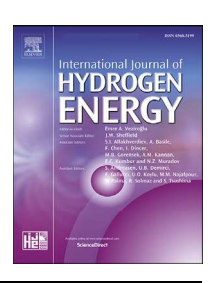
INTERNATIONAL JOURNAL OF HYDROGEN ENERGY XXX (XXXX) XXX



Available online at www.sciencedirect.com

#### **ScienceDirect**

journal homepage: www.elsevier.com/locate/he



# Nanocrystalline cobalt tungstate thin films prepared by SILAR method for electrocatalytic oxygen evolution reaction

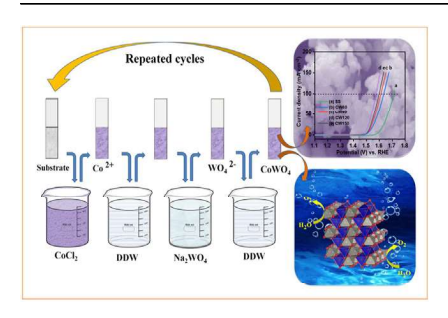
P.P. Bagwade, D.B. Malavekar, V.V. Magdum, S.D. Khot, R.P. Nikam, D.J. Patil, U.M. Patil, C.D. Lokhande\*

Centre for Interdisciplinary Research, D. Y. Patil Education Society, Kolhapur 416 006, India

#### HIGHLIGHTS

- CoWO<sub>4</sub> thin film electrocatalysts prepared by SILAR method was employed for oxygen evolution reaction.
- The CoWO<sub>4</sub> material exhibited porous morphology with specific surface area of 49.3 m<sup>2</sup> g<sup>-1</sup>.
- CoWO<sub>4</sub> electrode exhibited excellent OER functioning with overpotential of 330 mV at a current density of 100 mA cm<sup>-2</sup>.
- CoWO<sub>4</sub> thin film electrode exhibited remarkable stability (97%) after 24 h in 1 M KOH.

#### G R A P H I C A L A B S T R A C T



#### ARTICLE INFO

Article history:
Received 7 July 2022
Received in revised form
30 September 2022
Accepted 9 November 2022
Available online xxx

Keywords:
Cobalt tungstate
Thin film
Electrocatalyst
Oxygen evolution reaction
Successive ionic layer adsorption
and reaction (SILAR)

#### ABSTRACT

This study highlights on the application of nanocrystalline cobalt tungstate (CoWO<sub>4</sub>) thin films as an electrocatalyst for oxygen evolution reaction (OER) prepared using successive ionic layer adsorption and reaction (SILAR) method. The X-ray diffraction, scanning electron microscopy, X-ray photoelectron spectroscopy, Fourier transform infrared spectroscopy etc. were employed for the characterization of CoWO<sub>4</sub> thin films, revealing the formation of crystalline CoWO<sub>4</sub> with spherical morphology. Furthermore, CoWO<sub>4</sub> showed excellent electrochemical performance with the overpotential of 330 mV and Tafel slope of 153 mV dec $^{-1}$  with retaining 97% of electrochemical stability after 24 h of OER. The study confirmed the structural maintenance of CoWO<sub>4</sub> thin films after stability study.

© 2022 Hydrogen Energy Publications LLC. Published by Elsevier Ltd. All rights reserved.

E-mail address: l\_chandrakant@yahoo.com (C.D. Lokhande).

https://doi.org/10.1016/j.ijhydene.2022.11.090

0360-3199/© 2022 Hydrogen Energy Publications LLC. Published by Elsevier Ltd. All rights reserved.

Please cite this article as: Bagwade PP et al., Nanocrystalline cobalt tungstate thin films prepared by SILAR method for electrocatalytic oxygen evolution reaction, International Journal of Hydrogen Energy, https://doi.org/10.1016/j.ijhydene.2022.11.090

<sup>\*</sup> Corresponding author.

ELSEVIER

Contents lists available at ScienceDirect

#### Synthetic Metals

journal homepage: www.elsevier.com/locate/synmet





## SILAR synthesized dysprosium selenide (Dy<sub>2</sub>Se<sub>3</sub>) thin films for hybrid electrochemical capacitors

S.D. Khot <sup>a</sup>, D.B. Malavekar <sup>a</sup>, R.P. Nikam <sup>a</sup>, S.B. Ubale <sup>a</sup>, P.P. Bagwade <sup>a</sup>, D.J. Patil <sup>a</sup>, V.C. Lokhande <sup>b</sup>, C.D. Lokhande <sup>a</sup>, \*

- <sup>a</sup> Centre for Interdisciplinary Research, D.Y. Patil Education Society, Kolhapur 416006, India
- <sup>b</sup> Department of Electronics and Computer Engineering, Chonnam National University, Gwangju 61186, South Korea

#### ARTICLE INFO

# Keywords: Dysprosium selenide Flexible hybrid electrochemical capacitor Successive ionic layer adsorption and reaction (SILAR) method Thin film

#### ABSTRACT

As the necessity of energy storage is continuously increasing, new materials have been investigated for electrochemical energy storage, especially for electrochemical capacitors. These storage devices are rapidly convertible as well as air pollution free. Therefore, a number of materials have been explored as electrode materials for supercapacitors to fulfill different requirements of electrochemical energy storage. Herewith, dysprosium selenide (Dy<sub>2</sub>Se<sub>3</sub>) films were prepared using the simple successive ionic layer adsorption and reaction (SILAR) method and characterized using different physico-chemical techniques. The specific capacitance ( $C_s$ ) of 92 F g<sup>-1</sup> was obtained at the current density of 2.85 A g<sup>-1</sup> in 1 M LiClO<sub>4</sub> electrolyte with a retention of 85% over 5000 galvanostatic charge-discharge (GCD) cycles performed at a current density of 4 A g<sup>-1</sup>. The flexible solid-state hybrid electrochemical capacitor of configuration Dy<sub>2</sub>Se<sub>3</sub>/LiClO<sub>4</sub>-PVA/MnO<sub>2</sub> showed  $C_s$  of 83 F g<sup>-1</sup> and specific energy of 18 Wh kg<sup>-1</sup> at a specific power of 2.7 kW kg<sup>-1</sup>. This hybrid device retained 92% of capacitance at a device bending angle of 160°. These results demonstrate the facile synthesis of Dy<sub>2</sub>Se<sub>3</sub> and its possible use in electrochemical energy storage applications.

#### 1. Introduction

In everyday life, advancing technology has made the most significant impact on the working nature of people. Therefore, it is essential to develop cheap and sophisticated technologies in the electronics, automobile industry, home appliances, biomedical field, etc., to uplift the quality of the human lifestyle. For this, a sustainable, green, and high-performance energy storage system is required which will play a vital role in our modern society [1]. There are different energy storage systems, but batteries, capacitors, and electrochemical capacitors (EC) are most promising. Among these, the charge accumulation mechanism is dissimilar for each of them. Currently, batteries have high energy density but possess disadvantages like low power density, finite cycle life, high cost of manufacturing, and several hours of charging time. The use of ECs can reduce those disadvantages due to their ability to deliver energy at a high rate, fast charging and discharging, efficient fabrication process, and long cycle life and hence gained significant attention in recent time [2,3]

The types of ECs materials mainly depend on the charge storage

mechanism. They are broadly listed into three categories, i.e. electric double-layer capacitors (EDLC), pseudocapacitors and battery-type ECs. Charge accumulation in EDLCs is due to electrostatic mechanism across the electrode and electrolyte interface. The carbon derivatives and MXenes are of EDLCs type materials. In pseudocapacitors, redox reactions occurring on the surface and interior of the electrodes are responsible for charge accumulation. Metal oxides, chalcogenides as well as conducting polymers are the pseudocapacitive electrode materials. The battery-type ECs obey the faradic mechanism of charge storage [4,5]. Mostly nickel and iron oxides and phosphates are used as battery-type materials.

Due to their excellent redox activity, metal chalcogenides and conducting polymers show excellent pseudocapacitive behavior with high specific capacitance ( $C_s$ ) than EDLCs [6]. The electrode material structure plays an important role by providing access to the electrolyte ions to electrode material for interaction. Many factors affect the electrode's charge storage, i.e., type of crystal structure, surface morphology, elemental composition, electrical resistivity, deposited mass of the electrode, and chemical composition [7]. The method of preparation

E-mail address: 1\_chandrakant@yahoo.com (C.D. Lokhande).

<sup>\*</sup> Corresponding author.



## Dual functional SILAR deposited NiWO<sub>4</sub> electrocatalyst for non-enzymatic glucose sensing and hydrogen evolution reaction

S. B. Jadhav<sup>1</sup> D. D. B. Malavekar<sup>1</sup> · D. J. Patil<sup>1</sup> · S. S. Pujari<sup>1</sup> · U. M. Patil<sup>1</sup> · C. D. Lokhande<sup>1</sup> · P. N. Pawaskar<sup>1</sup>

Received: 7 February 2023 / Accepted: 19 June 2023 © The Author(s), under exclusive licence to Springer-Verlag GmbH, DE part of Springer Nature 2023

#### **Abstract**

An effective route towards improving the electrocatalytic performance of materials is the synthesis of nanocrystalline, porous, and layer-structured materials. Herein, porous nickel tungstate (NiWO<sub>4</sub>) film electrode was prepared on stainless steel (SS) substrate by inexpensive successive ionic layer adsorption and reaction (SILAR) method. This method provides a binder-free, porous, and nanocrystalline thin layer on a SS substrate. The electrocatalytic performance of the nanocrystalline NiWO<sub>4</sub> electrocatalyst was evaluated for enzymeless glucose measurement and water-splitting application. This electrocatalyst exhibited excellent sensitivity of 9731 μA mM<sup>-1</sup> cm<sup>-2</sup> within the linear range of 25–325 μM. Further, the glucose concentrations present in human blood samples were measured using the proposed nanocrystalline NiWO<sub>4</sub> electrocatalyst. Also, hydrogen evolution reaction, the electrocatalyst exhibited 171 mV of overpotential at 10 mA cm<sup>-2</sup> with a Tafel slope of 70 mV dec<sup>-1</sup>. Further, chronopotentiometry study was carried out at 100 mA cm<sup>-2</sup> and it showed 94% retention after 24 h. These findings greatly promote the outstanding electrocatalytic performance of nanocrystalline and porous NiWO<sub>4</sub> electrocatalysts that outline their applicability for electrochemical catalysis purposes.

**Keywords** Electrocatalyst · Hydrogen evolution reaction · Nickel tungstate · Non-enzymatic glucose sensing · Thin film

#### 1 Introduction

Several catalyst materials for various types of electrocatalytic processes have been invented so far. Research on the synthesis of economical catalyst materials has been persuaded for a long time. Inestimable research in electrochemical catalysis has been performed due to its clean, rapid, and economic nature [1]. Innovative ways have been implemented for the synthesis of electrocatalytic materials, such as the formation of meso/microporous materials, layered structures, synthesis of multi-metallic materials, and composite materials [2]. A reduction in crystallinity results in an enhancement of defect sites in the material, which will create the possibility of improvements in electrochemical activity. However, the surge in defects reduces

S. B. Jadhav, D. B. Malavekar have authors equally contributed.

P. N. Pawaskar samgrish@gmail.com

Published online: 30 June 2023

Centre for Interdisciplinary Research, D. Y. Patil Education Society (Institution Deemed to be University), Kolhapur 416 006, India the conductivity of the material and causes additional resistance from charge transfer at grain boundaries [3, 4]. So, the appropriate nature of crystallinity is crucial for an excellent electrocatalysis process [5]. The synthesis of porous catalyst materials will overcome the shortcomings caused by their excessive nanocrystalline nature. The porous nature allows the percolation of electrolytes inside the material [6]. Therefore, optimized nanocrystalline and porous nature will be beneficial for excellent electrocatalytic performance.

For non-enzymatic glucose sensing and water splitting, binder-free, nanocrystalline, and porous electrocatalytic materials are required. Binder-free nature reduces resistive parameters and provides more active sites for catalysis, which could not be the case with the binder [7]. The atomic defects generated in nanocrystalline nature provide tremendous amounts of electroactive sites. The homogeneous nature and short-range ordering of these materials favor electrocatalysis. In addition to this, the appropriate porosity of the material would be an advantage. The catalytic material's porosity will assist the electrolyte diffusion inside the electrode, providing additional active sites [8].

Considering the above points, the preparation of novel nanocrystalline materials for catalysis purposes has become







## دی انٹیلیکچولپراپرٹیگورنمنٹ آف انڈیا. அறிவுசா **पेटेंट**ा**प्रमाण्**भ**रपत्र**

बौद्धिङसंप्रधानुंडार्यावय, भारतसरङार, का**पेटेंट कायोलय,भारता सरकार** का The Patent Office, Government Of India Patent Certificate

बौद्धिक सम्पत्ति कार्यालयं, भारत सरकार, 👊 (पेटेंर्ट नियमावली का नियम 74) । 🎎 (Rule 74 of The Patents Rules) ప్రభుత్వము, 8 गिण अम्मारेस प्राधि परि 🏴 ैगmm ී ピん 🏗 万医ស र्रि रे, बुद्दिगोनां नबां बिसंथान , भारत सरकार, बौद्धिकं संपदा कार्यालय, भारत सरकार, Intellectual Property Office, Government o

पेटेंट सं ने Patent No. मनवान, Фъявл G2CME bakwa 479403m.c. Фвяряю короля, बौद्धिक संपदा चा कार्यालय, भारत सरकार, 60 .انشورانه ملكيت جو அற்திய அரசு, இவ் வெள்வ அலுவலகம், இந்திய அரசு, آفس آف دی انٹیلیکچولپراپرٹیگورنمنٹ آف انڈیا

आवेदन सं. / Application No.पत्ति कार्यालयं, भारत संरकार 202221039656 الطليكونال برابرتي, మేధో సంపత్తి కార్యాలయము, భారత ప్రభుత్వము

गर्यालय, जन्नज जन्म<u>1/07/2022 संपदा दफ्तर, भारत सरकार,</u> (वौद्धिक जम्भन कार्यालय, जा

आविष्कारकों का नाम /Name of Inventor(s)

फाइल करने की तारीख / Date of Filing भारत सरकार, भारित सरकार, भारत सरकार D.Y.PATIL EDUCATION SOCIETY (DEEMED TO BE

UNIVERSITY), KASABA BAWADA, KOLHAPUR

বৌদ্ধিক সম্পত্তিৰ কাৰ্যালয়, ভাৰত চৰকাৰ, बौद्धिक संपदा दफ्तर, भारत सरकार, বৌদ্ধিক সম্পদ কাৰ্যালয়,ভারত সরকার, ফ্র'ণ্ট্রেষ্ঠ শুঠ, ইঞ্চংট, ফ্রার্ট

1.PROF.CHANDRAKANT DNYANDEV LOKHANDE 2.MR.DILIP JAGANNATH PATIL 3.DR.DHANAJI BALASO MALAVEKAR കാര്യാലയം, ഭാരത സർക്കാർ, बौद्धिक संपदा कार्यालय, भारत 4.MR.SAMBHAJI DINKAR KHOT 5.MR.RAN<mark>JIT PAN</mark>DURANG **NIKAM** 

प्रमाणित किया जाता है कि पेटेंटी को, उपरोक्त आवेदन में यथाप्रकटित A METHOD OF SYNTHESIZING COMPOSITE OF REDUCED GRAPHENE OXIDE AND NICKEL TUNGSTATE FOR ENERGY STORAGE नामक आविष्कार के लिए, पेटेंट अधिनियम, 1970 के उपबंधों के अनुसार आज तारीख जुलाई 2022 के ग्यारहवें दिन से बीस वर्ष की अविध के लिए पेटेंट अनुदत्त किया गया है। வுசார் சொத்து அலுவலகம். இந்திய அர

It is hereby certified that a patent has been granted to the patentee for an invention entitled A METHOD OF SYNTHESIZING COMPOSITE OF REDUCED GRAPHENE OXIDE AND NICKEL TUNGSTATE FOR ENERGY STORAGE as disclosed in the above mentioned application for the term of 20 years from the 11th day of July 2022 in accordance with the provisions of the Patents Act, 1970. Accordance with the provisions of the Patents Act, 1970.

<sup>विकाब</sup> अनुदान की तारीख : भ 08/12/2023 Date of Grant :

அறிவுசார் சொத்து அலுவலகம், இந்திய



पदा कार्यालय, भा Controller of Patents

**टिप्पणी** - इस पेटेंट के नवीकरण के लिए फीस, यदि इसे बनाए रखा जाना है, जुलाई 2024 के ग्यारहवें दिन को और उसके पश्चात प्रत्येक वर्ष मे उसी दिन देय होगी। Note. - The fees for renewal of this patent, if it is to be maintained, will fall / has fallen due on 11<sup>th</sup> day of July 2024 and on the same day

انشورانه ملڪيت جو ,அறிவுசார் கொத்து அலுவலகம், இந்திய அரசு آفس آف دي انٹيليکچولپراپرٹيگورنمنٹ آف انڈيا ,बार्यिगालय, ଭାରତ ସରକାର, انشورانه ملڪيت جو

ಕ್ವಿಮ್ ಆ





## دى انٹیلیکچولپراپرٹیگورنمنٹ آف انڈیا, அறிவுசா**ऐटेंट**न**प्रमाण्**भुद्**रत्र**

बौद्धिङसंप्रधानुंडार्यावय, लारतसरङार, का**पेटेंट कायोलय,भारत**ासरकार कल The Patent Office, Government Of India Patent Certificate

🏴 ैग台集。 ७५ 🖒 🏗 万匹死 「ऐरे, बुद्दिगोनां नर्वा बिसंथान , भारत सरकार, बौद्धिकं संपदा कार्यालय, भारत सरकार, Intellectual Property Office, Governme

पेटेंट सं ने Patent No. मनवान, Фъявл G2CME bakw.a 473475m.c. Фвяряю короля, बौद्धिक संपदा चा कार्यालय, भारत सरकार, 60

आवेदन सं. / Application No. पति कार्यालयं, भारत र रकार 202121062097 التليكجوئل يرايرني Аpplication No. पति कार्यालयं, भारत र रकार 202121062097

फाइल करने की तारीख / Date of Filing

D.Y.PATIL EDUCATION SOCIETY (DEEMED TO BE UNIVERSITY), KASAB BAWADA, KOLHAPUR

1.PROF.CHANDRAKANT DYANDEV LOKHANDE 2.MR.RANJIT आविष्कारकों का नाम /Name of Inventor(s) PANDURANG NIKAM 3.MR. SAMBHAJI DINKAR KHOT കാര്യാലയം, ഭാരത സർക്കാർ, बौद्धिक संपदा कार्यालय, भारत 4.MISS.PRITY PRAKASH BAGWADE 5.MR.DILIP JAGANNATH മെ ര PATIL

.انشورانه ملكيت جو அற்திய அரசு, இவ் வெள்வ அலுவலகம், இந்திய அரசு, آفس آف دی انٹیلیکچولپراپرٹیگورنمنٹ آف انڈیا

प्रमाणित किया जाता है कि पेटेंटी को, उपरोक्त आवेदन में यथाप्रकटित "CHEMICAL SYNTHESIS OF CADMIUM SELENIDE/REDUCED GRAPHENE OXIDE COMPOSITE THIN FILM AND PHOTOELECTROCHEMICAL CELL APPLICATION." नामक आविष्कार के लिए, पेटेंट अधिनियम, 1970 के उपबंधों के अनुसार आज तारीख दिसम्बर 2021 के इकत्तीसवें दिन से बीस वर्ष की अवधि के लिए पेटेंट अनुदत्त किया गया है।

It is hereby certified that a patent has been granted to the patentee for an invention entitled "CHEMICAL SYNTHESIS OF CADMIUM SELENIDE/REDUCED GRAPHENE OXIDE COMPOSITE THIN FILM AND PHOTOELECTROCHEMICAL CELL APPLICATION." as disclosed in the above mentioned application for the term of 20 years from the 31st day of December 2021 in accordance with the provisions of the Patents Act.1970 الثليكجوئل برايرتي آفس، حكومت بند ,बौद्धिक सम्पत्ति कार्यालयं, भारत सरकार, دفتر، هنرAct.1970 دفتر، هنر

विकास अनदान की तारीख र : भा Date of Grant :

அறிவுசார் சொத்து அலுவலகம், இந்திய

28/11/2023

संपदा कार्यालय, भ Controller of Patents

**टिप्पणी** - इस पेटेंट के नवीकरण के लिए फीस, यदि इसे बनाए रखा जाना है, दिसम्बर 2023 के इकत्तीसवें दिन को और उसके पश्चात प्रत्येक वर्ष मे उसी दिन देय होगी। Note. - The fees for renewal of this patent, if it is to be maintained, will fall / has fallen due on 31st day of December 2023 and on the

انشورانه ملكيت حي அறிவுசார் சொத்து அலுவலகம், இந்திய அரசு, آفس آف دي انٹيليکچولپراپرٹيگورنمنٹ آف انڈیا ,बार्यिगालय, ଭାରତ ସରକାର, இந்திய அரசு